Multi-functionalized gold nanoparticles for the delivery of biomolecules

Memoria presentada para optar al título de

Doctor en Química Orgánica

por

Eduardo García Garrido

Director: Álvaro Somoza Calatrava

Tutor: M. Salomé Rodríguez-Morgade

Madrid, 2021

Agradecimientos

Una tesis doctoral es un periplo en el que solo unas pocas personas logran embarcarse y de la que es imposible salir ileso sin unas manos amigas que te apoyen incondicionalmente. Esos seres merecen ser inmortalizados en las siguientes líneas.

En primer lugar, a mi madre y mi abuela, por su amor incondicional que ha sido una constante estos años y que sin el cual habría sido imposible salir adelante. A mi dulce Patricia, mi compañera en esta aventura y en muchas más, cuya sola presencia me ha ayudado a levantarme y trabajar, y cuyo seguimiento en esta tesis debería ser recompensado por lo menos con un master. A mis peludos y plumíferos amigos, Drako, Eri y Grissam, que comenzaron conmigo este proyecto, aunque no puedan verme acabarlo en persona. Y a mis compañeros de piso Nevado, Manolito, Chirri, Pucho, Kairi y Naminé, que me animaron desde el salón con ladridos, “pios” y “cuis” todas las mañanas.

A Álvaro, mi director, al que agradezco infinitamente la oportunidad que me brindo ya hace más de 4 años. Gracias por tus enseñanzas y consejos, por darme libertad para explorar el mundo de la nanociencia y darme la oportunidad de crecer hasta quien soy ahora. Gracias a ello he podido conocer a gente muy especial a los que tengo que agradecer infinidad de buenos momentos. A Šárka, la corredora de elite y gran apoyo durante mis primeros meses en el grupo; a Ana B. por ayudarme a integrarme en el grupo; a Paula, por hacer las largas horas en el laboratorio muchísimo más divertidas (¡y también fuera!); a Ciro, el mayor *geek* que conozco, siempre animando; a Nuria, la chica de verde que ha cambiado mi percepción de ese color para siempre; a Demi, alegrando siempre las conversaciones con datos interesantes; a Cata, siempre dulce y positiva, alguien con la que siempre se puede contar; a Carmen, mi principal apoyo en discusiones de series y películas; a María, siempre alegre y principal *hater* de mis partículas; a Sonia, por siempre apoyarme dentro y fuera del laboratorio con mis ambiciones; a Zulay, por su risa contagios; a Mila, siempre alegrando el ambiente por su paso; a Rama, gran amiga, confidente y aventurera; a Arturo, por hacer los últimos meses más divertidos; a Irene P, por ser la única persona

igual de obsesionada con *The Office* que yo; a Irene I., por tan buenos momentos en el laboratorio en estos últimos meses; a Sara, gran amiga, siempre dispuesta a viajar o a relajarse entre la naturaleza; a Ana A., siempre siempre sonriente, un amiga que siempre está ahí; a Bea, mi más extrovertida amiga, siempre riendo y siempre con tema de conversación; a Lucía, la poeta, siempre apoyando mi lado artístico; a todos los que han pasado por IMDEA y que han hecho mi periodo en esta institución más fácil y agradable: Mercedes, Marco, Jordi, Bea A., Carol, David, Julia, Bego, Esther, Lucía, Sergio, Andrés, Roberto, Félix, Mercy, Mel; y a todos los amigos que se han quedado, dándome su apoyo desde fuera del laboratorio: Pablo, Shin, Ignacio, Elena, Loli, Ricardo y Carolina.

A todos. Muchas gracias por hacer este periodo inolvidable.

Abstract

This thesis is focused on the use of gold nanoparticles (AuNPs) for the delivery of biomolecules. These nanomaterials are of great interest in the nanomedicine field due to their low toxicity, high biocompatibility, and easy-to-tailor surface, making them suitable for different bio-applications. For this project, we focused on their potential role as carriers of biomolecules, such as oligonucleotides, plasmids or proteins, to treat cancer-related diseases.

In order to fulfill this objective, a novel system based on the multi-functionalization of gold nanoparticles with modified polymers has been developed. The gold nanoparticles formulation developed consists of a combination of polymeric mixed layer of polyethylene glycol (PEG) and branched polyethylenimine (bPEI), and layer-by-layer assembly of bPEI through a sensitive linker. The nanostructures generated here provide a non-toxic and powerful system for the electrostatic conjugation of different biomolecules, being mainly optimized for the delivery and transfection of oligonucleotides in tumoral cells.

The designed system was optimized using different gold nanoparticles core sizes and branched polyethylenimines chains, leading to the obtentions of 12 different formulations, which were evaluated in terms of stability, reproducibility, toxicity, conjugation and transfection efficacy. The one with the best properties was employed as a nanocarrier of antisense oligonucleotides to downregulated tumoral cell lines carrying mutant p53 proteins.

Additionally, a novel building block for the solid synthesis of oligonucleotides was developed. The building block, consisting of a sensitive stimulus cross-linker attached to a controlled pore glass (CPG) solid support. The oligonucleotides prepared with this derivative were able to be conjugated easily with biomolecules through the formation of a disulfide moiety.

Resumen

Esta tesis se ha enfocado en el uso de nano-partículas de oro para el transporte de biomoléculas. Estos nanomateriales son objeto de gran interés para el campo de la nanomedicina debido a su baja toxicidad, alta bio-compatibilidad y con una superficie fácil de modificar, convirtiéndolas en materiales muy aptos para distintas aplicaciones biológicas. Este proyecto se ha centrado en el potencial de las partículas como vehículos de bio-moléculas, como oligonucleótidos, plásmidos o proteínas, para tratar enfermedades relacionadas con el cáncer.

Con el objetivo de llevar a cabo este propósito, se ha desarrollado un novedoso sistema basado en nanopartículas de oro funcionalizadas con polímeros. Las nanopartículas de oro diseñadas consisten en una combinación de monocapa mixta de los polímeros polietilenglicol (PEG) y polietilenimina ramificada (bPEI), y un sistema de capa-por-capa de bPEI obtenido a través de un conector sensible a estímulos. Las nanoestructuras generadas no producen toxicidad y tienen la capacidad de interaccionar electro-estáticamente con distintas bio-moléculas, estando principalmente optimizadas para el transporte y transfección de oligonucleotidos en células tumorales.

El diseño ha sido optimizado usando distintos tamaños de nanopartículas de oro y de cadenas del polímero bPEI, llegando a obtenerse hasta 12 tipos distintos de estructuras, las cuales han sido evaluadas en términos de estabilidad, reproducibilidad, toxicidad y eficiencia para conjugar y transfectar biomoléculas. Aquella con las mejores propiedades ha sido utilizada como nano-vehículo de oligonucleotidos antisentido para reducir la expresión de líneas celulares tumorales portadores de la proteína mutada p53.

Además, se ha desarrollado un original "*building block"* para la síntesis sólida de oligonucleotidos, el cual consiste en la adición de un conector sensible a estímulos a un soporte sólido. Los oligonucleotidos preparados con esta modificación han demostrado su capacidad de conjugación con distintas biomoléculas a través de un enlace disulfuro.

Table of Contents

Abbreviations

Abbreviation	Full name
ACN	Acetonitrile
ASO	Antisense Oligonucleotide
AuNPs	Gold nanoparticles
bPEI	Branched polyethylenimine
CAP	Capping agent
CPG	Controlled pore glass
DCC	N,N'-Diciclohexylcarbodiimide
DCM	Dichloromethane
DLS	Dynamic light scattering
DMAP	4-Dimethylaminopyridine
DMTr	4,4'-dimethoxytrityl
DMTr-Cl	4,4'-dimethoxytrityl-clhoride
DMSO	Dimethyl sulfoxide
DNA	Deoxyribonucleic acid
EI	Electron ionization
ESI	Electrospray ionization
FAM	Fluorescein
FBS	Fetal bovine serum
GEM	Gemcitabine
GEN	Generation
GOF	Gain of function
GSH	Glutathione
HOBt	Hydroxybenzotriazole
LP	Lipoic acid
LP-NHS	2,5-dioxopyrrolidin-1-yl-5-(1,2-dithiolan-3-yl)pentanoate
MALDI	Matrix Assisted Laser Desorption/Ionization
MeOH	Methanol
MS	Mass spectrometry

Mutp53	Mutant tumor suppressor protein P53
MW	Molecular Weight
NHS	N-hydroxysuccinimide
NMR	Nuclear magnetic resonance
NPs	Nanoparticles
N/P	Ratio nitrogen to phosphate
Oligo	Oligonucleotide
p53	Tumor suppressor protein P53
PBS	Phosphate buffered saline
PDP	3-(2-pyridyldithio)propanoylamide
PEG	Polyethylenglycol
PEI	Polyethylenimine
RNA	Ribonucleic acid
RPM	Revolutions per minute
SPDP	N-Succinimidyl 3-(2-pyridyldithio)propionate
SPR	Surface plasmon resonance
TBE	Tris-borate-ethylenediaminetetraacetic acid
TEM	Transmission electron microscopy
THF	Tetrahydrofurane
TMED	Tetramethylethylenediamine
TP53	Tumor suppressor protein 53
UV	Ultraviolet
UV-vis	Ultraviolet visible
WT	Wild type
ε	Extinction coefficient

Chapter 1.

Introduction

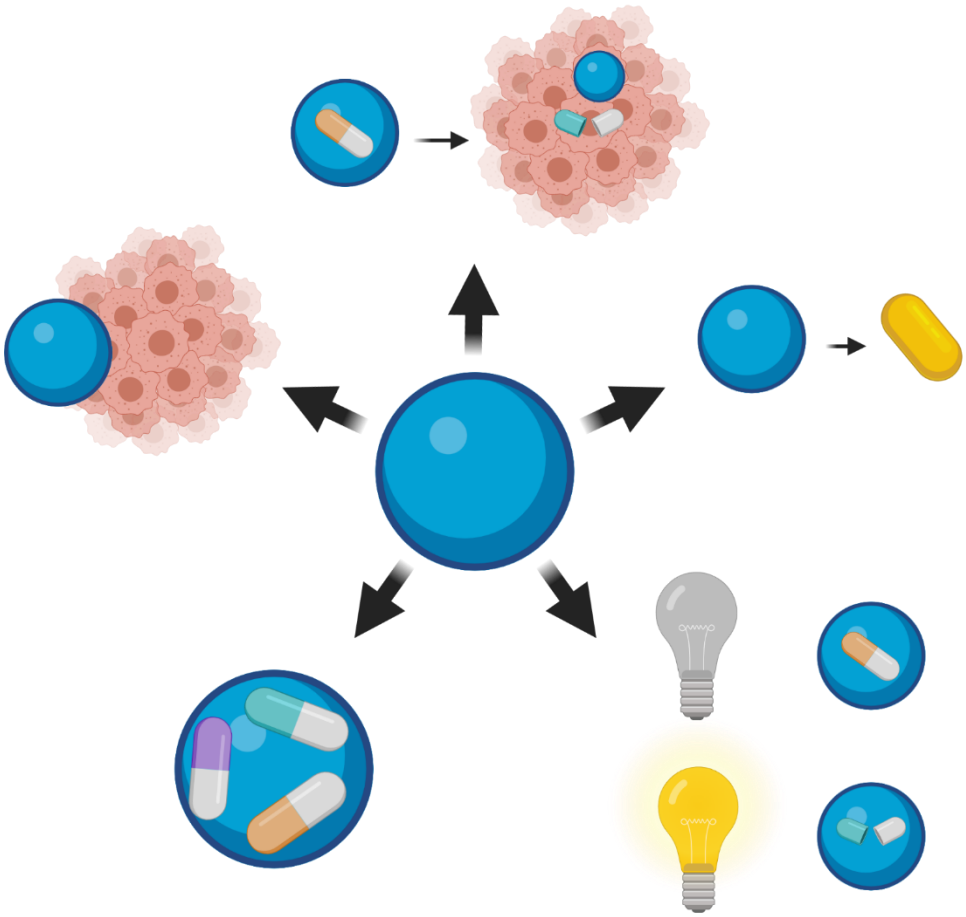

Chapter 1. Introduction

1.1. Cancer: Background, current situation and future opportunities

In our society, one of the leading causes of mortality is cancer, a term that involves more than 100 diseases related to abnormal growth and proliferation of cells that can invade other areas of the organism and metastasize to distant organs[1]. This group of diseases is produced by a series of mutations in the genes that alter the usual function of the cell. Those mutations can have an endogenous origin, such as errors during the DNA process replication or lack of chemical stability from DNA bases. It can also be exogenous, due to exposure to radiation or chemicals and environmental substances with carcinogenic properties[2-3]. The increasing exposure to those factors, added to the fact that the world population is increasing each year, with an increment in the life expectancy and sedentary lifestyle, makes the tumoral diseases a problem that each day is more present in our lives[4].

One of the great questions about cancer is its origin. Currently, different hypotheses have been proposed, such as the mutation, chromosomal imbalance and mitochondrial dysfunction theories[5]. They all present various arguments to explain how cancer appears but still, some questions and models cannot be explained. However, the mutation hypothesis is currently one of the most extended and accepted theories. In this case, it has been shown that some mutations lead to cancer development. Also, it has been observed that the predisposition to develop some cancers could be transferred to the offspring. In addition, it is known that some cancers can be induced by modulating specific genes.

Gene mutations take place very often in the organisms and do not have to be specifically harmful. They can be neutral and also beneficial. In most cases, the organisms might manage to correct these mutations through different pathways. In this regard, tumors do not develop from a single gene mutation, they usually require the accumulation of several mutations in a specific area. Anyhow, the most common genes, which mutations might lead to cancer, can be categorized into two main groups[6].

- Tumor suppressor genes, which are in charge of the DNA reparation, cell division monitorization, apoptosis control and metastasis suppression. The inactivation or loss of these genes is one of the leading causes of cancer development. Within this group, most of the mutations are found in these genes: BRCA1, BRCA2, and TP53.
- Proto-Oncogenes/Oncogenes, which activity is associated to uncontrolled cell proliferation. Mutations might activate them, leading to the formation of a tumor. The most common oncogenes are HER2 and the RAS gene family.

The lack of knowledge about the topic and the immense array of factors that may cause cancer, make it difficult to develop general and effective cures. Currently, the most common therapies for cancer treatment involve mainly surgery, radiation therapy and chemotherapy. It can also be applied treatments such as radiation frequency ablation or high intensity focused ultrasound, and novel treatments like immunotherapy[7].

Chemotherapy is probably one of the most extended and popular treatments. It is used in cancers sensitive to specific chemicals. It consists of the application of cytostatic or cytotoxic drugs that target the cellular DNA and RNA, interfering in their metabolism and proliferation. However, the chemicals are not specific, leading to severe side effects whose intensity can go from mild to life-threatening consequences. Some side effects can be observed easily as hair loss or skin pigmentation. Others affect organs such kidneys, intestinal tracts or lungs, causing nausea, vomits, fatigue or diarrhea, leading to anemia and weight loss, and increasing the risk of sepsis. Severe ones can generate drowsiness, paralysis, spasms and even coma. Additionally, chemotherapy can produce drug resistance, carcinogenicity and infertility [8].

A less harmful alternative to chemotherapy treatment is target therapy. In this case, the drug targets a factor that contributes to the growth and survival of the tumor, for example, genes or proteins, or the tumor itself and its environment. This therapy limits the damage to healthy cells and presents fewer and less severe side effects than conventional chemotherapy[9]. Targeted therapy uses the properties of antibodies and small drugs to alter or interfere in the specific area

or component that is generating the tumor[10]. Nowadays, there are several drugs approved for clinical use or in clinical developments. However, despite the advances that have been achieved in this field, there are still some challenges to face. An important one is the improvement of preclinical models to predict the efficacy of the treatment and the combination of different agents to treat various targets at the same time[11]. However, just finding the target and the "tool" to treat it, might not be enough and the implementation of an effective and selective delivery system could solve most of the current limitations. For this particular topic, nanoscience and nanotechnology can play a crucial role.

1.2. Nanoscience and Nanotechnology

Nanoscience and nanotechnology are scientific disciplines that involve the study, design and manipulation of matter at a scale that goes from the nanometer (nm) ($1x10^{-9}$ m) to close the micrometer (μm) ($1x10^{-6}$ m), around 100 nm (**Figure 1**). Although these terms may look brand new or even futuristic, there are pieces of evidence of the application of nanotechnology from ancient times. For example, nanoparticles were used by Mesopotamian's artisans in the ninth century to create a glittery effect on the surface of their creations. This effect was obtained by oxidizing silver and copper together along with other substances as vinegar, ochre and clay, leading to a colloidal solution of nanoparticles called luster. Applying this mixture to a glazed surface under certain temperature conditions was obtained a metallic glitter that still remains in our era[12].

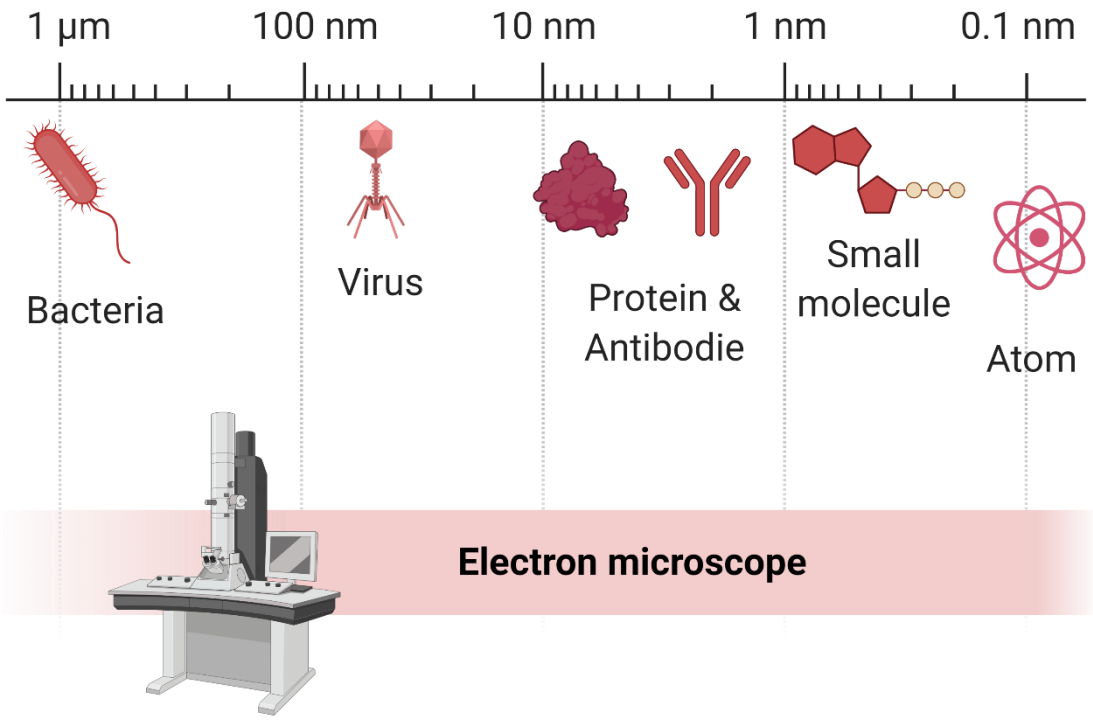

Figure 1. Nanoscopic scale. Length scale from 1000 nm (1 µm) to 0.1 nm. The elements found at this scale cannot be seen at plain sight, being necessary powerful and specialized technology as an electron microscope.

The nanotechnology era started after a conference in 1959 by the Nobel Prize awardee Dr. Richard Feynman. During the conference entitle: “There’s Plenty of Room at the Bottom”, he encouraged to find a way to manipulate matter at an atom and molecular scale where some physical properties as gravity would be less important and other as Van der Waals attraction or surface tension would be critical. He also remarked on the necessity of developing a set of tools able to carry this task. In 1974, the Japanese scientist Dr. Norio Taniguchi introduced and defined “nanotechnology” as “the processing of separation, consolidation, and deformation of materials by one atom or one molecule”, and in 1986 Dr. K. Eric Drexler made the term popular after the publication of his book “Engines of Creation: The Coming Era of Nanotechnology[13]. Also, technological advances gave, as a result, the invention of nanoscale transistors or the scanning tunneling microscope (STM), which allowed to obtain surface images at an atomic level. All these things helped in different science fields to move forward into the nanoscale direction. In chemistry, for example, the discovery of fullerene, the synthesis of

nanocrystals, or the description of atomic layer deposition settled the importance of the nanoscience[14].

In recent years, the nanoscale has been investigated more due to outstanding properties that appear in materials of this size. This is due to mainly three factors[15]:

- Surface effect: the small size of nanomaterials provides a great specific surface area, defined as the ratio of the surface area to volume. This ensures a high percentage of surface atoms with low atomic coordination numbers. This leads to higher surface energy that provides a more prominent reactivity or interaction with other materials.
- Small scale effect: Decreasing particle size also helps to decrease the surface molecular density of some amorphous nanoparticles, which produces changes in physical properties as optical, thermal, magnetic and mechanical.
- Quantum size effect: this affects the electron band gap of the Fermi level of some materials, which goes from continuous to discrete. That also affects the conductivity properties, magnetism and reactivity of the nanomaterials.

These facts explain the growing interest in nanomaterials, which can be applied in different fields as the environment, energy, electronics, food industry, and even medicine.

1.3. Nanomedicine

Nanomedicine is the application of nanotechnology for medical purposes such as diagnosis, monitorization, control, prevention and treatment of diseases[16].

Most of the applications related to nanomedicine involve the use of NPs, which can be obtained from different materials[17]. Among them, the most employed are those based on lipid micelles, polymeric nanostructures, protein constructs, ribonucleic acid (RNPs), carbon dots (C-dots), nanodiamonds (NDs), carbon nanotubes (CNTs), graphene, mesoporous silica NPs (MSNP), superparamagnetic iron oxide NPs (SPIONs), magnetic NPs (MNPs) quantum dots (QDs), plasmonic NPs or gold nanoparticles (AuNPs) (**Figure 2**). This large

array of nanoparticles can be synthesized in different sizes and shapes, which can modify their properties.

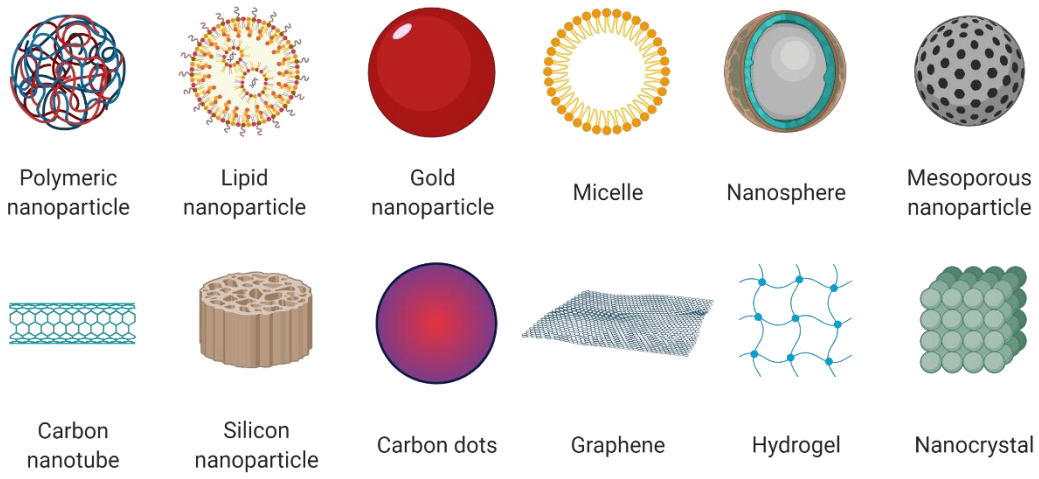

Figure 2. Graphical representation of some of the most known nanomaterials used in medicine

1.3.1. Imaging

Diagnosis tools that allow the precise distinction between healthy and disease tissues are vital to ease the selection of the most suitable treatment. In this regard, different types of nanoparticles can be employed as contrast agents for different techniques, such as computed tomography (CT), magnetic resonance imaging (MRI), position emission tomography (PET), or single-photon emission tomography (SPET).

1.3.2. Sensors

While imaging techniques are focused on the diagnosis *in vivo*, sensors can be employed for diagnosis using ex-vivo samples. In this case, the role of the NPs is to detect specific biomolecules associated with a disease. For this purpose, the NPs are usually functionalized with molecules that recognize specific areas or elements of the sample. The combined functionalization with different types of molecules or ligands allows the multiple detection of biological targets and reduces the limit detection. Sensors are usually designed to be detectable to the naked eye, therefore, expensive and sophisticated equipment is not required[18]. For this purpose, sensors based on colorimetric changes have been largely studied to implement a simple readout. One example is the semi-quantitative

method of the enzyme alkyl phosphatase developed by *Gao et al*.[19] consisting of the deposition of silver on gold nanorods mediated by the enzyme that provides a different colorimetric readout depending on the enzyme concentration.

1.3.3. Treatment

NPs have been employed mainly to treat cancer since they can be exploited to increase the selectivity of the therapy and reduce the side effects, compared to traditional approaches. There are currently some nanoformulations for cancer treatments accepted for clinic use; however, much work is needed to improve their selectivity and efficiency[20]. The main challenges to face in the delivery process for solid tumors are the ones involved in the CAPIR cascade: blood circulation, accumulation in the tumor and penetration, cellular internalization and release of the therapeutic agent (**Figure 3**). Because of this, the therapeutic efficiency of the treatment is determined by the efficiency of the nanoformulation in each of the steps[21].

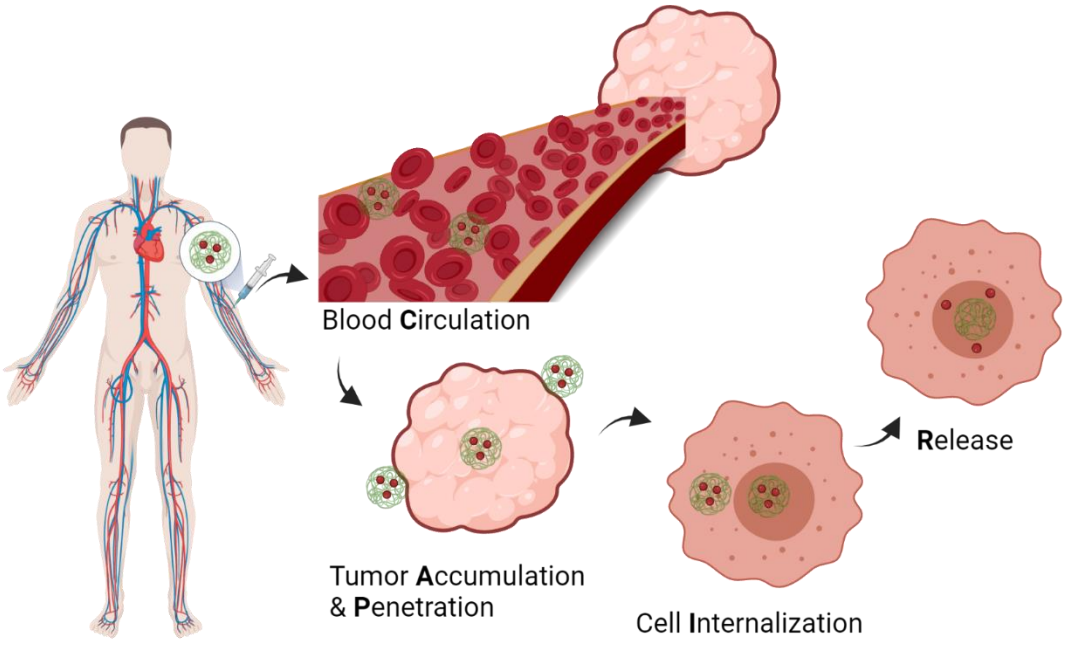

Figure 3. Graphical representation of the CAPIR cascade. Including all the steps since a nanoformulation is introduced in a living organism until the therapeutic agent is released on the target tumoral cell.

The primary role of the NPs in the whole process is to serve as carriers of the therapeutic molecules and enhance their accumulation in the tumoral environment. To fulfil this task, there are different strategies that may be followed (**Figure 4**):

- Targeting. In this regard, the term refers to design the NPs to deliver the cargo in a selected tissue or cell specifically. They must be stealthy enough to avoid their clearance from the blood stream and able to interact with the target area. Then, they can accumulate by a passive or active way, using mechanisms like vessel transport or adhering to biological structures through molecule recognition due to surface-bond ligands[22].
- Size-Shape control. Some NPs can simultaneously have the role of stabilizer and protector of the cargo, besides being the carriers. This leads to control of the size and shape of the particles to maximize the therapeutic effect. However, it is not an easy task due to some factor to take into account like metabolic stability, permeability to cross for some specific biological barriers as membranes or tissues, and excretion[23].
- Drug release control. Good timing in the release of the therapeutical cargo can have a significant impact on the reduction of the overall toxicity. In this regard, one of the better ways to control the release is through stimuli-responsive linkers, which can be activated by molecules present in the tumoral cells. For instance, the higher concentration of glutathione (GSH) inside the cells or protons, due to the Warburg effect[24] that tends to produce a more acidic environment. Therefore, NPs sensitive to these stimuli could degrade their shell, releasing the cargo in the process[25,26].
- Drug combination. Due to the complexity of most tumors in terms of multiple targets and the low specificity of the current drugs, an alternative strategy is the combined use of multiple drugs. However, the overall pharmacokinetics and biodistribution can also be affected[27].
- External stimulus. Some NPs can be triggered upon external stimuli to provide specific cell death. The most common therapies through this method are photodynamic therapy (PDT), magnetic hyperthermia and

photothermic therapy (PTT). PDT needs oxygen, light and a photosensitizer, which in combination produce reactive oxygen species (ROS), a kind of superoxide radical anions that cause cell death[28]. In contrast, hyperthermia causes cell death by heat, which could be obtained when magnetic nanoparticles are exposed to an alternating magnetic field[29]. In the case of PTT, a promising drug-free therapy, NPs absorb light above 700 nm and generate heat, burning out the tumoral cells[30].

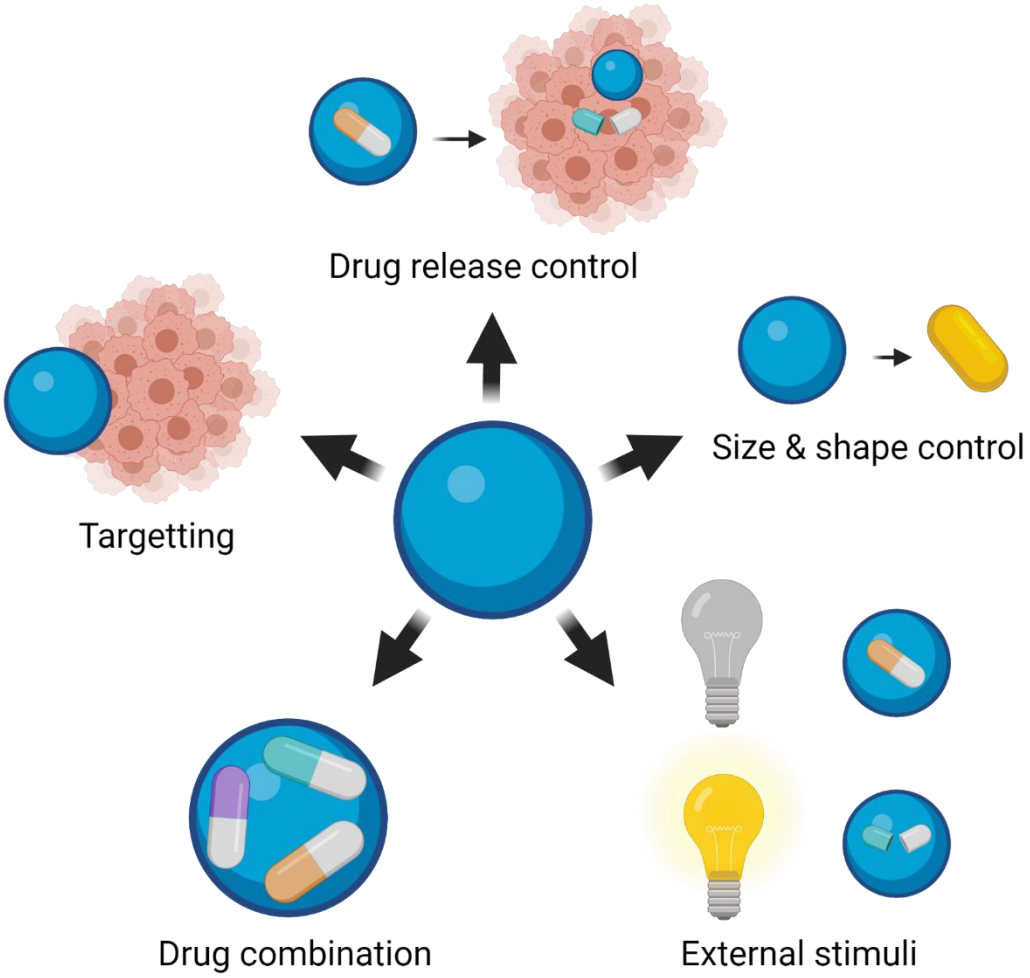

Figure 4. Summary of some of the relevant requirements of a nanoparticle to be a suitable carrier for drug delivery.

1.3.4. Theragnostic

The term involves the combined use of diagnosis and treatment strategies. In this regard, the role of the NPs is to label the tumoral environment, mainly metastatic areas and tumor borders, to ease the removal of the tumor by surgery. In addition, they can also be used as drug delivery carriers while tracking their pathway to the damaged area. Drug delivery tracking is a promising tool due to the complexity of the tumors and their intricate vascular structures and environment[31].

There are available a great variety of NPs formulations, with diverse properties. However, each year, therapies based on NPs become more complex, which makes the quality control parameters stricter, reducing the possibility of reaching the final stages of clinical trials. Because of that, it is essential to work with a proper methodology and study the state of the art of the desired material for *in vitro* and *in vivo* systems[32]. It is crucial to take into account and understand factors such as size, shape, surface and aggregation properties or biodegradation before start to produce therapeutic nanoparticles. Therefore, some approach strategies include designing NPs carriers that release their cargo with minimal side effects through the production of biodegradable, non-toxic and excretable subproducts[33]. Therefore, among the different nanomaterials, the research of this project will be centered on gold nanoparticles (AuNPs), which are very promising nanomaterials for nanomedicine applications.

1.4. Gold Nanoparticles

1.4.1. Background

Gold Nanoparticles have been employed since ancient times for different purposes. Gold nanoparticles is described in Chinese, Arabian and Indian manuscripts from the fifth and fourth century BC for medical uses and in the ancient Roman Empire for decorative purposes. Later, in Europe during the medieval era, it was studied in laboratories of alchemy. Paracelsus wrote an essay on the obtention of the gold quintessence from the reduction of gold chloride and vegetal oils and alcohols. He and others used this gold solution to treat diseases like syphilis, leprosy, epilepsy or even the plague's effects through oral administration. The first book about the topic was written by Francisco Antonii

in 1618, a philosopher and doctor of medicine, who wrote about the obtention of colloidal gold and its medical applications[34]. In the nineteenth century, Michael Faraday started a new era for the study of this form of gold when he discovered that its properties significantly differed from the ones observed in the bulk material[35].

1.4.2. Synthesis

Since Faraday, and almost from the second half of the past century, the study of AuNPs increased. The first efforts were centered in their synthesis to control the size and the shape of the final products, along with the surface functionality. One of the most remarkable scientists in this field was Turkevitch, who described the synthesis of AuNPs by reducing hydrogen tetrachloroaurate ($HAuCl_4$) by citrate, used as a stabilizer, and boiling water[36]. This method was later refined by Frens, who studied the control of the size of the final AuNPs through the ratio $HAuCl_4$/citrate[37]. The Turkevitch-Frens protocol allows the obtention of AuNPs with mainly spherical shape and sizes between 10-20 nm of diameter, though larger size can also be obtained. In the 90's, Brust and Schriffin discovered a new method to obtain AuNPs through the use of tetraoctylammonium bromide (TOAB) and sodium borohydride ($NaBH_4$) as reducing agents, providing AuNPs of sizes between 1.5-5 nm, with high stability and low aggregation[38]. The variation of one or various parameters from these protocols can offer a full array of sizes (1 nm to 8 μm) and shapes (**Figure 5**) such as clusters, rods, shells, stars, cubes, triangles or prisms[39].

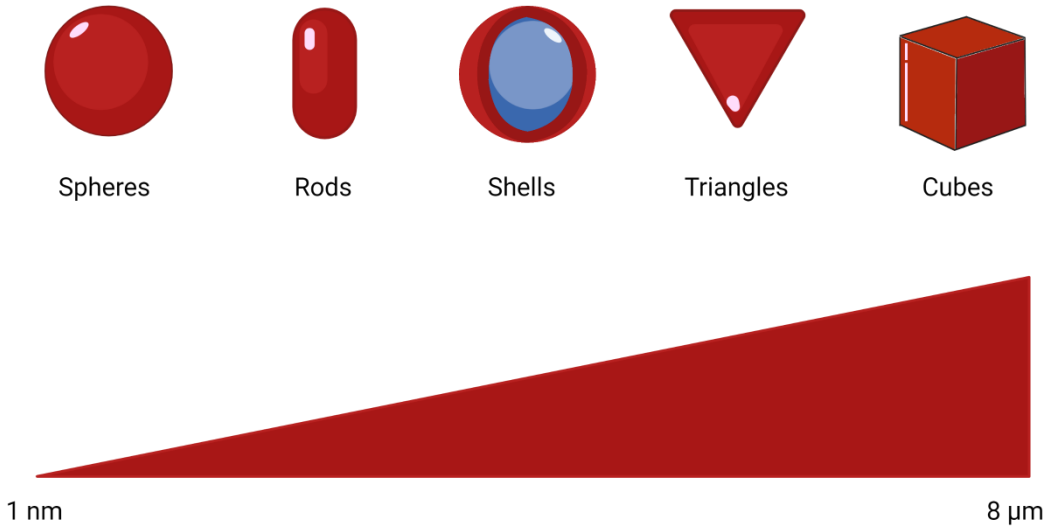

Figure 5. Array of sizes and shapes AuNPs obtained through the modification of different parameters.

1.4.3. Properties

AuNPs have many exciting features like their shape-size dependent optical properties, excellent surface-volume ratio, good biocompatibility, low cytotoxicity; they present surface plasmon resonance (SPR) and are natural fluorescent quenchers, which make them powerful material in nanomedicine[40-41]. Depending on their core size, they can display different colors in solution, such as orange, red, blue or violet. This also determines the wavelength of the maximum peak of their wide absorption band, which oscillates in a range of 500-550 nm, the so-called “surface plasmon band”[42].

Another useful property of the AuNPs is their high affinity for molecules bearing sulfur or selenium functional groups, which ease their functionalization[43]. This is because most synthesized AuNPs are capped with labile ligands such as citrate, which can be easily displaced by molecules that contain thiols, selenols or combinations of them, creating stronger bonds with the new ligands that would not be so easily replaced. Therefore, it can be introduced various ligands on the surface of the nanoparticles for different uses. The loading efficiency for each ligand will depend on the reaction time, ratios, affinity, length, competitivity, or steric hindrance[44]. There are different types of bindings that can be found for the

AuNPs/ligands and can be categorized into two groups: non-covalent and covalent. The non-covalent ones, such as electrostatic and hydrophobic interactions, are the simplest ways to functionalize the AuNPs and also ease their release in the desired area. On the other hand, a covalent conjugation, which involves the direct attachment of the ligand to the particle, provides a more stable product. Depending on the final role of the AuNPs, these are some of the most important parameters to take into account[45].

1.4.4. Applications

It has already been introduced that NPs play a key role in nanomedicine, and currently, AuNPs, with different formulations, can be found in most of its categories, as can be seen below.

- Diagnosis. In the last years, AuNPs have been the object of research to work as contras agents for X-ray imaging due to the low sensitivity that presents the current computed tomography techniques. They are usually functionalized with folic acid to highlight tissue structures[46]. Additionally, gold nanoclusters (AuNCs) have been studied, not only as contras agents in CT, but for molecular imaging since it was observed red fluorescence and due to their smaller size allows an easier elimination by renal vias[47].

- Sensors. AuNPs have been modified with ligands to recognize selected molecules, inducing a visual effect through aggregation or agglutination[48], providing an effective and fast colorimetric test[49]. Devices based on these systems are currently in clinical use[47]. These strategies are based upon the SPR properties of the NPs, where the aggregation is linked to changes in the absorption spectra. These can be obtained by selective molecule binding to the ligand-functionalized AuNPs. In this regard, Mirkin *et al* developed systems for DNA detection[50], which inspired the development of related assays by Stevens *et al*[51] and Pompa *et al*[52], with more complex structures.

- Treatment. AuNPs are promising tools for different *in vivo* therapies. Along with their easy to tailor surface, biocompatibility and low toxicity, they can also be naturally removed by the body after a while. They are prone to

accumulate in the liver and kidneys[53], but after different chemical process, they are finally excreted[54].

Therapies based on AuNPs can take different approaches. They would depend on the type of molecule to be carried and the target. For instance, in gene therapy for cancer and genetic disorders, Mirkin *et al*, developed DNA-AuNPs complexes to regulate and control the protein expression in cells[55]. And Rotelo *et al* designed cationic AuNPs, through the use of amino acids as surface modifier agents, for DNA transfection, proving a greater efficiency and reducing the toxicity of the process compared with analogous complexes of the amino acids without particles[56].

Another approach for AuNPs is their role as carriers for drug delivery, using covalent or non-covalent strategies. By non-covalent vias, encapsulation of the drug is the most common method, through the generation of pockets with a hydrophilic or hydrophobic behavior[57]. An interesting example of this strategy is the development by Burda *et al*, where the functionalization of AuNPs with polyethyleneglycol allows encapsulating a phthalocyanine drug use in photodynamic therapy, providing deep penetration in the tumoral environment with a fast release of the drug[58]. Regarding the covalent conjugation of drugs, the strategy is closely related to the release control methods through sensitive linkers. Some studies in tumoral models revealed that the cationic or anionic character of the stimuli sensitive ligands, mainly GSH sensitive, used to crosslink the NPs with the drug, contribute to the efficacy and depth penetration[59].

Inherent properties of AuNPs can also be used to generate therapeutics effects by themselves, without further functionalization. For example, bare AuNPs have been evaluated to control the proliferation of myeloma cells[60], by regulating the cell cycle of specific proteins, and inhibiting the growth of bacteria[61].

Despite the promising developments, AuNPs might face some obstacles to reach preclinical and clinical settings. The most relevant is the toxicity associate with some sizes and shapes of the nanostructrure[62]. Also, these parameters also have

a critical effect on the efficacy, biodistribution or physiological response, which should be considered[63]. Once the formulations are properly adjusted, the nanomaterials are safe and are suitable for clinical use, such as:

- Aurimune (CYT-6091). A drug delivery system developed by Astra Zeneca and Cytimmune. AuNPs coated with polyethylenglycol (PEG) are used as a carrier of recombinant human tumor necrosis factor alpha (rhTNF). The design provides a good defense against phagocytic clearance and improves accumulation by the EPR effect. They have demonstrated a safe delivery and high-efficiency release of the rhTNF. [64]

- Aurolase®. A drug-free PTT therapy designed by Nanospectra. It consists of silica-gold nanoparticles functionalized with PEG. It is focused on removing solid tumors by thermal ablation after being stimulated by near-infrared light. It has been tested in clinical trials to treat lung, head and neck cancer with minimum side effects. It had also been tested for imaging in prostate tumors[65].

- NU-0129. DNA delivery system. AuNPs are conjugated with spherical nucleic acids (SNA), composed of siRNAs, to target BCL2l12 protein, involved in tumor progression and apoptosis resistance. Currently, in phase I, it has demonstrated its efficacy in patients with recurrent gliosarcoma and glioblastoma[66].

- CNM-Au8. Drug delivery system developed by Clene Nanomedicine for the treatment of Neuromyelitis Optica (NMO)[67]. It consists of a suspension of gold nanocrystals with a drug, which has reduced toxicity due to its synthesis method and exhibits higher nano catalytic activity.

Despite the significant advances in delivery systems for the treatment of cancer, most of the therapies involved aim to kill the tumoral cells by the introduction of a toxic molecule. A more elegant approach could involve the restoration of the normal properties of the tumoral cells. In this case, the aim is to reprogram a tumoral cell to make it behave more like a healthy cell. In this line, approaches focused on gene editing and gene regulation have shown promising results[68].

1.5. Gene therapy and AuNPs

Gene therapy aims to cure a disease using genetic material. The origins of this therapy go back to 1960 and 1970, when the role of viruses was extensively studied to control diseases in animals and also the DNA recombinant technology was discovered. In this sense, in 1990, it was approved the first gene therapy to treat an immunodeficiency disorder[69].

Then, the efforts were focused on the introduction of genetic material into different cells, such as healthy, cancerous or immune meditated cells, and change their behavior temporal or permanently[70]. Once the nucleic acid is introduced in the cell, it can promote different processes such as apoptosis, cellular functions restoration, drug toxicity protection or immune cell activation[71]. Currently, there are two major therapeutic approaches where the introduction of nucleic acids into cells is exploited (**Figure 6**).

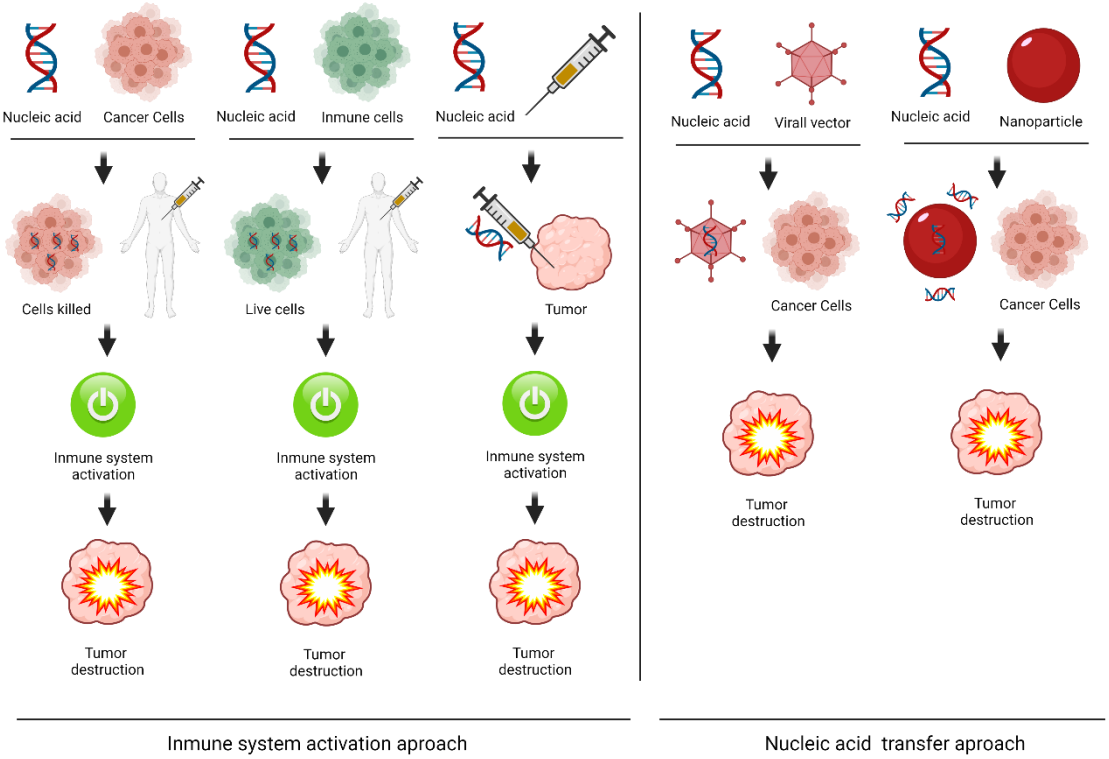

Figure 6. Graphical representation of the immune system activation and the nucleic acid transfer approach for gene therapy.

One is the use of immunotherapy. This method consists of the stimulation of the immune system to destroy cancer cells, which is problematic due to the

adaptation mechanism of tumors that allows them to evade the immune system[72]. Nowadays, there are three pathways to boost the immune system: a) through the ex-vivo manipulation of cancer cells, to introduce nucleic acids to promote the stimulation of the immune system, and the reintroduction of cancer cells back. b) incubation of immune cells with genes, like specific tumor antigens, that once in the organism would target and remove the selected type of cancer c) through the introduction of immune activation genes directly into a tumoral tissue that generates proteins that expose the cancer cells avoiding their evasion and promoting the generation of antibodies [73].

The other method is the use of transfer agent. A transfer agent is a vector developed to help introduce a foreign gene into the desired cell. The types of vectors can be basically subdivided into two sectors: viral and non-viral. In the case of a viral vector, the virus is attached to the selected cell as part of its replication process and, in the process, can introduce the nucleic acids previously introduced in it. In the case of non-viral vectors, the mechanism can undergo through physical or chemical meditated process. Once in the cell, the nucleic acids can promote apoptosis, silence genes, modify them or help in repair them[74].

1.5.1. AuNPs in nucleic acids delivery

In general, non-viral vectors present lower efficiency than the viral ones; however, they also offer a more significant range of delivery strategies, lower the cost and have superior safety profiles. In the last years, the study of non-viral vector based on nanoparticles derivatives have increase significantly. In fact, various nanoparticles systems for siRNA delivery have reached the clinical evaluation, mostly based on polymers or liposomes[75]. Among the different carrier systems, AuNPs are in the first place of metal-based nanoparticles for gene delivery. The first cases of AuNPs in gene therapy date from 1990s, when DNA-coated AuNPs were introduced into cells using physical forces[76]. The results were satisfactory, but the technique was limited to only peripheral organs. Since then, new strategies and approaches have been studied to take the maximum advantages of gold nanoparticles.

All the AuNPs properties mentioned before make them suitable for gene therapy. But in this field, one application is highlighted: their surface modification. In most cases, the mechanism pillar is the stabilization of the genetic material directly on the surface of the nanoparticles or through the use of ligands. There are different functionalization techniques worth mentioning (**Figure 7**):

- Nucleotide layer. This strategy is quite straightforward. It consists of the coating of the AuNPs with a single type of nucleotide by electrostatic or covalent vias. In the case of electrostatic binding, it happens due to the negative charges of phosphate groups present in the nucleotide, which is greater than the coating of the particles, generating a substitution. In the covalent case, it requires a previous modification of the nucleotides to make them bear a thiol derivative group that interacts directly with the gold surface. The method can affect the pharmacokinetics of the AuNPs. Some examples of this strategy have previously been mentioned in the treatments section. These systems present a good affinity for complementary nucleic acids, low degradation, and high cellular uptake.

- Cationic polymer layer. In this scenario, AuNPs coating is based on the use of highly charged polymers or molecules, allowing a strong electrostatic absorption by the nucleic acid. These molecules are generally cationic amino acids, polyethylenimine (PEI), chitosan or cationic lipids[77]. This method allows an excellent stabilization of the genetic material, high transfection efficacy and cellular uptake. However, large loading of the nucleotides requires the use of high molecular weight molecules that can greatly affect the toxicity of the system[78].

- Mixed layer. This method is, in summary, the combination of the two previous ones with some disparities. The AuNPs are generally covalently coated with two kinds of ligands: a nucleotide and a stabilizer. The stabilizer ligands are usually cyclodextrin or PEG. PEG polymers also work as a spacer and create a hydrophilic revetment that decreases the adsorption of cellular elements and increases the circulating time. The resulting NPs display excellent stability and efficiency. Other formulations involve the substitution of the nucleotide ligand by a cationic molecule that

later would bind the genetic material through electrostatic interactions. This way, the transfection efficiency can be increased[79].

- Cationic lipid assembly. The use of cationic lipids in combination with nucleic acids to form complexes (lipoplexes) is not new, but their use was limited due to low solubility in aqueous medium and high toxicity. The solution was the generation of a hybrid construction with AuNPs. Some examples that led to high transfection results and lower toxicity consist in the binding of nucleotides to the surface of the particles to then being encapsulated by lipids through an emulsification process. Therefore, the nucleotides are protected by degradation and well condensed for safe delivery[80].

- Layer-by-layer assembly. This versatile method consists of the generation of multiple thin layers by electrostatic interaction of oppositely charged ligands. The nanoparticles are coated with multiple layers of nucleic acid material sandwiched between polymers. These polymers could be sensitive to different triggers, allowing the controlled release of the nucleic acids and extend the efficacy of the system[81].

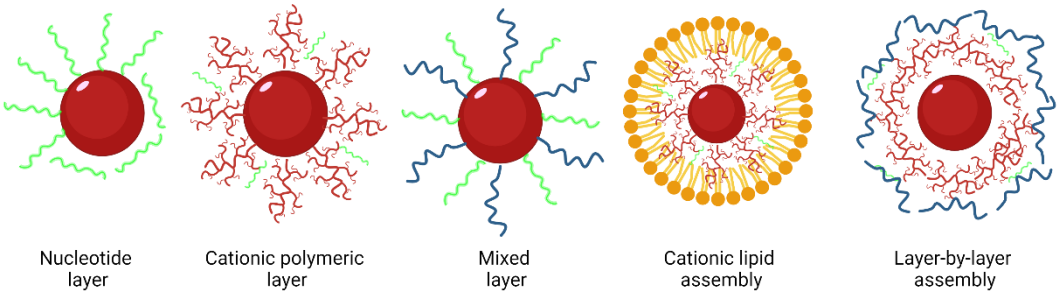

Figure 7. Graphical representation of some of the most popular AuNPs surface modification for their application in gene therapy.

1.6. Objectives

The main goal of this thesis consists in the preparation of AuNPs to work as carriers of biomolecules for their potential applications in gene therapy. It will imply the synthesis of nanoparticles with different modifications and assess their interaction with nucleic acids and their effect in cells.

Also, the development of a new solid support to ease the conjugation of oligonucleotides to biomolecules was planned.

To achieve these goals, the following objectives can be proposed:

- Objective 1 - Synthesis of gold nanoparticles. Assess the best route to synthesize different AuNPs to obtain suitable carriers for gene therapy in terms of size, shape, toxicity and surface modification.
- Objective 2 - Synthesis of ligands and functionalization of AuNPs. Assess the effect on the modification of the surface of the particles with synthetic ligands selected for the conjugation and transfection of biomolecules.
- Objective 3 –Assess the potential biological use of the AuNPs formulations. Particularly, the delivery of oligonucleotides into tumoral cells.
- Objective 4 – Preparation of a solid support for the introduction of an activated disulfide moiety in oligonucleotides and its conjugation with biomolecules.

Chapter 2.

Synthesis of gold nanoparticles.

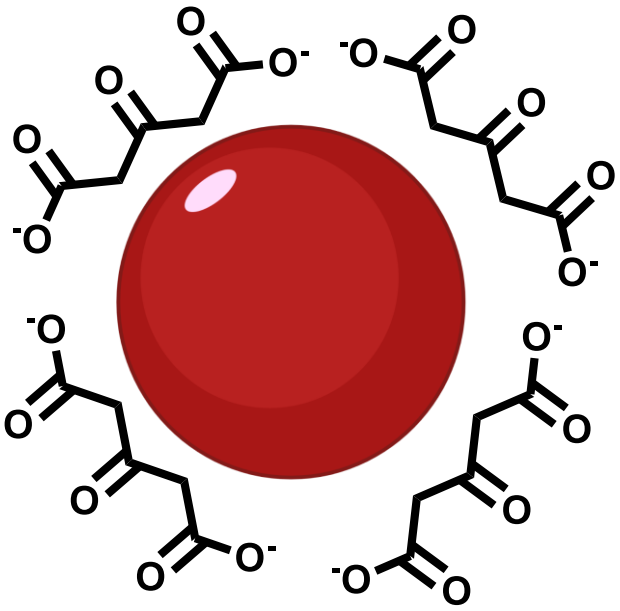

Chapter 2. Synthesis of gold nanoparticles.

2.1. Introduction

Among all the nanomaterials, gold nanoparticles were selected for this project as carriers of biomolecules due to their low toxicity, biocompatibility and ease to modify their surface[41]. This last point is critical for their application in the topic addressed herein, nucleic acid delivery [82]. This process can be done through the conjugation of the biomolecule to the AuNPs[83], or by the modification of the nanoparticles with molecules that interact electrostatically with the biomolecules.[75-84]. In both strategies, it is required the surface modification of the particles which depends on various factors such as shape and size. These two parameters also have a significant effect on the toxicity and the vehiculation properties,[85] and should be considered.

- Size. The activity of AuNPs in experiments in cell culture or animal models is size dependent. For instance, it has been studied that different size AuNPs distribute differently in the organism, where small size particles display a better organ distribution than larger ones[86]. In this regard, it has been reported that tumoral penetration is significantly better in smaller nanoparticles[87-88]. Also, the size has a significant effect on the toxicity, where the particles with larger diameters are more prone to induce these undesired effects[89]. On the other hand, it has to be considered that the loading capacity of the particles is size dependent, due to the increment in the surface area[90].

- Shape. Currently, the array of shapes of AuNPs that can be synthesized is vast, including spheres, clusters, rods, shells, stars, cubes, triangles or prisms[39]. Their synthesis can be carried out by different methods like chemical or physical, but for some shapes, the election of the process and control of parameters such as temperature or pH are key to the obtention of the desired shape[39]. The shape of these nanostructures has a dramatic impact on cellular uptake. In this regard, spheres-like gold nanoparticles have been widely employed due to their excellent uptake efficiency in contrast with other shapes as rods, which internalization is poor.

> Interestingly, recent reports have shown that other shapes, such as triangles, present better internalization properties than spherical structures [91].

Thus, these two parameters are critical for the development of nanocarriers for biological applications. Herein, we focus our work on the synthesis of AuNPs between 10 and 40 nm with a spherical shape. We expect that the small size of the nanostructure would provide better internalization at the tumoral environment with reduced toxicity. On the other hand, the spherical shape would improve the cellular uptake, and the homogeneity of the surface and area would ease the incorporation of molecules.

The most popular route for the synthesis of AuNPs of the selected characteristics is the one developed by Turkevitch et al in 1951[92]. This method is based on the reduction of the gold salt $HAuCl_4$ using sodium citrate. It consists of the rapid addition of a solution of the reducing agent over a boiling solution of the gold salt, leading to the obtention of AuNPs in a short time. Although the mechanism is not completely clear, a current consensus establishes that the sodium citrate reduces $AuCl_4^-$ ions to Au^+ and Au^0, getting oxidized at the same time to sodium acetone carboxylate (SAD). Then, when the Au^+ ions concentration reaches a critical point of disproportion with Au^0 triggers the nucleation and growth of the AuNPs[93].

Turkevitch's method allows the obtention of stable and quasi-spherical AuNPs in a range of 12-16 nm, with a good reproducibility and size distribution. Although this approach could be used to obtain larger nanoparticles, the quality and the reproducibility of the nanoparticles are not optimum due to the susceptibility of the method to different parameters, such as pH and temperature[94]. In 1973, Frens et al reported a variation of the Turkevitch's method, known as Frens' method, which allowed the obtention of larger AuNPs, up to 143 nm, with better reproducibility[37]. However, the size distribution and spherical shape of the particles are rather irregular, primarily for particles over 40 nm.

To overcome this problem, other methods based on Frens' method have been developed. Most of them focus on the role of sodium citrate, which beyond its reducing properties, also works as stabilizing agent and pH buffer. To minimize

the role of pH buffer[95], it was studied the addition of $AgNO_3$ as a catalyzer of the oxidation of the citrate,. This way silver ions helps in the fast oxidation of the sodium citrate to SAD, speeding the deposition and formation of the particles, helping in the obtention of better sphere shape AuNPs[96]. This route differs from the Turkevitch's and Frens' in that $HAuCl_4$, the citrate and the $AgNO_3$ are premixed before being added to the boiling water.

For the synthesis of our AuNPs, we choose the standard citrate method. In this case, the citrate, a weak ionic coating, would allow its easy and fast substitution with a strong biomolecule or ligand. Based on the different routes mentioned before, we decided to explore all of them to the obtention of different size particles:

- Turkevitch's method for 13 and 35 nm AuNPs. Due to the simplicity, reliability and popularity of this method, we choose to follow this route for the synthesis of two sizes close to the minimum and maximum of the size range selected.
- Fren's method for 23 nm AuNPs. Because Turkevitch's method presents more problems regarding the synthesis of AuNPs over 16 nm. In this case, it was selected 23 nm, as an intermediate size among the other two of 13 and 35 nm.
- Premixing method for 13 nm AuNPs. This method could provide better spherical shape AuNPs and a narrower size distribution. We chose it to explore the synthesis of 13 nm AuNPs and compared it with the ones obtained by Turkevitch's method.

After the obtention of the AuNPs by each route, they will be characterized by different methods: transmission electron microscopy (TEM), ultraviolet spectroscopy, dynamic light scattering and pH measurements. TEM allows quantifying the size of the core of the AuNPs and also to observe the shape and level of homogeneity of the particles. Along with the SPR band observed by ultraviolet spectroscopy, centered between 520-525 depending on the diameter of the AuNPs, the concentration of the colloidal solution prepared can be obtained[97]. DLS is used to determine the size distribution profile of small particles

in suspensions. It will provide information in terms of hydrodynamic size and zeta-potential of the particles with the citrate coating. In future experiments, when the citrate would be substituted by biomolecules or ligands, it would be a powerful tool to evaluate changes due to the functionalization. This complete characterization allows the assessment of the reproducibility of the AuNPs as well as their quality.

2.2. Results and Discussion

The objective at this early stage of the project was the synthesis of suitable AuNPs for their use in nucleic acid delivery. Among the possible sizes and shapes that can be obtained, it was decided to synthesize nanoparticles of 13, 23 and 35 nm with a spherical shape. These factors were chosen based on the balance between loading capacity, tumoral penetration, cellular uptake and toxicity.

To prepare these particles, it was chosen the route of the citrate reduction of the gold salt $HAuCl_4$ developed by Turkevitch, for the synthesis of 13 and 35 nm particles. However, as this route is less effective for sizes over 16 nm, thus, Fren's method was employed to prepare 23 nm AuNPs. This approach solves the problem of the reproducibility of Turkevitch's method, but its size distribution is wider in the case of AuNPs over 40 nm. Additionally, a third route, based on the premixing of the reagents and silver nitrate, was selected to synthesize 13 nm AuNPs. This route could provide AuNPs with a more homogeneous spherical shape and with a narrower size distribution in comparison with Turkevitch's method. The three routes were explored and the results were compared to determine the best route to follow.

2.2.1. AuNPs 13 nm – Turkevitch's method

Overall, the values obtained by the different characterization methods match with the expected. The TEM measurements show pretty homogenous amorphous AuNPs with an average size of 12.98±1.5 nm (**Figure 8**), as expected. The shape is not entirely spherical as expected for the route. The UV spectra show a wide SPR band between 500-550 nm with a maximum peak centered at 520 (**Figure 9**). Based on the TEM and the UV spectra, the concentration can be calculated using the Beer–Lambert law from the absorbance recorded at 450 nm and the

extinction coefficient of $1.39x10^8$ for 13 nm nanoparticles[97]. In this case, the concentration obtained was 10 nM. At this concentration, the pH of the AuNPs was measured, giving a value of 6.8. The DLS measures were performed without dilute the AuNPs to keep a ratio of 300-400 Kcps. The AuNPs show a hydrodynamic size of 19.33±9.31 nm and a zeta potential of -42.3±13.3 mV (**Figure 10**). The size distribution is wider than expected, probably due to the little aggregates and smaller particles that can be seen by TEM. This synthetic route was repeated three times, obtaining every time the same data.

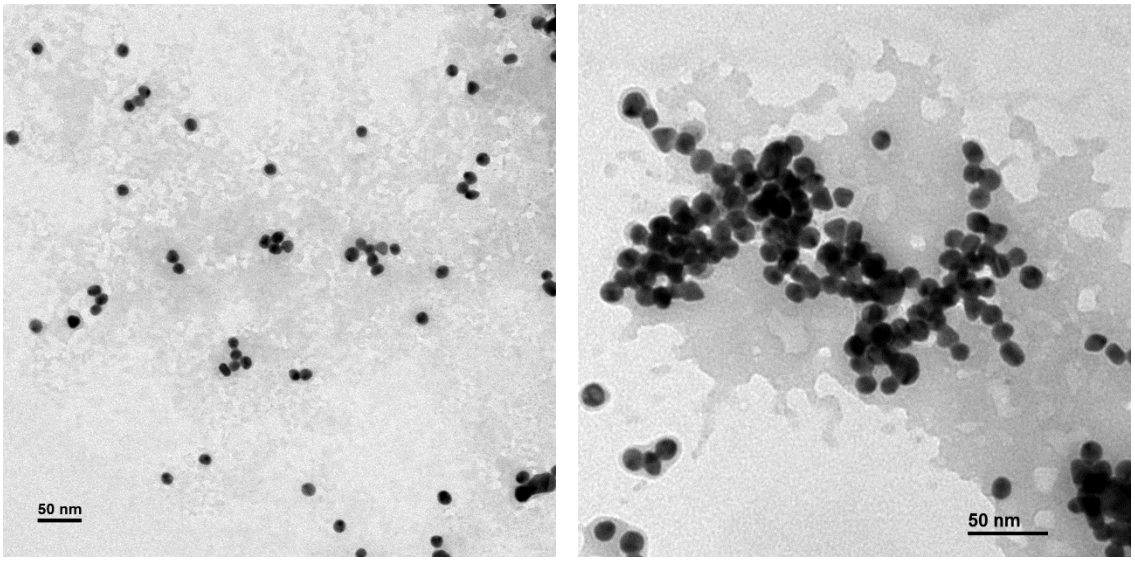

Size Aimed	Method	Number of measures	Average values
13 nm	Turkevitch's	47	12.98±1.5 nm

Figure 8. TEM images of AuNPs synthesized by the Turkevitch's method. Images are taken at 50 and 150k, respectively. The average size has been obtained evaluating the area of 47 nanoparticles of the first image with the software Fiji-ImageJ.

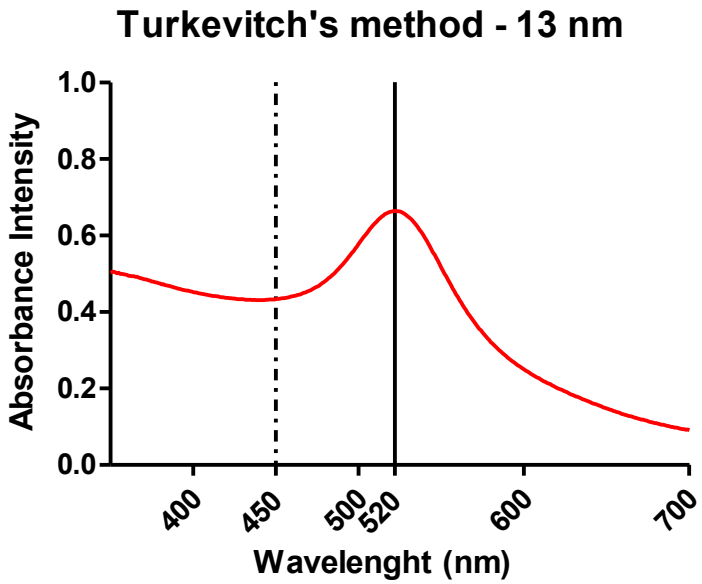

Figure 9. UV spectroscopy of the AuNPs of 13 nm synthesized by the Turkevitch's method. The graph shows the SPR band of the AuNPs centered at 520 nm.

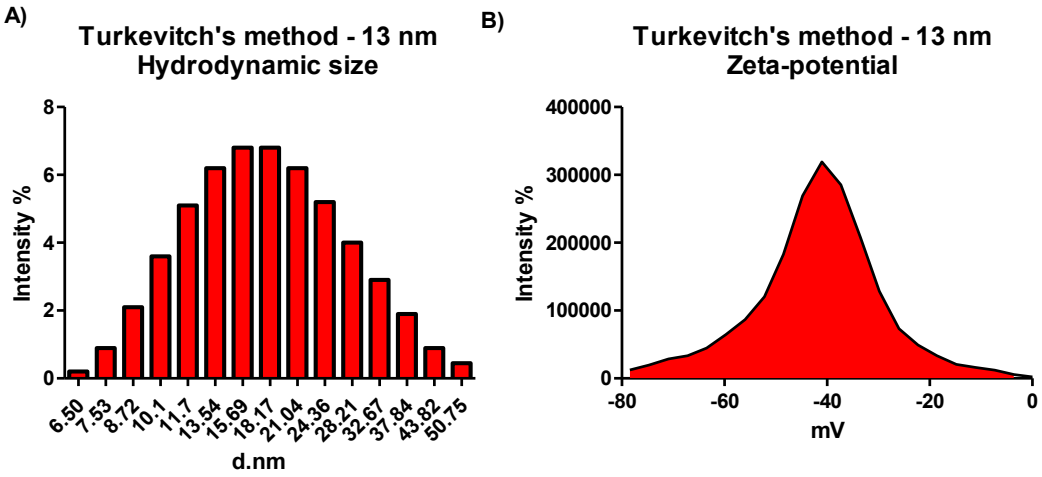

Figure 10. DLS size (A) and zeta-potential (B) characterization of AuNPs synthesized by the Turkevitch's' method to be 13 nm in diameter. The size distribution shows a maximum peak centered at 18.17 d.nm and the zeta-potential at -41.1 mV.

2.2.2. AuNPs 35 nm - Turkevitch's method

AuNPs of 35 nm were synthesized based on the Turkevitch's method, using a molar ratio HAuCl4/sodium citrate of 1.8:1. After their synthesis, the AuNP obtained a deep purple color that tends to pink after being filtrated. Protected from the light and stored at 4-6ºC, these nanoparticles have medium stability, keeping their properties from less than a month.

The TEM measurements show amorphous AuNPs with an average size of 36.13±5.45 nm (**Figure 11**), close to the value aimed. The UV spectra also show a wide SPR band, this time centered at 527 (**Figure 13**), which fits with its larger size. Based on the TEM and the UV spectra, the concentration of the nanoparticles can be determined using the Beer–Lambert law from the absorbance recorded at 450 nm and the extinction coefficient of $5.52x10^9$ for 36 nm nanoparticles[97] is 8 nM. At this concentration, the pH of the AuNPs was measured, providing a value of 6.4. The DLS measurements were performed without diluting the AuNPs, showing a hydrodynamic size of 60.85±25.65 nm and a zeta potential of -31±14 mV (**Figure 12**). The size distribution is wider than the one observed at 13 nm, around 3-fold, as expected for the Turkevitch's synthetic route for sizes over 16 nm. The potential is also irregular, and lower than expected. This synthetic route was repeated three times, obtaining every time different values for DLS, being the one displayed below the best ones obtained.

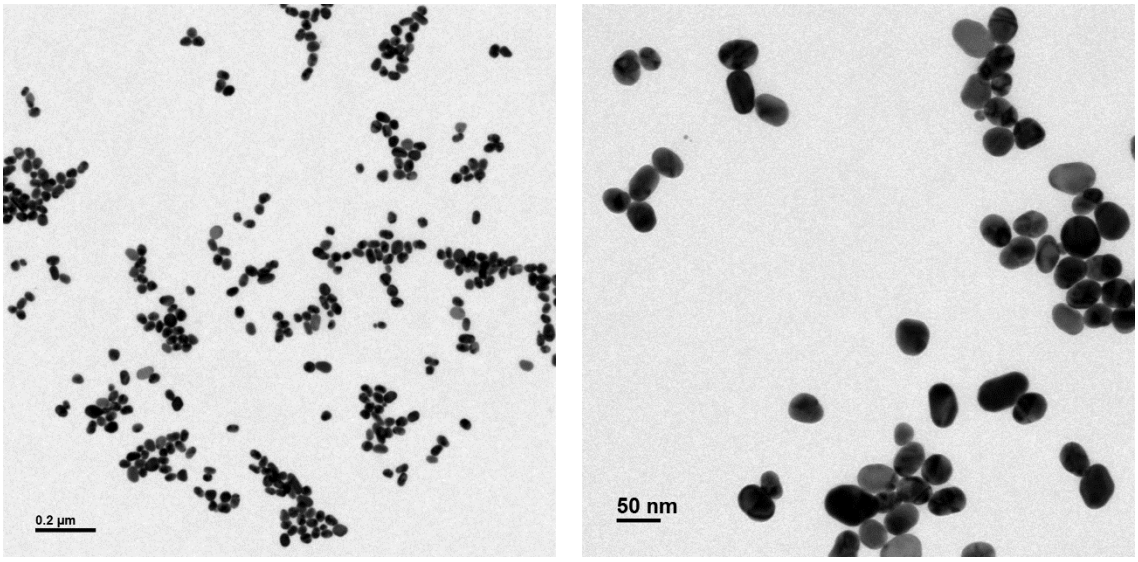

Size Aimed	Method	Number of measures	Average values
35 nm	Turkevitch's	230	36.13±5.45 nm

Figure 11. TEM images of AuNPs synthesized by the Turkevitch's method to be 35 nm in diameter. Images are taken at 50 and 150k, respectively. The average size has been obtained evaluating the area of 230 nanoparticles from the first image with the software Fiji-ImageJ.

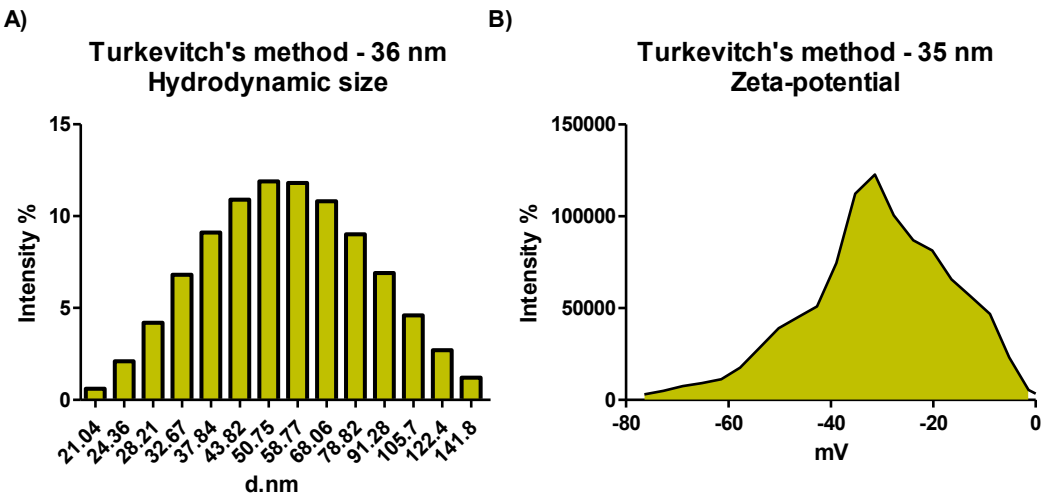

Figure 12. DLS size (A) and zeta-potential (B) characterization of AuNPs synthesized by the Turkevitch's' method to be 13 nm in diameter. The size distribution shows a maximum peak centered at 58.77 d.nm and the zeta-potential at -31.4 mV.

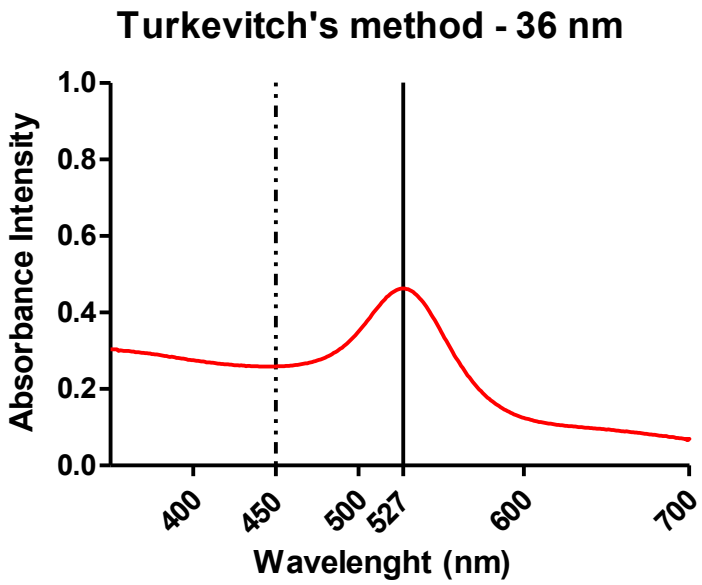

Figure 13. UV spectroscopy of the AuNPs of 35 nm synthesized by the Turkevitch's method. The graph shows the SPR band of the AuNPs centered at 527 nm

2.2.3. AuNPs 23 nm – Frens' method

AuNPs of 23 nm were synthesized based on Frens' method, using a molar ratio HAuCl4/sodium citrate of 1:1.84. These particles have a deeper red color after the synthesis and filtration. Protected from the light and stored in the fridge, they show to be stable for around a month.

As expected for this synthesis, the characterization data obtained is quite different with respect the Turkevitch's method. The TEM measurements also show amorphous AuNPs with an average size of 22.32±3.71 nm (**Figure 14**). The UV spectra show an SPR with a maximum peak centered at 525 (**Figure 16**). Based on the TEM and the UV spectra, the concentration is obtained using the Beer–Lambert law from the absorbance recorded at 450 nm and the extinction coefficient of $9.64x10^9$ for 23 nm nanoparticles[97] . Thus, the particles were obtained at 0.35 nM. This lower concentration is a consequence of the differences in the synthesis protocol. At this concentration, the pH of the AuNPs was measured, leading to a value of 6.8. Before performing the DLS measurements, the AuNPs were concentrated to 10 nM to compare the data obtained with the previous particles. The DLS measurements were performed without diluting the AuNPs, showing a hydrodynamic size of 47.26±25.29 nm and zeta potential of -37.8±6.32 mV (**Figure 15**). These values are in the middle between those obtained for the 13 and 35 nm, previously described. It was expected a broader size distribution than that obtained with the 13 nm nanoparticles, close to the values obtained with the 35 nm nanoparticles. On the other hand, the potential distribution is the narrowest of the three syntheses. This synthetic route was repeated three times, obtaining each time approximately the same data.

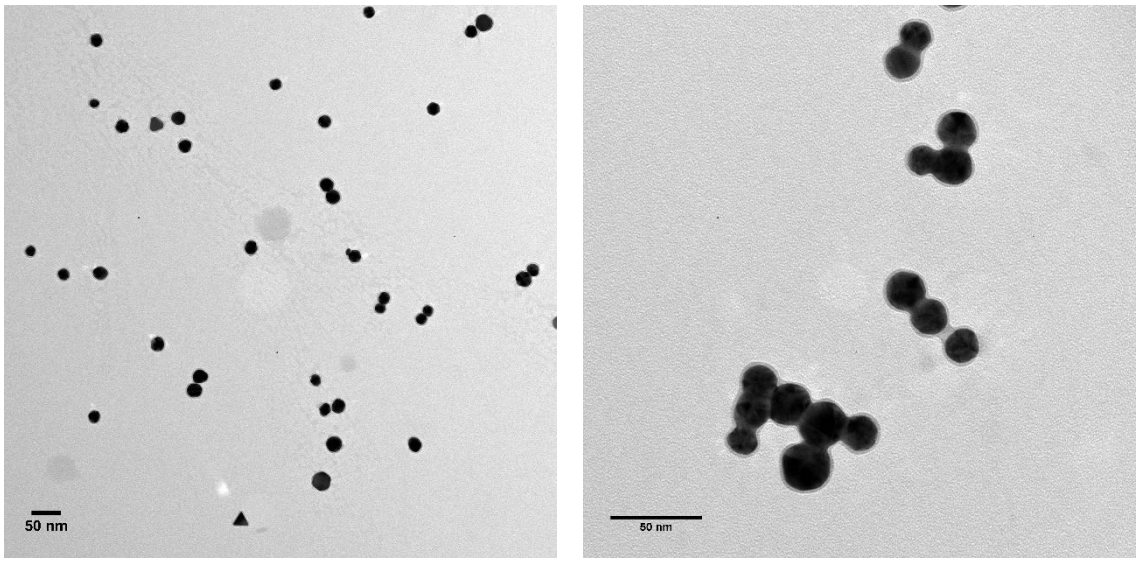

Size Aimed	Method	Number of measures	Average values
23 nm	Frens'	21	22.32±3.71 nm

Figure 14. TEM images of AuNPs synthesized by the Frens' method to be 23 nm in diameter. Images are taken at 50 and 150k. The average size has been obtained evaluating the area of 21 nanoparticles from the first image with the software Fiji-ImageJ.

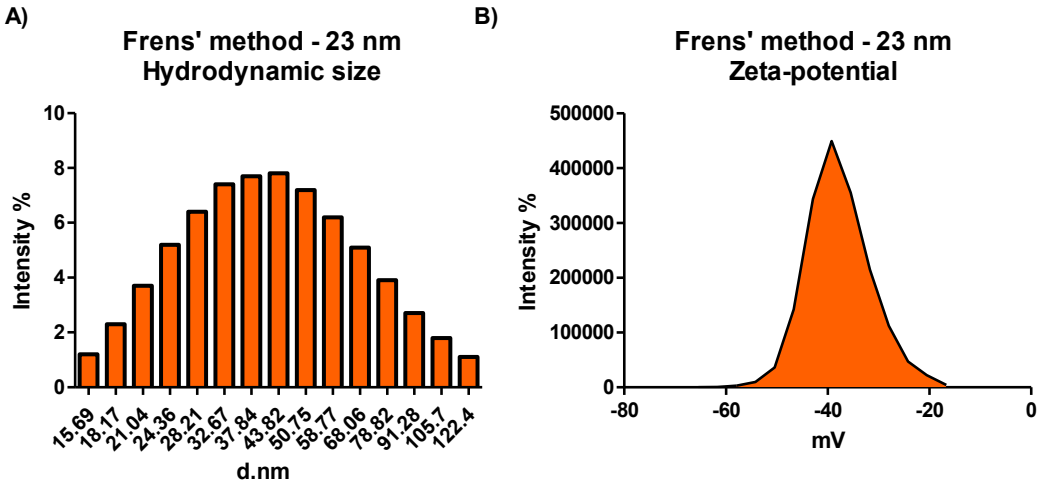

Figure 15. DLS size (A) and zeta-potential (B) characterization of AuNPs synthesized by the Frens' method to be 23 nm in diameter. The size distribution shows a maximum peak centered at 43.82 d.nm and the zeta-potential at -39.2 mV.

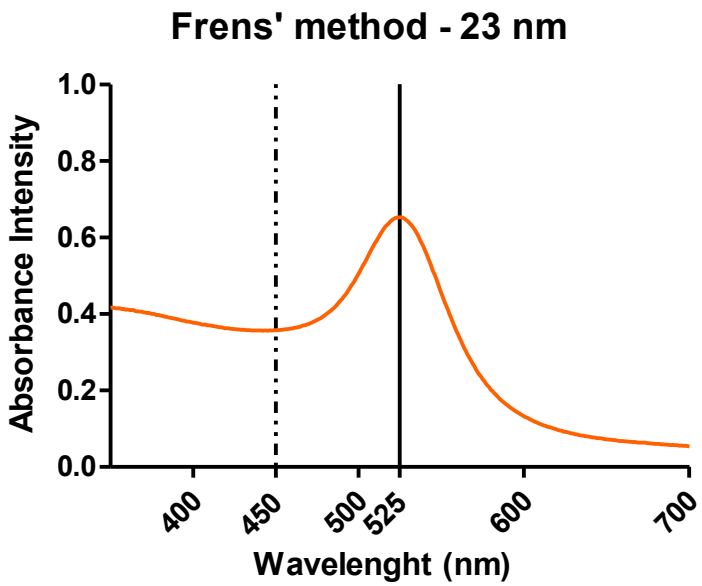

Figure 16. UV spectroscopy of the AuNPs of 23 nm synthesized by the Frens' method. The graph shows the SPR band of the AuNPs centered at 525 nm.

2.2.4. AuNPs 13 nm – Premixing method

AuNPs of 13 nm were synthesized based on the premixing method, using a molar HAuCl4/sodium citrate of 1:4.6 and with the addition of $AgNO_3$ as a catalyzer. These particles have a ruby red color after synthesis and filtration. Covered from the light and storage at 4-6ºC, these nanoparticles have good stability, keeping their properties from 1-2 months.

These AuNPs are very similar to the 13 nm obtained by Turkevitch's method. The TEM measurements show pretty homogenous amorphous AuNPs with an average size of 11.32±1.18 nm (**Figure 17**), close to the size aimed for. The UV spectra show an SPR centered at 518 (**Figure 19**), which correlates with the size obtained by TEM. Based on the TEM and the UV spectra, the concentration is obtained using the Beer–Lambert law from the absorbance recorded at 450 nm and the extinction coefficient of $8.27x10^7$ for 11 nm nanoparticles[97], giving a final concentration of 10 nM. At this concentration, the pH of the AuNPs was measured, obtaining a value of 6.8. DLS measurements were performed without diluting the AuNPs, showing a hydrodynamic size of 23.57±11.62 nm and a zeta potential of -32.9±13 mV (**Figure 18**). The hydrodynamic size is bigger than expected, taking into account that smaller nanoparticles were obtained. The size distribution

observed is also wider than expected. Because of this, this synthetic route did not present an advantage in our hands, with respect the Turkevitch's method for 13 nm AuNPs synthesis. This synthetic route was repeated three times, obtaining each time approximately the same data.

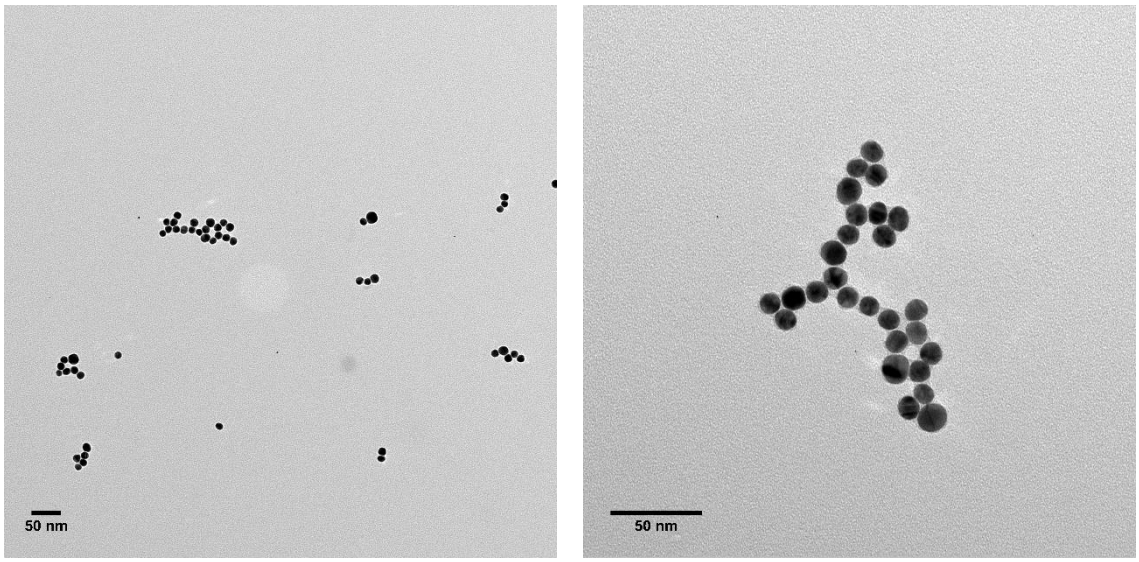

Size Aimed	Method	Number of measures	Average values
13 nm	Pre-mixing	49	11.32±1.18 nm

Figure 17. TEM images of AuNPs synthesized by the premixing method to be 13 nm in diameter. The average size has been obtained evaluating the area of 49 nanoparticles from the first image with the software Fiji-ImageJ.

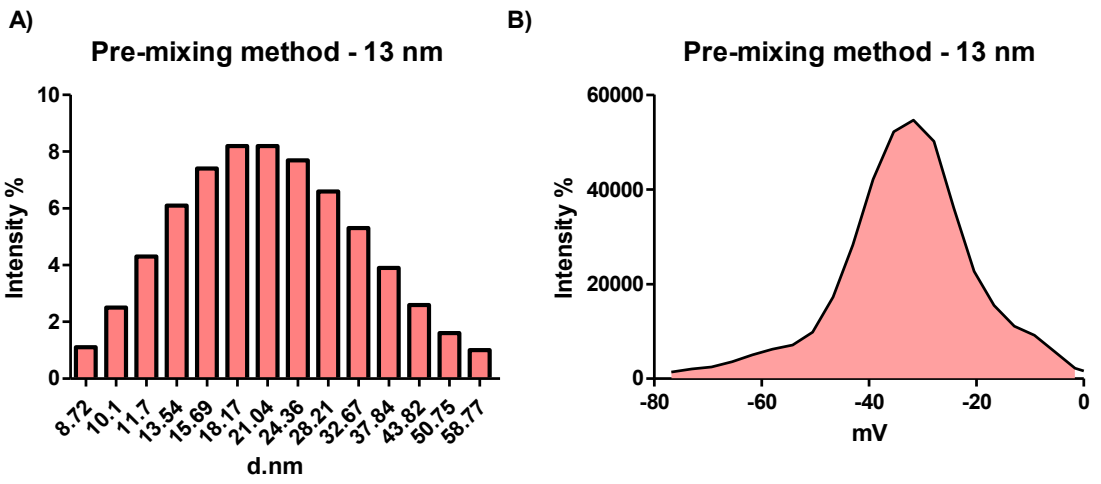

Figure 18. DLS size and zeta-potential characterization of AuNPs synthesized by the premixing method to be 13 nm of diameter. The size distribution shows a maximum peak centered at 21.04 d.nm and the zeta-potential at -31.7 mV.

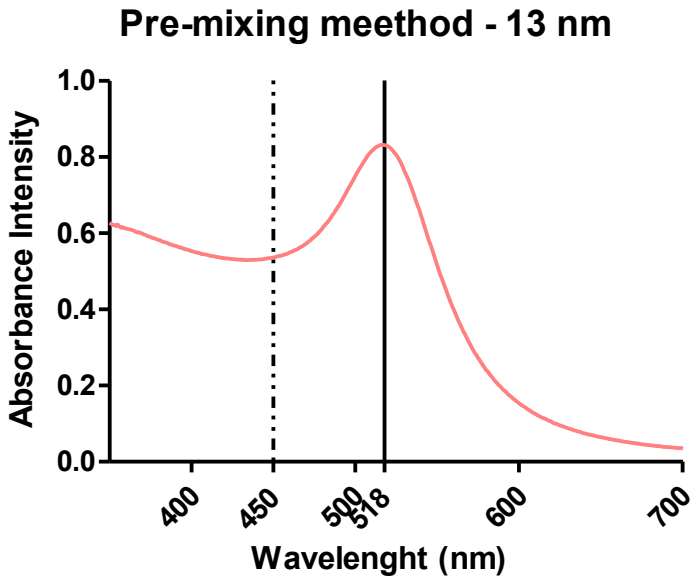

Figure 19. UV spectroscopy of the AuNPs of 11 nm synthesized by the premixing method. The graph shows the SPR band of the AuNPs centered at 518 nm.

2.3. Conclusions

Among the four different types of synthesized AuNPs, 13 nm AuNPs synthesized by the Turkevitch's method, from now on called 13-GEN0, are the ones that provided better results in terms of stability, reproducibility and characterization consistency. They present an acceptable spherical shape by TEM, a clear SPR band by UV and good hydrodynamic size and zeta potential by DLS. The 13 nm

AuNPs obtained by the premixing method show almost the same characterization profile. However, based on the lower consistency and the need for an additional reagent for their preparation, we decided to discard this approach for the following stages of the project.

Regarding the two other sizes AuNPs, the 35 nm AuNPs obtained by Turkevitch's method, 35-Gen0, presented low reproducibility and quality. Thus, we minimized its use in later stages of the project. The batches obtained with the best properties were used to explore the functionalization process. On the other hand, the 23 nm AuNPs obtained by Frens' method, now called 23-GEN0, were stable and reproducible. They also display a quasi-spherical shape by TEM, a size-according SPR band by UV and consistent hydrodynamic size and zeta potential by DLS. Because of this, they were maintained to later stages of the research, and their performance was compared with the 13 nm AuNPs selected.

Chapter 3.

Synthesis of ligands and functionalization of AuNPs.

Part 1.

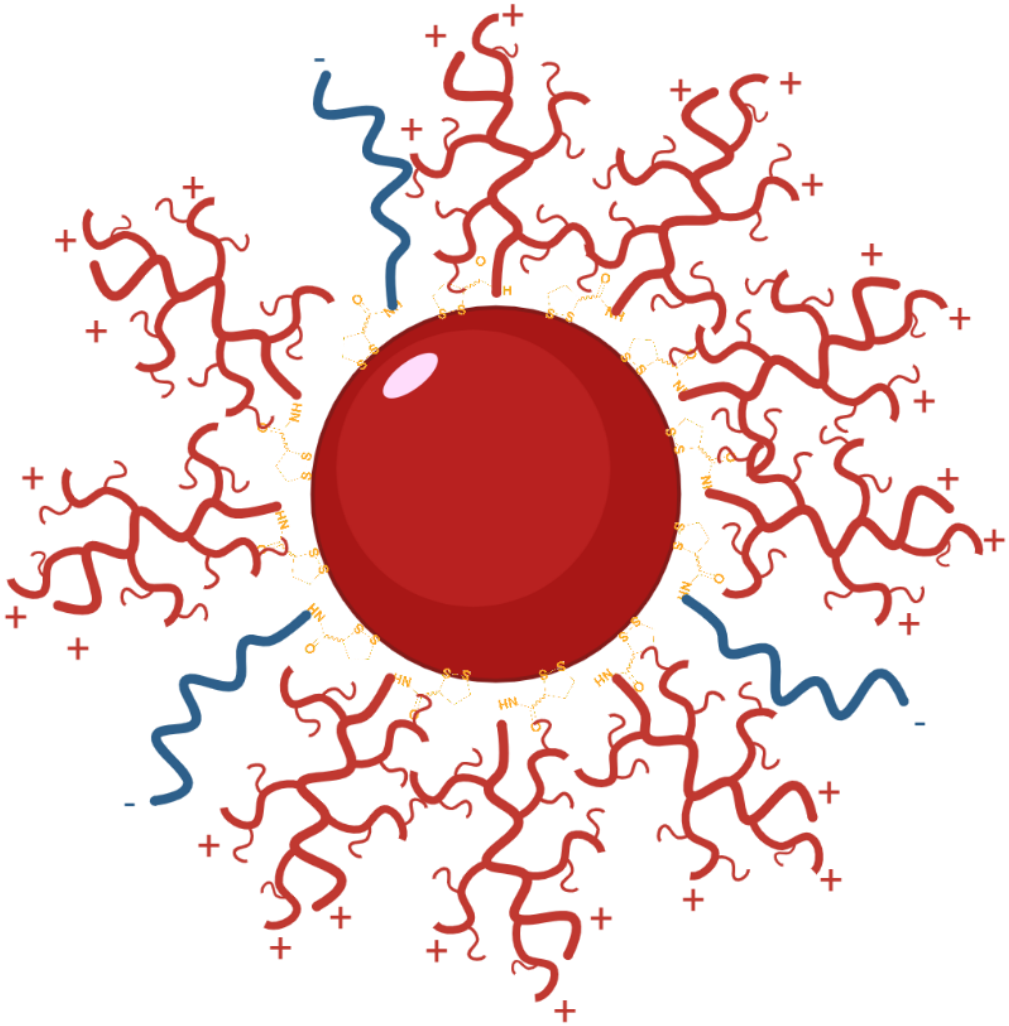

Chapter 3. Synthesis of ligands and functionalization of AuNPs. Part 1.

3.1. Introduction

AuNPs have been extensively used as nanocarriers of different bioactive molecules[98], such as antibodies, aptamers, peptides, or small molecules. There are two main approaches to incorporate the cargo into the particles: 1) through covalent modification or 2) by electrostatic interactions[99]. The election of the strategy will depend on the nature of the biomolecule and the possibilities of its covalent modification.

In this project, the main objective was to introduce different biomolecules, such as oligonucleotides, DNA plasmids or proteins, as the cargo of the AuNPs and assess the potential use of the modified nanoparticles in biomedical applications. To avoid changes in the chemical structure of the molecules and their properties[100], the electrostatic approach was explored. In this case, the molecules selected for the delivery present an overall negative charge. Thus, positive charges should be introduced in the AuNPs to provide good interaction with the molecules. In this regard, the use of positively charged polymers as coating of the AuNPs was evaluated.

3.1.1. Polyethylenimine (PEI)

Polyethylenimine (PEI) is a polymer constituted by a single monomer of ethylene oxide. There are two main types of PEI. Linear PEI, which contains only secondary amines, and branched PEI (bPEI), which has primary, secondary and tertiary amino groups in a 1:2:1 ratio (**Figure 20**). A third type, called totally branched, is considered the dendritic form of bPEI. The main applications of PEI are derived from its cationic characteristics and large water solubility.

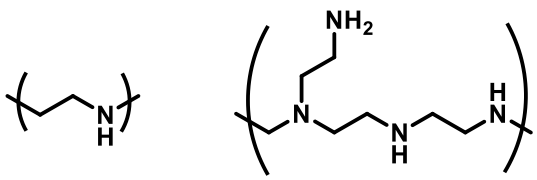

Figure 20. Chemical structure of linear PEI and branched PEI

Since 1995, when its efficacy as a non-viral transfer agent of nucleic acids[101] was highlighted, it has been considered the standard for polymer-based carriers due to its great transfection efficiencies in cell culture experiments and animal models. This polymer can condense the genetic material through electrostatic interactions, leading to a polymer/genetic material complex with positive charges. This allows the interaction of the complex with the negatively charged cellular membrane and favors the internalization into the cells. Besides, PEI presents an excellent buffer capacity at practically any pH, which also helps in the transfection process[102]. It is considered to have a "proton sponge" behavior that leads to osmotic swelling and rupture of endosomes. The introduction of large amounts of protons and counter anions, such as chloride anions, inside the endosome, generates its disruption and, consequently, the scape of the polymer[103].

Besides its use as a transfection agent, PEI has been used in various applications in medicine. For instance, it has been studied as a therapeutic agent in gastrointestinal activities, as a fibrin formation blocker, or as a permeability agent of the Gram-negative bacteria's outer membrane[104]. It has been used for antimicrobial coating, mainly as bactericidal in different materials. Furthermore, it has shown an essential role in the preparation of nanosized delivery vectors as drug and protein delivery systems. PEI is also present in photodynamic therapies for localized infections or antiangiogenic treatments, and in the development of optical imaging devices as quantum dots coating[104]. This polymer is also used in combination with assorted nanoparticles for cancer treatment[105], particularly in gene therapy[106], and chemotherapy[107-108].

Despite the several advantages of PEI, it has shown a significant toxicity, which prevents its clinical translation[109]. Although the mechanisms are unclear, the most probable theory is that it disrupts the cell and mitochondrial membrane, leading to necrotic cell death and apoptosis[110]. Also, many studies correlated the molecular weight and the geometry (linear and branched) with the toxicity and its efficacy as transfection agents[111] (**Figure 21**). Interestingly, it has been reported that the modification of PEI with small molecules (acetylation, succinylation) reduces its toxicity[112].

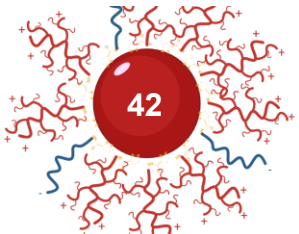

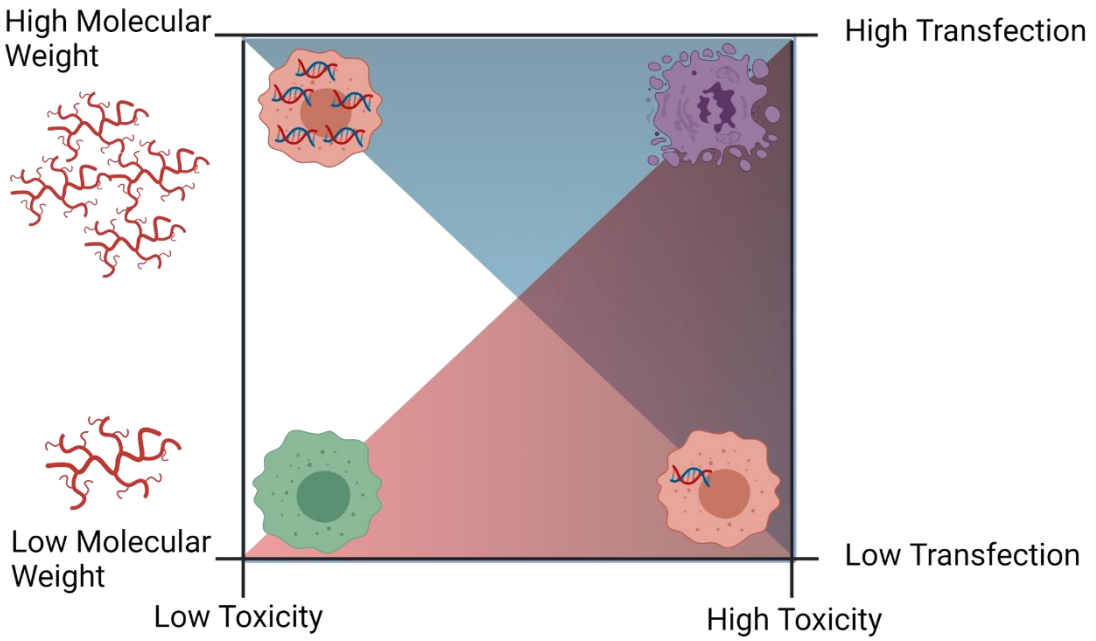

Figure 21. Polyethylenimine relationship between its molecular weight, its transfection efficacy and the toxicity that generate. As higher the molecular weight, better transfection efficacy but at cost of a higher toxicity

The use of PEI in combination with gold nanoparticles to ease the translocation of nucleic acids is well documented[113]. As mentioned before, the positive charge of the polymer facilitates the cellular uptake of the nanoparticles. Besides that, it can also be employed as a stabilizing agent, depending on the length and geometry of the polymer[114]. PEI-coated AuNPs can be obtained by modification of the ligand or using it as a reducing agent[115]. Between the linear and branched derivatives of PEI, the latter one can condense nucleic acid with higher efficiency. Thus, it was selected for the functionalization of AuNPs. This polymer should be able to stabilize the AuNPs, condense nucleic acids, and translocate the complex into the cells. bPEI is available in different lengths, and in this regard, we have selected two bPEI of different molecular weights (2 and 25 KDa) to assess better the effect of the polymers in the toxicity and efficacy (**Figure 22**). However, to increase the stability of the final particles and reduce their inherent toxicity, which is required to ease their translation into preclinical and clinical settings, the addition of an additional polymer was envisioned.

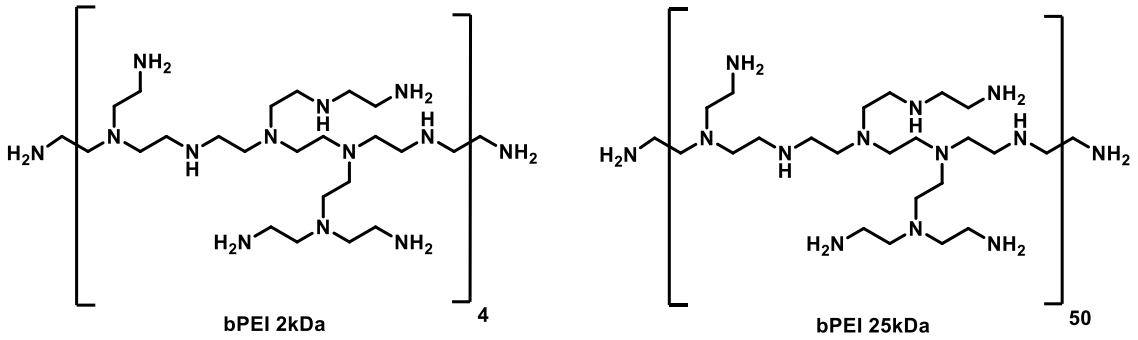

Figure 22. Chemical structure of 2 and 25 KDa bPEI, respectively.

3.1.2. Polyethylenglycol (PEG)

Polyethylenglycol (PEG) is a polymer constituted by a single monomer of ethylene oxide (**Figure 23**). Depending on its molecular weight (>20 KDa) can also be called polyethylene oxide (PEO) or polyoxyethylene (POE). This polymer is used in very different fields, so it can be found commercially with different lengths, geometries and modifications in one or both ends.

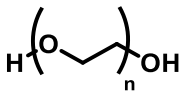

Figure 23. Chemical structure of PEG.

In medicine, PEG has been commonly used as an excipient of different drugs to increase their stabilization or enhance their therapeutic properties[116]. It has also been used in colon and colorectal cancer, where its role as a chemopreventive agent[117], epidermal growth factor receptor (EGFR) downregulator[118,] and sensitizer to chemotherapeutics was evaluated.[119].

Regarding its use in nanoparticles, the partial or complete PEGylation of their surface can modulate some of the inherent properties of the nanoparticles and, what is more, increase their biocompatibility. In this sense, PEG can reduce the interaction with the reticuloendothelial system (RES), the primary mechanism of nanoparticles clearance, leading to longer circulating times, which is desirable in most therapeutic approaches, particularly those involving intravenous administration[120-121]. However, the final behavior of the modified particles depends on several factors, such as the molecular weight (MW) of the polymer, its conformation and modifications, final surface density and, of course, the type

of nanoparticles used[122]. For instance, it has been used in liposomal nanoparticles, such as Doxil, a PEGylated liposomal formulation of doxorubicin, designed to reduce the toxicity of the chemotherapeutic agent. This system showed fewer side effects than the drug alone, better pharmacokinetics properties and biocompatibility. This nanoformulation is currently employed to treat ovarian cancer and Kaposi's sarcoma[123].

PEGylated gold nanoparticles present excellent stability compared to uncoated ones. It has been studied the effects of coating density and the media used have over the nanoparticles, showing high stability water, buffers and organic solvents[124]. The PEGylation of gold nanoparticles can be achieved during or after their synthesis through covalent linking or surface absorption, respectively. However, an excess of the polymer may lead to a loss in the efficacy of the nanoparticles[125].

Due to the properties discussed above, PEG was one of the chosen polymers to functionalize the nanoparticles. Its use will increase the colloidal stability in aqueous media of gold nanoparticles. These formulations will also be valuable for future "*in vivo*" experiments, since they can dope nanoparticles with stealth properties[126], preventing their recognition by the RES.

From the different commercial sources, the type of PEG chosen had a linear geometry and molecular weight of around 3000 MW with an amine and hydroxyl group in the extremes, respectively (**Figure 24**). These features have different purposes. On the one hand, a "low" molecular weight and linear geometry may ease their manipulation, modification and purification. Additionally, the two different functional groups at the ends can be exploited for their selective modification.

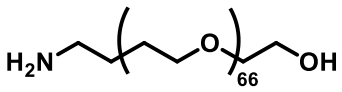

Figure 24. Chemical structure of NH_2-PEG-OH (3000 MW) used

Both the bPEIs and PEG ligands can be functionalized on the AuNPs surface by covalent o electrostatic conjugation. Nevertheless, the immobilization of the polymers by the covalent approach is recommended to obtain more stable

particles[127]. In this regard, the ligands can be chemically modified with a suitable linker to ease the covalent functionalization. For this project, lipoic acid was explored as the primary option.

3.1.3. Lipoic acid

Lipoic acid (LA) is a natural organosulfur compound that has been used in medicine as treatment in diabetes and hyperglycemia due to its antioxidant properties and its ability to help in the glucose uptake into the muscle cells[128]. Its chemical structure presents a carboxylic acid function, a dithiolane moiety and a chiral carbon (**Figure 25**). Of the two possible enantiomers, only the (R)-(+)-lipoic (RLA) is present in nature and has biological activity, whereas the (SLA) can only be obtained by chemical synthesis and inhibits the activity of RLA[129].

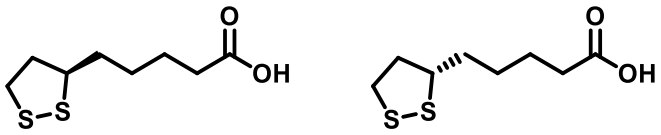

Figure 25. Chemical structure of (R)-(+)-lipoic acid (RLA) and (S)-(+)-lipoic acid (SLA) enantiomers.

LA is usually used as a cross-linker between AuNPs and a ligand. The disulfide bond produces a strong binding with the gold nanoparticles due to the great affinity of gold display for the sulfur groups[130], also making it a good stabilizing agent[131]. In addition, its carboxylic acid group can be easily activated to increase its reactivity with primary amino groups allowing the conjugation with different agents[132-133],

In our project, the presence of amino groups on both polymers allows their easy modification with lipoic acid by amide formation. Once modified with the linker, they can be used to functionalize the AuNPs by displacement of the citrate coating.

3.2. Results and Discussion

In this stage of the project, two polymers have been selected to functionalize the AuNPs previously synthesized. The first one is the bPEI, a polymer commonly used as a transfer agent due to its high cationic density. Its length correlates with

its transfection efficacy but also with its toxicity. Due to this, it was explored the use of a low molecular weight bPEI of 2 KDa. To carry out a comparison in terms of transfection efficacy and toxicity was also selected a high molecular weight bPEI of 25 KDa.

The second polymer was PEG, a polymer commonly used to functionalize nanoparticles to increase their colloidal stability in different media. This polymer can provide stealth properties, which are crucial to improve their blood circulation time in animal studies. It was chosen a PEG of 3 KDa due to the similar weight of the bPEI of 2 KDa.

The conjugation of both polymers to the AuNPs surface can be done by different means, such as electrostatic or covalent interactions. In this case, we have explored the covalent approach using lipoic acid as linker. This molecule is also commonly used to stabilize AuNPs due to the presence of a disulfide bond, which presents a strong affinity for the gold surface. Additionally, it bears a carboxylic acid that can be activated to conjugate with the polymers via amide formation.

3.2.1. Synthesis

To conjugate the lipoic acid to the polymers, the carboxylic acid was activated to ease the reaction with the amino groups of both polymers. The activation can be obtained with different leaving groups, such as hydroxybenzotriazole (HOBt), N-hydroxysuccinimide (NHS) or its analogous the N-hydroxysulfosuccinimide (Sulfo-NHS), used in reactions in aqueous media. Due to its extensive use and the excellent solubility of the polymers in organic solvents as DCM or THF, NHS was selected for this process (**Scheme 1**).

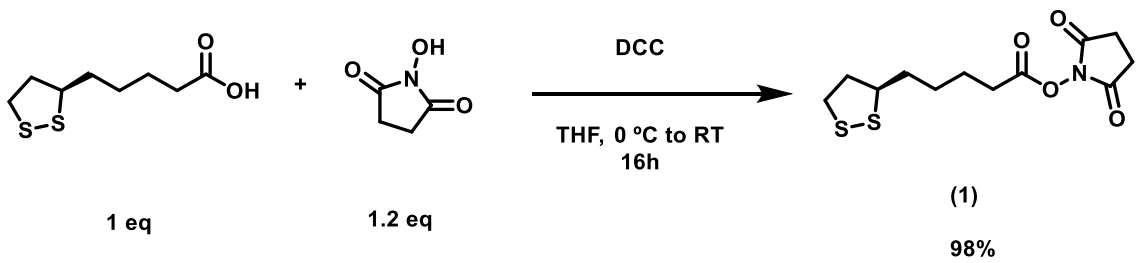

Scheme 1. Activation of the lipoic acid (LP) linker with N-hydroxysuccinimide (NHS). The reaction is carried out in the presence of DCC and using THF as solvent at 0 ºC to RT for 16h.

Once activated the lipoic acid with the NHS, the corresponding ester LP-NHS (**1**) was used in the conjugation with the polymers (**Scheme 2**). Both polymers show good solubility in organic solvents, which was required for the optimum conjugation with the LP-NHS. To increase the efficiency of the reaction, THF was selected as the solvent, which is better in amidation reactions[134]. However, in the case of bPEI, it is critical to stir the solution vigorously to obtain a homogeneous solution and avoid aggregation.

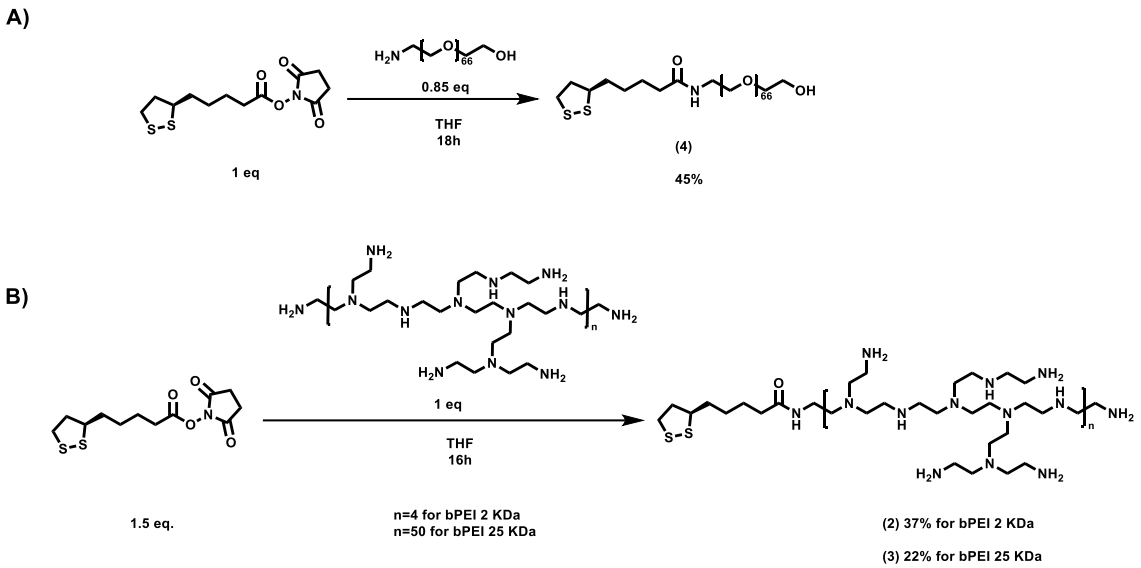

Scheme 2. Conjugation of the activated lipoic acid (LP-NHS) with the polymers bPEI 2 and 25 KDa (B) and PEG 3 KDa (A) using THF as solvent to favor the amide formation for 16h.

Once the reaction was completed, the purification of the modified polymers was carried out by dialysis. In this process, the reaction mixture was placed in a semi-permeable membrane with a specific pore size, which retains the desired molecule, whereas diffusing the others into the external media. For the modified bPEI (2 KDa) (**2**) and PEG (**4**) a 3.5 KDa dialysis tubing membrane was used. In the case of modified bPEI (25 KDa) (**3**), a 10 KDa dialysis tubing membrane was required. Other types of membranes, like membrane cassettes of the same pore size could be evaluated, but they were discarded due to the few amount of product that can be recovered.

This purification method removes the unreacted LP-NHS, retaining the modified polymers inside the membrane. However, the unreacted polymers could also be retained. In the case of the purification of LP-PEG (3 KDa), the final product

should remain inside the dialysis membrane, whereas the unreactive polymer and linker might be removed due to their lower molecular weight with respect to the pore size of the dialysis membrane. However, in the case of bPEI (25 KDa), the purification is more complicated and the unreactive polymer could be retained inside the membrane. Regarding the purification of LP-bPEI (2 KDa), the use of a 3.5 KDa membrane was compared with one of 2 KDa, observing a better purification with the first one. This was attributed to the branched nature and hydrophilic character of the polymer, making its diffusion through the membrane more difficult. After the purification, the solvent is removed under vacuum and the modified polymers quantified and characterized. It was observed that through lyophilization, the products obtained were easier to solve and presented clearer characterization spectrums.

The characterization of the modified polymers is not an easy task due to two facts: the slight difference in the molecular weight between the unmodified and the modified polymers and the big difference in signal intensity between the polymer and the linker.

The first one affects the characterization by mass spectroscopy. Due to the high molecular weight of the modified polymers was chosen to perform a MALDI experiment. This technique, in the case of polymers, provides a Gaussian distribution of peaks obtained by the polymer sample. Also, the molecular weight provided by the commercial source is an approximation, making difficult the differentiation with modifications of the polymer of low molecular weight[135]. In the case of LP-PEG (3 KDa) (**Annex Figure 24**), which shows a Gaussian distribution between 2000 and 4000 Da, centered in 3000 Da and with a maximum peak at 3046.8 Da, corresponding to the polymer with 66 monomer units with the linker modification. Regarding the LP-bPEI, the characterization by mass spectroscopy is more complex. In the bibliography, it can be found that for branched polyethylenimine the sensibility of the technique decreases directly with the length of the polymer, being the bPEI in a range of 600 and 1200 Da the ones which provides better results[136-137]. This happens due to multiple factors like the cationic nature of the polymer, high density and degradation process. This complex characterization can be observed in the MALDI-TOF obtained for the

two samples of LP-bPEI 2 KDa (**Annex Figure 25**) and 25 KDa (**Annex Figure 26**), which were analyzed using α-Cyano-4-hydroxycinnamic acid (CHCA) matrix and MeOH as solvent. In both cases, it is observed a complex spectrum with a large number of signals with overlapping isotopic distributions. Most of the peaks present a difference of 43 units, which corresponds with the monomer [C2H4NH]. In the case of LP-bPEI 2 KDa, the gaussian peak distribution appears centered in 1000 Da, and for the LP-bPEI 25 KDa, shows a peak distribution centered at 300 Da.

The second one affects the NMR characterization. The polymers present a repeated chemical structure, a monomer, with a specific signal. Due to the big difference in the molecular weight between the polymers and the lipoic acid, and the low ratio of modification of the polymer, most of the contribution to the spectra comes from the polymer. This is also affected by the characteristics of the NMR machine and the parameters used in the process. It has been observed that using a whole zg 90º pulse signal instead of a 30º one, allows a more precise integration of the signal. In the case of the LP-PEG ^{1}H-NMR spectrum, the polymer presents an intense narrow signal at 4 ppm, from the signal range of the linker (2.5-1 ppm). Along with the ^{13}C-NMR spectrum can be concluded the successful obtention and purification of the polymer. Regarding the LP-bPEI (2 KDa and 25 KDa), the difficulty relies on the signals of the polymers in the ^{1}H-NMR spectrum and the poor solubility of the dry modified polymer. The best solvent to perform the NMR experiments was the deuterated DMSO. In the case of the LP-bPEI 2KDa ^{1}H-NMR, the polymer band can be shown between 4-1.8 ppm and between 2-1 ppm (**Annex Figure 3)**, hiding most of the linker signal. Some signals in the range of 2-1 ppm can resemble the ones observed by the LP-NHS ^{1}H-NMR (**Annex Figure 1**) suggesting its presence. On the other hand, the ^{13}C-NMR was performed with a more powerful probe equipment (500 MHz) for 12h, observing a signal at 172 ppm (**Annex Figure 14**) that can confirm the modification. In the case of the LP-bPEI 25 KDa, the ^{1}H-NMR (**Annex Figure 4)** shows the polymer signal completely overlapping the possible signal of the modification. In the case of the ^{13}C-NMR (**Annex Figure 15**), it also can be seen a signal at 172 ppm. With these results, despite the purity of the modified bPEIs cannot be confirmed, they were employed in the functionalization of nanoparticles.

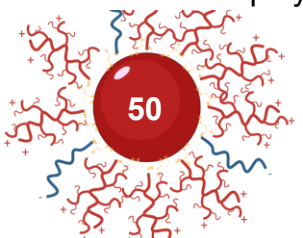

3.2.2. Functionalization

3.2.2.1. 13-Gen0.5 AuNPs

Once the polymers were modified with the linker, their use in the functionalization of the AuNPs was evaluated. The particles selected for the preliminary studies were the 13 nm AuNPs based on the Turkevitch's method, from now on called 13-GEN0 AuNPs. First of all, it was necessary to know the loading capacity of the GEN0 AuNPs with this size at the selected concentration (10 nM). The loading capacity not only depends on these two factors, but also on the properties of the selected ligands[138].

The direct functionalization of the AuNPs with LP-bPEI was not possible, leading to an irreversible aggregation process. This effect was probably produced due to the sudden difference of charges between the citrate anions and the polymer. Because of this, the loading capacity study was performed with LP-PEG due to its stabilizing role. Taking into account the AuNPs parameters of concentration and size, and the LP-PEG ones of length and geometry, it was expected loading capacity of around 10-15 nmol of the polymer per milliliter of AuNPs[139]. With these values in mind, it was studied the progressive addition of LP-PEG (1.5, 3, 4.5, 6, 7.5, 9 and 10.5 nmol) and the changes in the size and zeta-potential properties were assessed. The AuNPs with LP-PEG were called 13-GEN0.5-AuNPs.

The main changes can be observed in the zeta potential (**Figure 26)**. In this sense, the minimum addition of LP-PEG (1.5 nmol) to the nanoparticles increases the potential with respect to the no-functionalized ones, from -42.3mV to -28.14 mV (Δ14.16 mV). However, those nanoparticles presented low stability, generating a residue after a couple of days at room temperature, and were discharged.

However, after the addition of 3 nmol of the modified PEG, the potential only increased 3.4 mV with respect to the 1.5 nmol addition, but the stability of the AuNPs improved significantly. In this case, no precipitation was observed after 4 weeks at room temperature. For these reasons, 3 nmol of LP-PEG was selected as the minimum amount to produce stable particles. This formulation was called 13-GEN0.5.

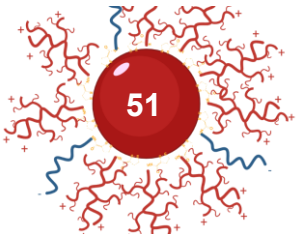

The additions of 4.5, 6 and 7.5 nmol did not change the potential measured significantly, but when 9 nmol were employed, the potential incremented from -25.53 mV to -16.3 mV (Δ9,23 mV). The addition of a bigger amount of the modified polymer did not alter the potential of the particles further. Thus, these data suggest that the nanoparticles are fully loaded with the polymer when 10 nmol are used, which agrees with previous reports[139].

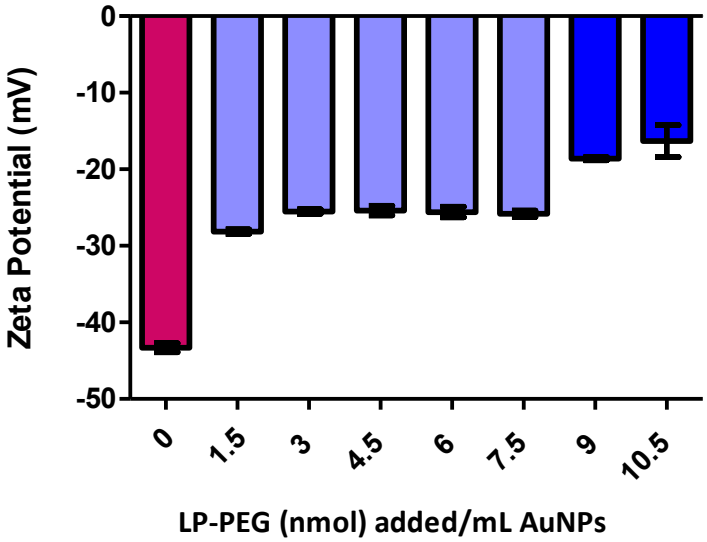

Figure 26. Zeta-potential measurements of AuNPs functionalized with different amounts of LP-PEG (blue) with no-functionalized AuNPs (purple) as control. The image shows the values of maximum intensity peaks reached. Functionalized AuNPs present an increment in the zeta-potential with respect to the control, showing a bigger increase at higher additions of the modified polymer (deep blue) that remains constant as the AuNPs reach a saturation point.

Regarding the size measurements, it can be observed an increment in the hydrodynamic diameter with respect to the no-functionalized ones, growing around 8.67-9.54 nm (**Figure 27**). With some variations, the diameter does not change too much independently of the amount of polymer added. This can be explained by the final conformation of the polymer, which can be organized in two ways: brush or mushroom[140]. The brush conformation allows the polymer to lay perpendicular to the gold surface while the mushroom one would be parallel. The first conformation can be observed when the surface is not saturated with the polymer, but the arrangement can change when more polymer is added. Also, the molecular weight of the polymer plays a role in the arrangement, being more

common the mushroom conformation at the high molecular weight. As the size obtained does not differ at the different loadings of polymer, it is probably a brush conformation. In addition to this theory, the hydrodynamic diameter of PEG 3 KDa is approximately 3 nm[141]. This would mean an increment of around 6 nm in the overall diameter for completely spherical nanoparticles, which is close to the increment observed by DLS. Otherwise, in the mushroom conformation, the polymer would fold, leading to significant changes in the diameter of the particles. Also, it can be observed that the diameter intensity curve becomes narrower and higher with respect to the no-functionalized ones. This is probably due to the obtention of a high concentration of stable nanoparticles, thanks to the polymer properties.

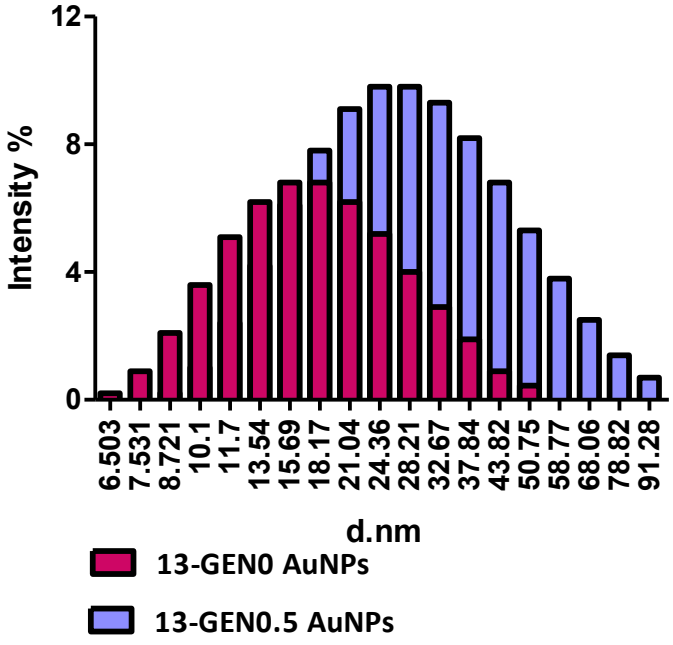

Figure 27. Hydrodynamic size measurements of AuNPs functionalized with only LP-PEG (blue) with no-functionalized AuNPs (purple) as control. It can be observed an increase in the size of the hydrodynamic size of 25-30 nm.

3.2.2.2. 13-Gen1-2 AuNPs

After establishing the loading capacity of the AuNPs based on the functionalization with LP-PEG, it was carried out the double functionalization of the AuNPs with LP-PEG and LP-bPEI. The first experiments were performed with LP-bPEI (2 KDa) due to the similar molecular weight and an expected lower probability to destabilize the particles due to its positive charge than the analogous LP-bPEI (25 KDa). Also, since the minimum amount of LP-PEG required to stabilize the AuNPs was 3 nmol, it was planned to coat the remaining surface with LP-PEI (2 KDa). This procedure led to AuNPs functionalized with a ratio of LP-PEG/ LP-PEI of 3:7, labeled as 13-GEN1 (**Figure 28**). The functionalized AuNPs with LP-PEG (3 nmol) were evaluated with an increased amount of LP-bPEI (2 KDa) (2.5, 5, 7.5, and 10 nmol).

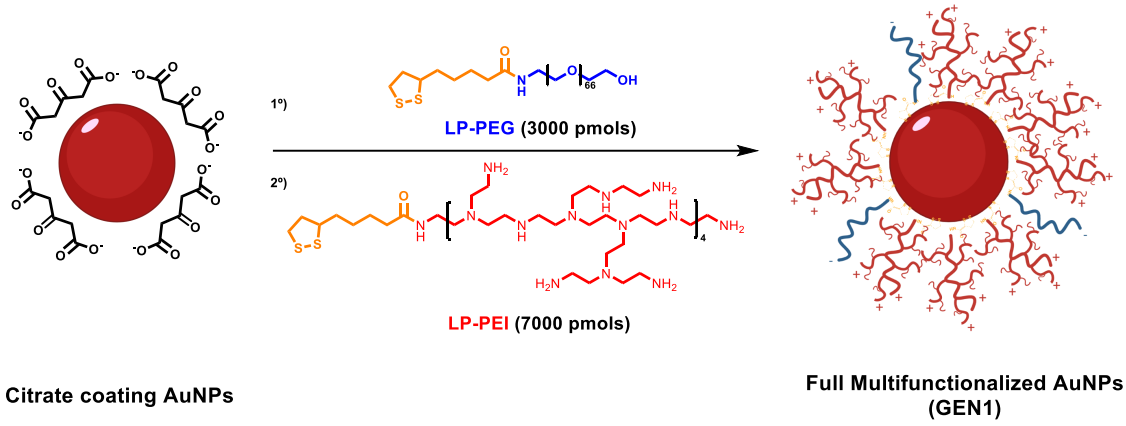

Figure 28. Schematic representation of the functionalization process of the AuNPs from the no-functionalized AuNPs (GEN0) to the functionalized ones with LP-PEG and LP-bPEI in a ratio 3:7 (GEN1).

The LP-bPEI (2 KDa) addition resulted in a significant increment in the zeta-potential (**Figure 29A**). A positive potential is achieved even at the minimum amount used of 2.5 nmol. The potential keeps increasing with the 5 and 7.5 nmol additions. No variations in the potential were observed after adding higher amounts of the polymer, which match the loading capacity expected. Fully functionalized AuNPs presented a great change in their zeta-potential, increasing it from around -25.53 mV, with only 3 nmol of LP-PEG, to +12.33 mV (**Figure 29B**). This results in an increment of Δ36 mV, with respect to the AuNPs functionalized with LP-PEG, and Δ52 mV, compared to the no functionalized ones.

Regarding the hydrodynamic size (**Figure 30**), its size distribution became narrower, probably due to the obtention of higher concentrated AuNPs, at 28.21 nm as the particles functionalized with only PEG. The conformation of bPEI is more complex due to its branched structure and its cationic nature, which depends not only on the molecular weight but also on the pH of the medium. Based on bibliography[142-143] and taking into account the 6.5 pH of particles (measured after the addition of bPEI) and the hydrodynamic diameter of larger bPEIs, the polymer should be folder over itself, measuring no more than 1 or 2 nm, which corresponds with the data obtained. Also, this conformation might not be affecting the PEG brush conformation, or the hydrodynamic size would decrease. The particles obtained by these procedures are labeled as 13-GEN1-2 AuNPs, and are a significant milestone for the first objective of this project.

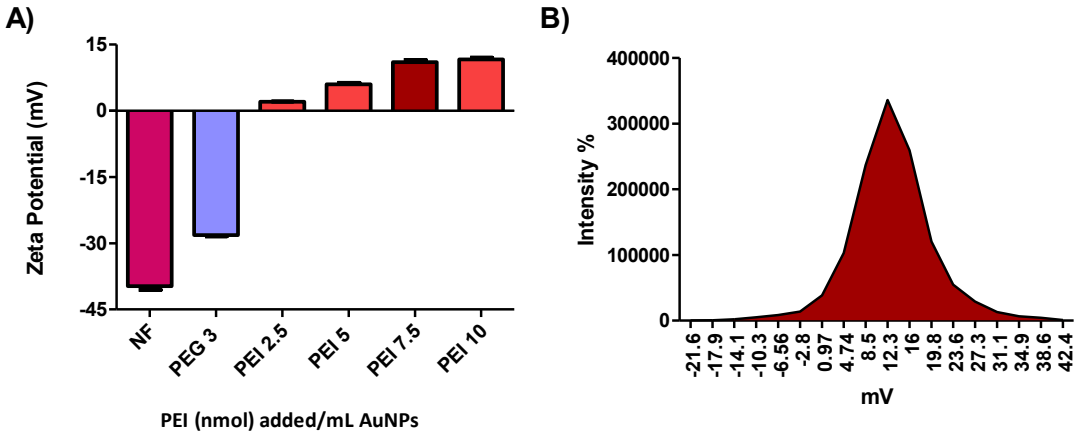

Figure 29. A) Zeta-potential measurements of AuNPs functionalized with different amounts of LP-bPEI (2 KDa) (red), LP-PEG (3 nmol) (blue) and no-functionalized AuNPs (purple) as controls. The image shows the average potential values reached. LP-bPEI functionalized AuNPs present an increment in the zeta-potential with respect to the control, showing a bigger increase at higher additions of the modified polymer. B) Zeta-potential at the (7.5 nmol of LP-bPEI 2 KDa and 3 nmol of LP-PEG

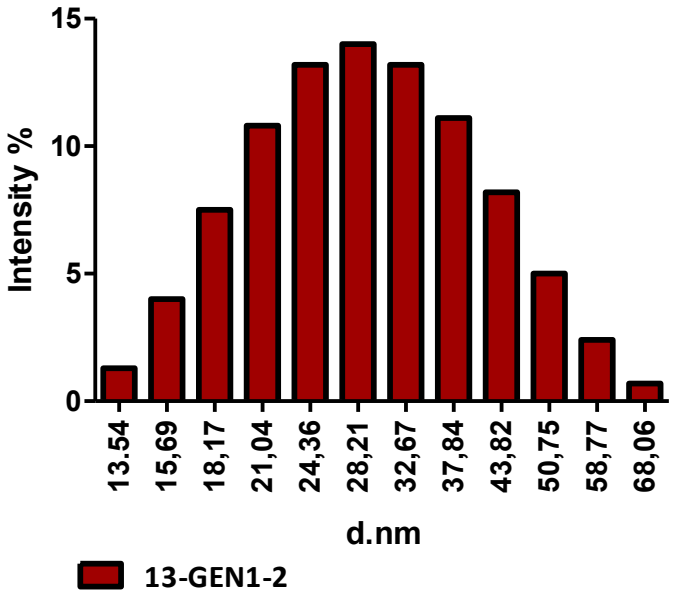

Figure 30. Hydrodynamic size measurements of 13 nm AuNPs functionalized with LP-PEG (3 nmol) and bPEI 2 KDa (7 nmol).

AuNPs were also characterized by UV spectroscopy (in a 1:10 AuNPs/water dilution) to observe possible aggregates of the particles not visible to the naked eye (**Figure 31**). It was observed that after the addition of the LP-PEG the SPR band kept centered at 520 nm and with the addition of LP-bPEI a shift was observed to 522 nm, maybe due to minor aggregations of the particles. After each addition, it was also reported a decrease in the absorbance intensity, which means a lower concentration of the final product, going from 10 nM before functionalized to around 8 nM after the obtention of the 13-GEN1-2 AuNPs. This is probably due to the treatment of the AuNPs during the functionalization, where a certain amount can be lost in the centrifugation stage (see **Functionalization Protocol**).

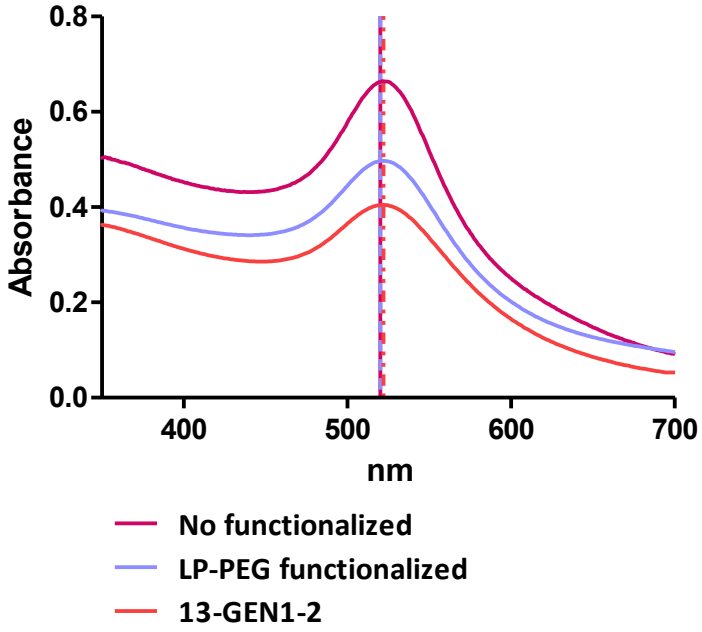

Figure 31. UV-Vis characterization of AuNPs without functionalization (purple), after the complete functionalization with PEG (blue) and after the functionalization with both LP-PEG and LP-bPEI (red). It can be observed that in each stage, it is observed a shift to the red of the spectrum and reduction of the absorbance signal.

In summary, the final AuNPs 13-GEN1-2, present a hydrodynamic size of 30.79±10.78 nm and a zeta-potential of 12.9±6.99 mV. These results suggest that the polymer LP-PEG and LP-bPEI has been incorporated and have a profound effect on the zeta-potential and size of the AuNPs. Interestingly, GEN1 AuNPs are very stable, presenting the same hydrodynamic size and zeta-potential after 3 weeks at room temperature or after 2 months at 4 °C.

In parallel to the PEG/bPEI 3:7 formulation, other functionalization ratios were prepared and characterized: 5:5 and 7:3. As expected, these alternative formulations displayed a lower zeta-potential (**Figure 32B**) due to the lower presence of bPEI on the surface of the particles. Regarding the hydrodynamic size (**Figure 32A**), the size distribution became narrower, although their centered peak increased 4.46 nm. These results confirm that the best ratio to work with, to maximize the stability and the positive charge, was the first ratio tested (LP-PEG/LP-PEI 3:7).

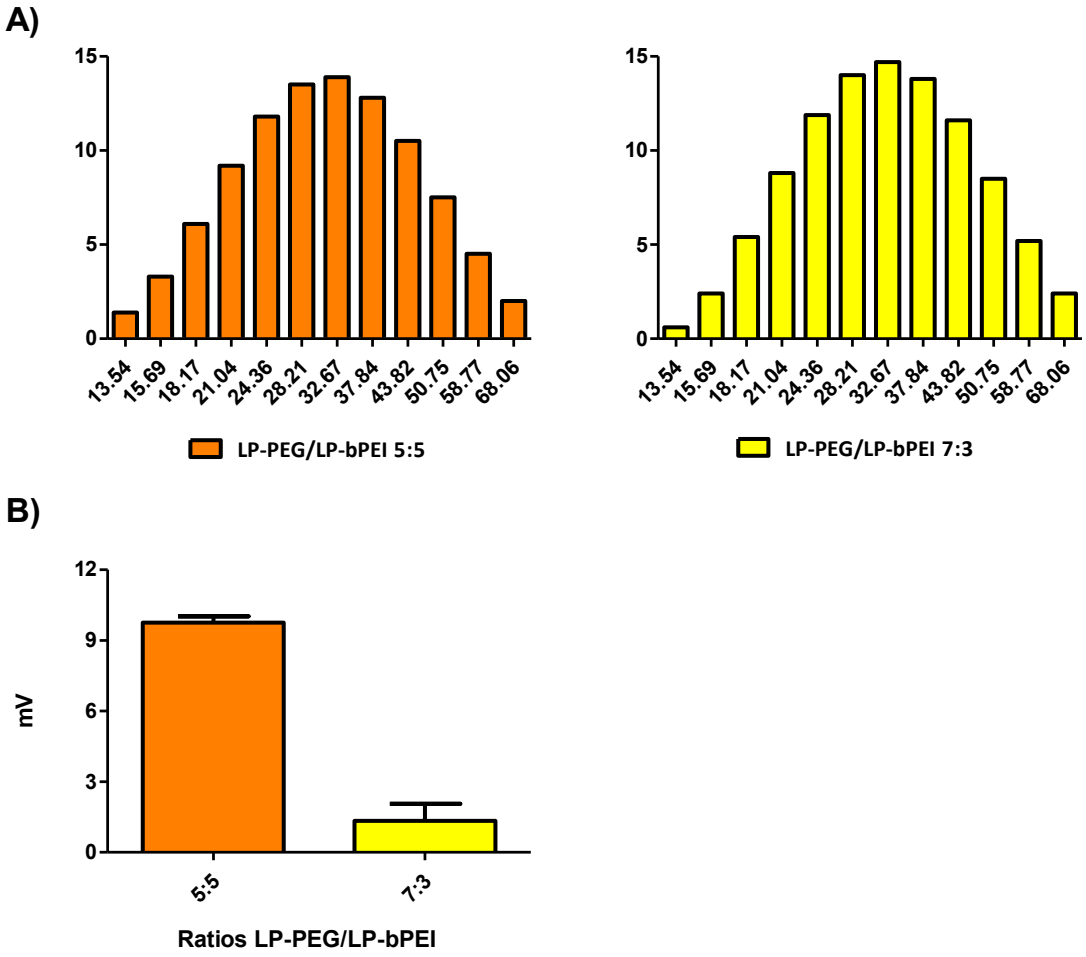

Figure 32. A) Hydrodynamic size and B) Zeta-potential measurements of AuNPs with different ratios of LP-PEG/LP-PEI (5:5 and 7:3).

3.2.2.3. 13-Gen1-25 – Functionalization with LP-bPEI (25 KDa)

As the AuNPs formulation with the ratio 3:7 LP-PEG/LP-PEI provided the best values in terms of potential and stability, it was used in further experiments, such as in the preparation of nanoparticles with LP-bPEI of 25 KDa. Due to its bigger size and molecular weight, around 13 times with respect to bPEI (2 KDa), it could be expected an increment in the overall charge. So that, the measurements (**Figure 33B**) show a zeta-potential distribution of 37±12.2 mV, which compared to the GEN1 functionalized LP-bPEI 2KDa (**Figure 29**) is an increment of +25.1mV. A higher potential was not expected, taking into account that most of the amine groups of the polymer would be hindered, preventing its participation in the measurements. Regarding the hydrodynamic size (**Figure 33A**), it is observed a narrow and intense size distribution, which suggests a very stable

conformation of 33.17±8.28 nm, centered at 32.67. This increment in size, of around 2.39 nm with respect to the 13-GEN1-2 AuNPs (**Figure 30**) implies that the bPEI 25 KDa surpasses the PEG length. According to the hydrodynamic size of the polymer, around 4 nm, this increment in the size was expected[142].

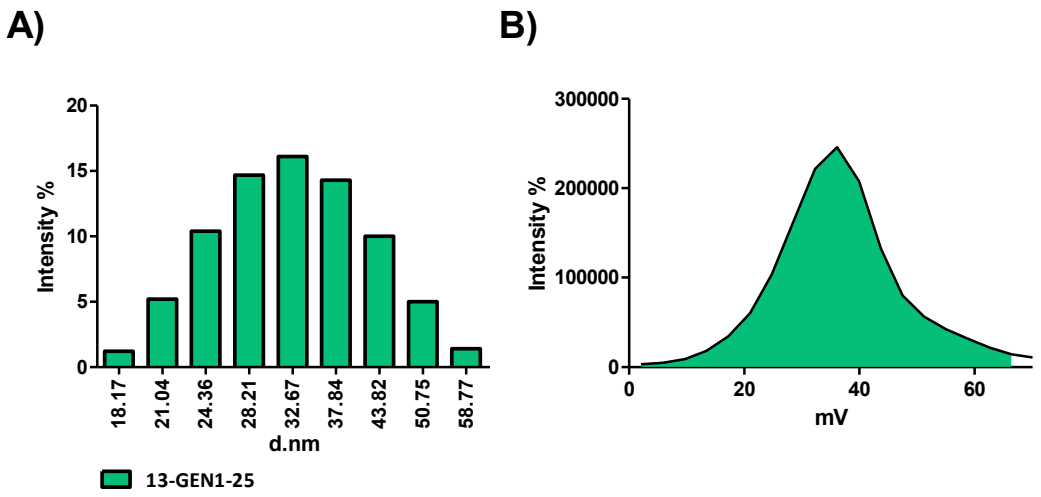

Figure 33. A) Zeta-potential of the GEN1 AuNPs functionalized with LP-bPEI (25 KDa) (green) and B) its comparison with the functionalized ones with LP-bPEI (2 KDa) (red), observing an increment in the zeta-potential of almost the double. C) Hydrodynamic size comparison of the two types of GEN1.

3.2.2.4. 35-Gen1-2 - LP-PEG/LP-bPEI (2 KDa) (35 nm)

For larger AuNPs, the same functionalization as the 13 nm ones was assessed ease their comparison. For this purpose, a similar concentration of 10 nM was tested. For these AuNPs, it was expected a 7-fold increase in the loading capacity compared to 13 nm AuNPs. This approximation was made considering the AuNPs as a perfect sphere and calculating their area. Therefore, in this case, the amount of the reagents used was increased 7-fold, particularly LP-PEG (21 nmol) and of LP-PEI (2 KDa) (63 nmol). To compare the results with the AuNPs of 13 nm, it was studied the functionalization of the AuNPs with only LP-PEG (21 nmol) (35-GEN0.5 AuNPs) and with the addition of both LP-PEG and LP-PEI (35-GEN1-2 AuNPs).

In these experiments, significant changes were appreciated in both the hydrodynamic size and the zeta potential. In the case of the size, the addition of LP-PEG (**Figure 34A**) induces an increment in the size, from 58.77 nm to 78.22 nm. This variation is 3-fold larger than the expected (**Figure 27**), which might be due to some aggregation of the nanoparticles. Once the bPEI was added (**Figure 34B**), the size distribution became narrower but less intense, shifting to a smaller size. This behavior could suggest an increase in the destabilization of the particles. After 24 hours (**Figure 34C**), this was confirmed with the formation of two different size populations. Regarding the zeta potential, the 35-AuNPs showed an increment after adding LP-PEG and the bPEI (**Figure 35A-B)**. However, due to the low stability of these nanoparticles and the difficulties on the preparation of the AuNPs, no more experiments were performed with this size.

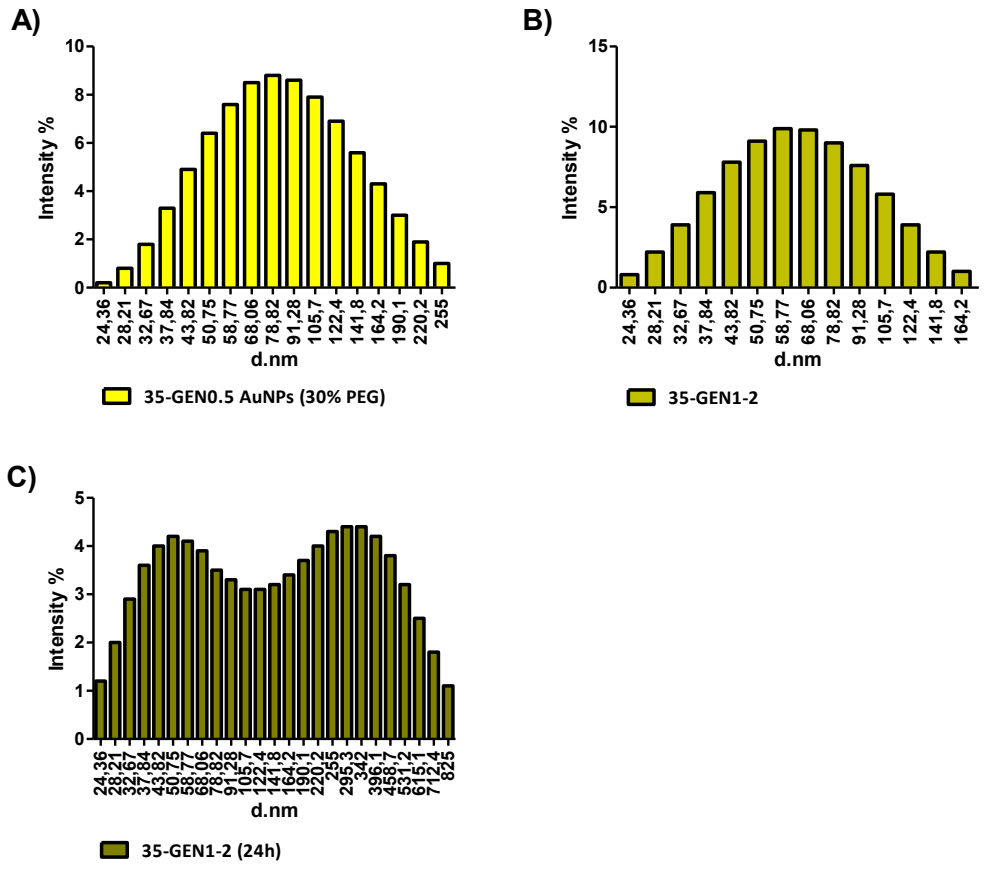

Figure 34. Hydrodynamic size characterization of 35 nm AuNPs without functionalized (A), after the addition of LP-PEG (B) and after the addition of both LP-PEG and LP-bPEI 2KDa (C). The AuNPs functionalized with both polymers were measured again after 24 h (D) after the initial aggregation.

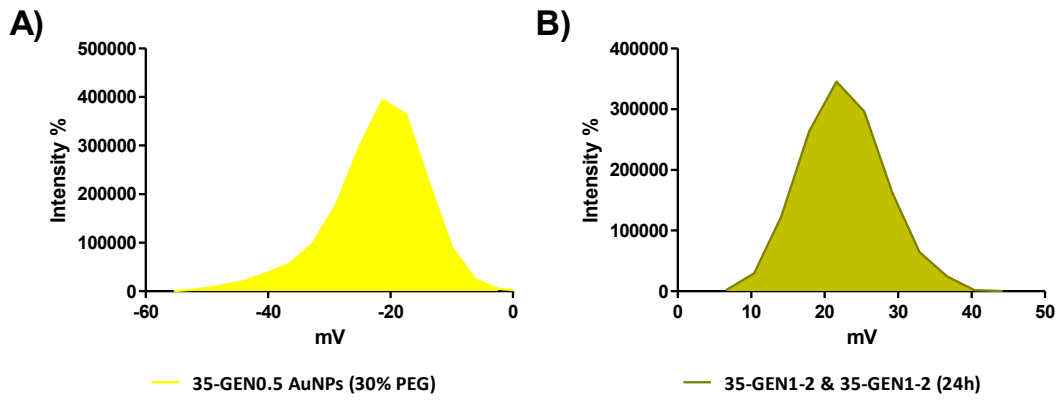

Figure 35. Zeta-potential characterization of 35-GEN0.5 (A) and 35-GEN1-2 (t=0 & 24 h) (B) AuNPs and its potential comparison respect the obtained in the 35-GEN0 AuNPs (C).

3.2.2.5. Gen1 - LP-PEG/LP-bPEI (2 & 25 KDa) (23 nm)

In this case, it was expected a 3-fold increase in the loading capacity with respect to the 13 nm AuNPs. The functionalization of these AuNPs was tested in two different ways. The first one consisted of functionalization with LP-PEG and LP-PEI in a ratio 3:7 (9 and 21nmol, respectively) to compare them with the 13-GEN1-2 AuNPs. The second one consisted of the functionalization of the AuNPs with the minimum amount of LP-PEG (3 nmol) to stabilize the nanostructure. The remaining available surface would be modified with LP-bPEI (27 nmol). This alternative ratio corresponding to 1:9, could provide new properties, like an increment in the potential. The 23 nm AuNPs, with the ratio 3:7, were called 23-GEN1-2 I and 23-GEN1-25 I for the ones functionalized with bPEI 2 and 25 KDa, respectively. Following the same terminology, the nanoparticles obtained with the ratio 1:9 were called 23-GEN1-2 II and 23-GEN1-25 II.

For the 23-GEN1-2 AuNPs I and II, the hydrodynamic size is pretty similar 64.09±39.1 and 65.3±33.85, respectively, and both centered at 58.77 nm (**Figure 36AB**). This implies an increment of around 16 nm, a bit more than expected, considering the previous functionalization. Regarding the zeta-potential, the value obtained for 23-GEN1-2 I and 23-GEN1-2 II were 12.99±6.99 mV and 16.2±6.56 mV, respectively (**Figure 36CD**). The results for both formulations are similar to the obtained for the analogous formulations of 13 nm, which was expected.

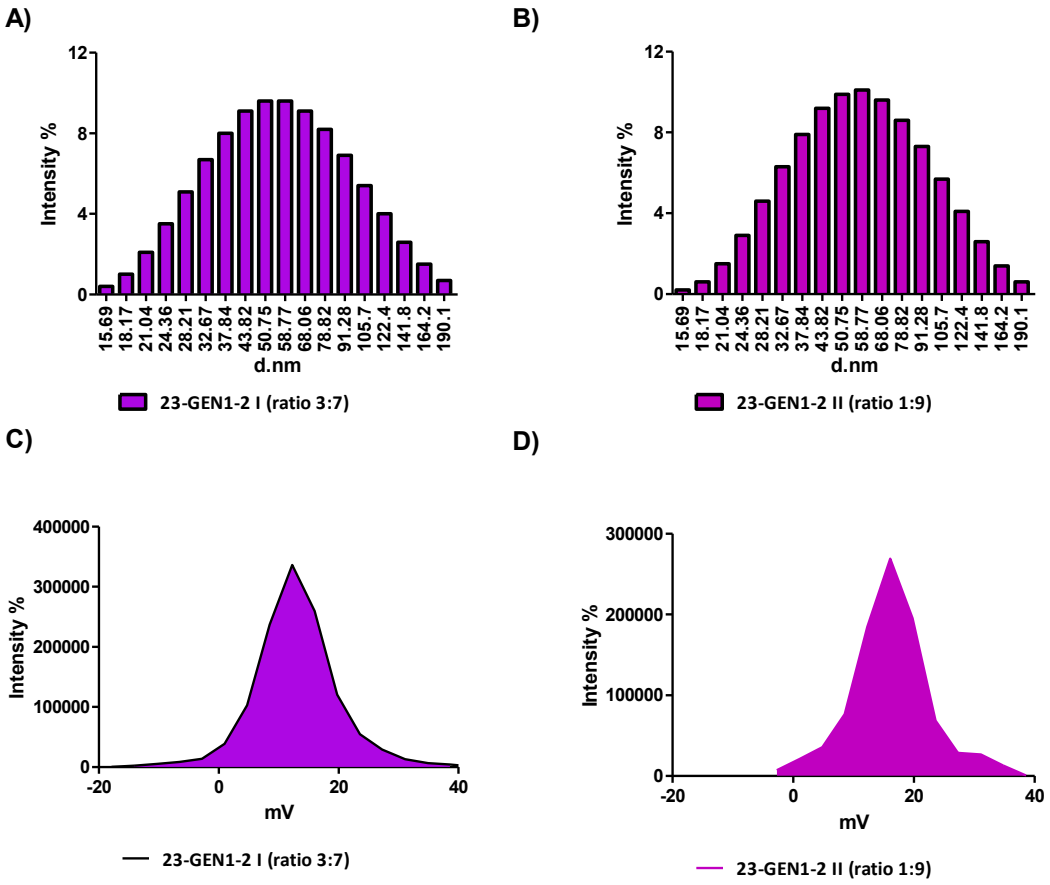

Figure 36. A-B) Hydrodynamic size and C-D) zeta-potential characterization of 23-GEN1-2 I and II AuNPs.

In the case of 23-GEN1-25 AuNPs I and II, the results match those obtained with bPEI 2 KDa. Their hydrodynamic size was 83.53±41.57 and 89.72±52.82, respectively, centered between 68.06 and 78.82 nm (**Figure 37AB**). The increment, around 30-40 nm is higher than expected for the addition of the polymer of 25 KDa, considering the 13-GEN1-25 (**Figure 33A**). Also, 23-GEN-25 II presents a more irregular size distribution and lower intensity, indicating some destabilization, although no aggregates were formed. Regarding the zeta-potential, 23-GEN1-25 I displays a potential of 35.9±9.59 mV (**Figure 37C**), similar to 13-GEN1-25 (**Figure 33B**), and for 23-GEN-25 II (**Figure 37D**) is 38.4±13.6 mV.

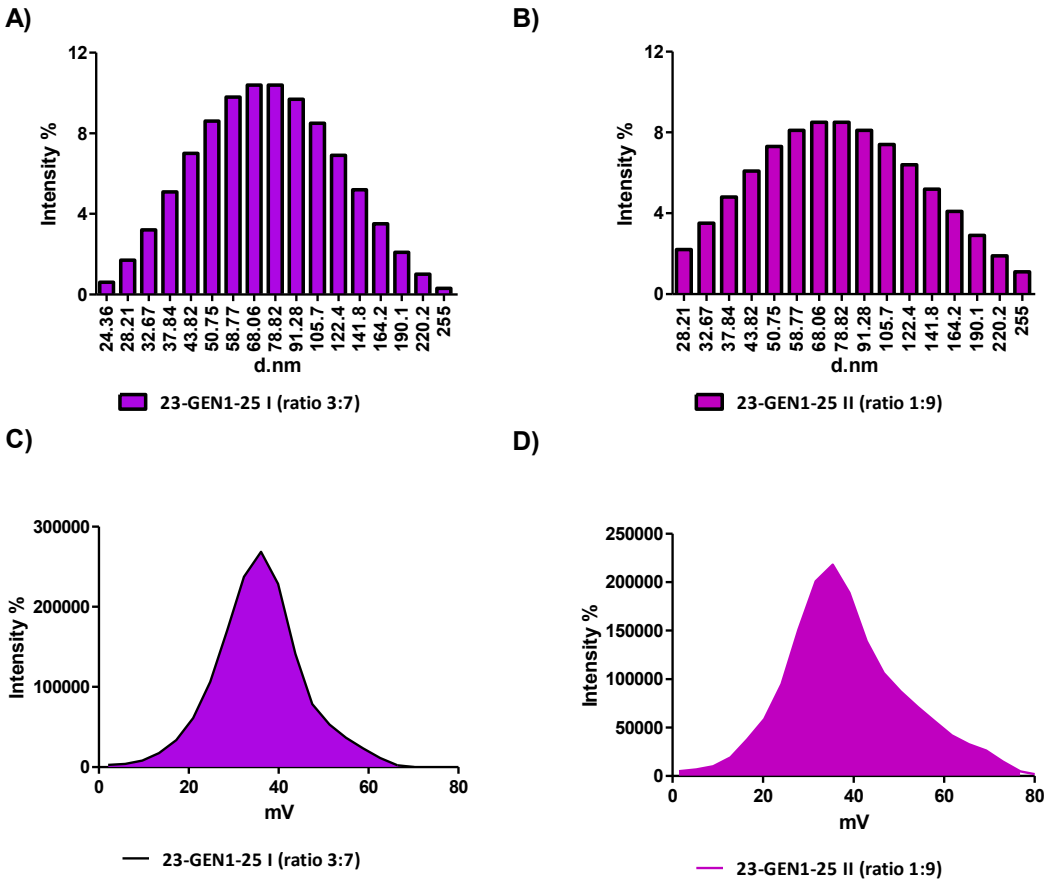

Figure 37. A-B) Hydrodynamic size and C-D) zeta-potential characterization of 23-GEN1-25 I and II AuNPs.

In summary, stable nanoparticles were obtained with 23-GEN1 and bPEI of 2 and 25 KDa. In this case, two different ratios of PEG/PEI were employed: 3:7 and 1:9. Among the nanoparticles obtained, 23-GEN1-25 II presented the lowest stability and therefore, we continue our work with 23-GEN1-2 I and 23-GEN1-25 I.

The summary of the characterization obtained for the 4 different GEN1 formulations considered suitable as carriers can be found in (**Table 1**). Despite the differences in the potential and hydrodynamic size between the eight AuNPs evaluated 13-GEN2 and 23-GEN2, all the formulation displays excellent stability properties keeping the same properties for 1 month at room temperature and 3-4 months at 4 ºC. After this time, aggregates appeared, particularly for 23-GEN2.

Name	Core (nm)	LP-bPEI (KDa)	Hydrodynamic Size (nm)	Zeta-potential (mv)
13-GEN1-2 (3:7)	13	2	30.79±10.78	12.9±6.99
13-GEN1-25	13	25	33.17±8.28	37±12.2
23-GEN1-2 I	23	2	64.09±39.1	12.99±6.99
23-GEN1-25 I	23	25	83.53±41.57	35.9±9.59

Table 1. Summary of the characterization obtained for GEN1 AuNPs with better properties for a carrier role.

3.2.3. Delivery of Biomolecules

Once stable nanoparticles were obtained using our approach, we started to assess the potential use of those systems as carriers of biomolecules. However, before using them for biological applications, their toxicity and loading capacity of biomolecules should be assessed.

3.2.3.1. Cytotoxicity assays.

To use the functionalized AuNPs as transfer agents, they should have negligible toxicity in the cells. For this reason, the corresponding cell viability assays were performed to test the effect of the functionalized AuNPs with respected the LP-bPEI alone. In these experiments, the concentrations of functionalized AuNPs were 1000, 500 and 250 nM. Regarding the LP-bPEI, the amounts used were 875, 437.5 and 218.75 pmol, the same amount as that present on the particles at the concentrations tested. These studies were carried out in two cell lines, PANC-1 (pancreatic adenocarcinoma) and MCF7 (breast cancer).

Regarding the toxicity of 13-GEN1-2, 23-GEN1-2 I and the LP-bPEI 2 KDa (**Figure 38**), the modified polymer induced some toxicity in PANC-1 (**Figure 38C**), particularly at the highest concentration tested (1 nM) with a 26% of viability. On the other hand, the 23-GEN1-2 I (**Figure 38B**) induced a significant toxicity (20%) at the same concentration but in MCF-7. These results highlight the different behavior of the cell lines and the importance of performing this type of experiment in multiple cell lines. In this case, it is remarkable that the toxicity of a molecule is enhanced or decreased by its conjugation to the nanoparticle, and the results

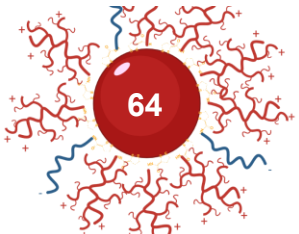

obtained depend on the cell line employed. Particularly, the polymer was toxic when used alone, however, it was dramatically reduced when used on the nanoparticle. This behavior was found in the PANC1 cell line, but the contrary was shown in MCF7. Further experiments are needed to understand these differences better.

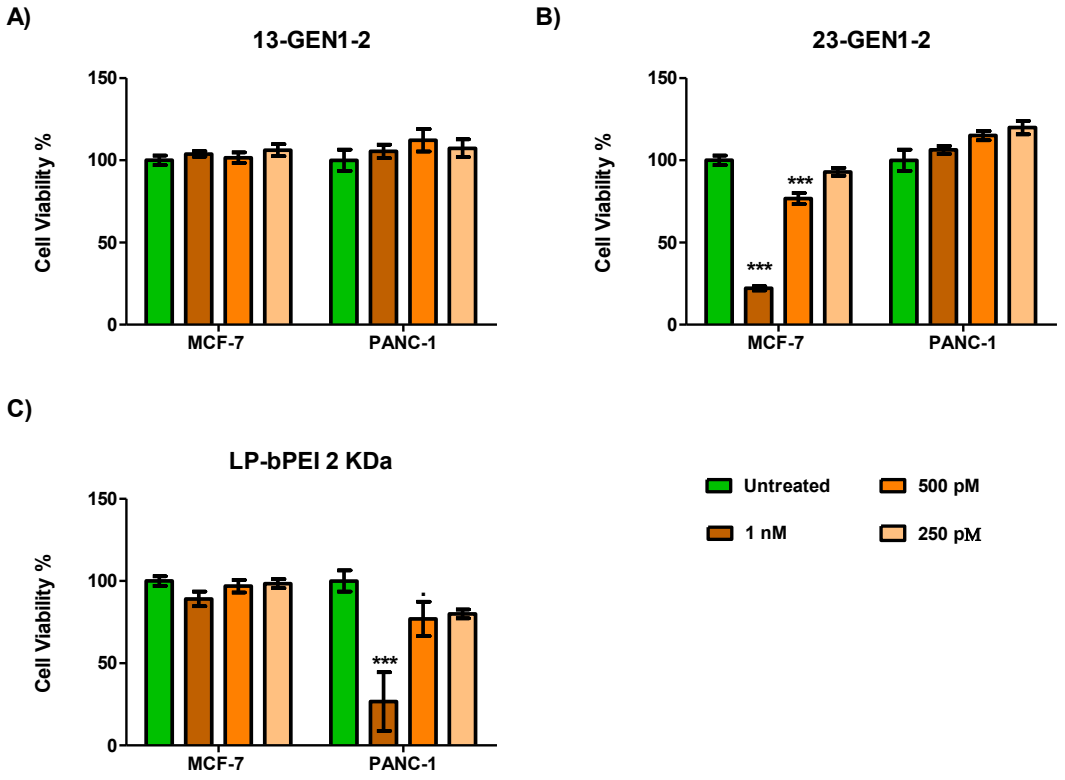

Figure 38. Cytotoxicity assay on MCF-7and PANC-1cell lines of the 13-GEN1-2 (A), 23-GEN1-2 I (B) AuNPs and the modified polymer LP-bPEI 2 KDa (C). The concentration of AuNPs added to the cells are 1 nM, 500 pM and 250 pM with untreated cells as control. The modified polymer concentrations tested corresponds to the one found in the AuNPs at the concentrations of 1 nM, 500 pM and 250 pM. The statistical analysis was performed using one-way ANOVA (each group vs. control) (*** $p < 0.001$, ** $p < 0.01$, * $p < 0.05$, · < 0.01).

In the case of 13-GEN1-25, 23-GEN1-25 I and the LP-bPEI 25 KDa (**Figure 39**). Using the 25 KDa polymer alone (**Figure 39C**) induces higher toxicity than in the previous experiments with a smaller polymer (2KDa) (**Figure 38**). This behavior is expected due to the higher amounts of charges compared with the bPEI of 2 KDa. As observed, the toxicity of the polymer is significantly reduced once it is attached to the nanoparticle (**Figure 39AB**) as desired.

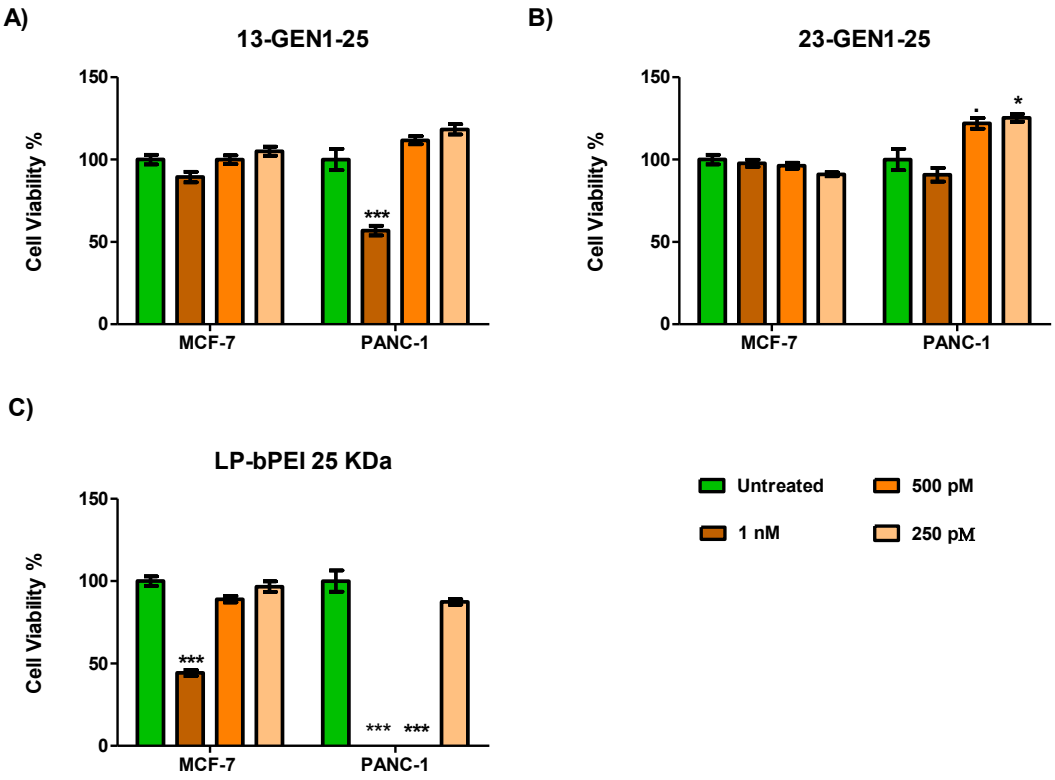

Figure 39. Cytotoxicity assay on MCF-7and PANC-1cell lines of the 13-GEN1 (A), 23-GEN1 I (B) AuNPs and the modified polymer LP-bPEI 25 KDa (C). The concentration of AuNPs added to the cells are 1 nM, 500 pM and 250 pM with untreated cells as control. The modified polymer concentrations tested corresponds to the one found in the AuNPs at the concentrations of 1 nM, 500 pM and 250 pM. The statistical analysis was performed using one-way ANOVA (each group vs. control) (*** $p < 0.001$, ** $p < 0.01$, * $p < 0.05$, · < 0.01).

3.2.3.2. Conjugation efficacy assays.

To test the capacity of the functionalized AuNPs as transfer agents, it was studied their interaction with oligonucleotides, which are short DNA or RNA molecules with an overall negative charge that allows the electrostatic interaction with the PEI. The oligonucleotide chosen to test the AuNPs was a decamer (10 units) composed only of thymine nucleobases and modified with a molecule of fluorescein (FAM) at the 5'-end. The fluorescein (FAM) eases the monitoring of the oligonucleotide, which can be useful to study the interaction with the nanoparticles. This sequence was selected because its interaction with gold is very weak compared with other nucleobases, such as adenine[144].

In order to assess the binding efficiency of the AuNPs to the oligonucleotide, they were incubated for 12 h and the samples centrifuged. The pellet and the

supernatant were loaded into an acrylamide gel retardation assay, an electrophoretic separation technique employed to analyze the size of biomolecules (**Scheme 3**). For each formulation, it was studied the optimal bPEI/oligonucleotide N/P, calculated as N/P ratio = 7.53 × weight ratio of PEI/DNA[101]. The N/P 80 is considered the optimal for bPEI 2KDa[145], while for bPEI 25 KDa is considered 35[146].

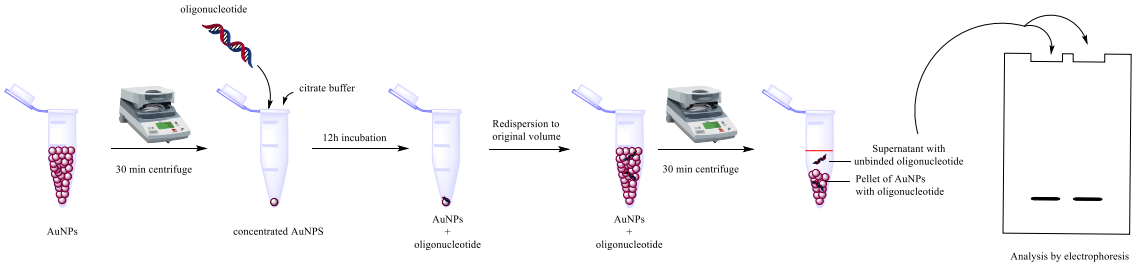

Scheme 3. AuNPs are concentrated by centrifugation and incubated with the oligonucleotide for 12 hours. The samples are dispersed and centrifuged to obtain both pellet and supernatant. Both are analyzed through an electrophoresis gel to determine the amount of bonded and unbonded oligonucleotide, respectively.

The results of the conjugation experiment can be observed in **Figure 40**. In this figure, the values obtained from the pellet are due to the bound material, whereas the data obtained from the washed fractions are due to the unbound one. In this case, only 11-27% of the total amount incubated was bound to the nanoparticle. Interestingly, the lowest conjugation values were obtained by the particles with LP-bPEI 25 KDa, which displayed the highest positive potential.

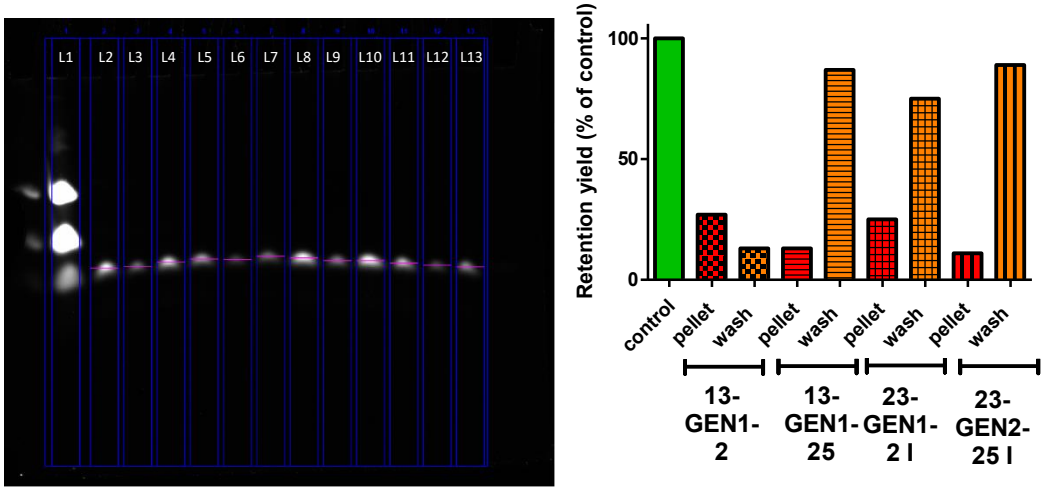

AuNPs	Pellet % (oligonucleotide bonded)	Wash % (oligonucleotide not-bonded)
13-GEN1-2	27	73
13-GEN1-25	13	87
23-GEN1-2	25	75
23-GEN1-25 I	11	89

Figure 40. 13-GEN1-2, 13-GEN1-25, 23-GEN1-2 I and 23-GEN1-25 I AuNPs conjugated with FAM-PolyT(10): gel retardation assay and quantification. Fixed N/P ratio of 80 and 35 for bPEI layer of 2 and 25 KDa respectively. L (line) 1: ladder, L2-4: 13-GEN2-2control, pellet, wash (c,p,w), L5-7: 13-GEN1-25c,p,w, L8-10: 23-GEN1-2 I c,p,w, L11-13: 23-GEN1-25 I c,p,w.

In order to increase these low conjugation yields, a buffer was introduced to lower the pH during the incubation process. This approach is based on the low pH assisted method, commonly employed to reduce the repulsion between oligonucleotides nucleobases and AuNPs[147,148].Additionally, it was thought that it would help in the protonation of the amino groups of the polymer, increasing the interaction with the oligonucleotide. The buffer was added after 1h of incubation of the particles with the oligonucleotide at a concentration of 1 mM. After that step, the procedure was the same as before. In this case, the binding increased in almost all the cases, where the formulations containing bPEI 25 KDa produced the highest increase (**Figure 41**). These results implies that the pH of the incubation media has a strong effect on the conjugation. However, the yield was still low, suggesting the need for complementary approaches to enhance the binding.

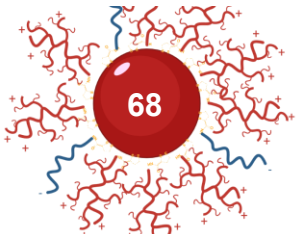

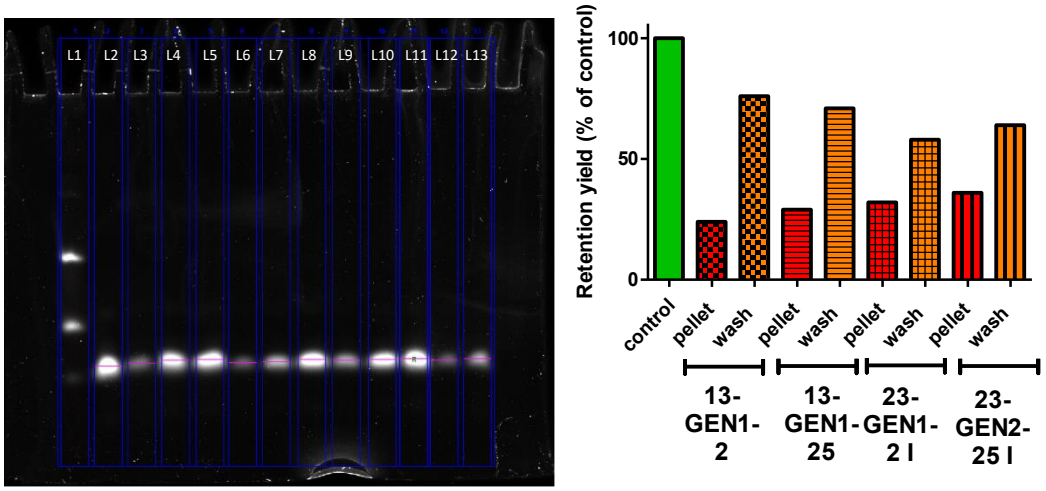

AuNPs	Pellet % (oligonucleotide bonded)	Wash % (oligonucleotide not-bonded)
13-GEN1-2	24	76
13-GEN1-25	29	71
23-GEN1-2	32	58
23-GEN1-25 I	36	64

Figure 41. 13-GEN1-2, 13-GEN1-25, 23-GEN1-2 I and 23-GEN1-25 I AuNPs conjugated with FAM-PolyT(10): gel retardation assay and quantification. Fixed N/P ratio of 80 and 35 for bPEI layer of 2 and 25 KDa, respectively. Fixed pH of 3.5. L (line) 1: ladder, L2-4: 13-GEN2-2control, pellet, wash (c,p,w), L5-7: 13-GEN1-25c,p,w, L8-10: 23-GEN1-2 I c,p,w, L11-13: 23-GEN1-25 I c,p,w.

3.3. Conclusions

The first part of the thesis, was focused on the obtention of positive and stable AuNPs for the delivery of biomolecules. Thus, AuNPs of different sizes, 13, 23 and 35 nm were modified with three polymers prepared in the laboratory, LP-PEG, LP-bPEI 2 KDa and LP-bPEI 25 KDa. Through the study of different combinations, several AuNPs formulations (GEN1) were obtained. The most promising systems are AuNPs of 13 nm with a LP-PEG/LP-bPEI (2 & 25 KDa) in a ratio 3:7 (13-GEN1-2 and 13-GEN1-25, respectively) and the analogous ones of 23 nm and with the same ratio (23-GEN1-2 I and 23-GEN1-25 I). These four AuNPs showed the best stability and reproducibility among the different AuNPs tested. Hence, they were evaluated as carriers.

Thus, their cytotoxicity and binding capacity were evaluated. The different AuNPs did not produce significant toxicity in comparison with the polymer alone in the tumoral cell lines tested. However, the binding assays performed at different conditions did not provide the desired results. The binding was improved by the use of an acid buffer, but, despite the better results, additional improvements are desired.

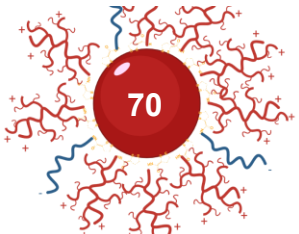

Chapter 4.

Synthesis of ligands and functionalization of AuNPs.

Part 2.

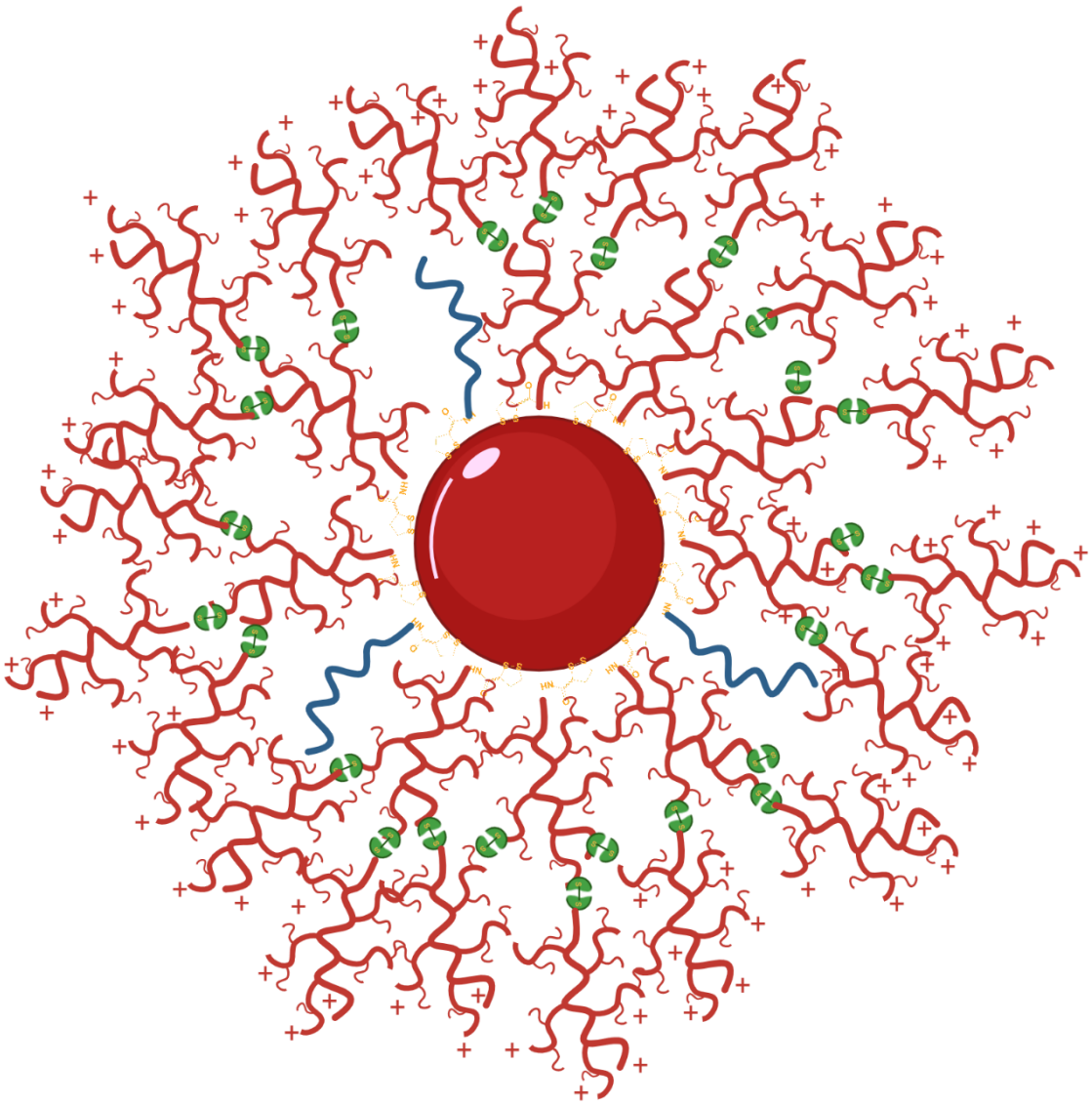

Chapter 4. Synthesis of ligands and functionalization of AuNPs. Part 2.

4.1. Introduction

The functionalized AuNPs obtained in the previous chapter did not bind oligonucleotides efficiently. This could be due to the positive potential reached with those formulations, which could be lower than needed. Another possibility, or in combination with the previous one, is that even though the nanoparticles present an overall positive potential, the bPEI could not interact efficiently with the oligonucleotide due to steric effects.

To overcome these limitations, new designs were developed. The AuNPs functionalized until now are considered mixed layer particles, since two polymers are combined in a single layer. In this regard, to increase the number of positive charges and make bPEI more accessible to interact with biomolecules, the addition of a second layer of bPEI was explored. For this purpose, the use of succinimidyl 3-(2-pyridyldithio)propionate (SPDP) was evaluated as a cross-linker.

4.1.1. SPDP Cross-linker

Succinimidyl 3-(2-pyridyldithio)propionate or SPDP is the activated ester form of the (2-pyridyldithio)propionic acid (**Figure 42**). Its chemical structure is based on a pyridildithiol group, a reactive moiety for sulfhydryl groups, and an activated ester that could react with amine groups. These reactive moieties make SPDP a widely used heterobifunctional cross-linker.

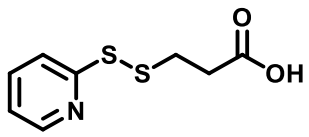

(2-pyridyldithio)propanoic acid

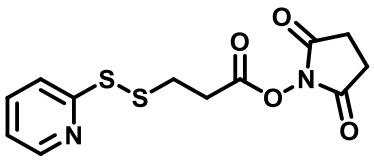

Succinimidyl 3-(2-pyridyldithio)propionate (SPDP)

Figure 42. Chemical structure of (2-pyridyldithio)propionic acid and its activated ester form with NHS, the Succinimidyl 3-(2-pyridyldithio)propionate (SPDP).

The SPDP cross-linker, and derivatives, are mainly used in biological applications that involve proteins, usually in protein-protein conjugation[149-150], protein-protein interaction analysis[151-152], protein labeling[153] or protein-antibody immobilization[154].

SPDP is considered a smart linker[155], a tool designed to join two molecules together and that can be cleaved under a certain stimulus. Specifically, SPDP is a redox-sensitive linker, which reacts with glutathione (GSH) (**Figure 43**), an abundant tripeptide in the cytoplasm and major reducing ligand[156]. Its structure presents a cysteine, where the sulfhydryl group is a strong nucleophile and powerful reducing agent. *In vivo*, GSH concentration varies depending on the tissue, but it is present at a higher amount in tumors, such as breast, ovarian, head and neck and lung. In addition, the concentration inside the cells is much higher than outside (around mM and μM, respectively)[157]. Due to this, formulations that present SPDP, or another disulfide linker, can be exploited to specifically release their therapeutic cargo in the tumoral tissue instead of blood plasma or normal cells (**Figure 44**).

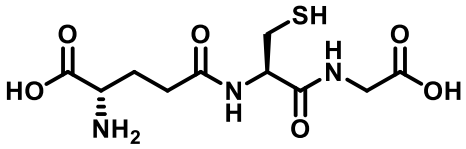

Figure 43. Chemical structure of GSH, a tri-peptide of glutamate, cysteine and glycine.

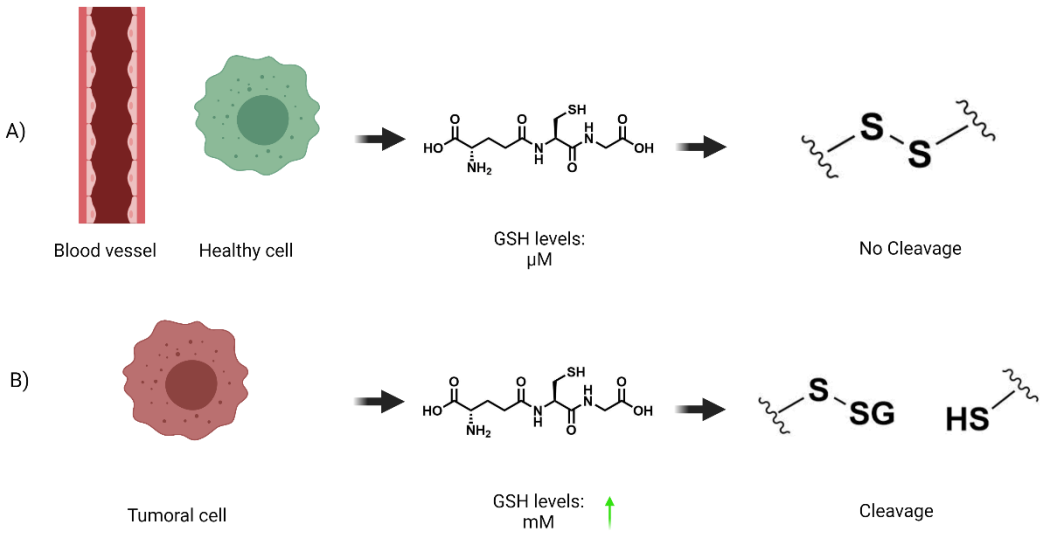

Figure 44. GSH concentration levels comparison between a) heathy cells/blood and b) tumoral cells and its effect on disulfide crosslinked structures.

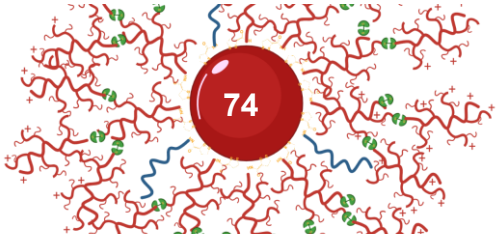

After the addition of SPDP to bPEI, it can be conjugated to the GEN1 AuNPs obtained in the previous chapter. Thus, the introduction of more bPEI to the nanostructures is expected to improve the transfection efficiency. What is more, the new formulation might be able to release the cargo of biomolecules in a tumoral environment preferably, due to the linker employed[158].

To obtain this new formulation, GEN1 AuNPs will be modified using 2-Iminothiolane (Traut's reagent), a cyclic thioimidate able to react with primary amino groups to form sulfhydryl groups (**Figure 45**). Thus, the primary amino groups of the bPEI will turn into sulfhydryl and will react with the SPDP modified bPEIs. This conjugation can be monitored by UV due to the release of the pyridine-2-thione during the process (UV-Vis: 343 nm; ε=8080 $mol^{-1}dm^3cm^{-1}$)[159].

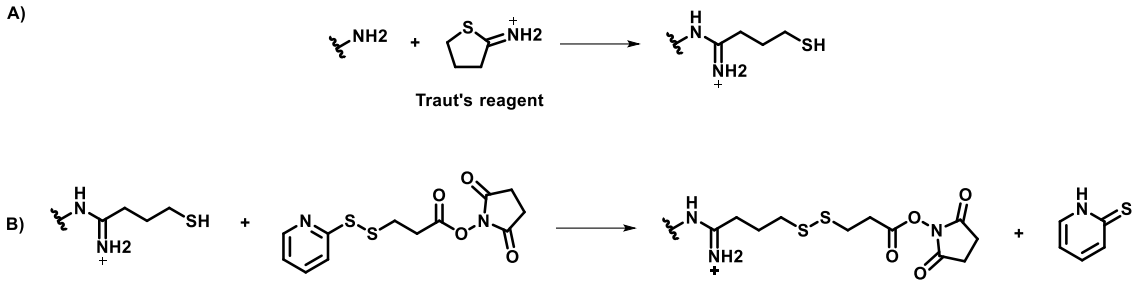

Figure 45. Traut's reagent reaction with primary amines to generate thiol groups (A) able to interact with the SPDP molecule (B) releasing a molecule of pyridine-2-thione in the process.

For this project, bPEIs of 2 & 25 KDa will be modified with the SPDP cross-linker and conjugated with GEN1 AuNPs. Multiple parameters of the new formulations, called GEN2, will be evaluated, including reproducibility, toxicity, redox sensitivity and transfection.

4.2. Results and Discussion

In this stage of the project, it was explored the addition of a second layer of bPEI (2 and 25 KDa) on the GEN1 AuNPs previously obtained in **Chapter 2**, and the effect on the transfection efficacy evaluated. Therefore, bPEIs were modified with SPDP and incubated with GEN1 AuNPs, previously treated with Traut's reagent to introduce the required sulfhydryl groups.

4.2.1. Synthesis

SPDP is a non-water soluble molecule, but thanks to the good solubility of the 2 and 25 KDa polymers in organic solvents, the modification can be performed without using a water-soluble SPDP derivative, such as the sulfo-SPDP. The SPDP was synthetized in a two-steps process (**Scheme 4**). First, the mercaptopropionic acid is reacted with the 2-aldrithiol in MeOH and AcOH (300:1), giving rise to the desired compound (2-pyridyldithio)propanoic acid (**5**) bearing the disulfide bond (**Scheme 4A**). Any traces of the acid or the pyridine-2-thione previously released as a byproduct have to be well removed to not affect the subsequent reaction. This one (**Scheme 4B**) consists in the activation of the acid (**5**) with NHS and DCC in THF to obtain the SPDP (**6**).

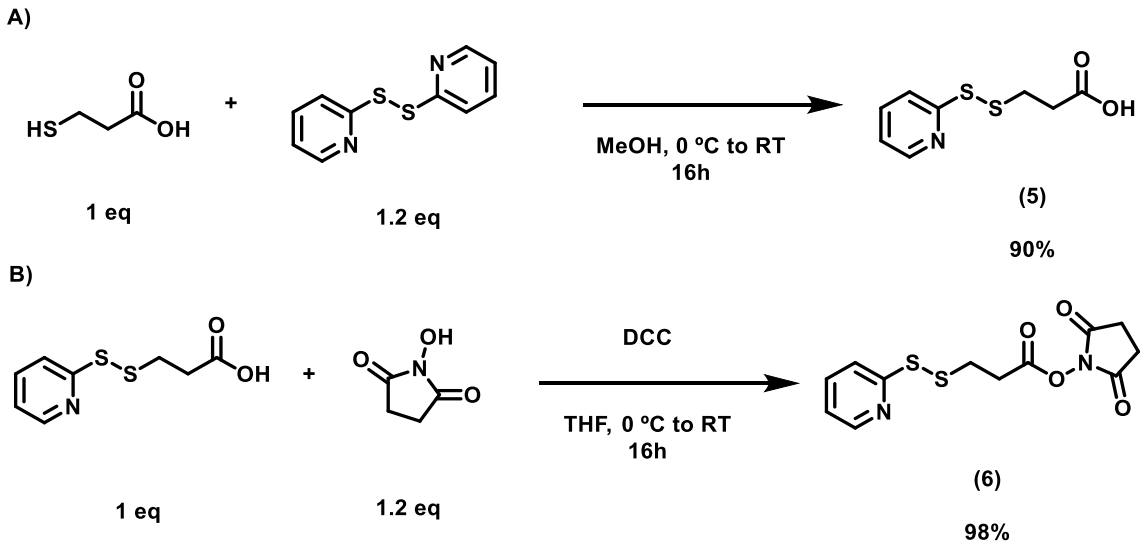

Scheme 4. Synthesis of the SPDP (6). From the mercaptopropionic acid reaction with 2-aldrithiol (A), to generate the disulfide pattern, and their later activation with NHS (B).

The modification of the bPEIs (**Scheme 5**) with the cross-linker was performed in THF, as it was made with the LP-NHS linker, due to its extended use in amidation reactions[134]. Compared with the lipoic ester, it was observed that SPDP reacts better with the polymer and produces lower aggregation during the reaction. Still, the vigorous stirring of the reaction is highly recommended to avoid aggregation of the polymer. After the modification of the polymers, the solvent was removed and re-dissolved in water to perform their purification by dialysis. It was used membranes of 3.5 and 10 KDa for the modified polymers PDP-bPEI 2 KDa (**7**)

and PDP-bPEI 25 KDa (**8**), respectively. After the dialysis, the water was removed by lyophilization.

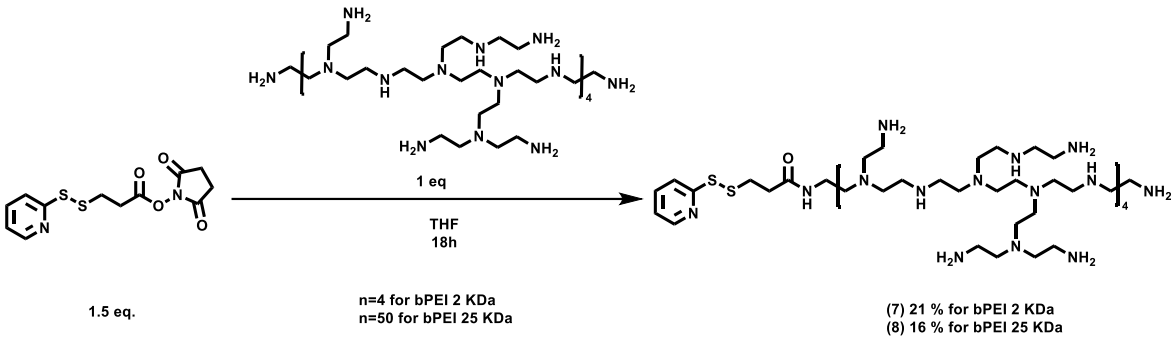

Scheme 5. Conjugation of the SPDP cross-linker with the polymers bPEI 2 and 25 KDa THF as solvent to favor the amide formation for 16h.

The characterization of the modified polymers faced the same obstacles as the observed previously. MALDI mass spectra were similar to the obtained for the lipoic modification, where the best results were obtained using CHCA as matrix and MeOH. For both polymers (**Annex Figure 29-30**), a large number of signals were observed with a difference of 43 units, which corresponds to the monomer [C2H4NH]. Using ^{1}H-NMR (**Annex Figure 7-8**) the proper integration of the signals below 4 ppm could not be done due to the overlap of the polymer and crosslinker signals. However, the presence of peaks in the aromatic area suggests the incorporation of the SPDP. These signals are overlapped with an intense signal at 8 ppm, attributed to protonated primary amines[160]. The presence of the SPDP was also confirmed through ^{13}C-NMR, where signals between 165 and 120 ppm correspond to the crosslinker, although the carbonyl group cannot be appreciated very well at 172 ppm due to the limitations of the equipment for a polymer of 2 KDa (**Annex Figure 18**). In the case of the PDP-bPEI 25 KDa (**Annex Figure 19**), the ^{13}C spectrum was performed at 121 MHz, providing clearer signals, considering its length, also confirming the addition of the cross-linker.

4.2.2. Functionalization

4.2.2.1. 13-GEN2-2-2 (bPEI (2 KDa)-bPEI (2 KDa))

Once the bPEIs were modified with the SPDP crosslinker, they were employed in the functionalization of the AuNPs to obtain a second layer. For this process, the 13-GEN2-2 were selected due to their excellent stability. To perform the functionalization, the AuNPs were previously functionalized with Traut's Reagent, 2-iminothiolane, to generate sulfhydryl groups (**Scheme 6**). To ensure that a large number of thiols were introduced, an excess of 2-iminotholane was employed, particularly 17-fold. Once activated the GEN1 AuNPs with the 2-iminothiolane, the AuNPs were incubated with the PDP-bPEI (2 KDa) (17-fold excess). Then, the AuNPs were centrifuged and the pellet obtained and the corresponding supernatant were evaluated. The supernatant was characterized by UV spectroscopy at 343 nm to quantify the pyridine-2-thione, and therefore, the yield of the reaction (**Figure 46**). Following the Beer-Lambert law (ε=8080 $mol^{-1}dm^3cm^{-1}$), it was calculated an average amount of 2-pyridinthione equal to 41.65 nmol, which corresponded with 35% of the amount of PDP-bPEI added. This low yield could be a consequence of the conformation of the polymer on the AuNPs, that due to the steric effect, does not allow a full interaction of the free primary amines with the rest of the reagents. After this result, the molar ratio for bPEI/2-iminothiolane and bPEI/PDP-bPEI was reduced to 1:6.

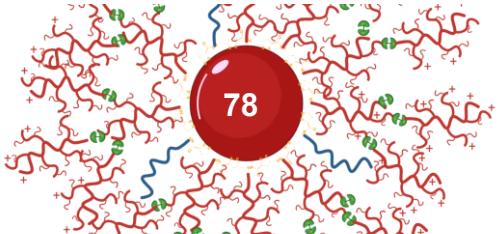

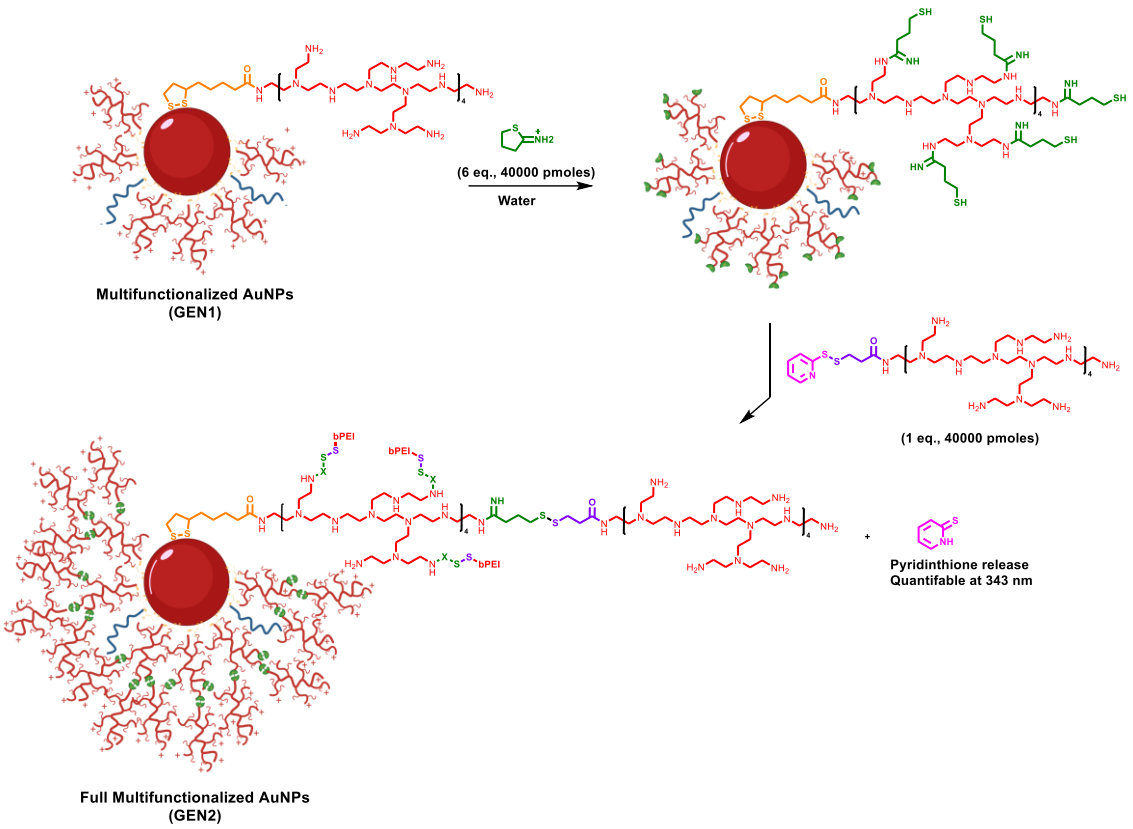

Scheme 6. Schematic representation of the whole functionalization process to obtain the GEN2 of AuNPs from the GEN1. GEN1 AuNPs are treated with 2-iminothiolane to generate sulfhydryl groups from the primary amine of the functionalized LP-bPEI that reacts with PDP-bPEI, obtaining the conjugation between the two polymers through a disulfide bond. During the process, pyridine-2-thione is released, which can be used to determine the efficiency of the process.

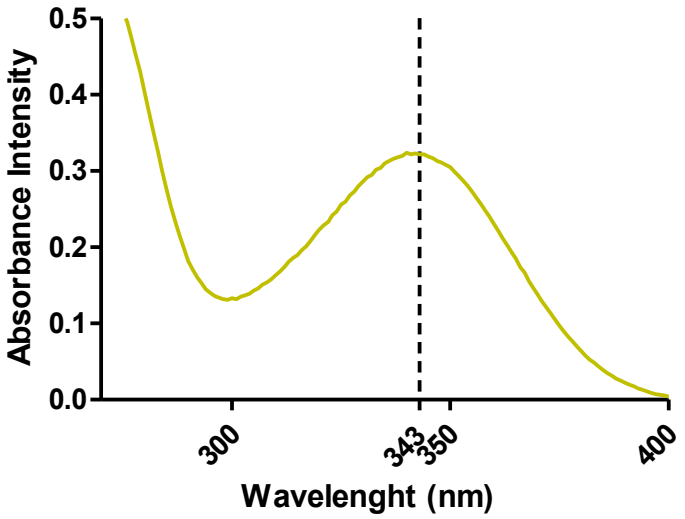

Figure 46. Pyridin-2-thione quantification. The molecule is released during the functionalization of 13-GEN1-2 AuNPs with PDP-bPEI 2 KDa. Through the Beer-Lambert law it was quantified an amount of the molecule equal to 41.65 nmol.

The AuNPs obtained, called 13-GEN2-2-2, were characterized by DLS. The changes can be appreciated mainly in the zeta-potential, which shows an average potential of 35±7.99 mV (**Figure 47A**), which means an increment of Δ22.1 mv respect the 13-GEN1-2 AuNPs. Regarding the hydrodynamic size, it can be observed a diameter of 35.02±12.94 nm (**Figure 47B**), and size distribution centered at 32.67 nm, which represents an increment in the overall size of 4.22 nm. Those results suggest that the new layer of bPEI has been successfully introduced and taking into account the previous data of the 13-GEN1-2, it is presumable that the new layer is more externally exposed. Also, GEN2 AuNPs have displayed a similar stability to the GEN1, being stable for 3 weeks at room temperature or after 2 months at 4 °C.

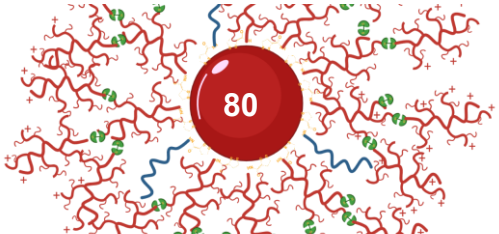

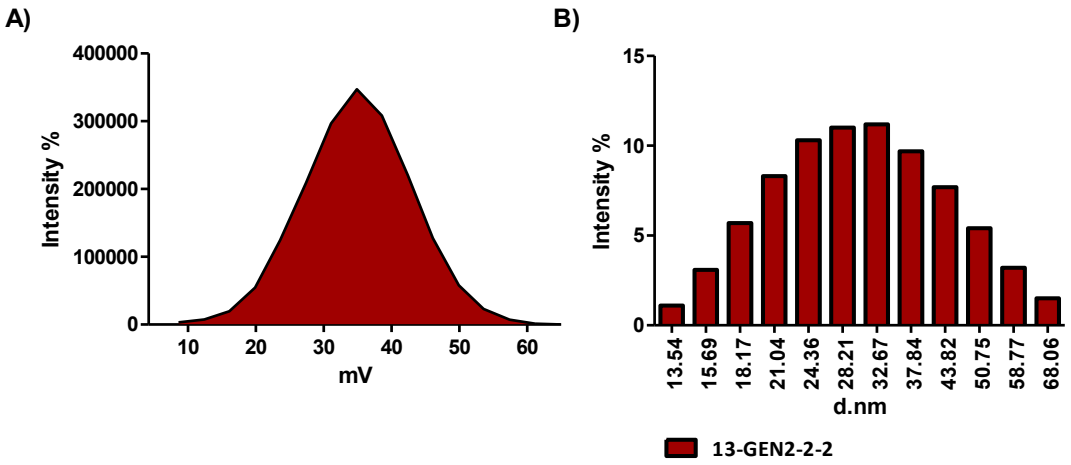

Figure 47. DLS zeta-potential characterization of 13-GEN2-2 AuNPs. It can be observed the zeta potential distribution measured, 35±7.99 mV (A) and the hydrodynamic size, 35.02±12.94 d.nm (B).

4.2.2.2. 13-GEN3-2-2-2 13 nm bPEI (2 KDa)-bPEI (2 KDa)-bPEI (2 KDa)

One of the advantages of this functionalization technique is that it allows the addition of layers of bPEI in a controlled way. To determine the limits of the technique, it was studied the same functionalization on the 13-GEN2-2-2 AuNPs, using again the PDP-bPEI 2 KDa to obtain a GEN3 AuNPs. The protocol followed was the same as for the obtention of the GEN2, using a molar ratio of bPEI 2 KDa/2-iminothiolane/PDP-bPEI 2 KDa equal to 1:17 for the activation and functionalization. In this case (**Figure 48**), the yield of functionalization based on the pyridine-2-thione release was 12%.

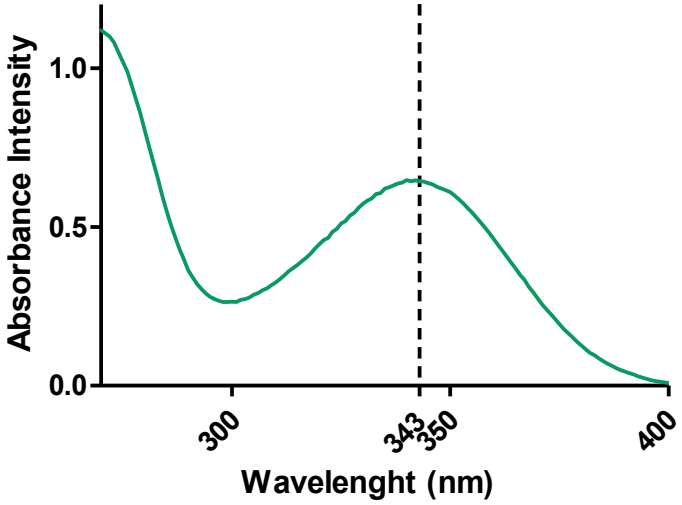

Figure 48. Pyridin-2-thione quantification. The molecules are released during the functionalization of 13-GEN2-2-2 AuNPs with PDP-bPEI 2 KDa. Through the Beer-Lambert law, it was quantified an amount of the molecule equal to 85 nmol.

The Z-potential of GEN3 AuNPs was 43.4±11.7 mV (**Figure 49A**), which is slightly higher (∆7.4 mV) than the one obtained from GEN2 AuNPs (**Figure 49B**). Due to the low yield in the functionalization, a low zeta-potential increment was expected. On the other hand, the hydrodynamic size measurements (**Figure 49C**) show a broad size distribution, much wider than the 13-GEN2-2-2 and with a lower intensity, with a size distribution centered at 43.82 and 58.77 nm of diameter. This significant increment of the size and irregular size distribution suggests lower stability. This was confirmed with the development of aggregates after 1 week at 4ºC. Based on these results, this formulation was not used in further experiments.

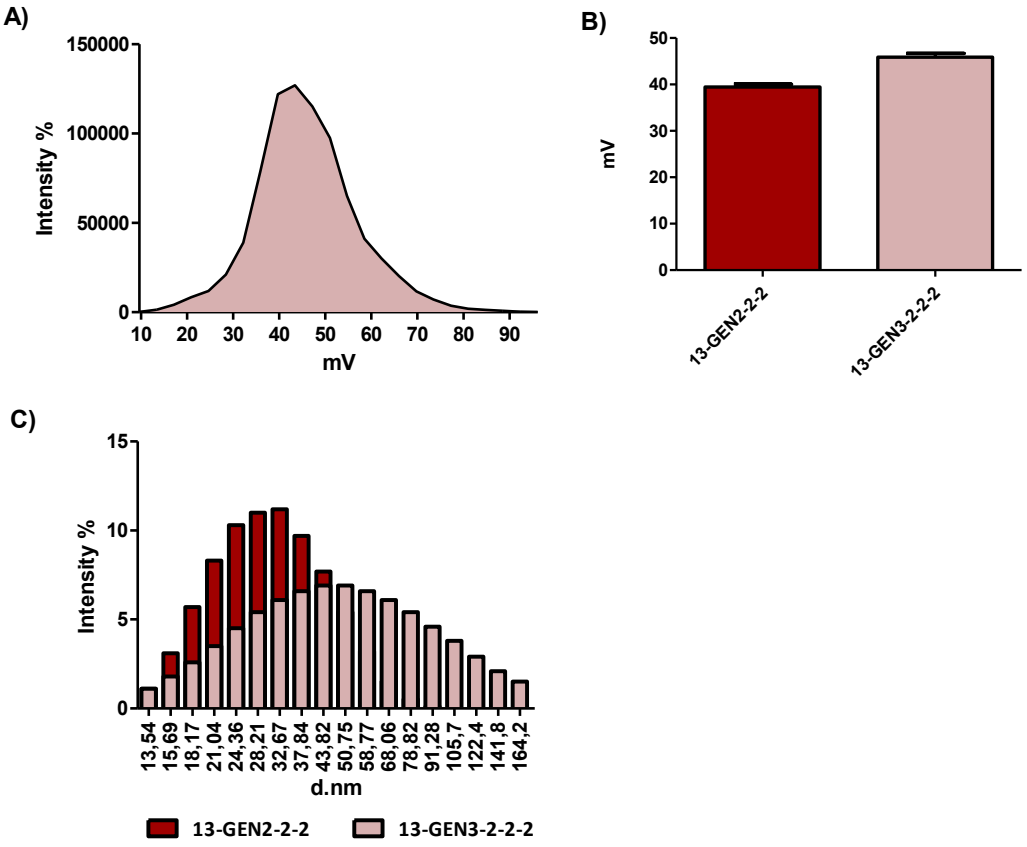

Figure 49. A) Zeta-potential of the GEN3 AuNPs (light brown) and B) its comparison with the GEN2 AuNPs (red), showing a difference of +7.4 mV between them. C) Hydrodynamic size comparison of the GEN3 and GEN2 AuNPs. It can be observed a different size distribution between them, mostly in terms of intensity and width, which indicates a lower stability by 13-GEN3-2.

4.2.2.3. 13-GEN2 –Formulations with bPEI 25 KDa

Based on the previous results, in this section, the aim was to prepare a derivative containing bPEI of 25KDa in the outer layer. Thus, the GEN1 AuNPs containing the 2KDa or 25 KDa bPEI were treated with PDP-bPEI 25 KDa

- 13-GEN2-2-25 - LP-bPEI (2 KDa) – PDP-bPEI (25 KDa)
- 13-GEN2-25-2 - LP-bPEI (25 KDa) – PDP-bPEI (2 KDa)
- 13-GEN2-25-25 - LP-bPEI (25 KDa) – PDP-bPEI (25 KDa)

The functionalization with the PDP-bPEI 25 KDa was expected to produce AuNPs with higher potential than the obtained till the moment and with a higher exposure of the bPEI in the surface of the particles. It was also studied the functionalization

of PDP-bPEI 2 KDa on the 13-GEN1-25 AuNPs to compare the properties of the final product 13-GEN2-25-2 with the inverse formulation 13-13-GEN2-2-25. If the second functionalization follows the trend observed previously in the 13-GEN2-2-2, it was expected to obtain the highest potential values with the combination of the two bPEIs (25 KDa), the 13-GEN2-25-25.

Regarding the activation with 2-iminothilane and following functionalization with the modified bPEI required in each case, the ratios used were based on those employed in 13-GEN2-2-2. Thus, for the 13-GEN1-2 was used a molar ratio of 1:6:6 (LP-bPEI/2-iminothione/PDP-bPEI), and for the 13-GEN1-25 was used a molar ratio 1:72:72. The quantification of 2-pyridinthione in each case gave similar values with respect to the amount of PDP-bPEI introduced (40 and 500 nmol for 13-GEN1-2 and 13-GEN1-25, respectively). This suggests that the functionalization of 13-GEN1-25 had a similar yield that 13-GEN1-2, and probably would follow the same trend for a GEN3.

After, the obtention of the 4 different types of 13-GEN2 AuNPs, they were characterized by DLS and their properties were compared. For the zeta potential characterization, it was observed that the potential in all of them is higher than the obtained in the 13-GEN2-2-2 (**Figure 47A**). Starting with 13-GEN2-25-2 (**Figure 50A**), it displays 44.8±10 mV. 13-GEN2-2-25 (**Figure 50B**) potential is 52.3±8.25 mV. The bigger potential of GEN2-2-25 can be justified due to the bigger size of the bPEI 25KDa and thus bigger amine exposure. Regarding the 13-GEN2-25-25 (**Figure 50C**), this formulation is the one that reached the highest potential of 62.2±9.53 mV, as expected.

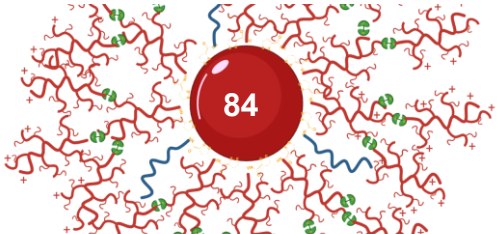

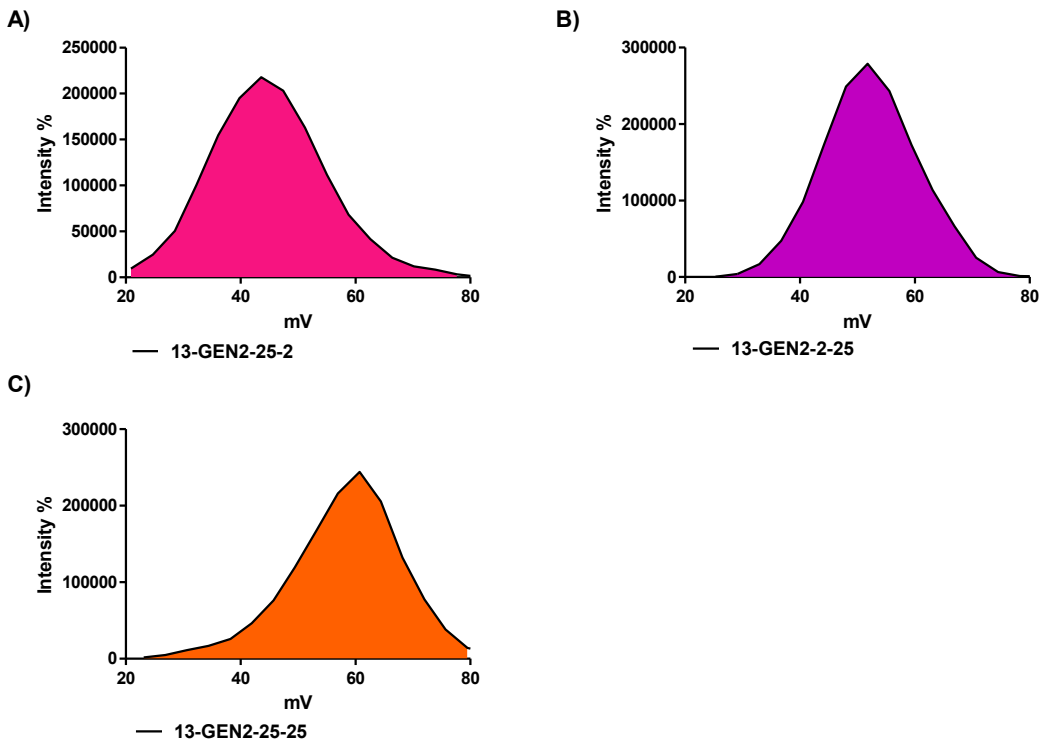

Figure 50. Zeta potential characterization of the 13 nm GEN2 AuNPs 13-GEN2-25-2 (A), 13-GEN2-2-25 (B) and 13-GEN2-25-25 (C).

On the other hand, it can also be appreciated some changes in the hydrodynamic size. For 13-GEN2-25-2 (**Figure 51A**) it was obtained a size of 38.05±11.25 nm, centered at 37.84, with a quite narrow and intense size distribution similar to the one obtained by 13-GEN2-25. This means an increment of 4.88 nm, which matches the size of the polymer introduced[143]. In the case of 13-GEN2-2-25 (**Figure 51B**), the size distribution is wider and also centered at 37.84 nm, with an overall hydrodynamic size of 43.85±21.73 d.nm. Actually, it was expected a similar size to 13-GEN2-25-2 due to the formulation of both are similar but in a reverse way. This difference could be due to the difference in size distribution between them, which can affect the correct determination of the overall size. For the 13-GEN2-25-25 AuNPs (**Figure 51C**), the hydrodynamic size is the largest obtained 54.97±30.14 nm, this time centered at 43.82. Same as in 13-GEN2-2-25, it presents a broad size distribution which can be affecting in the real size. Still, the increment of the size corresponds with the size of the polymer added[142].

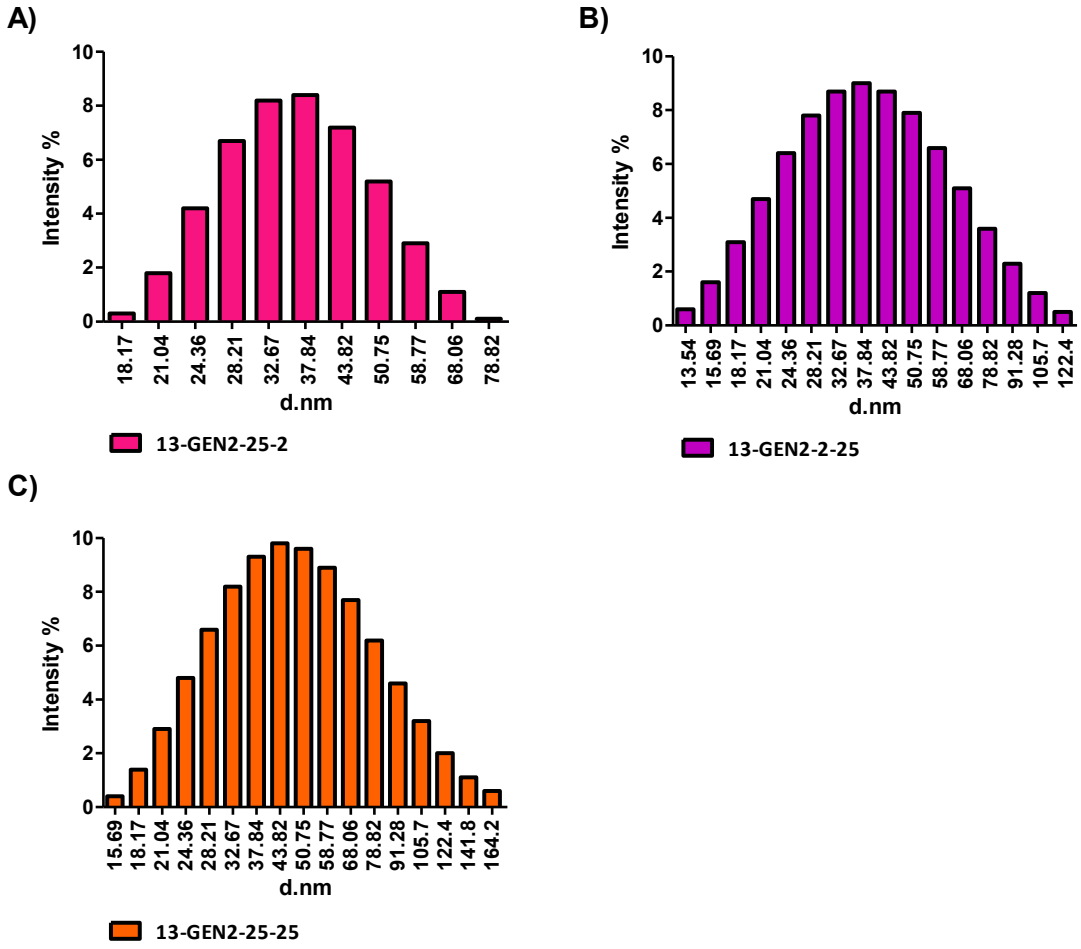

Figure 51. Comparison of the hydrodynamic size characterization of the AuNPs 13-GEN2-2-25 (A), 13-GEN2-25-2 (B), and 13-GEN2-25-25 (C).

4.2.2.4. GEN2 – 23 nm bPEI (2 & 25 KDa) second-layers formulations

Once the 13-GEN2 formulations were evaluated, the same studies were carried out with the system that contains a larger gold nanoparticle (23 nm). In this case, 23-GEN2 nanoparticles were obtained. For the functionalization of the 23 nm GEN1 AuNP, it was followed the same protocol as the one for 13 nm, but having into account the higher amount of bPEI that bear. Thus, the activation and functionalization ratios were 1:6 and 1:72, respectively, and then the DLS characterization was assessed.

Based on zeta potential measurements, the values obtained were lower than expected. Considering the trend observed in **Chapter 2**, the zeta potential was expected to be very similar to the 13-GEN2, or higher, due to the larger amount

of bPEI that was introduced. However, this was only the case of the 23-GEN2-2-25 (**Figure 52C**), where the potential obtained was 50.6±13.7 mV, similar to the obtained with the 13-GEN2-2-25. Also, 23-GEN2-25-25 reported a lower potential than expected 54.2±11.4 mV, which is 8 mV less than 13-GEN2-25-25 (**Figure 52D**). On the other hand, the formulations with bPEI 2 KDa introduced in the second layer display a much higher potential. Particularly, 23-GEN2-2-2 and 23-GEN2-25-2 display a potential of 57.8±12.8 and 58.2±13.1 mV, respectively (**Figure 52A-B**). The difference of potential of +22.7 +5.8 mV, -2 mv and -8 mV respect their analogous formulations 13-GEN2-2-2, 13-GEN2-25-2, 13-GEN2-2-25 and 13-GEN25-25, respectively, suggests that the more significant contribution to the potential is due to bPEI 25 KDa. Also, the higher loading in 23-GEN2 (around 3-fold) and the longer polymer employed (bPEI25 KDa) could limit the system's flexibility, limiting the accessibility of the amines. On the contrary, when bPEI 2 KDa is used, the amines might get better exposed.

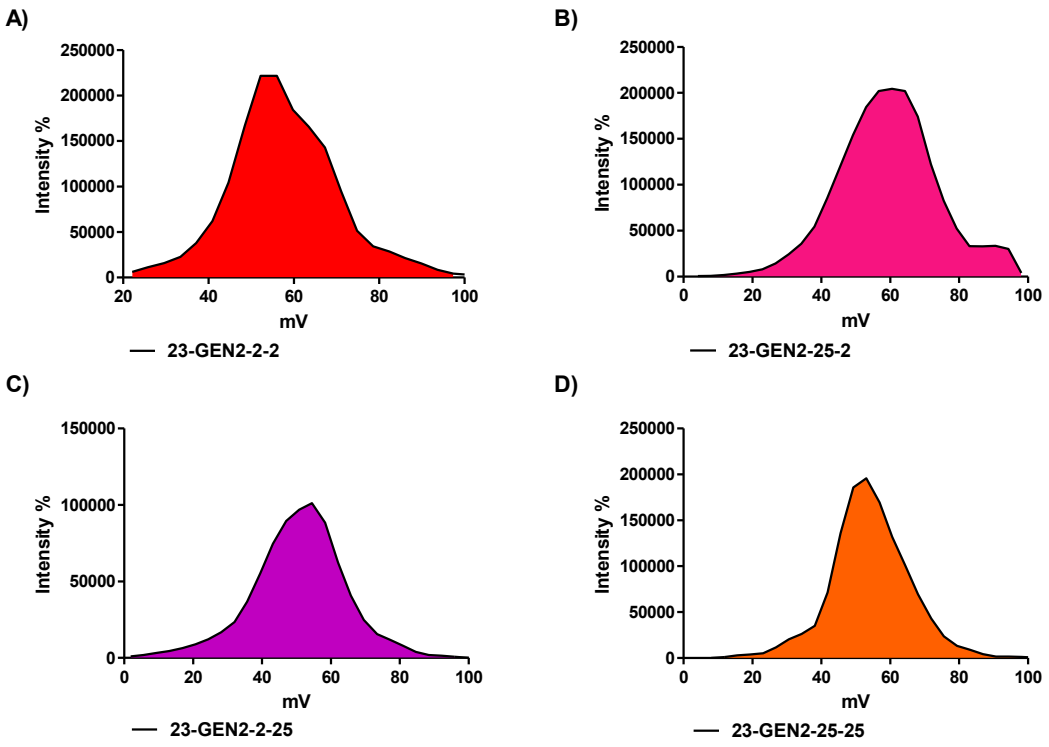

Figure 52. Zeta potential characterization of the 23 nm GEN2 AuNPs 23-GEN2-2-2 (A), 23-GEN2-25-2 (B), 23-GEN2-2-25 (C) and 23-GEN2-25-25 (D).

This theory is supported by the hydrodynamic size measurements. The biggest size increment can be observed in the 23-GEN2-2-2 (**Figure 53A**) with

76.45±37.74 d.nm, centered at 68.06 nm. This means an increment of 12.09 nm with respect to the 23-GEN1-2, a difference of almost 8 nm with respect to the increment obtained from 13-GEN1-2 to 13-GEN2-2-2. The 23-GEN2-25-2 (**Figure 53B**), 95.37±48.63 d.nm centered at 78.82, present a similar size increment of 9.34 nm with respect to the 23-GEN1-25. On the other hand, the 23-GEN2-2-25 and 23-GEN-25-25 (**Figure 53C-D**) present a hydrodynamic size of 76.94±37.77 and 87.28±41.64 d.nm, respectively, which represent an increment of 12 and 4 nm respect the previous stage particles 23-GEN1-2 and 23-GEN1-25.

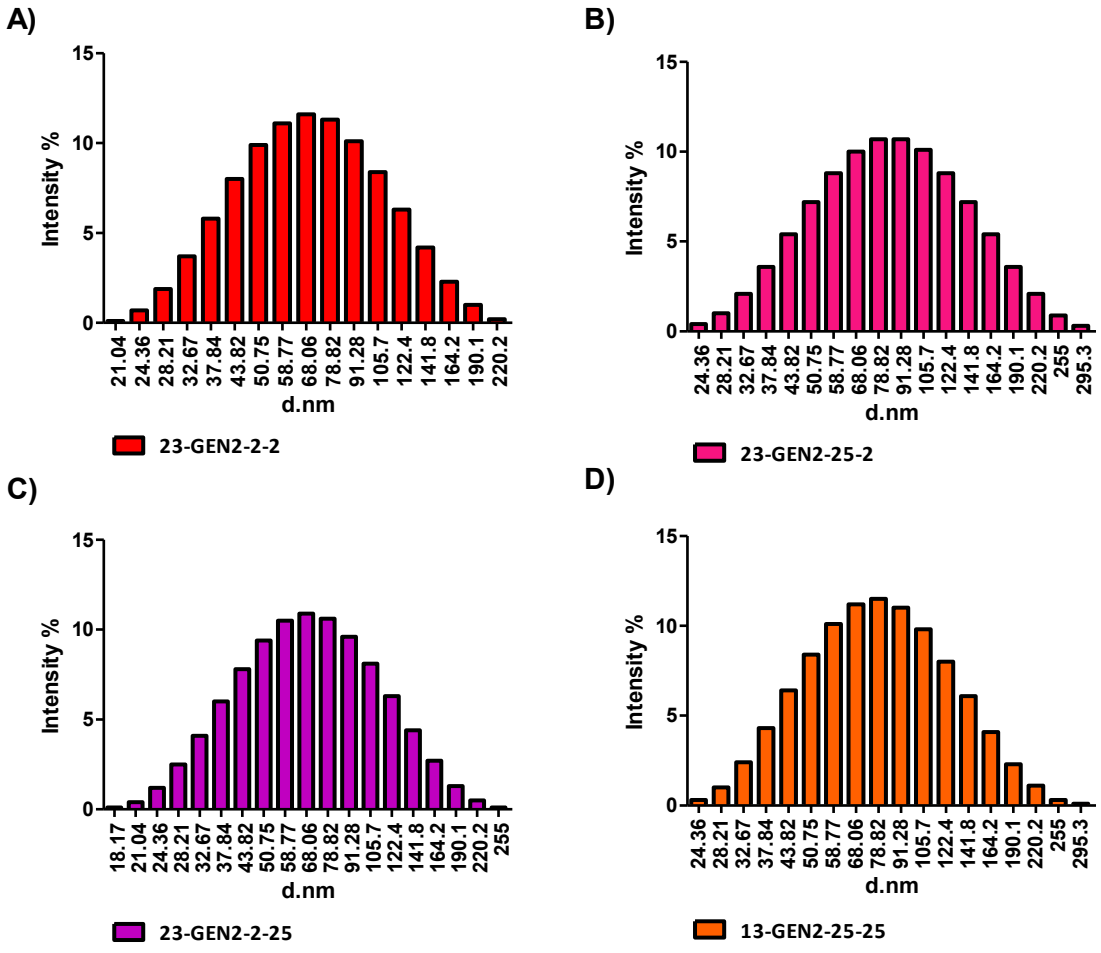

Figure 53. Comparison of the hydrodynamic size characterization of the 13 nm GEN2 AuNPs 13-GEN2-2-2 (A), AuNPs 13-GEN2-2-25 (B), AuNPs 13-GEN2-25-2 (C), and 13-GEN2-25-25 (D).

The summary of the characterization obtained for the 8 formulations can be found in (**Table 2**). Despite the differences in the potential and hydrodynamic size between the eight AuNPs evaluated 13-GEN2 and 23-GEN2, all the formulation

displays excellent stability properties keeping the same properties for 1 month at room temperature and 3-4 months at 4 ºC. After this time, aggregates appeared, particularly for 23-GEN2.

Name	Core (nm)	PDP-bPEI (KDa)	Hydrodynamic Size (nm)	Zeta-potential (mv)
13-GEN2-2-2	13	2	35.02±12.94	35±7.99
13-GEN2-25-2	13	2	38.05±11.25	44.8±10
13-GEN2-2-25	13	25	43.85±21.73	52.3±8.25
13-GEN2-25-25	13	25	54.97±30.14	62.2±9.53
23-GEN2-2-2	23	2	76.45±37.74	57.8±12.8
23-GEN2-25-2	23	2	95.37±48.63	58.2±13.1
23-GEN2-2-25	23	25	76.94±37.77	50.6±13.7
23-GEN2-25-25	23	25	87.28±41.64	54.2±11.4

Table 2. Summary of the characterization obtained for GEN2 AuNPs

4.2.3. Proof-of-Concept – Disulfide bond reduction

One of the features of this functionalization system is its reversibility. As it is have mentioned before, the conjugation between the different layers of bPEIs is obtained through the formation of a disulfide bond, which can be broken in the presence of thiolated molecules. Its reduction can lead to the disengagement of the second layer of the AuNPs, obtaining the GEN1 AuNPs again. This strategy could be advantageous in a targeted cellular environment, where the second bPEI layer carrying the biomolecules cargo would be released in the presence of GSH, which concentration is higher in tumoral cells than blood or healthy cells[157]. Therefore, to test this, 13-GEN2-2-2 were incubated with different GSH concentrations that emulated the extra (1 μM) and intracellular (1 mM) tumoral environment. The hydrodynamic size and zeta potential were evaluated at different times (10, 20, 30, 60, 120, 330, 400 and 1440 min) after the addition of the reducing agent.

In the experiment with the extracellular simulation (1 μM), it can be observed some effects due to the presence of the GSH, but without causing a reversion of

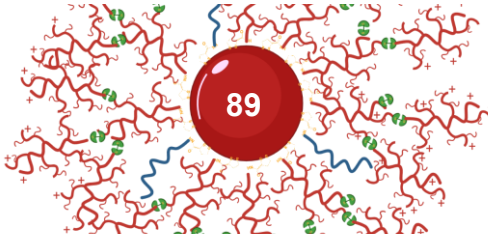

the GEN2 to GEN1. Particularly, in the hydrodynamic size characterization (**Figure 54A**), it can be observed that, only after 120 min, the AuNPs start to suffer some kind of destabilization or reorganization due to the increment of the intensity at very large sizes. This effect disappeared in the following measurements until the 1440 min (24 h), where can be observed a big change in the size distribution, but it was not observed any aggregation. However, in the zeta potential (**Figure 54B**), it can be observed a minor reduction in the overall charge, but it was kept in high values even after the 1440 min experiment. Probably, in this case, GSH was able to reduce a few disulfide bonds, explaining the low reduction of the charge of the zeta potential. After the reduction, the remaining bPEI on the second layer could have conjugated with two or more AuNPs, producing new disulfide bonds in the process.

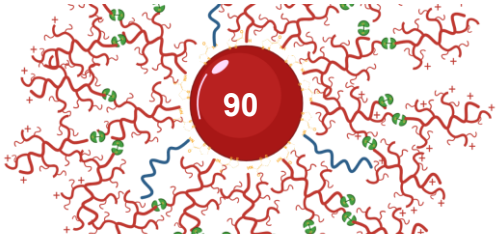

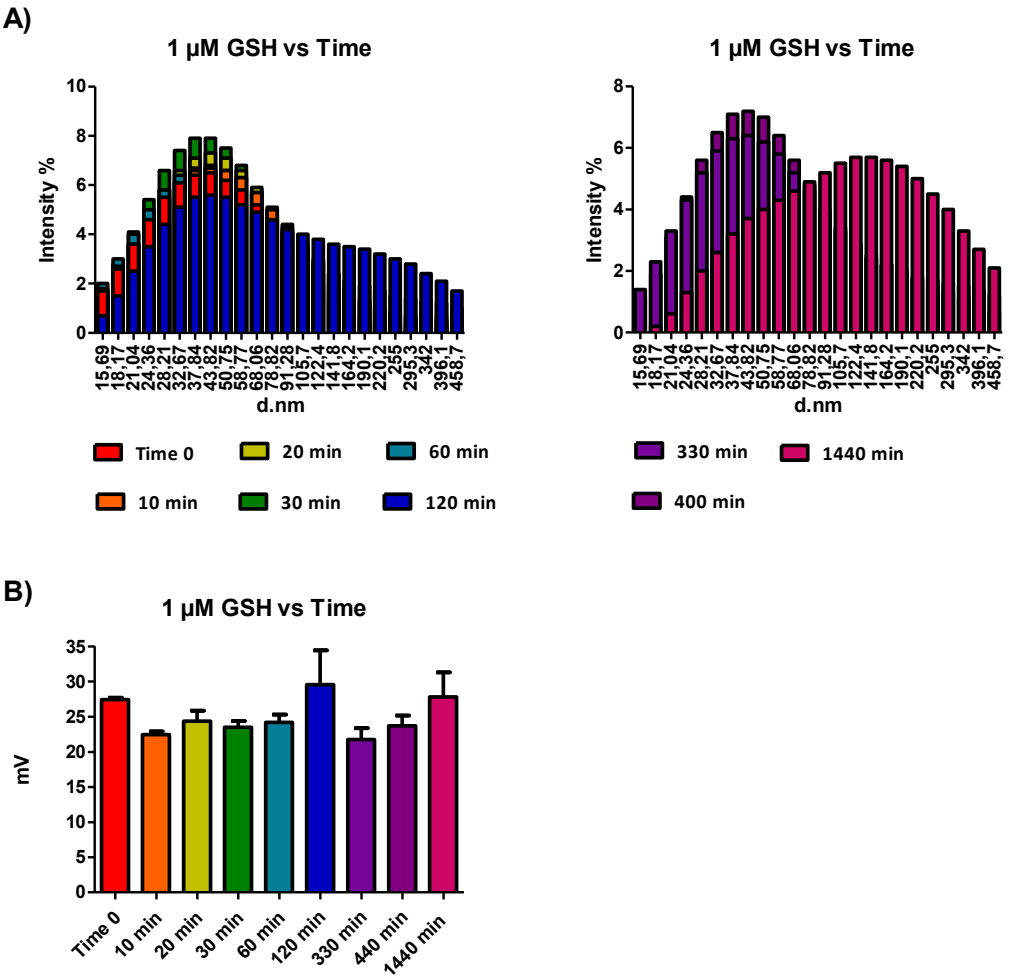

Figure 54. DLS hydrodynamic size (A) and zeta potential characterization (B) of the time dependent study of GSH at extracellular conditions (1 µM) on AuNPs. The measurements were performed after the addition of GSH at 10, 20, 30, 60, 120, 330, 440 and 1440 min, having the measurements before its addition (time 0) as control.

On the other hand, in the intracellular simulation (1 mM) can be observed more changes in the properties of the AuNPs. In the hydrodynamic size measurements (**Figure 55B**), it can be observed major changes at 60 min. In this case, the size distributions kept changing over time until some stable conformation was reached after 1440 min (24 h). In the zeta-potential (**Figure 55B**), it can be observed how the charge decrease in a staggered way. After 24 h, the potential shows a significant reduction in the overall charge, reaching around 1-2 mV. The explanation after this behavior is that the GSH reduces the disulfide bonds faster and more efficiently, removing the second layer of bPEI completely. Maybe, the effect of GSH also affects the first functionalization layer, which would explain the

strong decrease in the zeta-potential. In this regard, the remaining GEN1 AuNPs would interact with each other, forming some stable aggregate that explains their size distribution at 1440 min.

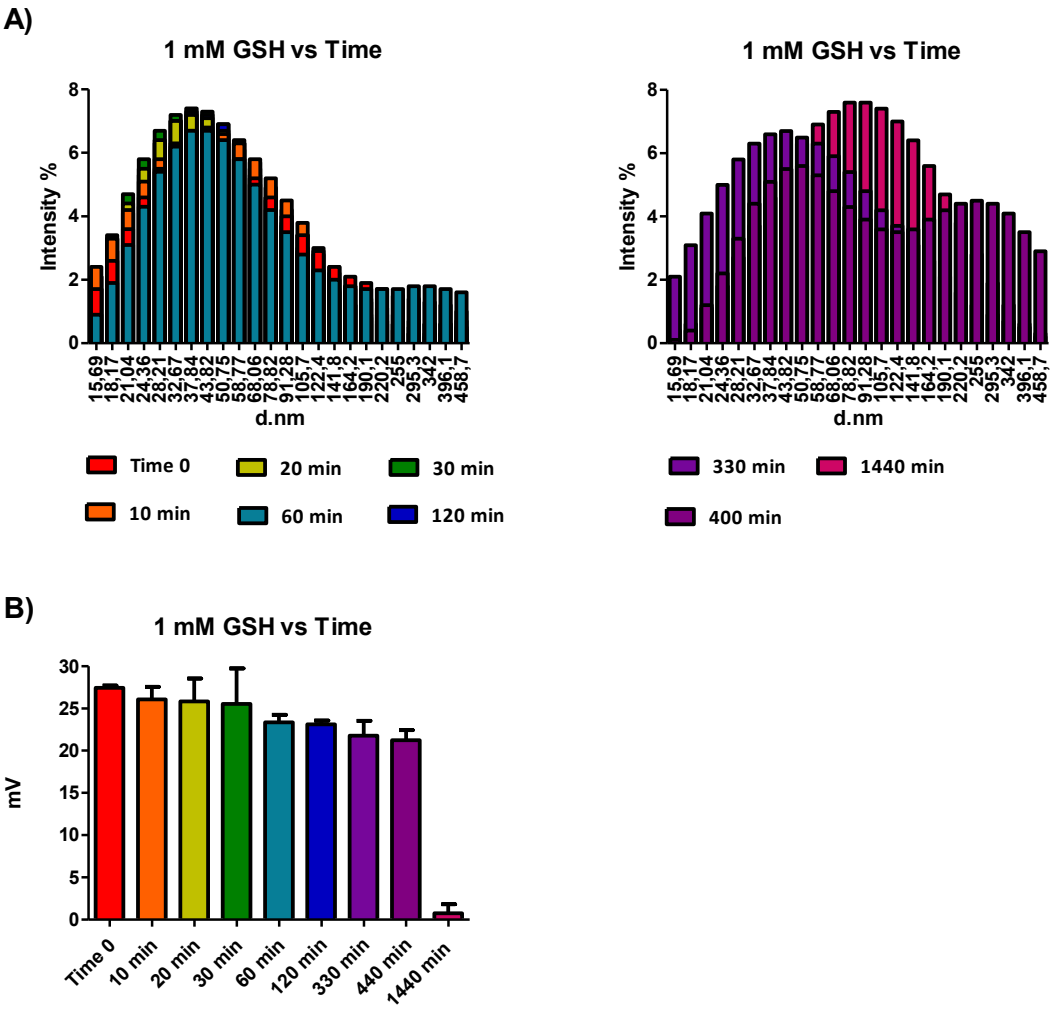

Figure 55. DLS hydrodynamic size (A) and zeta potential characterization (B) of the time dependent study of GSH at extracellular conditions (1 μM) on AuNPs. The measurements were performed after the addition of GSH at 10, 20, 30, 60, 120, 330, 440 and 1440 min, having the measurements before its addition (time 0) as control.

The AuNPs, after the exposure to GSH, show different levels of stabilization at RT. The ones treated with GSH 1mM did not last more than a day. On the other hand, the nanoparticles treated with GSH 1 μM showed higher stability, starting to aggregate after 3-4 days.

With these experiments, it was demonstrated that the GSH has a strong effect on the reversibility of the GEN2 AuNPs. These results suggest that the extracellular

environment will not be able to promote the degradation of the AuNPs. On the other hand, at the intracellular environment, the AuNPs would start to release the bPEI layer along with the cargo.

4.2.4. Proof-of-Concept – Oligonucleotide delivery

Once GEN2 AuNPs were evaluated, they were assessed as carriers of nucleic acids. As in the previous experiments with the GEN1, the studies have focused on assessing their cytotoxicity and capacity as transfer agents.

4.2.4.1 Cytotoxicity assays.

The cell viability assays were performed testing both the AuNPs and the PDP-bPEI 2 and 25 KDa. The concentrations of functionalized AuNPs tested were 1000, 500 and 250 nM. For the cytotoxicity test of PDP-bPEI alone, it was added the amount of the polymer on the particles at these concentrations (5950, 2975 and 1487.5 pmol, respectively, for 13 nm AuNPs). The cell lines used were Pancreatic adenocarcinoma PANC-1 and breast cancer MCF7 using untreated one as a control.

The toxicity assays performed with the AuNPs formulations functionalized with PDP-bPEI 2 KDa can be observed in **Figure 56**. Interestingly, no toxicity was found for the polymer alone, while the LP-PEI showed intense toxicity in the PANC-1 cell line. Additionally, only significant toxicity was found in two cases. One in the MCF-7 line, using 23-GEN2-2-2 (**Figure 56A**) and in PANC-1 using 23-GEN2-25-2 (**Figure 56D**), both at 1 μM. In both cases, the results were attributed to the higher amount of functionalized polymer, but in the case of 23-GEN2-25-2, the higher exposure of the charges, as described by z-potential, could justify the results.

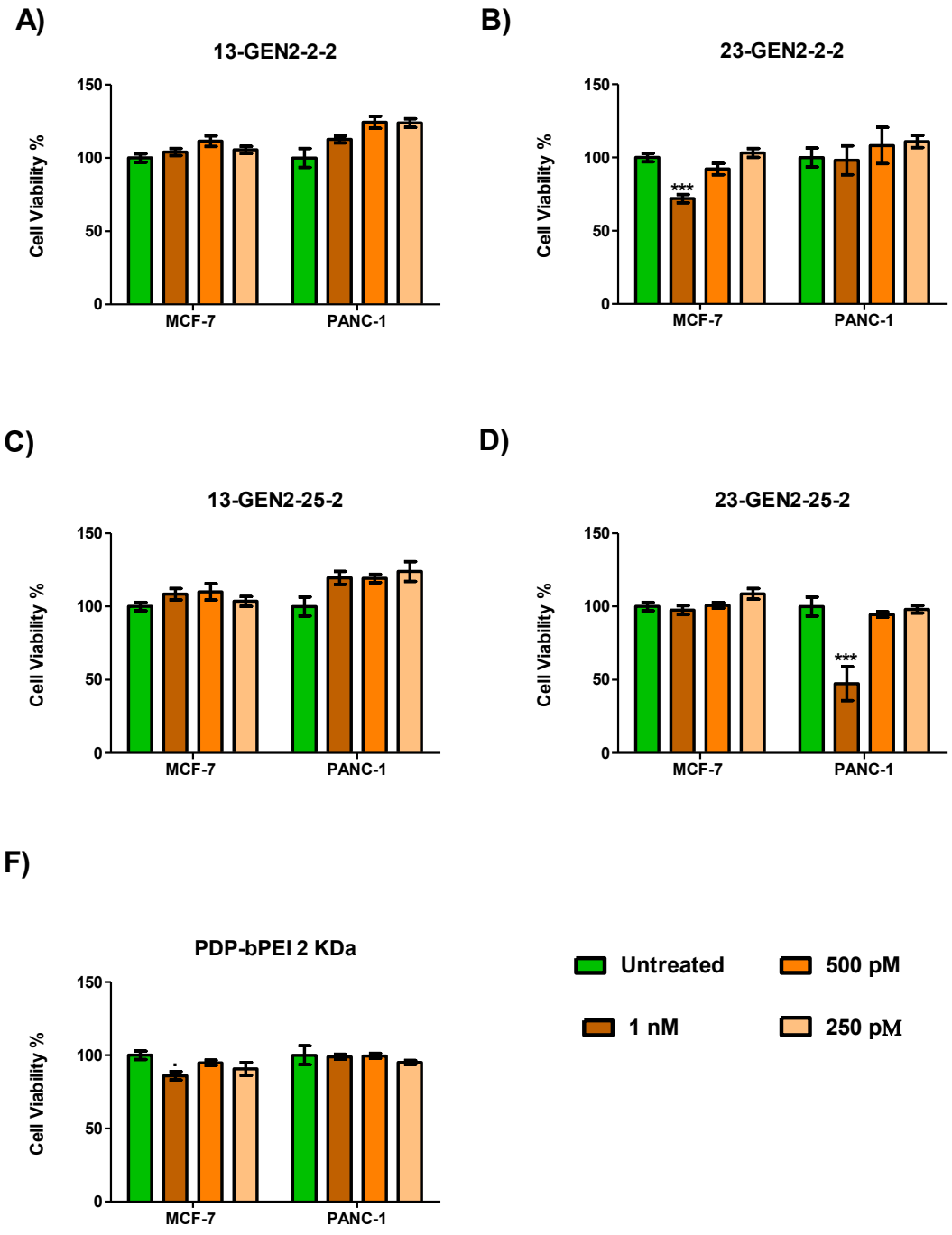

Figure 56. Cytotoxicity assay on MCF-7and PANC-1 cell lines of the 13-GEN2-2-2 (A), 23-GEN2-2-2 (B), 13-GEN2-25-2 (C), 23-GEN2-25-2 (D) and the modified polymer PDP-bPEI 2 KDa (F). The concentration of AuNPs added to the cells are 1 nM, 500 pM and 250 pM with untreated cells as control. The modified polymer concentrations tested corresponds to the one found in the AuNPs at the concentrations of 1 nM, 500 pM and 250 pM. The statistical analysis was performed using one-way ANOVA (each group vs. control) (*** $p < 0.001$, ** $p < 0.01$, * $p < 0.05$, · < 0.01).

Regarding the PDP-bPEI 25 KDa formulations, the toxicity assays can be observed in **Figure 57**. In this case, the toxicity of the polymer is clearly significant at the highest concentrations, being the cell viability of almost 10% in both cell lines at 5950 pmol. In the case of 13-GEN2 nanoparticles, slight toxicity can be observed, which is better than the results obtained with 23-GEN2 nanoparticles. In the case of 23-GEN-2-25 (**Figure 57B**), the toxicity can be only observed in the PANC-1 cell line, being pretty similar to the one obtained with the polymer alone. The same behavior was observed for 23-GEN2-25-25 (**Figure 57D**), but additionally, it presented intense toxicity in the MCF-7 lines at every concentration tested. In this case, the presence of two units of bPEI 25 KDa increases the toxicity of the nanoparticle.

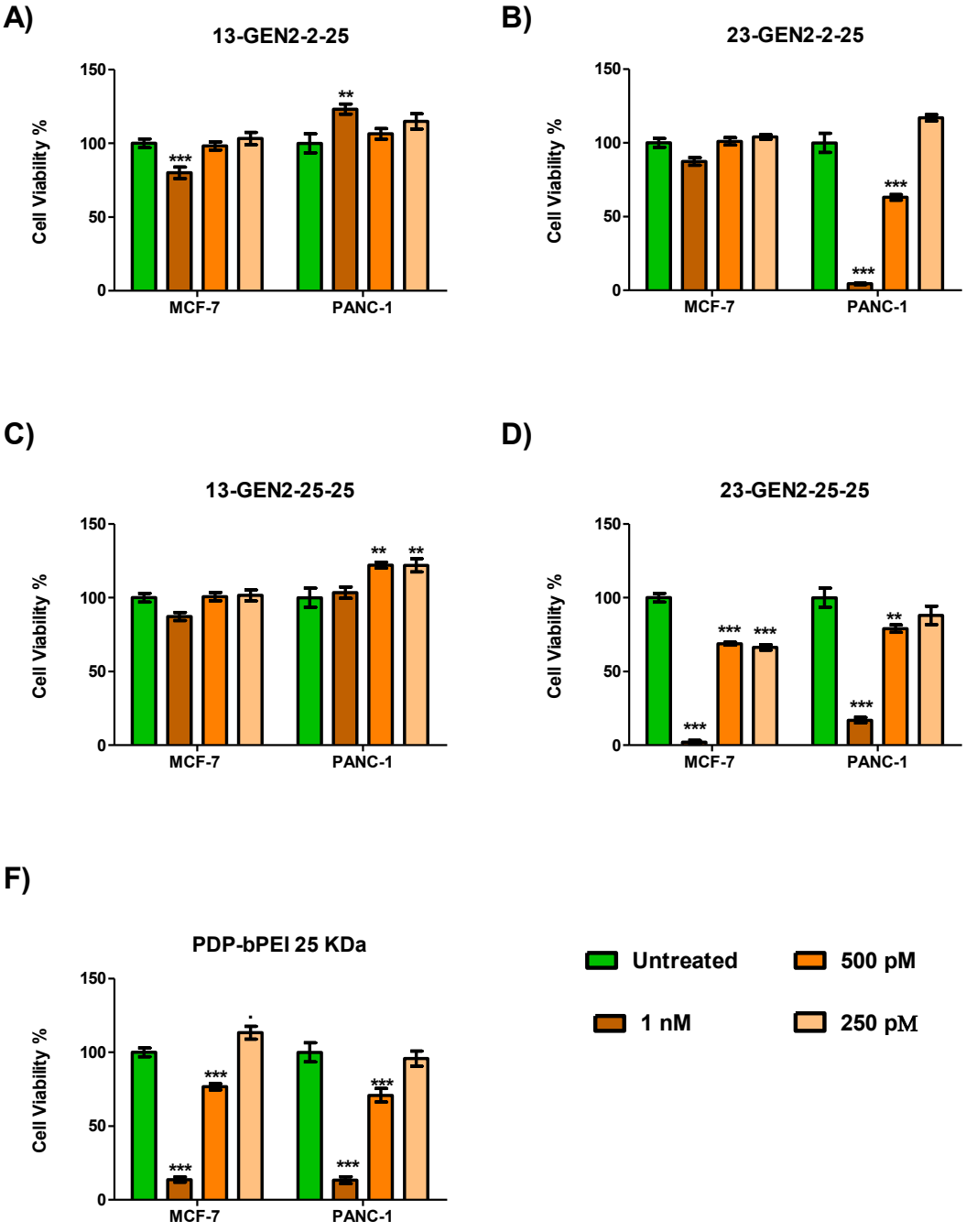

Figure 57. Cytotoxicity assay on MCF-7and PANC-1 cell lines of the 13-GEN2-2-25 (A), 23-GEN2-2-25 (B), 13-GEN2-25-25 (C), 23-GEN2-25-25 (D) and the modified polymer PDP-bPEI 25 KDa (F). The concentration of AuNPs added to the cells are 1 nM, 500 pM and 250 pM with untreated cells as control. The modified polymer concentrations tested corresponds to the one found in the AuNPs at the concentrations of 1 nM, 500 pM and 250 pM. The statistical analysis was performed using one-way ANOVA (each group vs. control) (*** $p < 0.001$, ** $p < 0.01$, * $p < 0.05$, · < 0.01).

After these results, it can be confirmed that at the concentration tested, the 13 nm formulations display a safer profile than the 23 nm ones, mainly due to the difference in polymer amount. Within the 13 nm formulations, 13-GEN2-2-2 (**Figure 56A**) particles were the less toxic, followed by the 13-GEN-25-25 (**Figure 56D**), which might be a little counterintuitive considering the bigger size and potential of these nanoparticles. Based on these results, 13-GEN2-2-2 were used in further experiments

4.2.4.2. Conjugation efficacy assays. 13-GEN2-2-2.

The protocol for this study was similar to the one performed in the previous chapter, using the oligonucleotide FAM-PolyT(10). The AuNPs were incubated with the oligonucleotides, centrifuged, and the pellet and supernatant analyzed through the acrylamide gel retardation assay. On the experiments, different factors were studied to optimize the oligonucleotide binding:

- **pH**

Based on the previous results obtained with 13 and 23-GEN1 AuNPs, the pH was lowered using a citrate/citric acid buffer. This approach is based on the low pH assisted method, commonly employed to reduce the repulsion between oligonucleotides nucleobases and AuNPs[147,148]. The pH of the GEN2 AuNPs is usually around 6-6.5 after the whole functionalization process. Due to this, it was explored the gradual pH lowering, studying the binding at these pHs, 5.5, 4.5 and 3.5. For each pH, it was studied a bPEI/oligonucleotide N/P ratio of 80, calculated as N/P ratio = 7.53 × weight ratio of PEI/DNA[101]. The N/P 80 is considered the optimal for bPEI 2KDa[145], and it was only considered the amount of bPEI in the second layer. The citrate buffer was added to the AuNPs around 1 h before incubating the particles with oligonucleotide, considering a final concentration of 1 mM. The volume of the buffer added was calculated not to exceed 10% of the AuNPs/oligonucleotides volume. After the incubation and treatment, the pellet and the supernatant were evaluated (**Figure 58**) through the gel retardation assay. As can be observed, even at pH 6.5 corresponding to the AuNPs without any buffer, the oligonucleotide binding is 60%. When the pH was lowered, the binding increased 15% at pH 5.5 and 40% for pH 4.5 and 3.5, which means that

all the oligonucleotide was conjugated into the particles. These results highlight the potential of the approach, which was one of the primary objectives of the project.

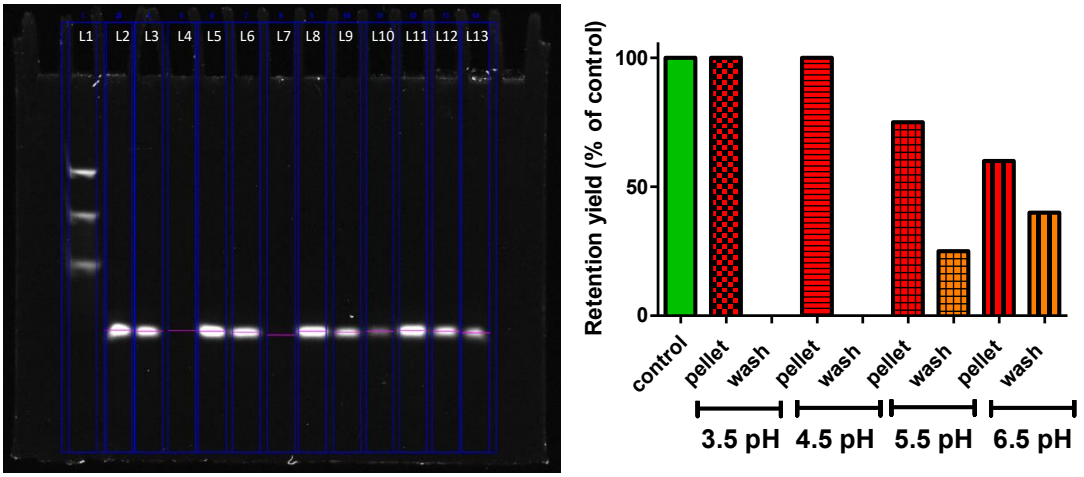

pH	Pellet % (oligonucleotide bonded)	Wash % (oligonucleotide not-bonded)
6.5	60	40
5.5	75	25
4.5	100	0
3.5	100	0

Figure 58. GEN2-2-2 AuNPs conjugation with FAM-PolyT(10) gel retardation assay and quantification at pHs of 3.5, 4.5, 5.5 and 6.5. Fixed buffer concentration to 1 mM and bPEI/PolyT(10)FAM N/P ratio 80. L (line) 1: ladder, L2-4: 3.5 pH control, pellet, wash (c,p,w), L5-7: 4.5 pH c,p,w, L8-10: 5.5 pH c,p,w, L11-13: 6.5 pH c,p,w.

❖ bPEI/oligonucleotide N/P ratio

As observed, the N/P ratio used allowed the complete conjugation with the oligonucleotide experiment when the pH was 4.5 and 3.5. Then the effect of different N/P ratios was assessed using: 80, 40, 20 and 10. The results of this study are summarized in (**Figure 59**). In this case, it was observed that by reducing the N/P ratio to 40, 20 and 10, a retention of 92%, 33% and 15%, respectively, could be obtained. Thus, by this approach, using the bPEI alone, the N/P ratio could be reduced to 40 without losing efficiency, which is remarkable considering that the optimal ratio for the polymer of 25 KDa alone is 35[146].

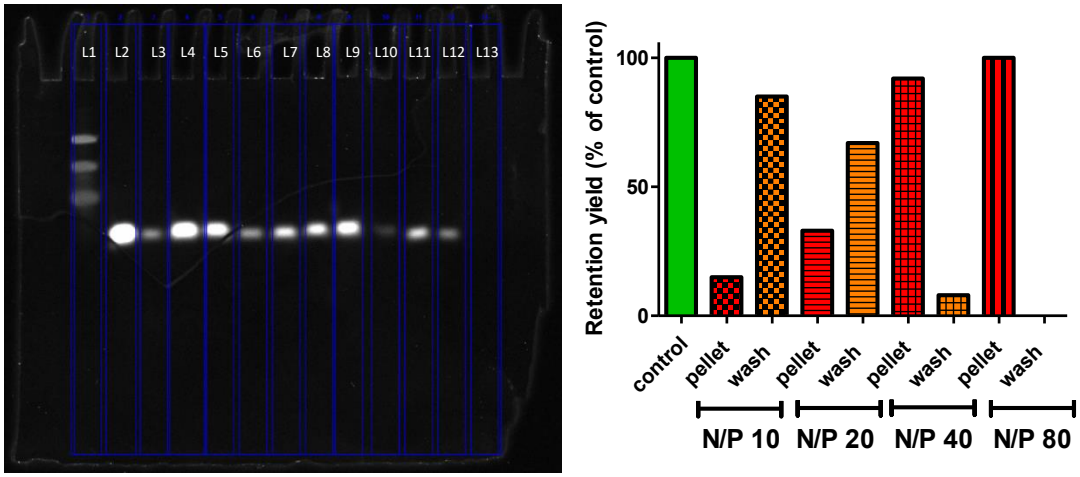

N/P	Pellet % (oligonucleotide bonded)	Wash % (oligonucleotide not-bonded)
80	100	0
40	92	8
20	33	67
10	15	85

Figure 59. GEN2-2-2 AuNPs conjugation with FAM-PolyT(10) gel retardation assay and quantification at bPEI/oligonucleotide N/P ratio of 80, 40, 20 and 10. Fixed buffer concentration to 1 mM and pH of 3.5. L (line) 1: ladder, L2-4: N/P 80 control, pellet, wash (c,p,w), L5-7: N/P 40 c,p,w, L8-10: N/P 20 c,p,w, L11-13: N/P 10 pH c,p,w.

❖ Buffer concentration

The last factor studied for the optimal binding of the particles with the oligonucleotides was the buffer concentration. Until this point, it was employed a final concentration of the buffer on the mixture equivalent to 1 mM. It was explored other concentrations (1, 0.75, 0.5 and 0.25 mM) to observe if the binding would be affected. For this experiment, the pH was fixed at 3.5 and the N/P ratio at 20. The results are summarized in **Figure 60**. The general trend observed is that the binding decreases when the buffer concentration is reduced, however at 0.75 mM the binding obtained was significantly better.

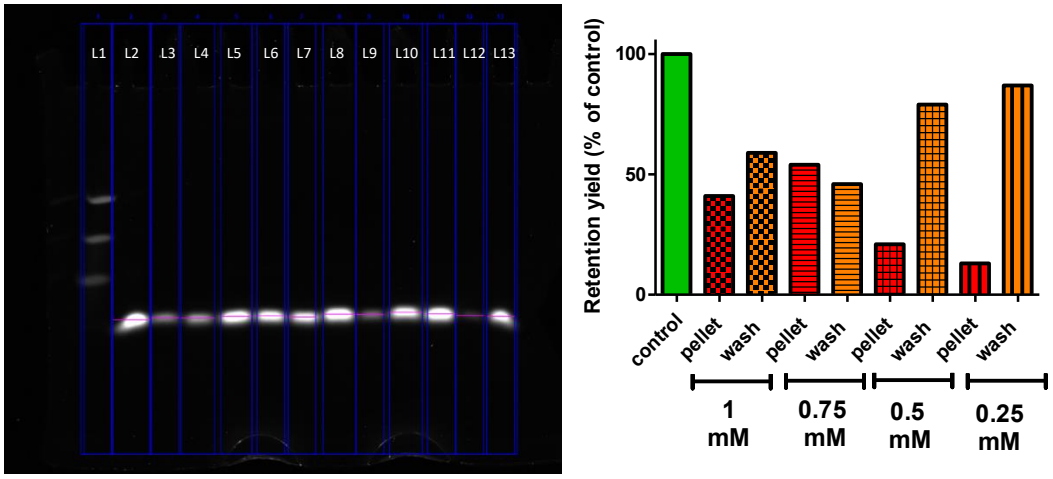

Buffer (mM)	Pellet % (oligonucleotide bonded)	Wash % (oligonucleotide not-bonded)
1	41	59
0.75	54	46
0.5	21	79
0.25	13	87

Figure 60. GEN2-2-2 AuNPs conjugation with FAM-PolyT(10) gel retardation assay and quantification at citrate/citric acid buffer concentrations of 1, 0.75, 0.5 and 0.25. Fixed N/P ratio of 20 and pH of 3.5. L (line) 1: ladder, L2-4: buffer concentration 1 mM control, pellet, wash (c,p,w), L5-7: buffer concentration 0.75 mM c,p,w, L8-10: buffer concentration 0.5 mM c,p,w, L11-13: buffer concentration 0.25 mM c,p,w.

4.2.4.3. Conjugation efficacy assays. 13-GEN2 formulation comparison.

Thus, based on the previous optimization experiments, the conditions selected were pH 3.5, using a citrate/citric acid buffer concentration of 0.75 mM and a AuNPs/oligonucleotide N/P ratio of 40 for the 13-GEN2-2-2 AuNPs. The next step planned was to test these parameters with the rest of 13-GEN2 formulations prepared. Due to this, it was incubated the different AuNPs 13-GEN2-2-2, 13-GEN2-25-2, 13-GEN2-2-25 and 13-GEN2-25-25 with the polyT(10)-FAM under the same conditions. To observe better changes in the binding, the N/P ratio was fixed at 30 instead of 40, where the 13-GEN2-2-2 should provide approximately a 50-70% binding ratio. We expected that a similar or better result could be obtained for the 13-GEN2-25-2 particles, whereas for the 13-GEN2-2-25 and 13-

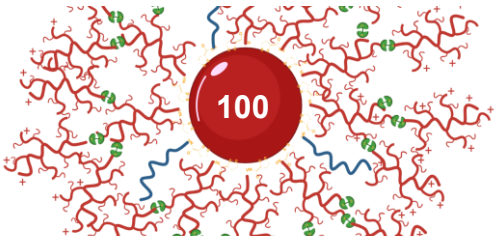

GEN2-25-25 the binding ratio could be 100%[146]. However, the results obtained (**Figure 61**) were the opposite. The formulations with the PDP-bPEI 2 KDa as the second layer afforded the best results, whereas the 13-GEN2-25-25 the worst ones. To better understand this phenomenon, both the unmodified bPEI 25 KDa and its two modified species with LP and SPDP were incubated with the PolyT(10)-FAM oligonucleotide under the same conditions. To remove the supernatant from the polymer pellet, a 10 KDa centrifugal filter was used and the gel retardation assay was carried out. In this case (**Figure 62**), the oligonucleotide was completely bound to the polymer. Based on these results, it was hypothesized that the cause of the low bindings in **Figure 61** could be caused by the "packing" effect obtained when the bPEI 25 KDa is presented in any of the layer of the GEN2 formulation. Even the results observed in **Chapter 2** for GEN1-25 formulations, show a higher conjugation at pH 3.5. This suggests that in this two-layers conjugation formula, the binding performance decreases when is the bPEI 25 KDa, being this effect more intense when it is used in the second layer.

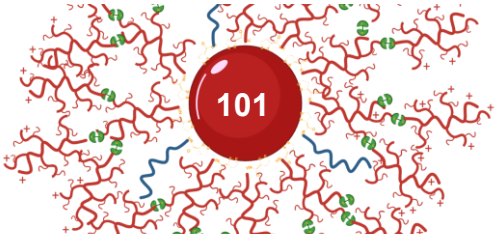

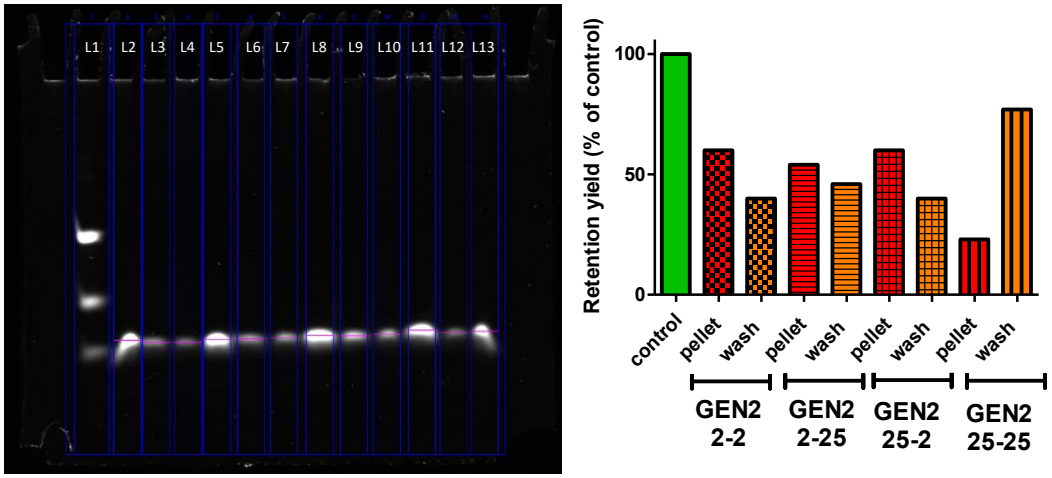

GEN2	Pellet % (oligonucleotide bonded)	Wash % (oligonucleotide not-bonded)
2-2	60	40
2-25	54	46
25-2	60	40
25-25	23	77

Figure 61. 13-GEN2-2-2, 13-GEN2-25-2, 13-GEN2-2-25 and 13-GEN2-25-25 AuNPs conjugated with FAM-PolyT(10): gel retardation assay and quantification. Fixed N/P ratio of 30, 0.75 mM buffer concentration and pH of 3.5. L (line) 1: ladder, L2-4: 13-GEN2-2-2 control, pellet, wash (c,p,w), L5-7: 13-GEN2-2-25 c,p,w, L8-10: 13-GEN2-25-2 c,p,w, L11-13: 13-GEN2-25-25 c,p,w.

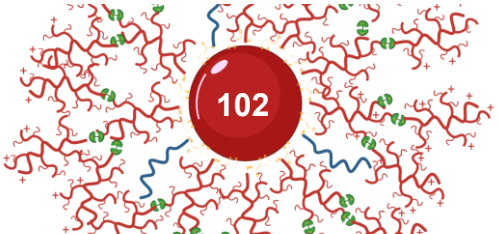

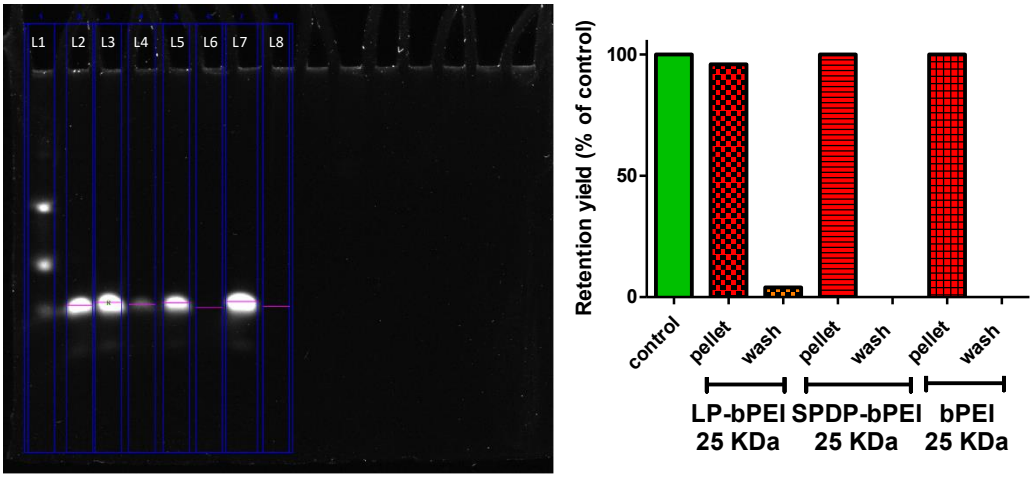

Polymer	Pellet % (oligonucleotide bonded)	Wash % (oligonucleotide not-bonded)
LP-bPEI 25 KDA	96	4
PDP-bPEI 25 KDa	100	0
bPEI 25 KDa	100	0

Figure 62. LP-PEI 25 KDa, PDP-bPEI 25 KDa and bPEI 25kDA conjugated with FAM-PolyT(10) gel retardation assay and quantification. Fixed N/P ratio of 30, 0.75 mM buffer concentration and pH of 3.5. L (line) 1: ladder, L2: control L3-4: LP-bPEI 25 KDa pellet, wash (p,w), L5-6: PDP-bPEI 25 KDa c,p,w, L7-8: bPEI 25 KDa p,w.

Thus, 13-GEN2-2-2 was selected for further studies.

4.2.4.4. Transfection efficacy assays. 13-GEN2-2-2.

Once the toxicity and binding properties of the nanoparticles were evaluated, the system was employed in the transfection of oligonucleotides into cells. Therefore, the complex was incubated for 24 h in the cell lines PANC-1 and MCF-7. As a control condition, the oligonucleotide was transfected using the liposomal agent lipofectamine 2000. After the incubation time, the transfection of the PolyT(10)-FAM was observed by fluorescence microscopy and quantified by fluorescence spectroscopy. The results (**Figure 63**) indicate that the AuNPs are able to successfully deliver the oligonucleotide inside both tumoral cell lines and release it through the intracellular stimulus. As expected, liposomal transfection increased the fluorescence in such cell lines by approximately 70%, but their potential toxicity makes it not viable for clinical studies[161]. This study confirms that

the particles prepared are suitable carriers for the delivery and transfection of oligonucleotides.

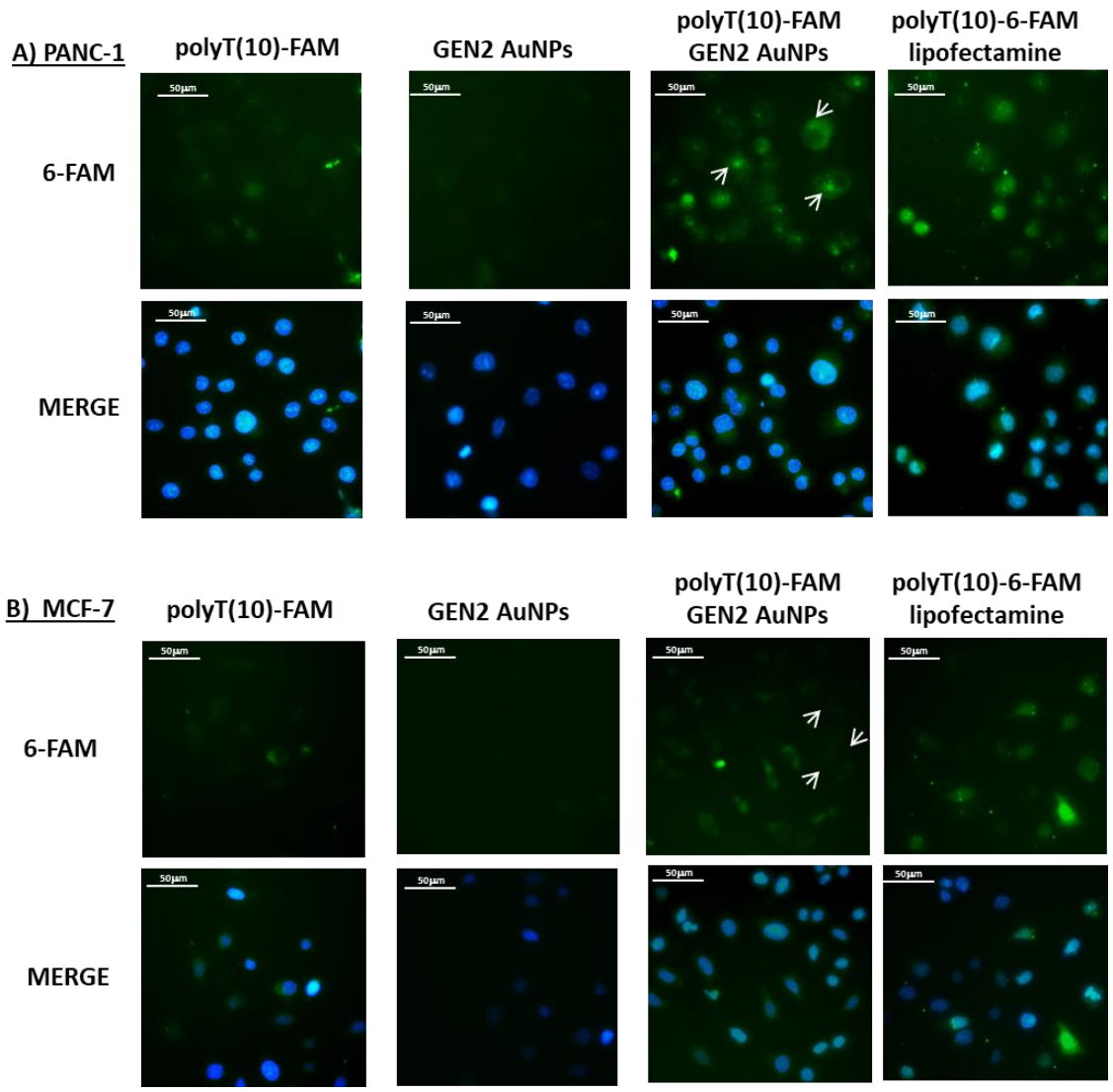

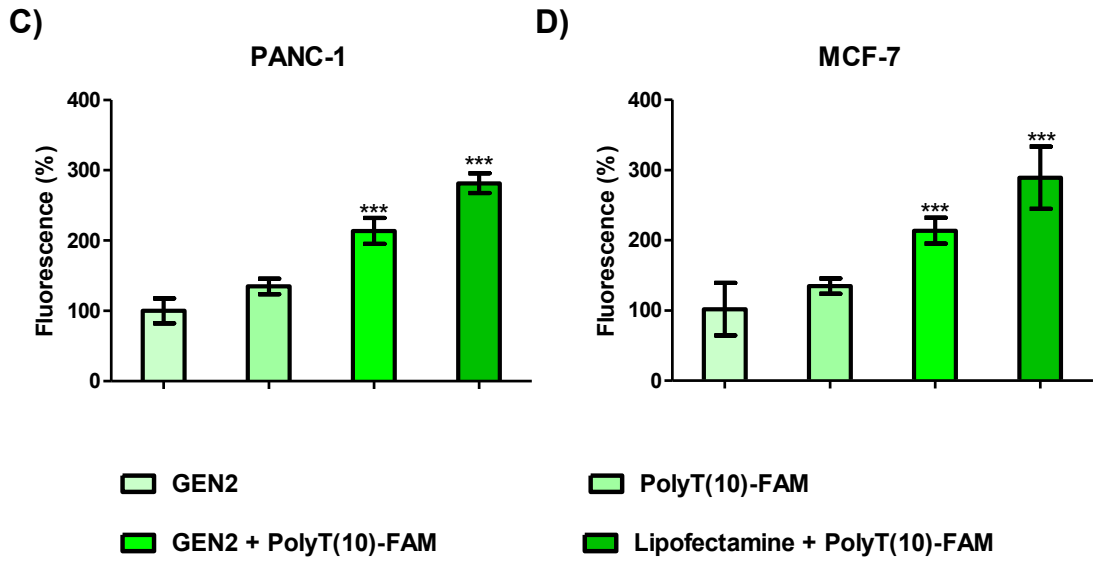

Figure 63. Fluorescent microscopy and the quantification of polyT(10)-FAM transfected in PANC-1 (A-C) and MCF-7 (B-D) tumoral cell lines using 13-GEN2-2-2 AuNPs as transfer agents. FAM in green and nucleus are labeled in blue by Hoechst staining as fluorescence control, it was measured the fluorescence of the particles and the oligonucleotide alone. Lipofectamine 2000 was introduced as a reference. The transfection experiment was carried out for 24 h. The statistical analysis was performed using one-way ANOVA (each group vs. GEN2 control) (*** $p < 0.001$, ** $p < 0.01$, * $p < 0.05$, · < 0.01).

4.2.4.5. Conjugation efficacy assays of 13-GEN2-2-2 with various biomolecules.

Once the 13-GEN2-2-2 was selected as a carrier of oligonucleotides, larger oligonucleotide sequences were evaluated. Therefore, two additional oligonucleotides modified with FAM with sequences of 20 and 40 nucleobases: polyT(20)-FAM and polyT(40)-FAM were employed. The conditions tested where the optimal previously obtained and having the polyT(10)-FAM as control. As observed in **Figure 64**, under the same optimized conditions of N/P ratio, buffer concentration and pH, the conjugation of the oligonucleotide sequences, independently of the size, is close to 100%.

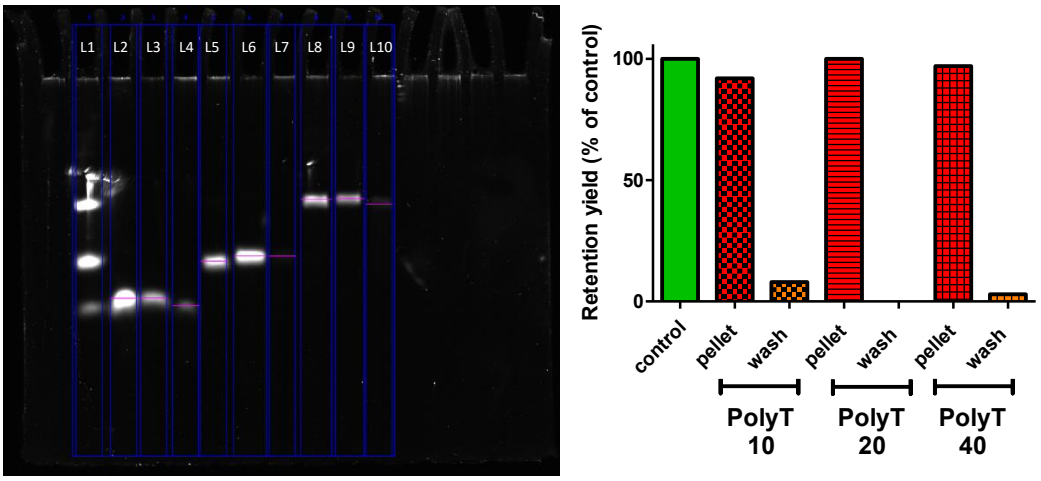

PolyT	Pellet % (oligonucleotide bonded)	Wash % (oligonucleotide not-bonded)
10	91	9
20	100	0
40	97	3

Figure 64. 13-GEN2-2-2 and FAM-PolyT(10), (20) and (40) gel retardation assay and quantification. Fixed N/P ratio of 40, 0.75 mM buffer concentration and pH of 3.5. L (line) 1: ladder, L2-4: FAM-PolyT(10) control, pellet, wash (c,p,w), L5-7: FAM-PolyT(20) c,p,w, L8-10: FAM-PolyT(40) c,p,w.

These results suggest that as long as the conditions tested are used, can be conjugated most of the types of biomolecules in that range of size. However, the sequences used in the experiment are simple, being exclusively composed by thymine nucleobases. Thus, other sequences, which can yield a more complex 3D structure should be tested. These structures can prevent an efficient interaction between the phosphate groups and the polymers.[162], Thus, the antitumoral aptamer AS1411 (5'-GGTGGTGGTGGTTGTGGTGGTGGTGG-3') was evaluated[163]. It was synthesized with a FAM modification in 5' for better tracking and quantification. The conjugation with the particles was carried out using increasing N/P ratios 40, 60 and 80. The N/P ratio 40 was the optimal found previously, but it was considered that the more complex structure of the aptamer with respect to the PolyTs tested till the moment could require a higher N/P. This was confirmed with the gel retardation assay **Figure 65**, where the conjugation

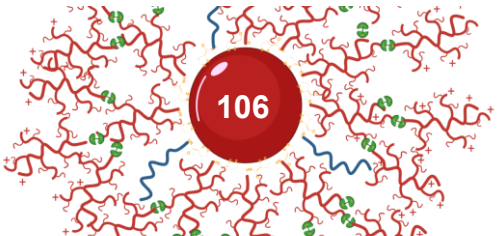

at the 40 N/P ratio was 50%, while at N/P ratio of 60 and higher, the binding was 100%.

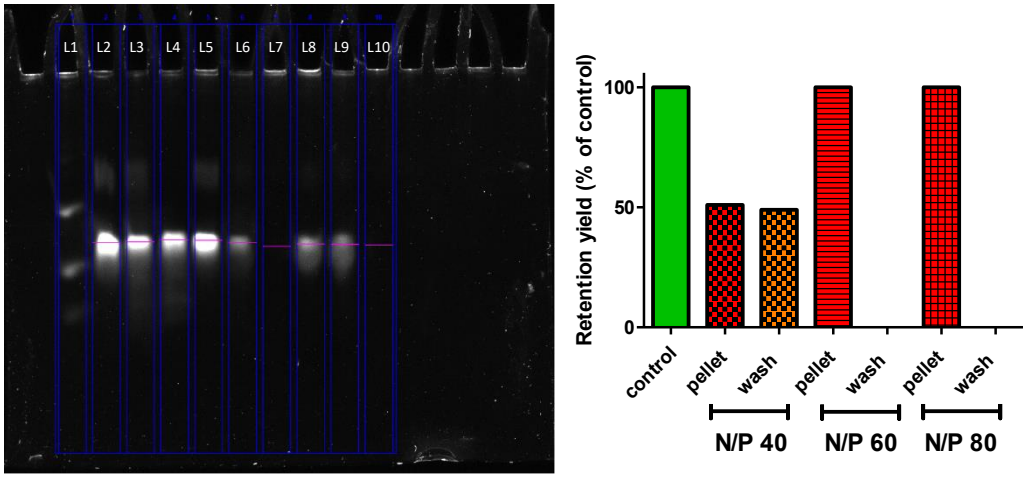

N/P	Pellet % (oligonucleotide bonded)	Wash % (oligonucleotide non-bonded)
40	51	49
60	100	0
80	100	0

Figure 65. 13-GEN2-2-2 and AS1411-FAM aptamer gel retardation assay and quantification at N/P ratios of 40, 80 and 120. Fixed 0.75 mM buffer concentration and pH of 3.5. L (line) 1: ladder, L2-4: N/P 40 control, pellet, wash (c,p,w), L5-7: N/P 80 c,p,w, L8-10: N/P 120 c,p,w.

4.3. Conclusions

This part of the project was focused on the obtention of new AuNPs from the GEN1 to increase the charge of the AuNPs and increase the exposure of the bPEI to promote the interaction with the genetic material. For this purpose, it was designed a system that consists of the generation of a second layer of bPEI over the already functionalized GEN1 AuNPs. This strategy implied the modification of bPEI with a crosslinker, the SPDP, and the obtention of sulfhydryl groups in the particles.

The strategy was studied and optimized in different structures, such as GEN1 AuNPs of 13 and 23 nm of core size, with functionalized bPEI of 2 and 25 KDa. Using these elements 8 different combinations of the new GEN2 AuNPs were prepared.

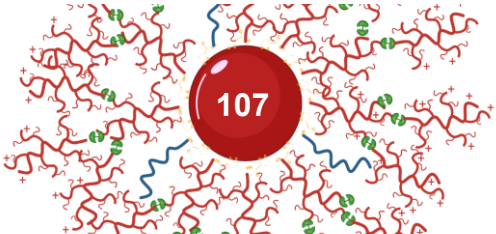

Those GEN2 AuNPs have been characterized by DLS showing significant changes in the potential of the AuNPs obtaining a range of charge from 40 to 60 mV, which suppose a great difference against the 12 mV obtained previously. These AuNPs have been tested in different ways. First, their interaction with GSH, mimicking the intracellular conditions.

The formulations were also tested in cytotoxicity assays, observing that the formulations based on the 23 nm one presented a more toxic profile than the 13 nm, attributed to the higher amount of polymer carrying. The safer formulations were then tested for electrostatic binding with oligonucleotides. It was confirmed that the new layer provided a better conjugation, which was increased when the pH was lowered. The factors to obtain the maximum conjugation and load were also optimized. These optimized factors were employed for all the formulations, revealing that 13-GEN2-2-2 presented the best properties. This formulation was tested using different oligonucleotides lengths and sequences. The nanoparticles we also tested as carriers in tumoral cells with promising results.

In summary, the 13-GEN2-2-2 AuNPs formulation obtained in this stage of the project has been demonstrated to be suitable to work in a cellular environment and work with nucleic acids.

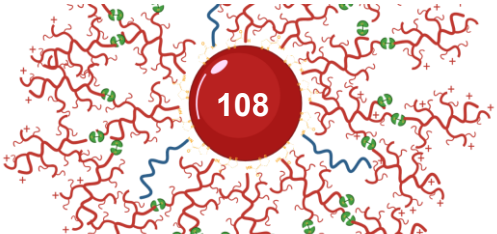

Chapter 4.

Bio-applications of GEN2 AuNPs

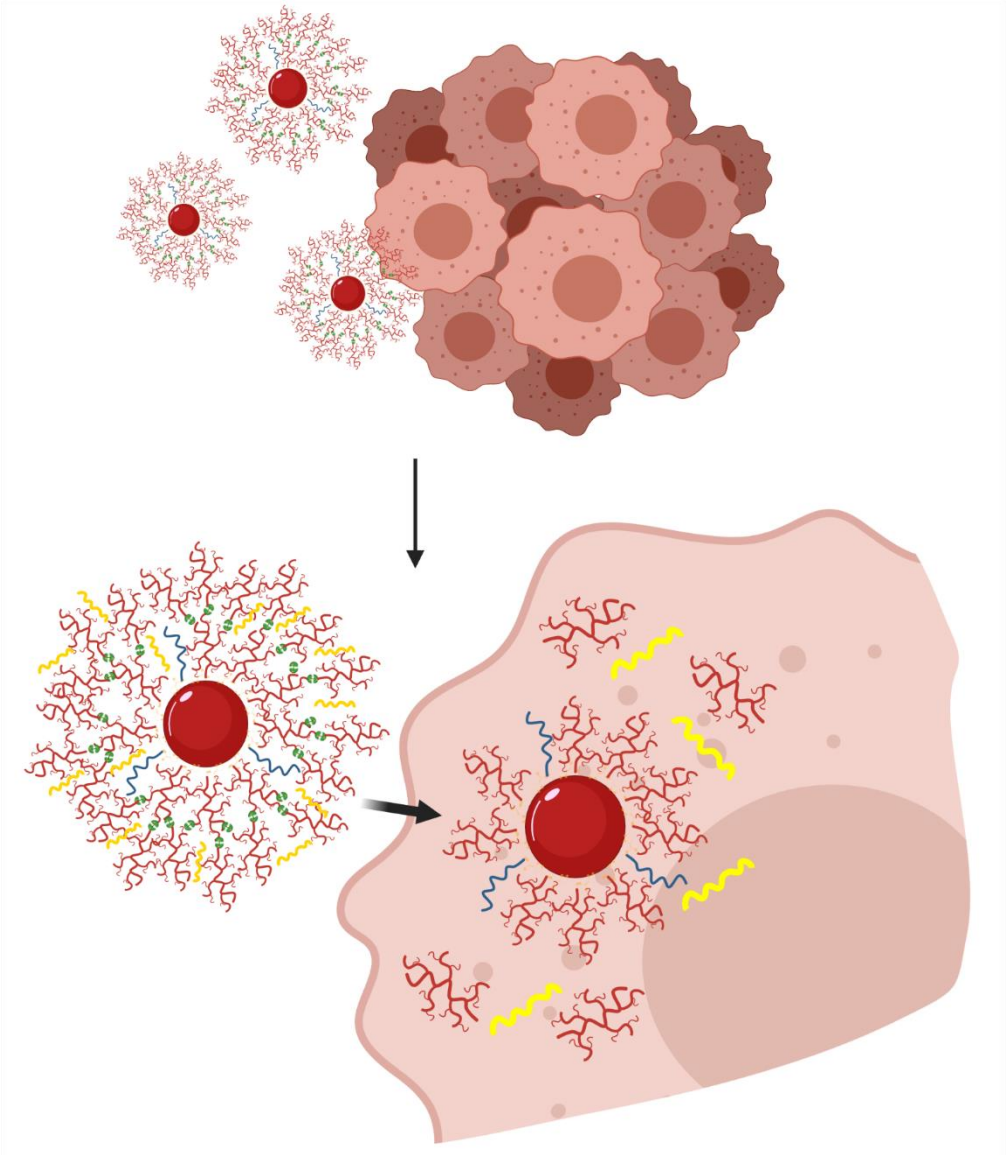

Chapter 5. GEN2-AuNPs bio-applications

5.1. Introduction

Throughout this project, it has been developed a gold-based system made of modified polymeric ligands, the GEN2-AuNPs. The formulation of these AuNPs consists of two polymers layers, an inner one with bPEI and PEG and an outer one with bPEI, connected through a sensitive linker. This formulation, tested in different size particles and different ratios, has displayed low cytotoxicity, high binding with oligonucleotides, and efficient cellular transfection.

Due to this, the GEN2 AuNPs have been studied as carriers of oligonucleotides, which can be used for the regulation of genes.

5.1.1. Oligonucleotide therapies

Oligonucleotides are short single-stranded DNA or RNA molecules[164]. Their properties and biological applications depend on their sequence and length due to their capacity to interact in a specific manner with other complementary sequences, leading to duplexes stabilized by Watson-Crick base pairing. Through this interaction, oligonucleotides can be employed to treat a wide range of diseases, because they can be used for the regulation of disease-related genes. It is worth mentioning that oligonucleotides present high specificity for their target molecules (e.g., mRNA, microRNAs), and minimal predictable side effects, making them powerful tools for personalized medicine[165].

Different types of therapeutic oligonucleotides have been employed, such as antisense oligonucleotides (ASOs), small interfering RNA (siRNA), microRNAs (miRNAs), aptamers or CpG oligonucleotides. These oligonucleotides can be found in different applications like PCR primers, molecular diagnosis or gene therapies. The treatments based on oligonucleotides have shown remarkable results in various diseases, including neurodegenerative and respiratory disorders, diabetes and cancer[166].

However, despite their potential, one major issue that prevents their use as therapeutics is their inefficiency delivery to most target organs and tissues. Additionally, other hurdles must be considered, such as off-target interactions[167],

chemistry-dependent toxicity or saturation of RNA pathways[168]. To overcome these limitations, the use of nanocarriers has shown promising results to increase cell targeting and penetration.

Among the different types of therapeutic oligonucleotides, in this project, we have focused on the use of antisense oligonucleotides (ASOs) for gene therapy against cancer.

5.1.2. Antisense oligonucleotides (ASOs)

ASOs are synthetic oligonucleotides, single-stranded, employed to regulate gene expression. They can be divided into two major groups depending on their function: steric block and RNAse H competence.

Regarding the steric block antisense oligonucleotides, they are designed to bind target transcripts with high affinity but do not induce target transcript degradation as they lack RNase H competence. Their role includes the mask of specific sequences, interfering with the RNA-RNA or RNA-protein transcription, which can be used to exclude or maintain target sequences selectively [169]. This approach helps in the restoration of therapeutic proteins or the reduction of the expression of harmful ones[170-171].

The second case is based on the activity of the RNAse H enzyme (RNASEH1), which recognizes RNA-DNA heteroduplex substrates and degrades the RNA strand. Thus, ASO can be designed to bind RNAs selectively and exploit the presence of RNAse H to degrade the target RNA sequence,[172] which causes gene silencing . This strategy has been applied to treat diseases promoted by defective genes[173]. Currently, RNase H-competent ASOs usually display a 'gapmer' pattern (**Figure 66**), which presents a central DNA sequence (gap) surrounded by modified RNA moiety (2'-Modification in the sugar ring) that promote target binding[174]. The introduction of chemical modifications at both sides of the central region improves their binding affinity, leading to stable DNA-RNA duplexes, which can be recognized by RNAse H[175]. Additionally, the modifications can increase their biostability, target specificity and delivery, leading to more prolonged effects[176]

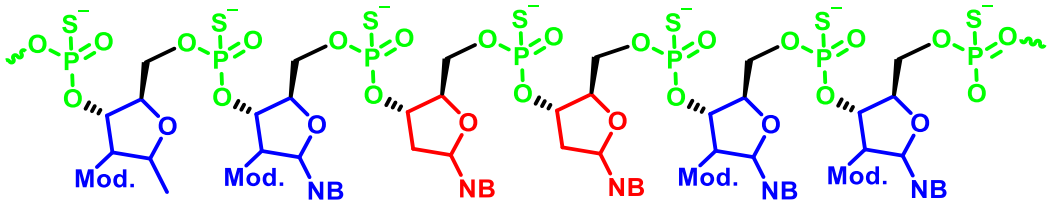

Figure 66. "Gapmer" pattern on an oligonucleotide sequence. The central area (Red) displays a DNA sequence without any modification on the nucleobases, while the extremes (Blue) present an RNA moiety with a modification in 2'-.

As these two methods target the origin of the development of the disease, ASOs have a high potential as therapies compared to conventional treatments. However, the limits of the techniques are related to the delivery. As an example, the RNAse H enzyme can be found mainly in the cytoplasm and the nucleus of the cell, which is difficult to reach by oligonucleotides[177].

5.1.3. p53. Loss and mutation in cancer development

p53 protein, encoded by the gene TP53, is a protein well known for its role as tumor suppressor in humans and other mammals[178]. It has been extensively studied to discover how its transcription functions works in the regulation of gene expression, hence p53-responsive genes have a dramatic impact on the cell-cycle arrest, senescence and apoptosis[179-180].

Because of the impact of its tumor suppressor functions, its loss leads to the accumulation of genomic alterations culminating in cancer progression. In fact, p53 is the most frequently inactivated tumor suppressor gene in tumors, being mutated in over 50% of human cancer types and indirectly inactivated in many others[181]. Additionally, the p53 can undergo mutations (mutp53), acquiring new biological properties, namely gain-of-function (GOF), which contribute to the maintenance and stimulation of cancer growth[182].

In many tumors, GOF p53 mutations are associated with high genomic instability, low prognosis, poor response to chemotherapy, promotion of migration, invasion, metastasis, and accelerated tumor recurrence[183-184].The mechanism associated with GOF mutp53 has been studied through the modulation of the activity of different transcriptions factors or with the use of DNA damage molecular sensors[185]. In recent studies, it has been reported that the DNA damage

produced by the chemotherapy drug gemcitabine (GEM), helps to stabilize the mutp53, which leads to the expression of cell cycle genes, causing hyperviability and chemoresistance[186]. Also, mutp53 variants can alter the cancer cell mitochondrial metabolism[187], autophagy responds to different stimuli[188] and microenvironment[189], indicating a large array of cellular pathways that increase tumor progression and aggressiveness.

Hence, novel approaches that inhibit the expression and function of mutp53 proteins could represent a valid therapeutic approach for cancer patients. The current pharmacological strategies based on this approach are limited to the use of small molecules (e.g., RITA[190], PRIMA-1[191] or NSC59984[192]), which can restore the tumor suppressor function of mutp53 proteins, or induce their degradation, inducing cell death[193]. However, these approaches are not suitable for clinical application due to problems related to delivery, drug stability and toxicity[194]. Therefore, the discovery of efficient and safe therapeutic strategies that specifically target mutp53 remains challenging.

Recently, strategies based on nucleic acids have been explored as a highly specific therapy against cancer, by downregulating mutp53 protein levels, triggering apoptosis, and delaying cancer growth in mice [195-196].

5.1.4. GEN2 AuNPs as carriers of Antisense Oligonucleotides

To overcome the limitations of antisense oligonucleotides as therapeutics, the use of GEN2 AuNPs as carriers, was assessed to target mutp53. In this regard, 4 ASO gapmers were designed and synthesized to target mutp53. These molecules were expected to reduce mutp53 expression and the cell viability in cancer cells. Another two ASO gapmers, without therapeutic effect, were used as controls. The tumoral cell lines explored carrying mutp53 or wild-type p53 were PANC-1 (mutp53 R273H), pancreatic tumor cells, and MCF-7 (wtp53) and MDA-MB-231 (mutp53 R280K), breast cancer cells. Additionally, it was also planned to evaluate the system in combination with gemcitabine (GEM).

5.2. Results and Discussion

Tumor protein p53 is one of the most frequently inactivated tumor suppressor genes, which is found mutated in over 50% of human cancer types. Its absence

leads to tumor progression, and the mutated form (mutp53) can obtain new properties, called gain of function (GOF), that help in the development of the tumor and its metastasis. It also produces chemoresistance to therapeutic drugs such as gemcitabine (GEM), a popular antineoplastic chemotherapy medication employed to treat different carcinomas as pancreatic or breast cancer[197].

To inhibit the expression of p53, it is usually employed small molecules to trigger autophagy mechanisms that end in the degradation of the mutant p53. However, they are difficult to use in clinical experiments due to their toxicity, low stability and delivery problems. New approaches are focused on the use of Antisense oligonucleotides, usually presenting a gapmer pattern[198-199]. Those gapmers oligonucleotides can be designed to target mutant p53 to downregulate its levels, presenting higher specificity and efficacy. But as with many nucleic acids, the main challenge to face is their delivery. In this regard, the GEN2 AuNPs prepared previously can help due to their tested role as carriers, conjugating the gapmers electrostatically and delivering them into the target cells bearing mutant and wild type p53.

Among the 8 different GEN2-AuNPs prepared and evaluated in previous chapters, 13-GEN2-2-2 AuNPs was selected to deliver the ASO gapmers due to their stability, reproducibility, null toxicity and efficacy in the delivery of nucleic acids.

5.2.1. Cytotoxicity assays

The toxicity of 13-GEN2-2-2 AuNPs was evaluated in PANC-1, MCF7 and MDA-MB-231 cell lines. This experiment was performed to select the highest concentration of the particles that do not induce significant toxicity. Thus, increasing concentrations of 13-GEN2-2-2 AuNPs from 0.25 to 2 nM were tested.

The cytotoxicity results obtained (**Figure 67**) are similar to those obtained in **Chapter 3** for the PANC-1 and MCF-7 cell lines and concentrations tested. In MCF-7 (**Figure 67B**), the toxicity trend is very similar at 48 and 72 hours, showing a significant decrease in cell viability at 1.75 nM. In PANC-1(**Figure 67A)**, the same concentration induced toxicity, which is more pronounced after 72 hours than 48. In the new cell line tested (MDA-MB-231) (**Figure 67C)**, the toxicity trend is similar to PANC-1, but the toxicity can be appreciated at 1.5 nM after 72 hours.

Based on these experiments, the concentration selected for the gapmer vehiculation was 1 nM, which did not induce toxicity in the 3 cell lines at 48 and 72 hours.

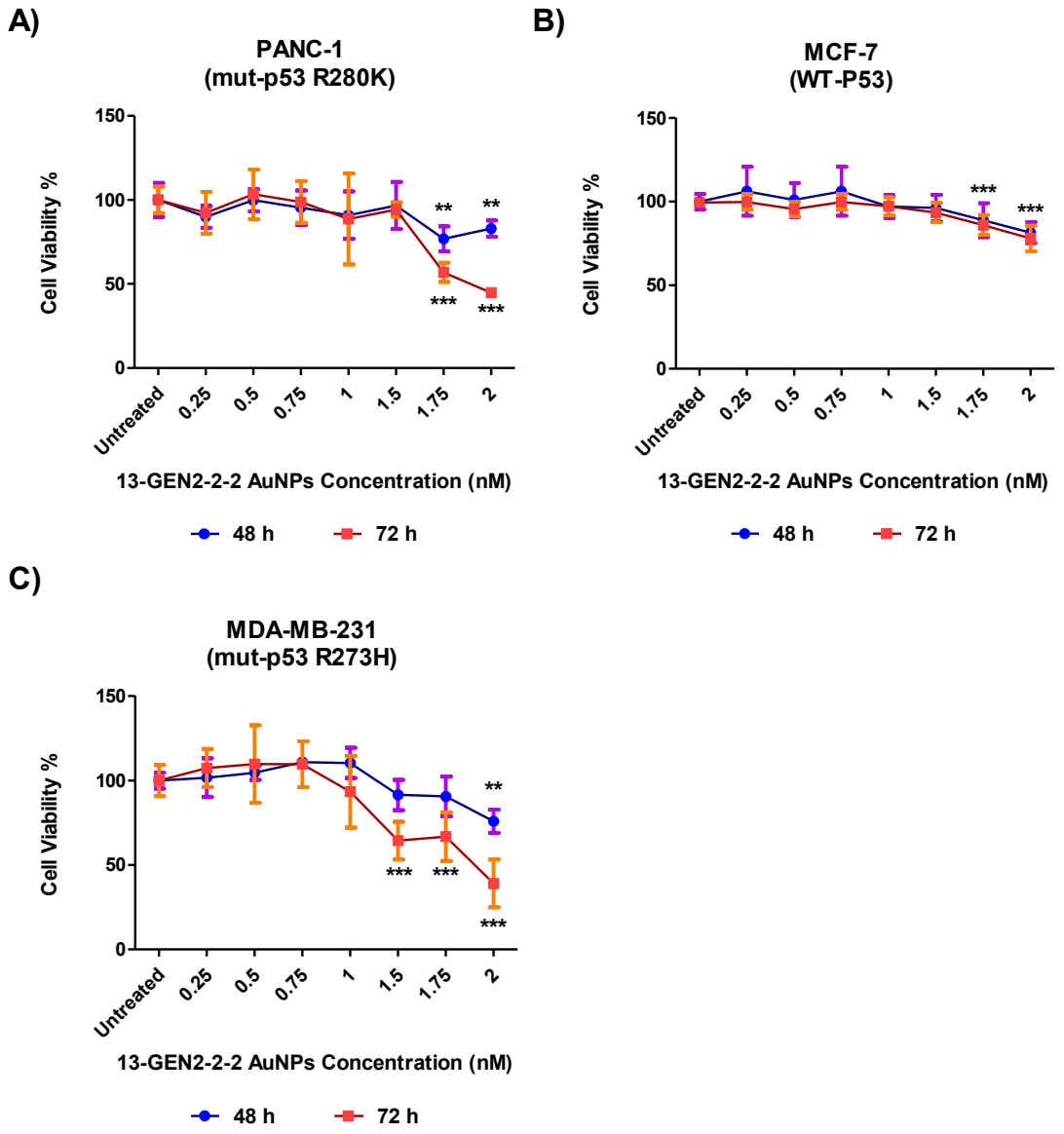

Figure 67. Cytotoxicity assay of 13-GEN2-2-2 AuNPs in the cell lines PANC-1 (mutant p53-R273H) (A), MCF7 (WTp53) (B) and MDA-MB-231 (mutant p53-R280K) (C). The concentrations tested were 0.25, 0.5, 0.75, 1, 1.5, 1.75 and 2 nM having untreated cells as control. Cell viability was assessed using the alamar blue assay after 48 h and 72 h. The statistical analysis was performed using one-way ANOVA (each group vs. control) (*** $p < 0.001$, ** $p < 0.01$, * $p < 0.05$, · < 0.01).

5.2.2. Chemotherapy sensitivity assays

As it was mentioned before, one of the characteristics of cell lines bearing mutp53 is their chemoresistance to GEM. To confirm this, we assessed the cell viability in mutant and wild-type p53 cancer cells after incubation with increasing concentrations of GEM for 48 and 72 h (**Figure 68**). The results obtained show a drastic difference in the chemoresistance between the cell lines bearing the mutation in p53 (PANC-1 and MDA-MB-231) (**Figure 68AC**) and the cell line with the wt p53 (MCF-7) (**Figure 68B**). The cell viability in the mutated cell lines was reduced between 15-40% after 72 hours. On the other hand, the viability of the cell line with the wt p53 gene (MCF-7), was dramatically reduced (60%). These results are in agreement with previous reports[186-188], and are attributed to the existence of a mechanism leading to the stabilization and induction of p53 in response to DNA damaging agents as the GEM[200].

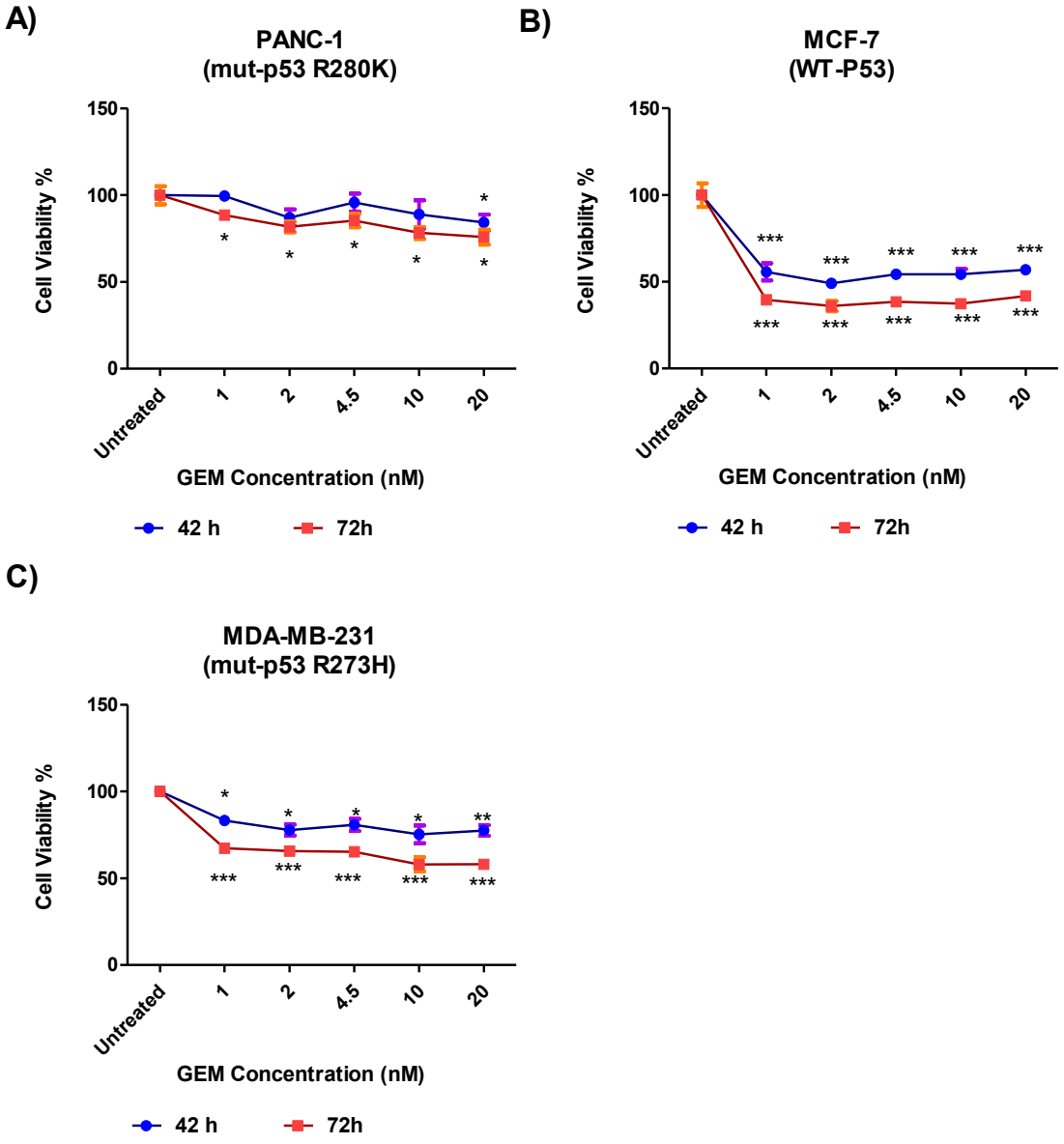

Figure 68. Cytotoxicity assay of gemcitabine (GEM) in the cell lines PANC-1 (mutant p53-R273H) (A), MCF7 (WTp53) (B) and MDA-MB-231 (mutant p53-R280K) (C). The concentrations tested were 1, 2, 4.5, 10 and 20 nM having untreated cells as control. Cell viability was assessed using the alamar blue assay after 48 h and 72 h. The statistical analysis was performed using one-way ANOVA (each group vs. control) (*** $p < 0.001$, ** $p < 0.01$, * $p < 0.05$, · < 0.01).

To better understand the mechanism behind the chemoresistance to GEM in mutp53 cancer cells, some molecular markers related to apoptosis and cell growth in PANC-1, MDA-MB-231 and MCF-7 cancer cells were evaluated by western blots. After treating them with GEM (4.5 nM) for 72 hours, a decrease in p53 protein levels, in mutant and wild-type p53 cancer cells, was observed (**Figure 69**). Additionally, the level of the antiapoptotic protein Bcl-2, which

contributes to cancer formation and progression by promoting the survival of cancer cells, was assessed. The increase of the Bcl-2 signal was observed in PANC-1 cells, whereas no significant changes in this protein were observed in the breast cancer cells. Lastly, it was evaluated the phosphorylation of Ser371-p70S6 protein, related to the activation of mTOR signaling commonly attributed to chemoresistance[201]. In this case, each cell line displays a different behavior, being activated in PANC-1 (**Figure 69A**), almost without changes in MDA-MB-231 (**Figure 69B**) and significantly reduced in MCF-7(**Figure 69C**). These data strongly suggest that oncogenic mutant p53 proteins confer chemoresistance to gemcitabine and help in the survival of the tumor, while the wild type does not present the same characteristic.

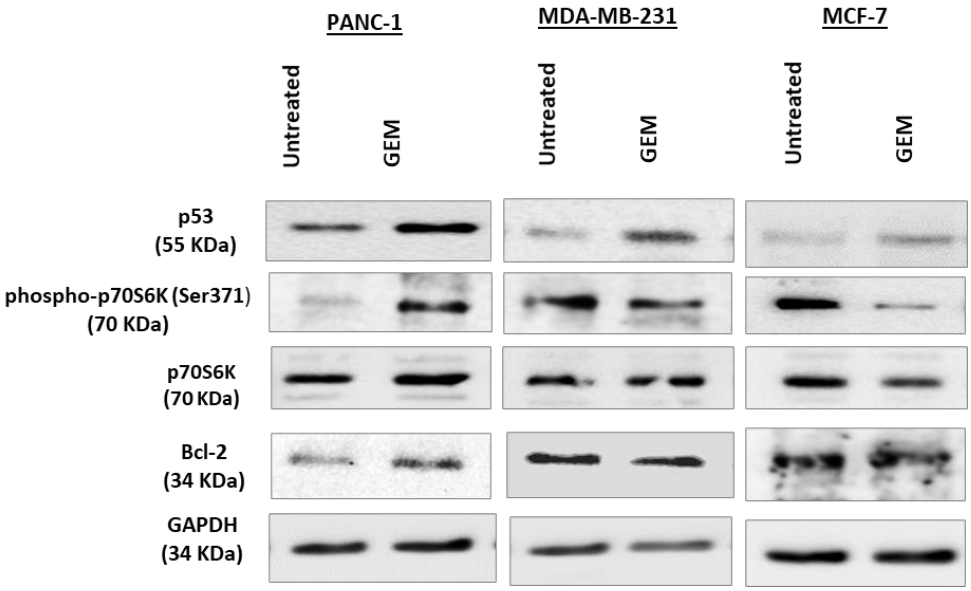

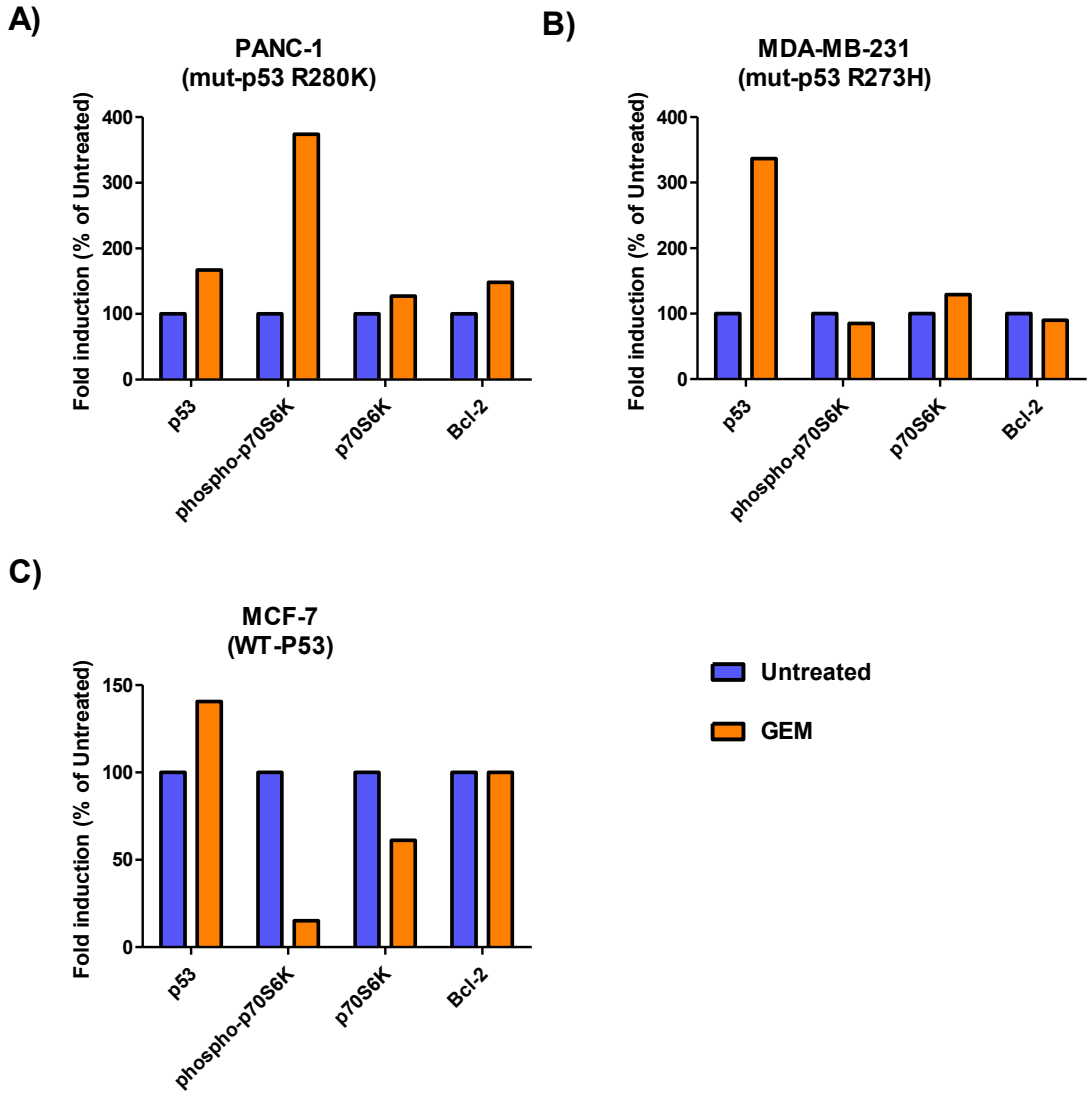

Figure 69. Cell extracts of PANC-1 (mutant p53-R273H) (A), MDA-MB-231 (mutant p53-R280K) (B) and MCF7 (WTp53) (C) quantified by western blots after 72h treatment with 4.5 nM of GEM and untreated ones as controls. GAPDH protein level in the same extract was used as a control loading. The bands shown in the western blot were scanned as digital peaks and the areas of the peaks were reported as fold induction in percentage respect to the untreated.

5.2.3. Efficacy of gapmers to target p53

The 4 gapmers designed were tested together to confirm their activity in the reduction of the p53 expression in the selected cell lines. It has been reported that mutant p53 proteins suppress the autophagic cell death[188], and the stimulation of cell growth. This occurs through upregulation of several cyclins and cdk1-associated kinases activities, which lead to a mutant p53/NF-Y-dependent increase in DNA synthesis[185]. Because of this, it was expected a reduction in the

cell viability using the designed oligonucleotides gapmers. As control, it was employed non-therapeutic oligonucleotides, called scrambles, and the transfection was carried out by a liposomal agent (**Figure 70**). As expected, it can be observed a significant reduction in the cell viability, pretty similar in PANC-1 and MCF-7 (**Figure 70AC**) with a 20% decreased, and more intense in MDA-MB-231 (**Figure 70B**) with a 40% decrease. A western blot analysis was also performed (**Figure 71**) only for p53, observing a reduction in the p53 expression accorded with the results observed by the cytotoxicity assays, around a 40% decrease for PANC-1 and MCF-7 and 60% for MDA-MB-231. The results suggest that the combined ASO gapmers have a powerful effect on the expression of p53 and can help to restore the normal functions of the cells.

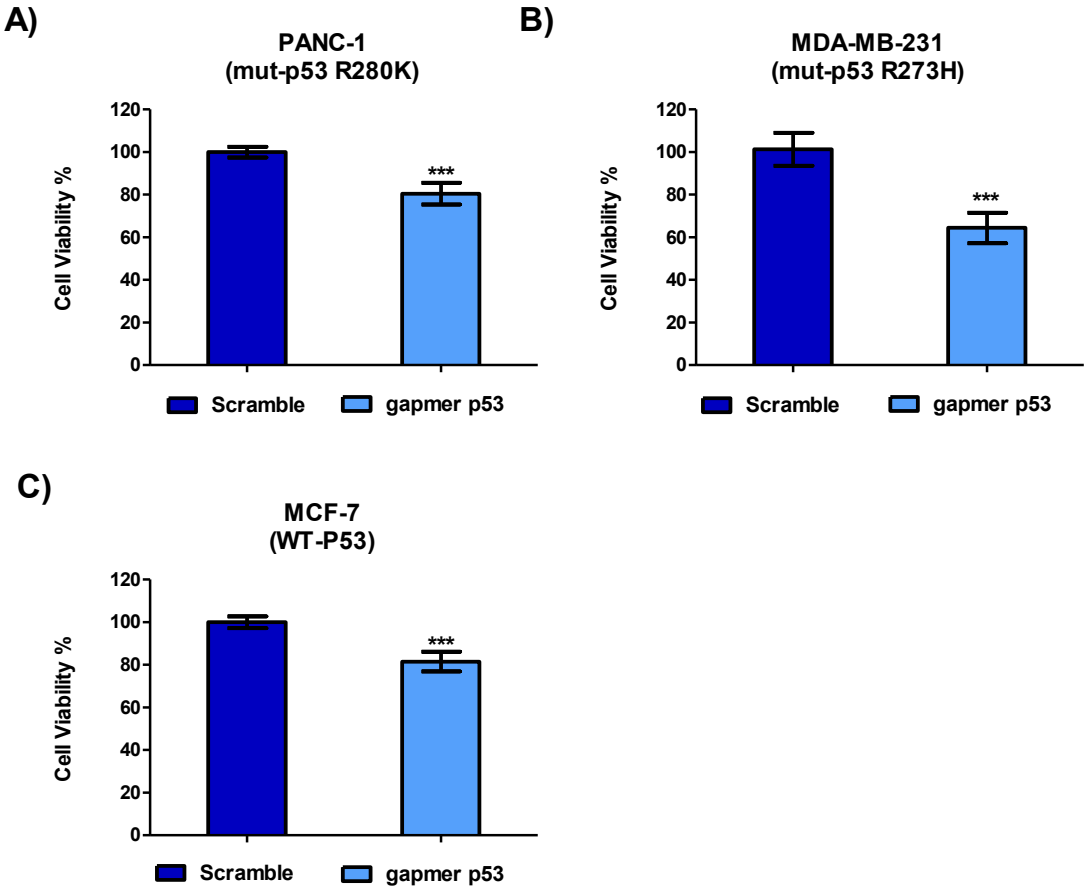

Figure 70. The cells lines containing 4 designed gapmers against p53 and a scramble sequence as control, incubated overnight, and transfected with Lipofectamine 2000 mix for 72 hours in the cell lines PANC-1 (mutant p53-R273H) (A), MDA-MB-231 (mutant p53-R280K) (B) and MCF7 (WTp53) (C), after which their viability was assessed with the alamar blue test.

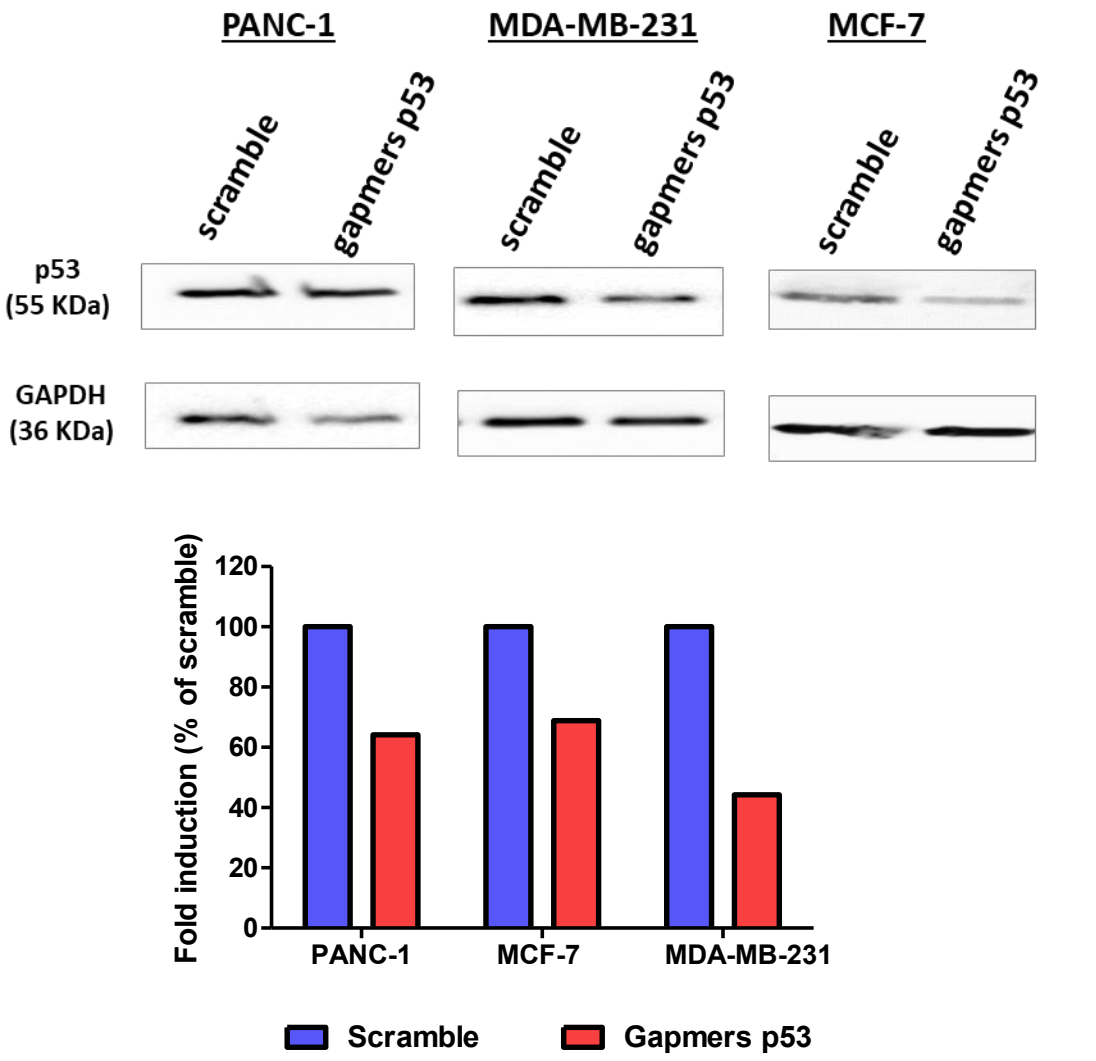

Figure 71. Cell extracts of PANC-1 (mutant p53-R273H), MCF7 (WTp53) and MDA-MB-231 (mutant p53-R280K) quantified by western blots after 72h treatment with designed gapmers to target p53 having a non-therapeutic oligonucleotide, scramble, as control. Whole-cell extracts were processed for western blot analysis of the indicated antibodies. GAPDH protein level in the same extract was used as a control loading. The bands shown in the western blot were scanned as digital peaks and the areas of the peaks were reported as fold induction in percentage respect to the untreated.

5.2.4. Efficacy of gapmers and 13-GEN2-2-2 AuNPs to target p53

Once assessed the efficacy of the gapmers designed, it was studied their delivery using the 13-GEN-2-2 AuNPs as carriers. The conditions to carry out the incubation with the gapmers are the optimal found in Chapter 3 (**See Oligonucleotides Incubation**) in terms of N/P ratio, pH and buffer concentration. The activity of the gapmers incubated with the particles was evaluated through a

cytotoxicity assay as before, using the scramble sequences with the particles as controls. In this case, the results observed in the assay (**Figure 72**) show similar cell viability in PANC-1 (**Figure 72A**) than previously obtained (**Figure 70A**) with a reduction of 24%. In the case of MDA-MB-231 (**Figure 72B**), a lower viability reduction is observed with respect to the lipofectamine, and null for MCF-7 (**Figure 72C**). On the other hand, the western blot analysis (**Figure 73**) revealed a reduction in the protein expression even higher than without the transfection with the AuNPs (**Figure 71**). In PANC-1 and MCF-7 can be observed a protein expression reduction of 68% and 44%, respectively, a significant reduction compared with the results obtained with the commercial reagent lipofectamine (36% and 32%, respectively). On the other hand, in MDA-MB-231 the reduction in expression of p53 was less pronounced, from 56% with lipofectamine to 32% using the AuNPs. The results highlight the potential use of 13-GEN2-2 as carriers of the combination of gapmers.

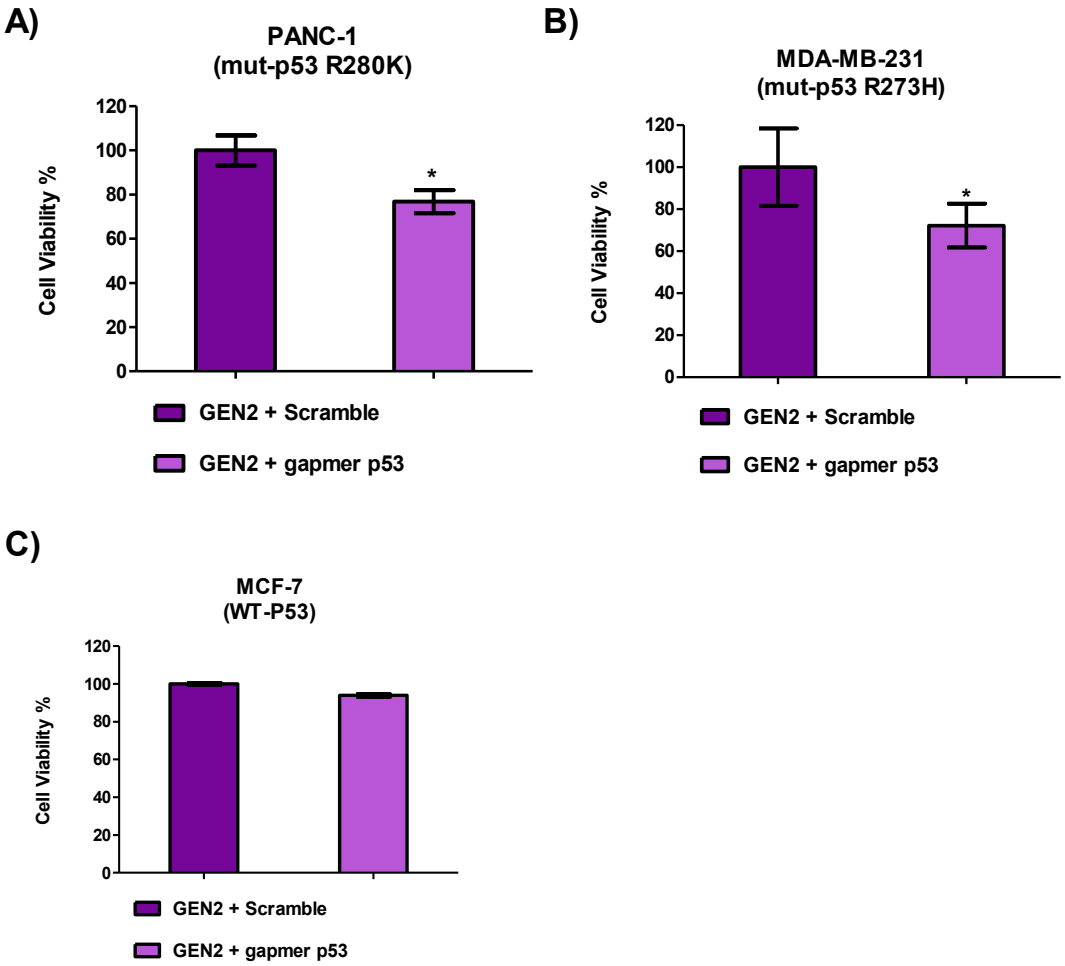

Figure 72. The cells lines treated with 4 designed gapmers against p53 and a scramble sequence as control, incubated overnight with the 13-GEN2-2-2 AuNPs and transfected for 72 hours PANC-1 (mutant p53-R273H) (A), MCF7 (WTp53) (B) and MDA-MB-231 (mutant p53-R280K) (C), after which their viability was assessed with the alamar blue test.

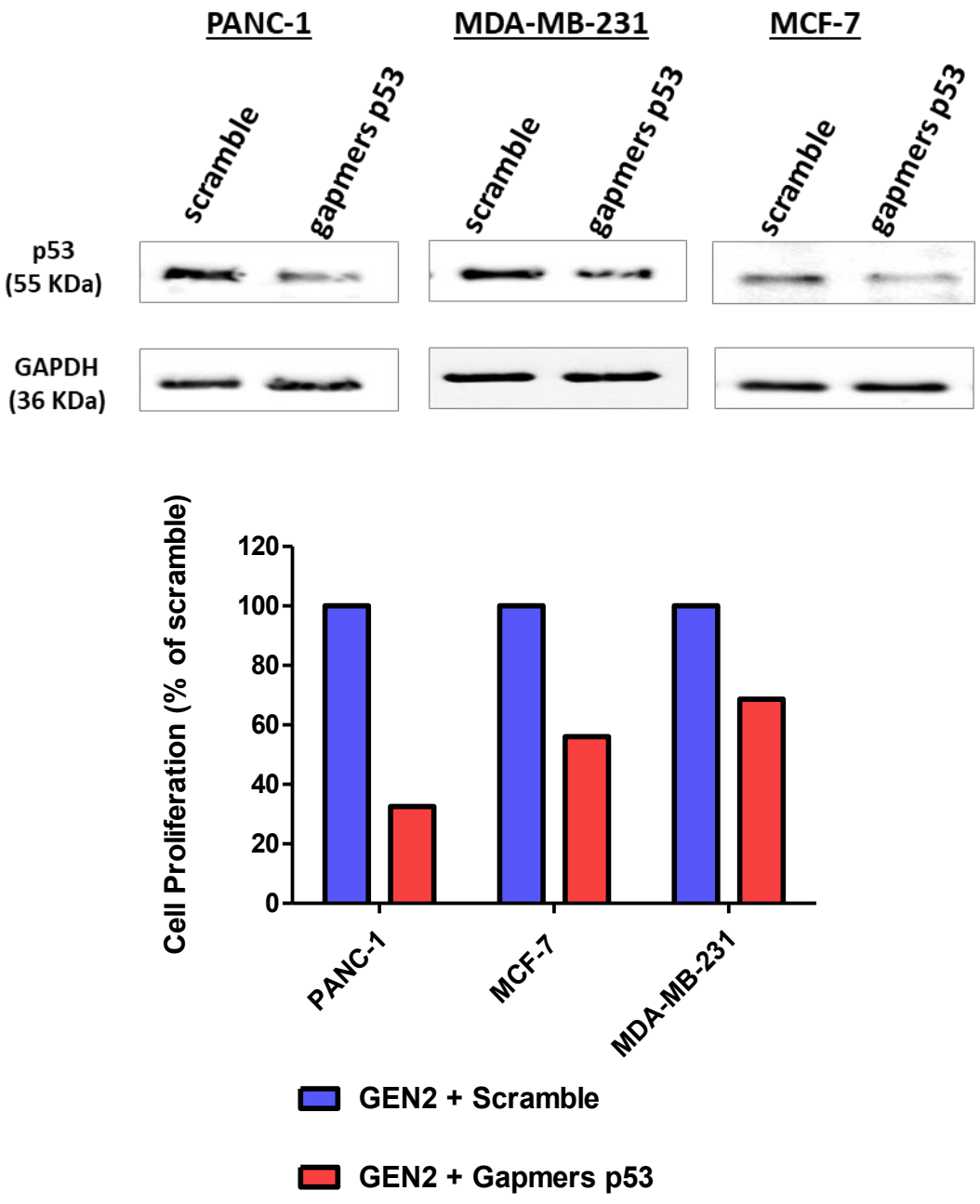

Figure 73. Cell extracts of PANC-1 (mutant p53-R273H), MCF7 (WTp53) and MDA-MB-231 (mutant p53-R280K) quantified by western blots after 72h treatment with designed gapmers to target p53 having a non-therapeutic oligonucleotide, scramble, as control after being incubated with the GEN2 AuNPs. Whole-cell extracts were processed for western blot analysis of the indicated antibodies. GAPDH protein level in the same extract was used as a control loading. The bands shown in the western blot were scanned as digital peaks and the areas of the peaks were reported as fold induction in percentage respect to the untreated.

5.2.5. Effect on the chemoresistance to GEM using gapmers and 13-GEN2-2-2 AuNPs

The role of GEM has already been explored, being able to promote the expression of the mutant p53 protein and, depending on the cell lines, up or downregulate the expression of other proteins that can help in cancer survival and chemoresistance. Also, it has been confirmed the efficacy of the ASO gapmers designed to target mutant and wild-type p53 tumoral cell lines and the potential of the 13-GEN2-2-2 AuNPs to carry and transfect them into them. Because of this, it was explored the combined use of the gapmers incubated with the nanoparticles into the cell lines in the presence of GEM to evaluate if the treatment can overcome the chemoresistance of the tumoral cells. As controls, the scramble sequence and the use of lipofectamine as transfer agents were also used.

First, it was assessed the cytotoxicity assay to observe changes in the cell viability (**Figure 74**). In MCF-7 (**Figure 74C**), it was observed a similar result using lipofectamine or AuNPs, without a reduction in the survival rate in the presence of the gapmers. This was expected, taking into account that the wild type does not present chemoresistance, as was described above. In the case of PANC-1 (**Figure 74A**), it can be observed a significant lower cell viability when the gapmers are transfected, suggesting a synergetic effect comparing reduction obtained with the GEM and gapmers in the previous experiments. A similar behavior can be observed for the MDA-MB-231 cell line (**Figure 74B**), although in this case, the reduction is more prominent using lipofectamine, as was observed in the previous experiments. These experiments suggest that therapeutic targeting of mutant p53 can overcome the resistance to chemotherapy.

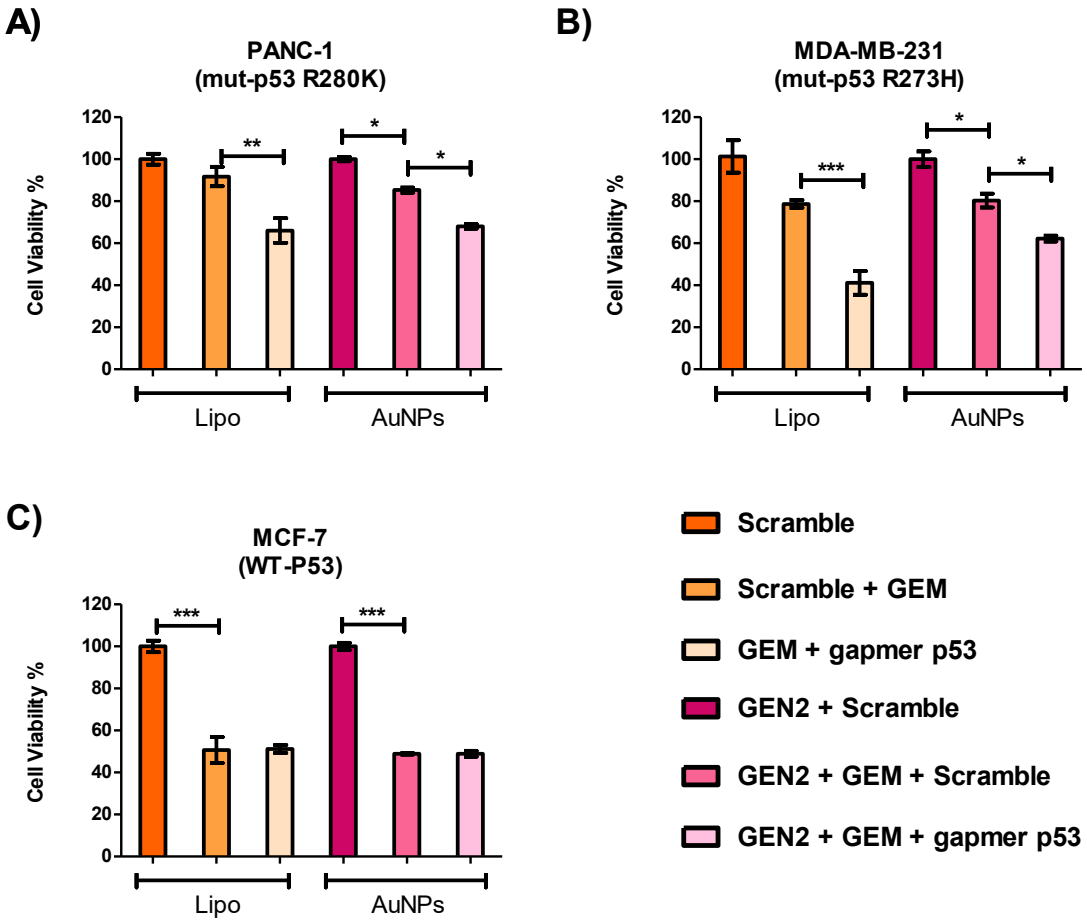

Figure 74. The cells lines containing 4 designed gapmers against p53 and a scramble sequence as control, incubated overnight with the 13-GEN2-2-2 AuNPs and lipofectamine 2000 mix and transfected for 72 hours in the cell lines PANC-1 (mutant p53-R273H) (A), MCF7 (WTp53) (C) and MDA-MB-231 (mutant p53-R280K) (B). After that, their viability was assessed with the alamar blue test.

After that, it was performed a new western blot (**Figure 75**) to observe potential changes in the expression of the protein p53, the anti-apoptotic protein Bcl-2 and the phosphorylation of Ser371-p70S6 protein, related to the activation of mTOR signaling. Again, GAPH protein was used as control. After GEM treatment, the p53 protein expression increased in all the tumoral cell lines as expected, but as can be observed, when the gapmers are added, the expression decreases in a trend similar to the observed in **Figure 73**. The effect is different for each cell line depending on their sensitivity to the gapmers. For instance, mutp53 gets a reduction of 54% in MCF-7 (**Figure 75C**) reverting to the original value. In PANC-1 (**Figure 75A**), the reduction is higher, getting the expression reduced to half the

standard. In MDA-MB-231 (**Figure 75B**), the reduction is about 50%, and due to its larger increment with GEM treatment, the mutp53 expression remains high. Regarding the mTOR signaling, related to the phosphorylation of Ser371-p70S6, the GEM treatment produces a signal enhancement only on the PANC-1, as observed previously. When combined with the nanoparticles and the gapmers, the mTOR signaling was reduced in both mutant p53 cells PANC-1 and MDA-MB-231. In the case of MCF-7, the expression was not affected. In the case of Bcl-2, the protein levels also decreased in PANC-1 and MDA-MB-231 after combined treatment, suggesting the activation of the apoptotic program to overcome chemoresistance to GEM. Again, no changes were observed in MCF-7 regarding the expression of this protein. These data confirm the differences between the chemoresistance behavior among the tumoral lines with mutantp53 and wild-type, and how the gapmer treatment can overcome the chemoresistance to GEM. Also, it has been confirmed the potential of our AuNPs as carriers for their use in this type of therapies.

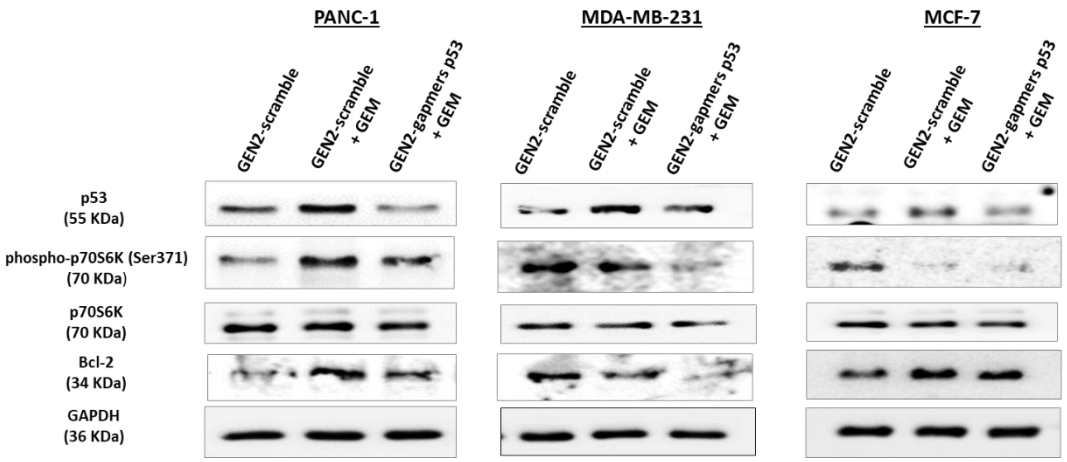

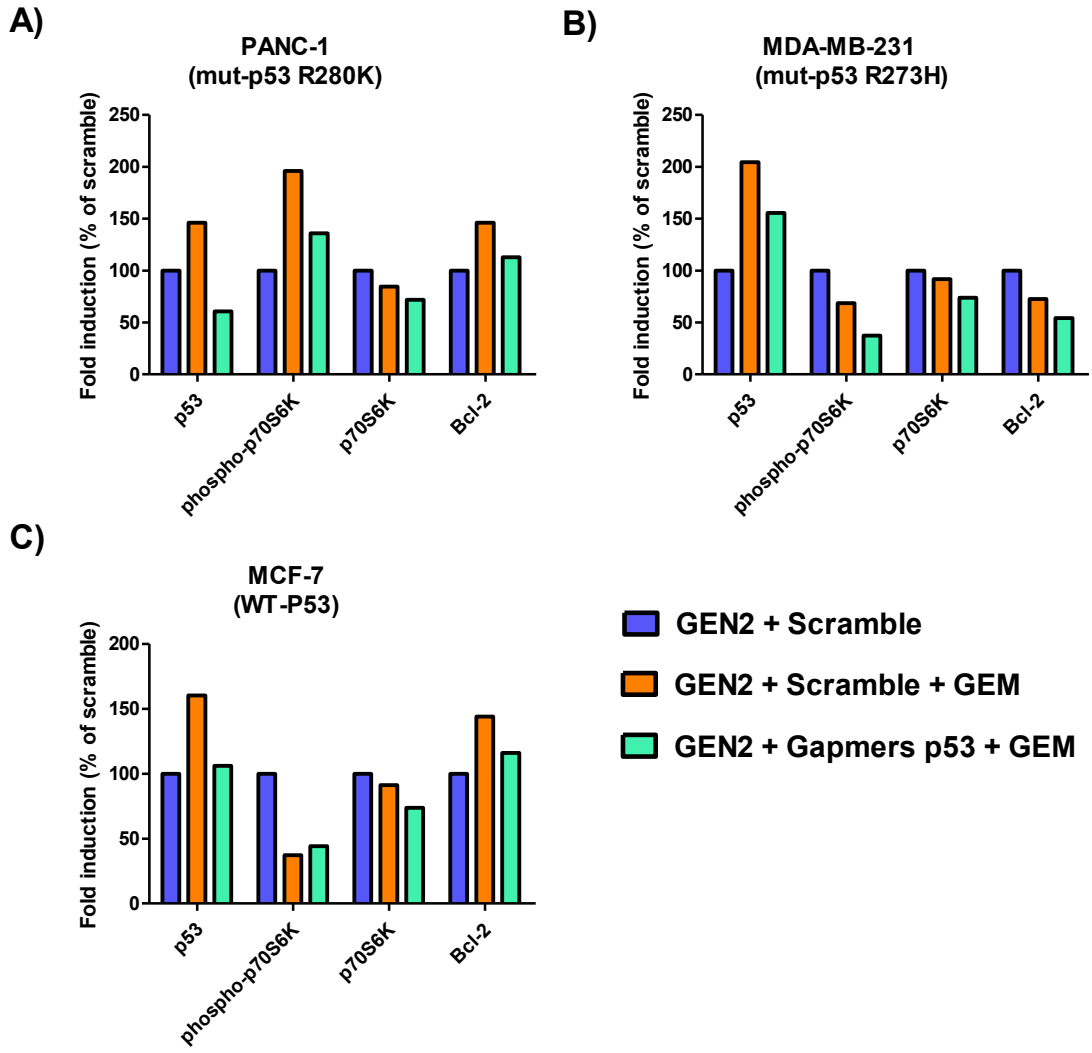

Figure 75. Cell extracts of PANC-1 (mutant p53-R273H), MCF7 (WTp53) and MDA-MB-231 (mutant p53-R280K) quantified by western blots after transfection with 13-GEN2-2-2 AuNPs, 72h treatment using designed gapmers to target p53, having a scramble as control, and in presence of GEM. Whole-cell extracts were processed for western blot analysis of the indicated antibodies. GAPDH protein level in the same extract was used as a control loading. The bands shown in the western blot were scanned as digital peaks and the areas of the peaks were reported as fold induction in percentage respect to the untreated.

5.3. Conclusions

This chapter had the objective to demonstrate that the AuNPs 13-GEN2-2-2 designed and developed herein could be used as carriers for therapeutic purposes. For that, it was selected an emerging problem related to the mutant p53 protein, able to contribute to the maintenance and stimulation of cancer growth and chemoresistance development. Novel therapeutic approaches aim to

downregulate the mutp53 levels through antisense oligonucleotides (ASO). However, they lack good delivery systems, and therefore, we decided to test our nanocarriers for this purpose.

Therefore, 4 gapmers were designed to target mutp53 and being delivered by the 13-GEN2-2-2 AuNPs into two cell lines carrying mutp53 PANC-1 (mutant p53-R273H) and MDA-MB-231 (mutant p53-R280K), and one with the wild type p53 MCF7 (WTp53). We observed that our particles could reduce the levels of p53 proteins in a panel of cancer cells. Interestingly, the cell viability was affected exclusively in cancer cells carrying the mutp53 proteins (PANC-1 and MDA-MB-231), but not the wild-type counterpart (MCF-7). The results suggest that the treatment is safe in cellular models carrying wild-type p53 and can be exploited for its use in cancer cells bearing mutant p53 proteins, expanding their potential *in vivo* applications.

In addition, it was also studied the impact of the therapeutic drug gemcitabine (GEM) on the tumoral cell to understand how to overcome chemoresistance. In this regard, the expression of the mutant and wild-type p53 protein and other markers related to the tumor survival were evaluated. It was observed that GEM leads to an increase of both wild-type and mutp53 protein levels. The expression of other markers depended on the cell line and the type of p53 bearing. In the case of PANC-1, GEM increased the activity of mTOR pathway, detected through the phosphorylation of p70S6 kinase, and the levels of Bcl-2 protein. On the other hand, these two markers were not affected on MDA-MB-231 cancer cells and reduced in wild-type p53 MCF-7 cells. These results may indicate that the different modulation of Bcl-2 and p70S6K are linked to the different p53 status in cancer cells. In the case of PANC-1, the induction of Bcl-2, may partially explain their drug resistance.

Lastly, it was tested the combined treatment of GEM and particles carrying the gapmers to assess if the chemoresistance could be overcome. Remarkably, it was observed an increment in the therapeutic activity of GEM in PANC-1 and MDA-MB-231 cancer cell lines but not in MCF-7 cancer cells, attributed to the differences between the mutp53 and the wild type. Observing the markers, the treatment was able to inhibit mTOR signaling pathway and the anti-apoptotic

protein Bcl-2, thus overcoming drug resistance and helping in the reduction of tumor survival.

Thus, the AuNPs developed can be used as carriers of gapmers to treat tumors with mutant p53 protein, and it is worth highlighting that this approach could be exploited for the development of personalized treatments.

Chapter 6.

Synthesis of CPG

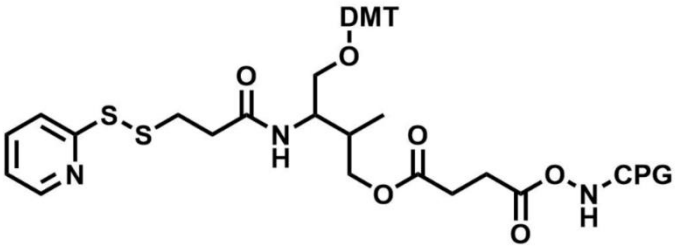

Chapter 6. Synthesis of CPG

6.1. Introduction

The importance of oligonucleotides has already been discussed in this thesis. They have been used to test the binding capacity of the developed AuNPs with a fluorescent oligonucleotide (FAM-PolyT(10)) and to carry out experiments with antisense oligonucleotides (ASO) using AuNPs to block the effect of mutp53.

In the two cases, the oligonucleotides were synthesized in the laboratory through solid-phase chemical synthesis. This type of synthesis allows the obtention of custom-made DNA or RNA oligonucleotides in a fast way. The methodology of the synthesis was based on the phosphoramidite method, which uses phosphoramidite building blocks. This method, developed and optimized since the second half of the 20th century, was fully automated in the 80s and allowed the fast synthesis of oligonucleotides with different lengths and the introduction of useful modifications[202].

6.1.1. Solid-phase chemical synthesis

The solid-phase chemical synthesis of oligonucleotides using the phosphoramidite method displays a complex reactivity and methodology to take into account. First of all, to carry out the synthesis, it is required the use of a solid support, an insoluble particle, in which the oligonucleotide will be synthesized. The most common supports are controlled pore glass (CPG) or polystyrene (PS). Their use is conditioned by the length of the desired oligonucleotides and their amount[203].

The main elements of this method are the phosphoramidite building blocks, which would compose the sequence of the oligonucleotides[204]. The process can be used to prepare DNA and RNA oligonucleotides. The building blocks must have the reactive moieties protected to prevent undesired reactions, for instance, the hydroxyl and amino groups of the nucleobases, and the hydroxyl groups of the sugar rings. Most of the protecting groups are only removed at the end of the whole process. However, the protecting group at the 5’ position in the sugar ring, usually the 4,4’-dimethoxytrityl group (DMT), has to be removed during the

synthesis using mild acid conditions.[205] Therefore, the hydroxyl group can be involved in the phosphoramidite coupling required to build the oligonucleotide. At the 3' hydroxyl group, a as 2-Cyanoethyl N,N-diisopropylphosphoramidite[206] is placed to react with the free hydroxyl group at the 5' position of the bounded nucleotide. The 3'-hydroxyl group is also employed in the modification of solid supports, required to start the synthesis. A summary of the structures mentioned can be found below (**Figure 76**).

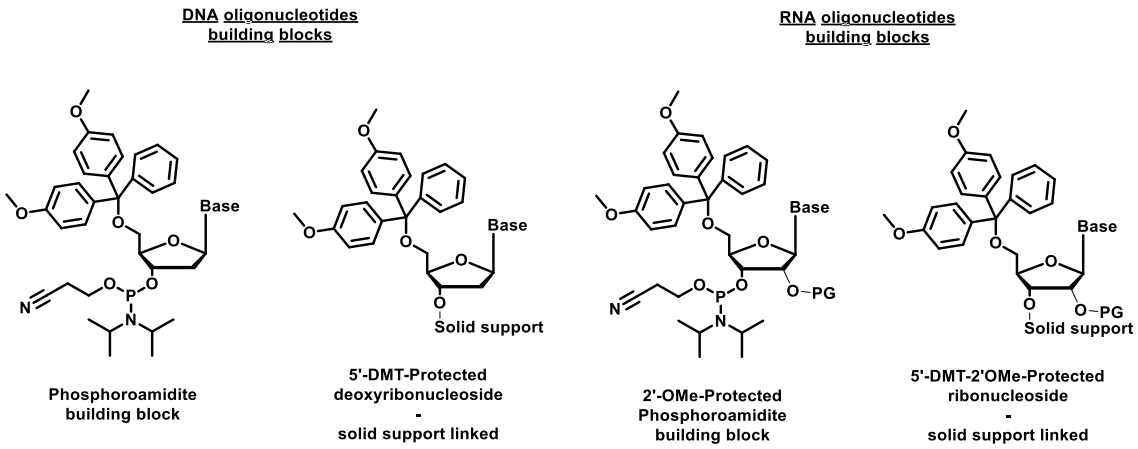

Figure 76. Schematic structures of building block for DNA and RNA oligonucleotides synthesis, including phosphoroamidite building block (DMT at 5' and 2-Cyanoethyl N,N-diisopropylphosphoramidite at 3') and DMT-protected nucleosides covalently linked to the solid support. For RNA nucleosides, the hydroxyl group at 2' has a protective group.

6.1.2. DNA oligonucleotides synthesis

The standard synthesis of DNA oligonucleotides using the phosphoramidite method take place in 3'-5' direction, opposite to the natural synthesis, adding nucleotides one by one following a cyclic procedure[207]. The steps can be visualized in **Scheme 7**.

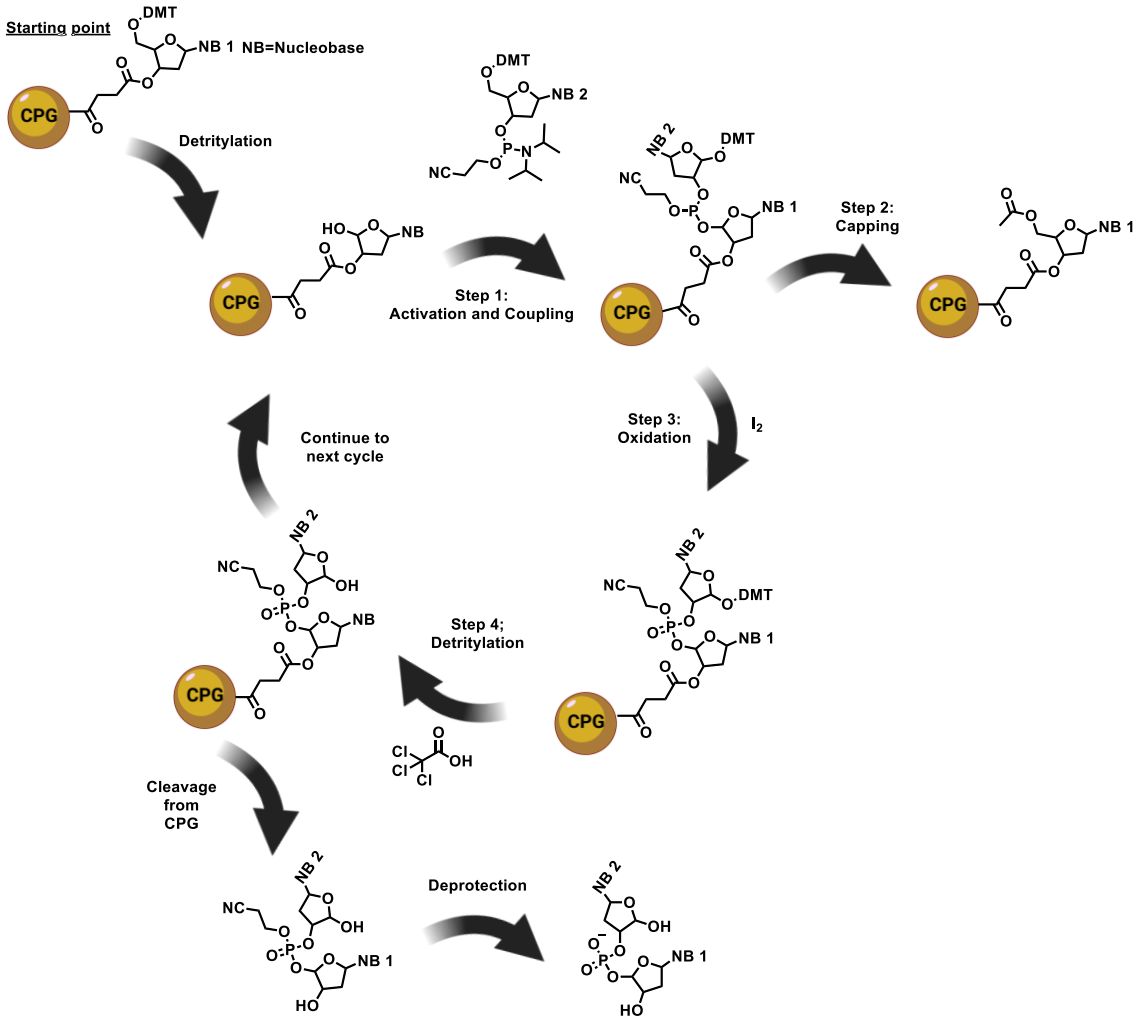

Scheme 7. Schematic phosphoramidite solid-phase synthesis cycle.

The synthesis starts from a deoxyribose molecule attached to the solid support at the 3' hydroxyl group, where the corresponding 5'-DMTr hydroxyl group is deprotected. During this process, the characteristic orange color corresponding to the DMT cation can be observed, which is quantifiable at 495 nm.

After removing the protecting group from 5', the next ribonucleoside of the sequence is inserted as phosphoroamidite. The coupling reaction also requires an activator such as tetrazole or related. This reagent protonates the diisopropyl amino group in the phosphoramidite, making it a better leaving group, and subsequent replacement by the activator. This new functional group is quickly attacked by the 5'-hydroxyl group obtained after the detritylation process, forming a new phosphorous-oxygen bond. Before continuing to the next step, a capping process with acetic anhydride is performed. This stage only affects the unreacted ribonucleoside on the previous to avoid the obtention of oligonucleotides with

wrong sequences. This process requires the addition of *N*-methylimidazole as an activator, in a solution of pyridine and THF, to ensure that the reaction takes place at a basic pH to prevent the deprotection of the DMTr group.

Then, before a cycle starts, it is required to oxidize the phosphorous atom of the phosphite-triester group, from P (III) to P (V). This is needed to prevent undesired reactions due to the reactivity of this group. For instance, it can react under acidic conditions during the detritylation step, while the phosphate generated tolerates it well. The oxidation is performed by the addition of iodine (I_2) in water and pyridine. After this process, the backbone of the oligonucleotide is similar to the natural one, with the difference of the cyanoethyl group, which is considered an intermediary protective group.

After all these steps, a new detritylation reaction is required to remove the DMT group. At this point, two different routes are possible. One is the continuation of the oligonucleotide synthesis, starting the cycle again. The other possibility is the cleavage of the synthesized sequence from the solid support and deprotection to obtain the final oligonucleotide.

The cleavage from the solid support requires the addition of an amine to break a succinyl linker, which presents high stability during the whole process. This step also promotes the removal of the cyanoethyl group and the protecting groups of the nucleobases. In the last step, the oligonucleotide is purified to remove the impurities accumulated during the whole process, which can be done using different methods, such as HPLC, gel filtration or gel electrophoresis.

As it can be observed, the synthesis of oligonucleotides by the phosphoramidite method is a complex procedure but allows the synthesis of any desired DNA or RNA oligonucleotide. It also allows the introduction of any modification in the sequence as long as the corresponding phosphoramidite building block is available. In this regard, to introduce modifications at the 3’ position of the sequence, the most common and efficient approach implies the use of a solid support modified with the molecule of interest.

6.1.3. Covalently linked oligonucleotides to nanoparticles

As mentioned in previous chapters, nucleic acids can be attached to nanoparticles by covalent bonding or by electrostatic interactions, having both advantages and drawbacks. The electrostatic interactions attachment has been demonstrated to be a straightforward method that does not require a linker modification. However, this type of immobilization displays weaker binding, which depending on the experiment, can be either an advantage or a disadvantage. On the other hand, covalent bonding presents stronger and more lasting attachment, but the immobilization process requires the presence of linker modification in the nucleic acid, and the release of the material could be difficult. As in the other approach, these characteristics might be beneficial or counterproductive[208].

The strategy to incorporate a linker to a nucleic acid depends on two factors. First, the properties of the material, which dictates the appropriate linker to use. For example, due to the high affinity of the gold for the sulfur groups[130], a linker that incorporates this type of moiety would provide a good covalent link. This is the case of the experiment of Mirkin *et al.*[209] that developed a trithiol-capped oligonucleotide to functionalize AuNPs. Other structures, as lipoic acid, have also been reported for the conjugation of oligonucleotides and AuNPs[210]. The other factor to consider is the selectivity in the release of the cargo, if the nanomaterial wants to be used for delivery. As has been mentioned, the covalent conjugation of nucleic acid makes it more difficult to be released. Hence it is required the addition of a sensitive crosslinker that allows the release of the genetic material under specific stimuli[211].

6.1.4. Design of a sensitive crosslinker building block for oligonucleotide synthesis

Due to the previous experience with the redox-sensitive linker SPDP, it was planned to incorporate this moiety in a DNA building block. The incorporation of an SPDP crosslinker to the oligonucleotide synthesis would allow its conjugation with any material presenting sulfhydryl groups, which avoid the carrier material limitation. Additionally, it would be sensitive to a reductive environment like the tumoral one, which would provide a selective release of the oligonucleotide[212-157].

During the conjugation of the PDP-oligonucleotide the molecule of 2-pyridinthione[213] will be released, which can be used to quantify the amount of the oligonucleotide conjugated [214].

We planned to place this modification at the 3' position of the oligonucleotide, thus, the best approach required the preparation of a modified CPG containing this system. In this regard, to make this modification compatible with the automated synthesis of oligonucleotides, the SPDP building block should have a structure that mimics the sugar ring present in standard nucleosides (**Scheme 8A**). Particularly, two hydroxyl groups, one secondary to be used in the conjugation with the solid support and another primary, to be protected by DMT. Therefore, threoninol (2-amino-1,3-butanodiol), was used as a mimic of the sugar ring. This molecule has been reported previously as a scaffold for the synthesis of building blocks[215]. This molecule contains a primary amine that can be used to introduce the SPDP moiety easily. Also, this molecule has the primary and secondary hydroxyl groups mentioned before, required for DMTr protection[216] and conjugation with the solid support, respectively. As solid support, it was selected a CPG containing primary amines (CPG-NH_2), which are required for the conjugation with the modification through the formation of an amide bond. This CPG was selected with a pore size of 1000 Å, which is optimum for synthesizing long oligonucleotides. For the conjugation, the linker must bear a carboxylic acid group, as the succinic acid, widely used in the synthesis of building blocks[217]. The target structure is represented in **Scheme 8**.

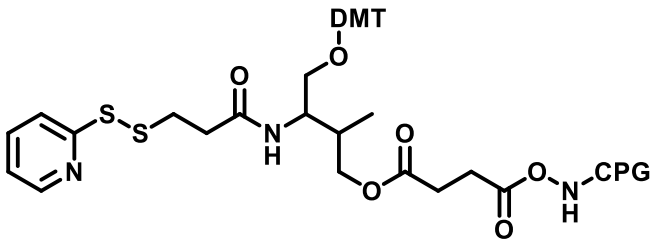

Building block

-

Proposed structure

Scheme 8. Schematic chemical structure of the designed building block with the SPDP crosslinker.

This project aims to prepare the building block mentioned above, its evaluation for the synthesis of an oligonucleotide sequence, and the study of its use in the conjugation of oligonucleotides.

6.2. Results and Discussion

The preparation of oligonucleotides modified with groups that ease the conjugation with biomolecules is of utmost interest because it can provide sophisticated nanostructures with novel properties. However, in many biological applications, covalent immobilization can be a double-edge weapon due to the increased difficulty of releasing the bioactive molecules. Motivated by these limitations, a linker was designed based on the crosslinker SPDP, able to conjugate with molecules presenting a sulfhydryl functional group where the resulting disulfide bond is sensitive to redox stimuli. This way, the oligonucleotide can get immobilized to the carrier and being released in the target tumoral cell. To add this modification to the oligonucleotides, a procedure was designed to attach the SPDP moiety to a solid support based on CPG, which can be employed in the oligonucleotide synthesis.

6.2.1. Synthesis

The synthesis of the designed building block consists of four chemical steps. First, the threoninol and the 3-Mercaptopropionic acid are conjugated by forming an amide bond using the standard NHS approach (**Scheme 9**). The resulting compound **9** presents three crucial functional groups: a) the sulfhydryl group, required to form a labile disulfide bond, b) a primary hydroxyl group, which is selective for DMT protection and c) a secondary hydroxyl group to link with the CPG.

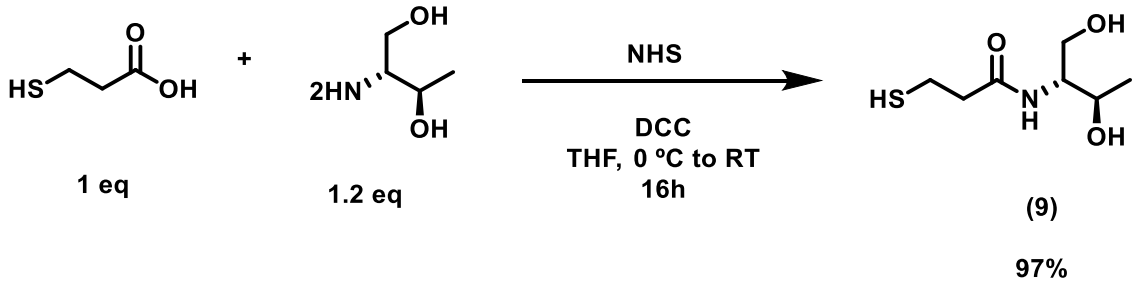

Scheme 9. Synthesis of N-(1,3-dihydroxybutan-2-yl)-3-mercaptopropanamide (9).

The second chemical step consisted of the conjugation of **9** with 2-aldrithiol, to form the disulfide bond with the labile moiety 2-pyridinthione (**Scheme 10**). This molecule itself is produced during the reaction, which displays an intense yellow color, which can be used to follow the reaction by UV. As result, **10** was obtained. Compound **10** cannot present any trace of 2-pyridinthione, to avoid adverse effects in the next stage.

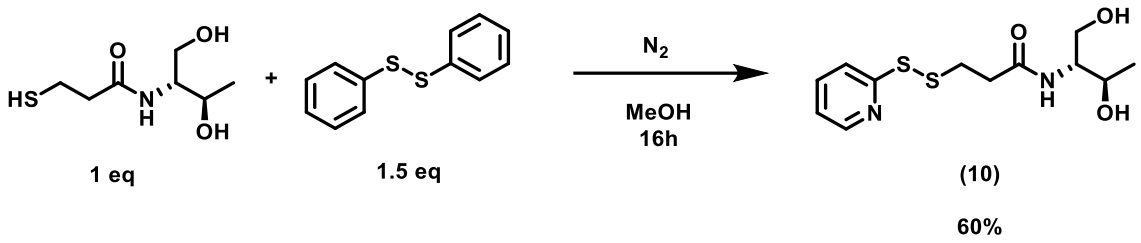

Scheme 10. Synthesis of N-((2R,3R)-1,3-dihydroxybutan-2-yl)-3-(pyridin-2-yldisulfanyl)-propanamide (10).

The third chemical step consisted of the protection with DMT-Cl of the primary hydroxyl group of compound **10** (**Scheme 11**). DMTr-Cl is a water and acid sensible compound[218], hence the reaction has to be performed in anhydrous conditions. In this process, DMAP[219] was used as catalyzer of the reaction and pyridine as solvent to neutralize the acid by-products of the reaction. For the same reason, the purification of the resulting compound **11** had to be performed in neutralized silica gel to avoid the detritylation of the compound.

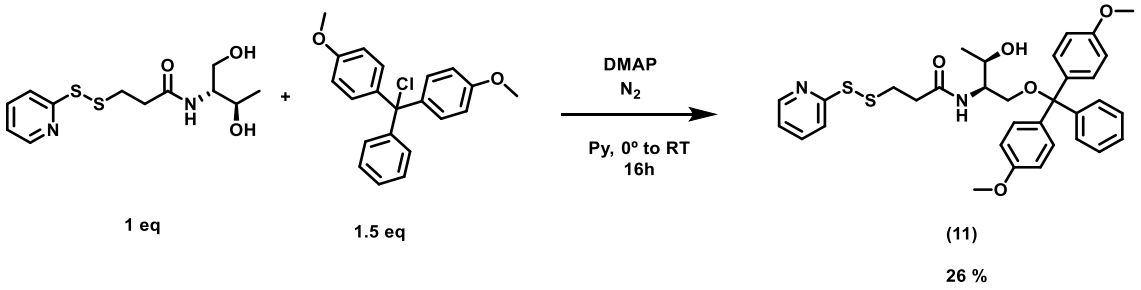

Scheme 11. Synthesis of N-((2R,3R)-1-(bis(4-methoxyphenyl)(phenyl)methoxy)-3-hydroxybutan-2-yl)-3-(pyridin-2-yldisulfanyl)propenamide (11)

In the last chemical step of the procedure, the primary hydroxyl group has to be used to modify the solid support (CPG-NH2). In this case, a crosslinker able to conjugate both molecules were required. To do this, it was selected the succinic acid moiety, which could be obtained through the conjugation of **11** with succinic anhydride (**Scheme 12**). In this step, performed in anhydrous conditions, with

DMAP and pyridine, due to the presence of DMT, the hydroxyl group reacts with the succinic anhydride, producing the succinic acid (**Scheme 12A**). This reaction is not selective between primary or secondary hydroxyl groups; hence it was performed after the DMT protection step. Due to the sensitivity of the DMT, we decided to proceed with the second part of the reaction without further purification and isolation of the compound. The pyridine was removed and then solved in dry ACN, under anhydrous conditions. Then, the succinic anhydride moiety was activated with HOBt (**Scheme 12B**), to convert the carboxylic acid into an ester with a labile group, able to react with the amino group of the CPG. After the conjugation, the CPG (**12**) is thoroughly washed with ACN, DCM and hexane to remove the unreactive compounds (**Scheme 12C**). The CPG is allowed to dry under reduced pressure and a mixture of capping agents A and B in a relation 1:1 to cap all the unreacted amine groups of the CPG, were added. The capping agents are removed through MeOH and ACN washing and the CPG is allowed to dry under reduced pressure.

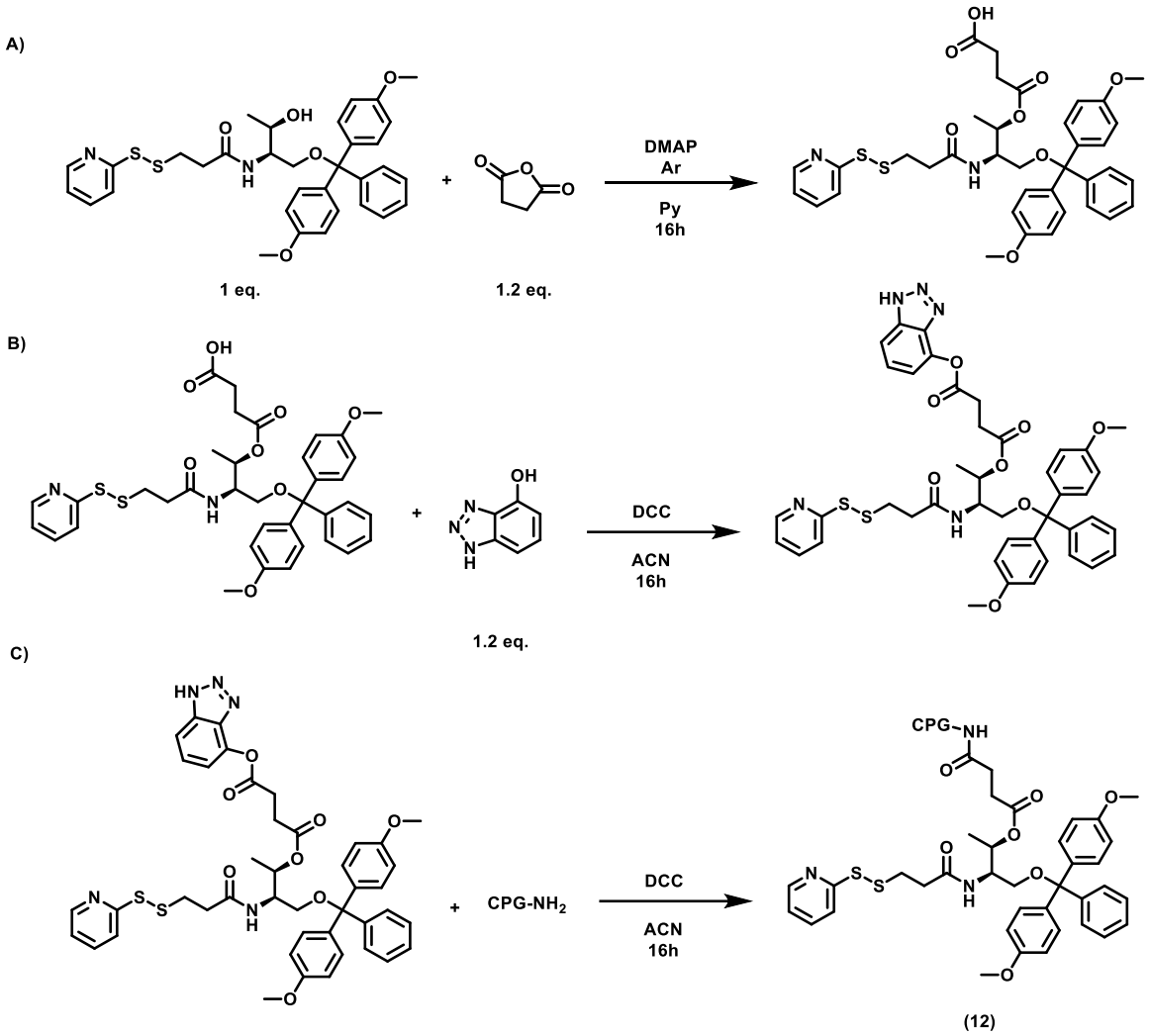

Scheme 12. Synthesis of (4-(((2R,3R)-4-(bis(4-methoxyphenyl)(phenyl)methoxy)-3-(3-(pyridin-2-yldisulfanyl)propanamido)butan-2-yl)oxy)-4-oxobutanamido)CPG (12).

After the reaction, it was calculated the molar amount of building block (with DMTr) attached per gram of CPG, defined as Functionalization (*F* (μmol/g)), using the trityl quantification method, where a selected amount of modified CPG is treated with a detritylation solution to remove the DMTr protective group, and the resulting amount of trityl cation is quantified. *F* (μmol/g) is calculated through Beer-Lambert law as in **Equation 1** based on the data obtained by UV (**Figure 77**). The value of F also determines the yield of the oligonucleotide synthesis. CPGs with F values under 20 were excluded from oligonucleotides synthesis. Different syntheses of CPG with the designed building block gave F values in a range of 14 to 39, being 22 one of the most recurrent values obtained.

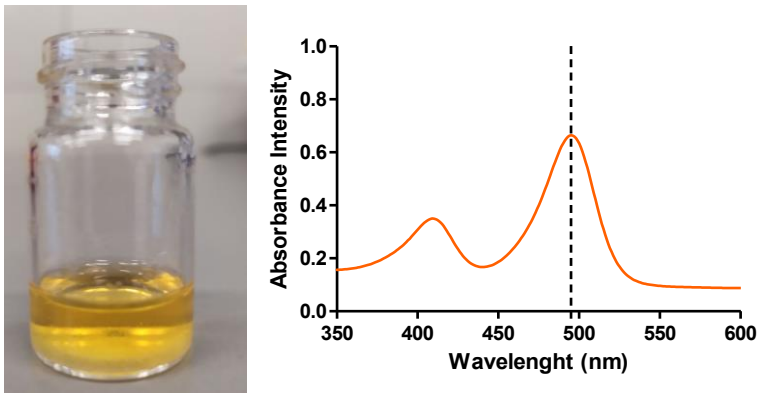

Figure 77. UV characterization of 9.8 mg of the prepared CPG after being treated with 5 mL of a detritylation solution, which was diluted in a ratio 1:80. The absorbance value at 498 nm (0.664) was used in Beer-Lambert law, taking into account a ε_{498}=70000 $mol^{-1}dm^3cm^{-1}$. F (μmol/g) obtained was 38.73.

6.2.2. Oligonucleotide synthesis with the modified CPG

To test the modified CPG, two oligonucleotides were prepared: PDP-PolyT(10)-FAM and PDP-PolyT(10). After their synthesis and purification, they were characterized by UV (**Figure 78**), showing a characteristic band at 265 nm. Using the Beer-Lambert law and the estimated extinction coefficient (ε_{265}= 102560 and 81600 $mol^{-1}dm^3cm^{-1}$ for PDP-PolyT(10)-FAM and PDP-PolyT(10) respectively), it was calculated the concentration of the sequences: 422.45 and 554.33 μM respectively.

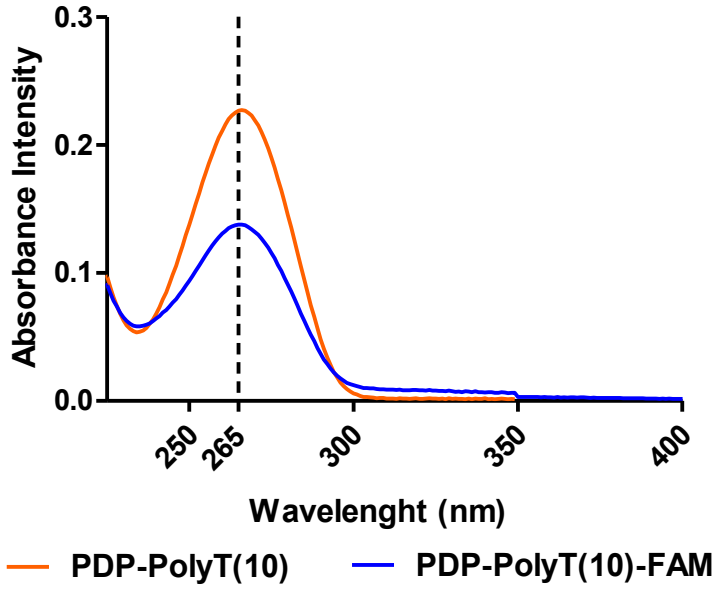

Figure 78. UV-spectra of the oligonucleotides synthesized using the CPG designed: PDP-PolyT(10)-FAM and PDP-PolyT(10). The samples were diluted in a ratio 1:250.

To confirm that after the synthesis the PDP modification was still bound to the oligonucleotide, the samples were treated with GSH. As was mentioned in previous chapters, the GSH allows the interaction with the PDP through its thiol group, releasing a quantifiable pyridine-2-thione molecule in the process. The experiment required the incubation of 10 µL of the oligonucleotide (710.8 nmol), and 990 µL of GSH 10mM (9.9 µmol). The samples were incubated for 16 hours and then studied by UV-Vis spectrophotometry. In this case (**Figure 79**), besides the oligonucleotide band at 265 nm, a second one at 343 nm corresponding to the pyridine-2-thione. When the absorbance ($51.93 \cdot 10^{-3}$) was introduced in the Beer-Lambert law (ε_{343}= 8080 $mol^{-1}dm^3cm^{-1}$), taking into account the dilution, the amount of the released molecule was 640.4 nmol. This value corresponds to 90.1% of the amount of oligonucleotide introduced, confirming that the PDP modification was properly introduced and was sensitive to sulfhydryl groups.

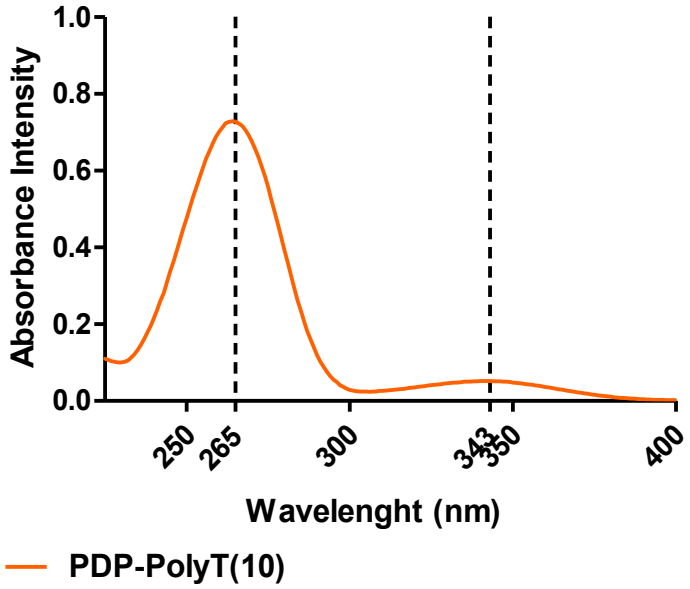

Figure 79. UV-spectra of the oligonucleotide PDP-polyT(10) after being incubated for 24 h with GSH 10 mM. It can observe two different bands at 265 nm, corresponding to the oligonucleotide, and at 343 nm corresponding to the release of the pyridine-2-thione. The samples were diluted in a ratio 1:100.

6.2.3. Covalent conjugation with BSA protein

The oligonucleotide sequences were evaluated for the covalent conjugation with biological systems. Particularly, bovine serum albumin (BSA) protein was used after being treated with Traut's reagent to convert its amino groups into thiols. Thus, 0.2 mg (3.2 nmol) of modified BSA on 200 µL of water was incubated in a molar ratio 1:1 with both sequences PDP-PolyT(10) and PDP-PolyT(10)-FAM. After 16 hours, the samples were dialyzed using a centrifuge filter (10 KDa), and the samples were analyzed by an acrylamide gel retardation assay. It can be observed (**Figure 80**) that for both samples the oligonucleotides can be found in the supernatant. However, in the pellet sample can be observed a band for both oligonucleotides, which could not be possible without the addition of a reducing agent. Another band, found at the pellet well can also be observed, suggesting that part of the oligonucleotides were covalently conjugated. (57% and 65% for the PDP-PolyT(10)-FAM and PDP-PolyT(10) respectively) while the rest was not bonded or well released for other vias.

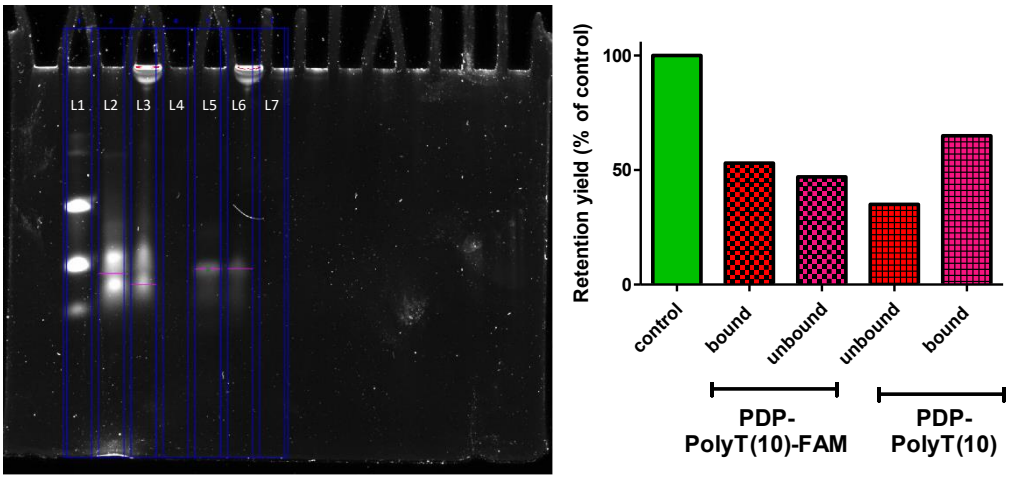

Oligonucleotide	Pellet % (oligonucleotide bonded)	Pellet % (oligonucleotide not-bonded)
PDP-PolyT(10)-FAM	57	43
PDP-PolyT(10)	65	35

Figure 80. BSA conjugated with PDP-PolyT(10)-FAM and PDP-PolyT(10) : gel retardation assay and quantification. L (line) 1: ladder, L2-3-4: PDP-PolyT(10)-FAM and BSA control, pellet, wash (c,p,w), L5-6-7: PDP-PolyT(10)-FAM and BSA c,p,w.

6.3. Conclusions

Oligonucleotide solid-phase synthesis is a powerful tool to create sequences of different types and lengths. The current status of the technique also allows the introduction of modification in any section of the sequence to add properties or enhance them. In this project, it was explored the design of a building block with an SPDP moiety in order to include in oligonucleotides sequence to add the possibility to be covalently attached to systems carrying sulfhydryl groups and quantified the amount introduced.

The building block bearing the PDP modification was carried out by a 4 steps synthetic route, included the immobilization to the solid support CPG. The applicability of the synthesized molecule was tested, in the synthesis of two different oligonucleotides PDP-PolyT(10)-FAM and PDP-PolyT(10). The successful introduction and stability of the SPDP moiety were evaluated by treating one sequence with the reducing agent GSH, showing a 90.1% release of the characteristic pyridine-2-thione. It was also tested the covalent conjugation

with a biological system, the BSA. The first results suggest that the PDP oligonucleotide can get covalently attached to the protein, but it is required further experiments to optimize the process.

These results are an essential for future projects. With the PDP building block synthesized, it can be employed in the synthesis of sequences with more complex structures or for therapies that requires molecules with a covalent attachment or a precise loading.

General conclusions

This thesis has been focused on the role of AuNPs as carriers of biomolecules and their potential use in cancer therapies. With this aim, different approaches based on the modified polymers branched polyethylenimine (bPEI) and polyethylenglycol (PEG) have been applied to develop a novel AuNPs formulations combining a polymeric mixed layer system and layer-by-layer assembly. The results obtained during the process can be highlighted as follow:

- The obtention of AuNPs have been studied through different synthetic routes in order to find the more suitable sizes and morphologies for the surface functionalization of the polymer. It was found that AuNPs of 13 and 23 nm obtained by the Turkevitch's and Frens's method provided the best properties, in terms of stability and reproducibility, to carry out the modification of their surface.

- bPEI and PEG polymers have been modified with a lipoic acid derivative, where dithiolane moiety allows a strong immobilization of the polymers to the surface of the gold particles. In the case of bPEI, two sizes, 2 and 25 KDa, were employed to study their effect in the toxicity and binding affinity. The use of the modified polymers in the functionalization of AuNPs (13 nm and 23 nm), provided 4 formulations stable and highly positively charged (GEN1). Despite their positive potential and low toxicity, the formulations could not produce a good interaction with oligonucleotides.

- A second modification based on the crosslinker SPDP on the bPEIs was explored. The modification presents a redox-sensitive linker that allows their interaction with sulfhydryl groups, introduced in GEN1 AuNPs with the Traut's reagent. This way, a controlled and reversible system to increase the length of the polymer chain was obtained, leading to 8 formulations (GEN2). These AuNPs presents higher potentials and excellent stability. However, the GEN2 formulations obtained using the 23 nm particles were toxic and were discarded. On the other hand, 13 nm systems presented reduced toxicity and their interaction was biomolecules was evaluated. Different parameters as N/P ratio, incubation media pH

and buffer concentration were optimized to improve the binding with different oligonucleotides. These studies revealed that 13-GEN2-2-2, provided the best results.

- The 13-GEN2-2-2 AuNPs were employed in a novel antisense oligonucleotide treatment using a combination of gapmers to target tumoral cell lines carrying mutant p53. This approach reduced the viability in tumoral cells. Moreover, the approach was able to overcome the chemoresistance of the tumoral cell lines.

Additionally, a building block for the solid synthesis of oligonucleotides has been developed. The building block was designed to carry a modification based on the SPDP, which introduced in an oligonucleotide sequence would allow the conjugation with biological systems presenting sulfhydryl. After the obtention of the building block, it was studied its use in the synthesis of oligonucleotides. These oligonucleotides were employed in the conjugation with a protein. The preliminary results are very promising, and further optimization and conjugation experiments will be carried on.

Conclusiones generales

Esta tesis se ha enfocado en el papel de las AuNPs como vehículos de bio-moléculas y su posible aplicación en terapias contra el cáncer. Con este objetivo, se han desarrollado distintas estrategias basadas en el uso de polímero modificados como la polietilenimina ramificada (bPEI) y el polietilenglicol (PEG) para el desarrollo de nuevas estructuras que combinan sistemas polímeros mixtos y ensamblajes capa-capa. Los resultados más destacados obtenidos en el proceso son los siguientes:

- La obtención de AuNPs se ha estudiado mediante distintas rutas sintéticas con el propósito de elucidar los tamaños y morfologías más aptas para su funcionalización con polímeros. Se observó que las partículas de 13 y 23 nm, obtenidas a través de los métodos de Turkevitch y Frens, proporcionaban las mejores propiedades en términos de estabilidad y reproducibilidad para realizar la funcionalización.

- Los polímeros bPEI and PEG se han modificado con derivado del ácido lipoico, portador de una estructura ditiolano, permitiendo una fuerte inmovilización de los polímeros a la superficie del oro. En el caso del bPEI, se emplearon dos tamaños de cadena distintos, 2 y 25 KDa, para estudiar su efecto en la toxicidad y la afinidad en la conjugación de bio-moléculas. El uso de los polímeros modificados para su funcionalización en las AuNPs (13 y 23 nm) dio lugar a la obtención de 4 estructuras estables y con alta carga positiva (GEN1). A pesar de su potencial y baja toxicidad, las estructuras no consiguieron dar buenos rendimientos de conjugación con oligonucleótidos.

- Una segunda modificación basada en el conector cruzado SPDP para el polímero bPEI fue estudiado. La modificación presenta un conector sensible a reacciones redox que permite su interacción con grupos sulfhidrilo, introducidos en las estructuras GEN1 AuNPs mediante el uso del reactivo de Traut. De esta forma se consigue un sistema reversible en el que se puede controlar el crecimiento de la cadena polimérica, obteniendo de esta manera 8 nuevas estructuras (GEN2). Estas AuNPs

presentan un potencial mucho mayor y gran estabilidad. Sin embargo, las estructuras obtenidas con las partículas de 23 nm resultaron ser tóxicas y se descartaron. Por otro lado, los sistemas de 13 nm presentaban una menos toxicidad, por lo que su interacción con bio-moléculas fue evaluado. Distintos parámetros como el ratio N/P, el pH del medio de incubación y la concentración del tampón químico usado se optimizaron para mejorar la interacción con oligonucleótidos. Los estudios revelaron que de los sistemas restantes, las AuNPs 13-GEN2-2-2 proporcionaban los mejores resultados.

- Las AuNPs 13-GEN2-2-2 se utilizaron para en un nuevo tratamiento como oligonucleótidos antisentido, usando una combinación de gapmers para atacar líneas tumorales portadoras de p53 mutado. Esta estrategia consiguió reducir la viabilidad de las líneas tumorales además de superar la quimio resistencia que presentaban.

Adicionalmente se desarrolló un soporte sólido "*building block*" para la síntesis sólida de oligonucleótidos. El "*building block*" se diseñó con una modificación basada en el conector SPDP, el cual aporta la posibilidad de que una secuencia de oligonucleótido pueda interaccionar covalentemente con bio-moléculas si estos presentan grupos sulfihidrilo. Tras la obtención del "*building block*", se estudió su uso en la síntesis de oligonucleótidos, los cuales se emplearon en la conjugación con una proteína. Los resultados preliminares son muy prometedores, aunque es necesario la optimización del proceso y más experimentos en el futuro.

Scientific Contributions

A list of scientific publications obtained through collaborations obtained along the thesis project:

- Royuela, S.; Garcia-Garrido, E.; Martín Arroyo, M.; J. Mancheño, M.; M. Ramos, M.; González-Rodríguez, D.; Somoza, Á.; Zamora, F.; L. Segura, J. *Uracil grafted imine-based covalent organic framework for nucleobase recognition*. ***Chem. Commun.***, **2018**, **54**, 8729-8732. *https://doi.org/10.1039/C8CC04346A*

- Prajapati, R.; Garcia-Garrido, E.; Somoza, Á. *Albumin-Based Nanoparticles for the Delivery of Doxorubicin in Breast Cancer. Cancers* ***2021****, 13, 3011. https://doi.org/10.3390/cancers13123011*

- Garcia-Garrido, E.; Cordani, M.; Somoza, Á. *Modified gold nanoparticles to overcome the chemoresistance to gemcitabine in mutant p53 cancer cells. (Publication under review)*

Chapter 7.

Materials and Methods

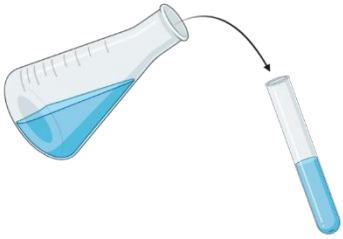

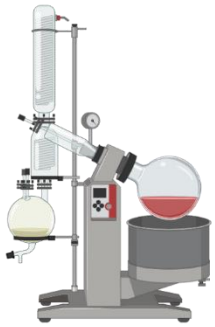

Chapter 7. Materials and Methods

7.1. Materials

The materials used along the research project are: gold (III) chloride trihydrate ($HAuCl_4$), trisodium citrate, silver nitrate, (R)-(+)-α-Lipoic acid (LP), branched polyethylenimine (MW. 2000 and 25000) (bPEI), N,N′-Dicyclohexylcarbodiimide (DCC) and N-Hydroxysuccinimide (NHS), citric acid, acrylamide, Tris-Borate-EDTA (TBE) and Tetramethylethylenediamine (TMED), L-threoninol, 3-mercaptopropionic acid, 2-aldithriol, 4-Dimethylaminopyridine (DMAP), succinic anhydride and Hydroxybenzotriazole (HOBt) were purchased in Sigma Aldrich. L-threoninol and 4,4'-Dimethoxytrityl chloride (DMTr-Cl) were purchased in abcr GmbH. NH2-CPG, CAP MIX A (Acetic anhydride (400 µL)/ Pyridine (600 µL)/THF (500 µL)), CAP MIX B (1-Methylimidazol (400 µL)/ THF (1 mL)) were purchased by Biosearch Technologies. Alpha-amino-omega-hydroxy poly(ethylene glycol) (NH2-PEG-OH MW.3091) (PEG) was provided by Iris Biotech GMBH. Spectra/por 3.5 and 10 KDa tubing membranes were purchased in Fisher. Dulbecco's Modified Eagle's (DMEM) medium, streptomycin–penicillin (100X), fetal bovine serum (FBS), l-glutamine (100X), trypsin (10X), phosphate-buffered saline (PBS) and deuterated solvents were purchased from VWR. Gemcitabine was purchased from Fluorochem. Lipofectamine 2000 and Opti-MEM was purchased from Thermo Fisher Scientific Milli-Q water was used in the synthesis and characterization. All solvents were purchased in Scharlab. The chemicals and the reagents have been used as received following the indications reported without further purification.

All reactions were monitored by thin-layer chromatography that was performed on pre-coated sheets of silica gel 60, and flash column chromatography was done with silica gel 60 (230-400 mesh) of Scharlau. Eluting solvents are indicated in the text. Column Chromatography for acid-sensitive compound: Deactivation of silica gel for column chromatography. The silica gel was prepared by treating it with a mixture of $CHCl_3$/NEt_3 100/1. Thereafter, solvents were removed under reduced pressure, and the resulting dry silica was used, when necessary, with the appropriate solvent. All the synthesized compounds have been analyzed by 1H and 13C using a Bruker DPX (400 MHz) spectrometer and Bruker DPX (500

MHz) at SidI-UAM Mass spectra were obtained at SIdI-UAM using electronic ionization (EI), electrospray ionization (ESI) and matrix-assisted laser ionization (MALDI).

7.2. Instrumental Analysis and Assay Protocols

7.2.1. TEM

AuNPs were visualized using a 100 KeV JEM1010 (Jeol) at CBMSO-CSIC. Samples were prepared by placing a copper grid (AGAR.) over one drop of AuNPs for 2 min and drying the excess of the sample. The average diameter value was determined through an automated analysis of TEM images with Fiji ImageJ software.

7.2.2. DLS characterization

DLS and Zeta potential measurements were performed using a Malvern Zetasizer Nano ZS. The scattered light was measured at an angle of 175° for DLS measurements and at 12.8° for zeta potential measurements using disposable folded capillary cells. The temperature of each sample was stabilized at 25±0.1 °C for 45 s before the measurement. The measurements are performed using 1 mL of the gold nanoparticles without any dilution. For hydrodynamic size measurements, the polydispersity of the sample is taken into account to discard samples with high heterogeneity. A normalized size and zeta potential distribution are obtained from three different measurements, and the mean value is indicated.

7.2.3. UV spectroscopy

UV-Vis spectra were recorded in a quartz cuvette using a CARY 5000 spectrometer from Agilent at 25 °C. The measurements are performed using a dilution 1:10. A normalized band is obtained from three different measurements.

7.2.4. pH-measurements

pH measurements were performed using a Mettler Toledo FiveEasy Plus pH-meter. The pH-meter was calibrated using 4.01, 7.01 and 10.01 pH standard buffers. An average value is obtained from three different measurements.

7.2.5. Functionalization protocol

7.2.5.1. GEN 0.5 & 1

The functionalization of all the AuNPs was always performed in a volume of 1 mL at the same concentration (10 nM). AuNPs at higher concentrations were diluted to 10 nM with Milli-Q water. AuNPs at lower concentrations were concentrated through centrifugation at 4 ºC and 13.2K rpm. For each functionalization, the corresponding amount of the modified polymer was added to the AuNPs, followed by vigorous agitation for 1 min using a vortex shaker. Then, the AuNPs mixture was left for 16h at room temperature and under gentle agitation. After this time, the sample was centrifugated twice at 4 ºC and 13000 rpm for 30 min and the supernatant was separated from the pellet to remove the unbonded polymer. The sample was then stored at 4 ºC until measurements or further functionalization were executed.

7.2.5.2. GEN 2 & 3

The functionalization of all the AuNPs were always performed in a volume of 1 mL at the same concentration (8 nM). AuNPs at higher concentrations were diluted with Milli-Q water until reach this concentration. AuNPs at lower concentrations were concentrated through centrifugation at 4 ºC and 13.2K rpm. For each functionalization, the AuNPs were incubated, for at least 6 hours, with 2-iminothiolane in a ratio of bPEI/2-iminothiolane of 1:17 and 1:204 for bPEI 2 and 25 KDa, respectively. After that, the corresponding amount of PDP-bPEI 2 or 25 KDa was added to the AuNPs, followed by a vigorous agitation for 1 min using a vortex shaker. Then, the AuNPs mixture was left for 16h at room temperature and under gentle agitation. After this time, the sample was centrifugated twice at 4 ºC and 13.2K rpm for 30 min and the supernatant was separated from the pellet and the molecule pyridine-2-thione was characterized by UV to quantified the yield of the reaction (343 (ε=8080 $mol^{-1}dm^3cm^{-1}$)). The AuNPs were then storage at 4 ºC until measurements or further functionalization were executed.

7.2.6. Oligonucleotides incubation and Gel Retardation assay

The oligonucleotides were prepared using a Mermade 4 DNA synthesizer and purified using Biosearch columns. The sequences of the oligonucleotides employed are described in **Table 3**. Nucleosides in bold contain a 2'-OMe modification corresponding to a gapmer pattern. Entries 9 and 10 correspond to the oligonucleotides synthesized with the SPDP modification through the use of the CPG designed.

Any oligonucleotide was incubated with the AuNPs following the same standards. For each experiment, variable factors such a N/P ratio (7.53 × weight ratio of PEI/DNA), pH or buffer concentration is specified in the corresponding section with exception of the gapmer experiments (**See section below**). Before the oligonucleotide addition, the AuNPs were concentrated through centrifugation at 4 °C and 13.2K rpm, and the supernatant was removed. The oligonucleotides are then added to the pellet and incubated for 12 hours at room temperature. Then, the nanoparticles are centrifuged at 4 ºC and 13.2K rpm, and both pellet and supernatant are separated for its evaluation through a gel retardation assay. The samples (10 µL) are mixed with a gel loading buffer 2x (10 µL) at room temperature for 30 min. Then they were electrophoresed through a 12% (w/v) acrylamide gel in TBE 1X (tris base-boric acid-EDTA) buffer at 120 mV and 500mA for 60 min. The gel was analyzed on a BioRad GelDoc Go gel documentation system.

Entry	Name	Sequence	Type	Chapter
1	PolyT(10)-FAM	5'-Fluorescein-TTTTTTTTTT-3'	DNA	2,3
2	AS1411-FAM	5'-Fluorescein-GGTGGTGGTGGTTGTGGTGGTGGTGG -3'	DNA	3
3	Scramble 1	5'-**ACGTG**ACACGTTCGGA**GAATT**-3'	Gapmer	4
4	Scramble 1	5'-**TGCGC**TCCTGGACGT**AGCCT**-3'	Gapmer	4
5	Gapmer-p53.1	5'-**CAAAG**CTGTTCCGTC**CCAGT**-3'	Gapmer	4
6	Gapmer-p53.2	5'-**GACTC**CAGTGGTAA**TCTAC**-3'	Gapmer	4
7	Gapmer-p53.3	5'-**GAAAT**TTGCGTGTG**GAGTA**-3'	Gapmer	4
8	Gapmer-p53.4	5'-**GGACA**TACCAGCTTAG**ATTTT**-3'	Gapmer	4
9	PDP-PolyT(10)	5'-Fluorescein-TTTTTTTTTT-PDP-3'	DNA	5
10	PDP-PolyT(10)-FAM	5'-Fluorescein-TTTTTTTTTT-PDP-3'	DNA	5

Table 3. Oligonucleotides used in this research.

7.2.6.1 Incubation of Gapmers with nanoparticles

AuNPs concentration was fixed at 1 nm at a volume of 50 µL. The N/P ratio was fixed at 80 for the combination of the gapmer/scramble sequence designed. Both particles and oligonucleotides are incubated for 1 hour at room temperature, after which a citrate buffer at p*H* 3.5 is added. Its volume was 10% of the final volume of the mixture of AuNPs and oligonucleotides with a final concentration of 0.75 mM. Once the buffer was added, the samples were incubated for 12 hours. Then, the nanoparticles were centrifuged 4 ºC and 13.2K rpm to remove the unbound oligonucleotides.

7.2.7. Cell lines and culture conditions

Pancreatic adenocarcinoma PANC-1 & PANC-1 (mutant p53-R273H) and breast cancer MCF-7 & MCF-7 (WTp53) cell lines were purchased from American Type Culture Collection (ATCC, Rockville MD) and cultured in low-glucose DMEM medium with 10% FBS, 1% streptomycin–penicillin and 1% l-glutamine at 37 °C in a Binder CB210 incubator (5% CO2). Triple-negative breast cancer MDA-MB-231 (mutant p53-R280K) cell line was purchased from American Type Culture Collection (ATCC, Rockville MD) and cultured in high glucose-glucose DMEM medium with 10% FBS, 1% streptomycin–penicillin and 1% l-glutamine at 37 °C in a Binder CB210 incubator (5% CO2). All the procedures were performed inside a laminar flow hood Telstar CV-30/70 (Telstar, Terrassa, Spain).

Entry	Cell line	Tumor tissue	P53 mutation	Chapter
1	PANC-1	Pancreas	-	2,3
2	MCF-7	Breast	-	2,3
3	PANC-1	Pancreas	R273H	4
4	MCF-7	Breast	Wild type	4
5	MDA-MB-231	Breast	R280K	4

Table 4. Status of cell lines used in this study.

7.2.8. Alamar Blue Viability Assay

A stock solution of resazurin sodium salt (Sigma-Aldrich, St. Louis, MO, USA) (1 mg/mL) in PBS was diluted 1% (*v*/*v*) in complete RPMI medium and added to the cells. After 3 h in the incubator (37 °C), the fluorescence was measured at 25 °C in a plate reader Synergy H4 Hybrid reader (BioTEK), λ_{ex} = 550 nm, λ_{em} = 590 nm. The fluorescent intensity measurements were processed using the following Equation: % Cell viability = ((Sample data − Negative control)/(Positive control − Negative control)) × 100. The positive control corresponds with untreated cells. A resazurin solution without cells was used as negative control.

7.2.9. GSH concentration-time dependent experiment

The incubation of GSH, as reductor agent, with the GEN2 AuNPs (13 nm) was performed as follows. In parallel, 1 mL volume of GEN2 AuNPs were added GSH until reach a concentration of 1 μM and 1mM, respectively. The AuNPs were left at RT under gentle shaking for 10, 20, 30, 60, 120, 330, 400 and 1440 min. After each time, the AuNPs were centrifuged at 4 ºC and 13'2 rpm for 30 min, then the supernatant was removed. The AuNPs were resuspended in 1 mL of water and DLS characterized.

7.2.10. Fluorescence of polyT(10)-FAM

Cells were plated in 96 or 12-well plates (5× 10^3 or 8 × 10^4 cells/well, respectively) and 24 hours later were treated with GEN2-AuNPs functionalized with 100 pmol of polyT(10)FAM or transfected by Lipofectamine 2000 as described above. After 24 hours of treatment, cells were washed with 1X PBS (Phosphate Buffered Saline), pH 7.4 (VWR) and the fluorescence was analyzed. For microscopy images, the nucleus was stained with Hoechst 33342 and FAM fluorescence was measured using a Leica DMI3000 M inverted microscope (Leica, Wetzlar, Germany) at 20 × magnification. Images were analyzed using ImageJ software (NIH Image, Bethesda, MD). FAM fluorescence was also measured using a multimode plate reader (λ_{ex}=395nm and λ_{em}=509 nm) (Synergy H4 Hybrid reader (BioTEK).

7.2.11. Oligonucleotide Transfection

Exponentially growing cells were seeded at 5 × 10^3 cells/well in 96-well plates or at 1 × 10^4 cells in 12-well plates. Wild-type and mutant p53 protein expression was transiently knocked down by transfection with a mixture containing 60 pmol of gapmers targeting different exons of TP53 gene. Scramble sequences as non-silencing control were used as a negative control. The silencing transfections were carried out for 48 h using Lipofectamine 2000 (Life Technologies), according to the manufacturer's instructions. Cells were transfected by gapmers at a final concentration of 50 nM using Lipofectamine 2000 (Life Technologies), according to the manufacturer's instructions. For fluorescence studies, PANC-1 cancer cells were transfected with 100 pmol of polyT(10)FAM using Lipofectamine 2000.

7.2.12. Chemotherapy

Gemcitabine stock solution was prepared at 100 μM in DMSO. Then different concentrations of GEM (1, 2, 4.5, 10 and 20 μM) were prepared in DMEM medium. It was incubated for 24 h with the cells, then washed three times with PBS and DMEM medium was added. After an additional time of 24 or 48 h, the viability assay was carried out as described in Section 2.3.11.

7.2.13. Nanoparticles Treatment

A volume of 100 μL functionalized AuNPs were added in Opti-MEM (500 μL, total volume). The cells were incubated for 24 h, washed with PBS and DMEM medium was added. 24 or 48 hours later, the viability was assessed, as described in Section 2.3.11.

7.2.14. Combination Treatment

In this case, the nanoparticles were incubated as previous section. After 5 h GEM (4.5 μM/well) was added and incubated for an additional 24. Then, the cells were washed with PBS and DMEM medium was added. The cell viability was evaluated after their incubation for an additional 24 or 48 hours.

7.2.15. Western blot analysis

Cells were harvested, washed in PBS, and re-suspended in RIPA buffer (Tebu-BIO #AR0105) in the presence of a protease inhibitor cocktail (Thermo Scientific™ #A32955). After incubation on ice for 30 min, the lysates were centrifuged at 14,000 × g for 10 min at 4 °C and the supernatant fractions were used for Western blot analysis. Protein concentration was measured by Bradford reagent (Bio-Rad protein assay) using bovine serum albumin as a standard. Protein extracts (30 μg/lane) were resolved on a 10% SDS-polyacrylamide gel and electro-blotted onto PVDF membranes (Amersham™ Protran™ 0.45um NC). Membranes were blocked in 5% low-fat milk in TBST or 5% BSA (50 mM Tris pH 7.5, 0.9% NaCl, 0.1% Tween 20) for 1 h at room temperature and probed overnight at 4 °C with a rabbit polyclonal anti-Bcl-2 (1:1000) (Cell Signaling, #2872), rabbit polyclonal anti-p70 S6 Kinase (1:1000) (Cell Signaling, #9202), rabbit polyclonal anti-phospho- p70 S6 Kinase (Ser371) (1:1000) (Cell Signaling,

#9208), mouse monoclonal anti-GAPDH (1:1000) (Santa Cruz, sc-47724) and mouse monoclonal anti-p53 (1:1000) (Santa Cruz, sc-47698). Horseradish peroxidase conjugated anti-mouse or anti-rabbit IgGs (1:5000 in blocking solution) (Santa Cruz, Spain) were used as secondary antibodies. Immunodetection was carried out using Bio-Rad chemiluminescent substrates and recorded using a ChemiDoc (Synergy). ECL results were scanned and the amount of each protein band was quantified using NIH Image J software.

7.2.16. CPG functionalization (F) quantification

The CPG loading was calculated using the trityl quantification method. To 10 mg of the modified CPG was added 5 mL of a detritylation solution (3 mL of perchloric acid and 2 mL of EtOH) and stirred for 1 h. Then, 50 µL of the mixture was diluted to 1mL, and the absorbance was measured at 498 nm (ε_{498}=70000 $mol^{-1}dm^3cm^{-1}$) to quantify the trityl cation. Functionalization (F) (µmol/g), defined as the molar amount of building block attached per gram of CPG, was determined by Beer-Lambert law (**Equation 1**).

$$\boldsymbol{F = \frac{A * D}{\varepsilon * b} * \frac{V}{m} * (10^6)}$$

Equation 1. Equation to calculate *F* (µmol/g), where *A* is the absorbance value obtained at 498 nm from the trityl cation, *D* is the dilution coefficient used in the cuvette, *b* (cm) is the length of the optical path, *ε* ($mol^{-1}dm^3cm^{-1}$) is the molar extinction coefficient, *V* is the volume taken to prepare the solution (L) and *m* (g) is the amount of modified CPG used.

7.3. Experimental section

7.3.1. Chapter 1

7.3.1.1. Synthesis AuNPs 13 nm (Turkevitch's method)[92]

To 100 mL of boiling water is added gold (III) chloride (34 mg, 0.1 mmol) under vigorous stirring. Once the gold salt is dissolved and the temperature of the solution stable, a solution of sodium citrate (118 mg, 0.46 mmol) in 10 ml of water is added. The mixture is stirred at the same temperature for 15 min and then is stirred at room temperature for 12 hours. Finally, the gold nanoparticles are filtrated through a 0.45 µm porous filter and stored in the fridge.

7.3.1.2. Synthesis AuNPs 35 nm (Turkevitch's method)[92]

To 50 mL of boiling water is added gold (III) chloride (5 mg, 0.015 mmol) under vigorous stirring. Once the gold salt is dissolved and the temperature of the solution stable, a solution of sodium citrate (2.1 mg, 0.008 mmol) in 1 ml of water is added. The mixture is stirred at the same temperature for 15 min and then is stirred at room temperature for 12 hours. Finally, the gold nanoparticles are filtrated through a 0.45 µm porous filter and stored in the fridge.

7.3.1.3. Synthesis AuNPs 23 nm (Frens' method)[37]

To 150 mL of boiling water is added gold (III) chloride (13 mg, 0.326 mmol) under vigorous stirring. Once the gold salt is dissolved and the temperature of the solution stable, a solution of sodium citrate (154.8mg, 0.6 mmol) in 15 ml of water is added. The mixture is stirred at the same temperature for 20 min and then is stirred at room temperature for 12 hours. Finally, the gold nanoparticles are filtrated through a 0.3 µm porous filter and stored in the fridge.

7.3.1.4. Synthesis AuNPs 13 nm (premixing method)[96]

To 0.5 mL of water is added gold (III) chloride (5 mg, 0.015 mmol), a solution of 42.5 µL of silver nitrate (0,1 wt %, 0.25 nmol) and a solution of 1.5 ml of sodium citrate (15 mg, 0.058 mmol) in water under vigorous stirring. Then, water is added to the mixture to bring the total solution volume to 2.5 ml. Then, this mixture is injected into 47.5 mL of stirring boiling water. The reaction is stirred for 30 min and then left stirring at room temperature for 6 hours. Finally, the gold nanoparticles are filtrated through a 0.45 µm porous filter and stored in the fridge.

7.3.2. Chapter 2

7.3.2.1. Synthesis of the 2,5-dioxopyrrolidin-1-yl-5-(1,2-dithiolan-3-yl)pentanoate) (LP-NHS) [220] (1)

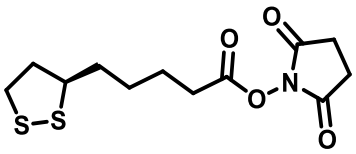

To a solution of lipoic acid (3.6 g, 17.4 mmol) in dichloromethane (DCM, 65 mL) at 0 °C, a solution of N-hydroxysuccinimide (NHS) (2.2 g, 20.9 mmol) and dicyclohexylcarbodiimide (DCC) (4.32 g, 20.9 nmol) in tetrahydrofurane (THF) (15 mL) was added under vigorous stirring. Then, the reaction was allowed to warm up to room temperature and the mixture was stirred for 16 hours. Finally, the white precipitate was filtrated and the solvent removed under vacuum. The solid was dissolved in the minimum amount of ethyl acetate (AcOEt) and stored in the fridge for 6 hours. The newly formed precipitate was removed as before. The solvent was removed again under vacuum, obtaining the desired lipoic ester (98% of yield, 5.17 g) derivative as a yellow oil. **^{1}H NMR** ($CDCl_3$, 400 MHz): δ 3.54 (dq, 1H), 3.11 (m, 2H), 2.8 (s, 4H), 2.57 (t, 2H), 2.41 (m, 1H), 1.88 (m, 1H), 1.72 (m, 2H), 1.67 (m, 2H), 1.52 (m, 2H). **^{13}C NMR** ($CDCl_3$, 101 MHz): δ 169.27, 168.44, 56.19, 40.25, 38.73, 34.78, 30.87, 28.32, 25.69, 24.45. **MS (EI)**: *m/z* calculated for $C_{12}H_{17}NO_4S_2$ (M^+) 303.05, found 303.05.

7.3.2.2. Synthesis of LP-bPEI (2000MW)[221] (2)

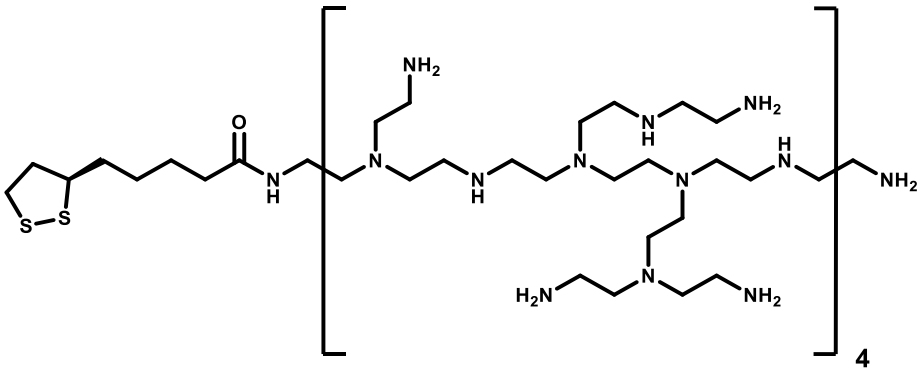

The procedure for the synthesis of LP-bPEI (2000 MW) is based on the synthesis of Zong *et al.* with some modifications. To a stirring solution of lipoic acid ester

(9.37 mg, 0.0315 mmol) in THF (0.5 mL) at 0 °C a solution of polyethylenimine (2000 M.W.) (42 mg, 0.021 mmol) in THF was added. Once a grey oil-like compound appears, the solvent is removed under vacuum and re-dissolved in methanol (MeOH, 2 mL). The product was purified by dialysis using a 3.5 KDa. dialysis membrane during 16 h at 6 °C against distilled water. After this time, the solution turned cloudy and the solvent was removed under vacuum. The desired product was obtained as an orangish oil (37% of yield, 17 mg). **^{1}H NMR** (DMSO-D6, 400 MHz): δ 8 (m, 3H), 4-2.82 (m, 199H), 1.88-0.98 (m, 57H). **^{13}C NMR** (DMSO-D6, 121 MHz): δ 173.02, 150.84, 149.86, 68.73, 60.85, 56.60, 52.29, 46.31, 35.76, 30.09, 29.62, 29.13, 28.41, 26.26, 25.63, 21.82, 15.19, 11.20. **MS (MALDI)**: 130.1 corresponding to the polymer fragment $[C2H4NH]_3$.

7.3.2.3. Synthesis of LP-bPEI (25000MW) (3)

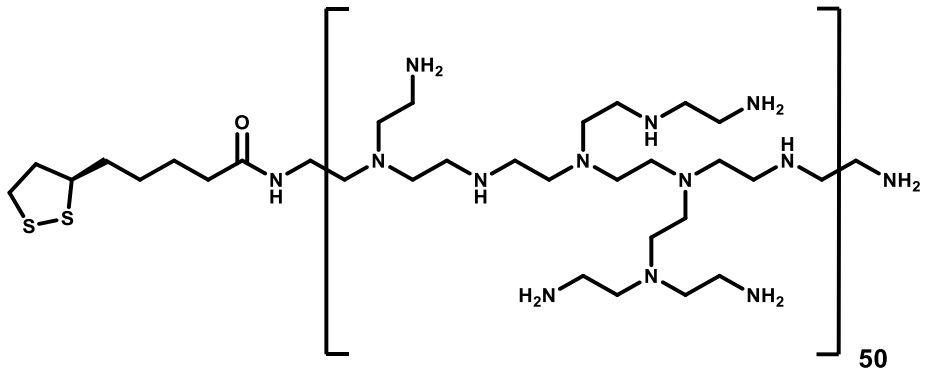

The preparation of this derivative is based on the previous one but using bPEI 25 KDa instead. Particularly, to a stirring solution of lipoic acid ester (4.61 mg, 0.015 mmol) in THF (3 mL) at 0 °C a solution of polyethylenimine (25000 M.W.) (250 mg, 0.01 mmol) in THF (10 mL) was added. Once a grey oil-like compound appears, the solvent is removed under vacuum and re-dissolved in methanol (MeOH, 2 mL). The product was purified by dialysis using a 10 KDa. dialysis membrane for 16 h at 6 °C against distilled water. After this time, the solution turned cloudy and the solvent was removed under vacuum. The desired product was obtained as a pale oil (22% of yield, 54.85 mg). **^{1}H NMR** (DMSO-D6, 400 MHz): δ 8 (m, 3H), 4-2.82 (m, 199H), 1.88-0.98 (m, 57H). **^{13}C NMR** (DMSO-D6, 121 MHz,) δ 172.81, 161.70, 125.31, 60.66, 52.72, 47.74, 37.86, 36.24, 32.64, 29.98, 29.47, 29.10, 26.30, 22.01. **MS (MALDI)**: 159.1 corresponding to the polymer fragment $[C2H4NH]_3$

7.3.2.4. Synthesis of LP-PEG (3000 MW)[222] (4)

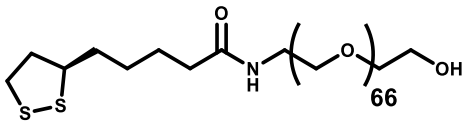

The procedure for the synthesis of LP-PEG (3000 MW) is based on the synthesis of Pyo *et al.* with some modifications. To a solution of lipoic acid ester (5.7 mg, 0.087mmol) in THF (0.5 mL) at room temperature a solution of polyethylenglycol (50 mg, 0.016) THF (0.5 mL) was added and stirred for 16 h. Then, the solvent was removed under vacuum and re-dissolved in methanol (MeOH, 2 mL). The product was purified by dialysis using a 3.5 KDa. dialysis membrane for 16 h at 6 °C against distilled water. Then, the solvent was removed under vacuum, obtaining a yellowish solid as the desired compound. (45% of yield, 24 mg). **^{1}H NMR** ($CDCl_3$, 400 MHz): δ 3.74 (s, 258H), 3.42 (t, 2H), 3.24 (dd.47 (m, 1H), 2.53 (t, 2H), 2,3(t,2H), 2.03 (m, 1H), 1.79 (m, 1H), 1.66 (m, 4H), 1.46 (m, 2H). **^{13}C NMR** ($CDCl_3$, 400 MHz): δ 173.1, 171.9, 70.6, 56.4, 40.3, 39.28, 38.5, 36.3, 34.7, 33.51, 29.8, 25.5, 24.8. **MS (MALDI)**: *m/z* calculated for $C_8H_{13}OS_2(PEG)_{66}$ 3047.7, found 3046.8

7.3.3. Chapter 3

7.3.3.1. Synthesis of (2-pyridyldithio)propanoic acid (5) [223]

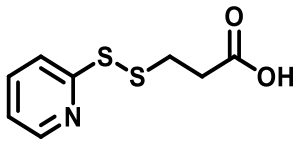

To a solution of mercaptopropionic acid (380.02 mg, 3.6 mmol) in methanol (MeOH, 30 mL) a mixture of 2-aldrithiol (1.213 g, 5.52 mmol) and acetic acid (0.150 mL) in methanol (15 mL) was added and stirred for 16 h. Then, the solvent is removed under vacuum and the product was purified by column chromatography in silica gel with Hexane/AcOEt (1:1) affording a yellowish oil (90% of yield, 700.6 mg). **^{1}H NMR** ($CDCl_3$, 400 MHz): δ 8.43 (d, 1H), 7.67 (m, 2H), 7.09 (td, 1H), 3.01 (t, 2H), 2.75 (t, 2H). **^{13}C NMR** ($CDCl_3$, 101 MHz): δ 175.72, 159.52, 149.06, 137.69, 121.14, 120.29, 33.82, 33.55. **MS (ESI)**: 216 (100) [M+H], 218 (5) [M+Na]. (ESI) calculated for C8H9NO2S2 (M+H) 216.01, found 216.014

2.3.3.2. Synthesis of Succinimidyl 3-(2-pyridyldithio)propionate (SPDP) [223] (6)

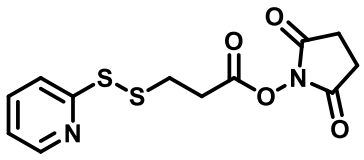

To a stirring solution (2-pyridyldithio)-propanoic acid (700.6 mg, 3.25 mmol) in tetrahydrofurane (THF, 12 mL) at 0 °C, a solution of NHS (452 mg, 3.9 mmol) and DCC (805 mg, 3.9 nmol) in THF (3 mL) was added. The reaction was allowed to warm up to room temperature and stirred for 16 h. Then, the precipitated solid is filtrated and the solvent was removed under vacuum. The product was stored at -20°C for 6 h, then dissolved in dichloromethane (DCM) and the formed precipitate was filtrated. The solvent was removed again under vacuum obtaining a white solid corresponding to the ester (37% of yield, 375 mg). **^{1}H NMR** ($CDCl_3$, 400 MHz): δ 8.37 (d, 1H), 7.58 (m, 2H), 7.01 (dt, 1H), 2.87 (m, 4H), 2.71 (s, 4H). **^{13}C NMR** (CDCl3, 101 MHz): δ 169.05, 167.02, 159.15, 149.69, 137.54, 121.17, 120.11, 32.89, 30.95, 25.6**. MS (ESI)**: 313 (100) [M+H], 335(47) [M+Na]. (ESI) calculated for C13H13NO4S2 (M+H) 312.03, found 313.01

7.3.3.3. Synthesis of PDP-bPEI (2 KDa) (7)

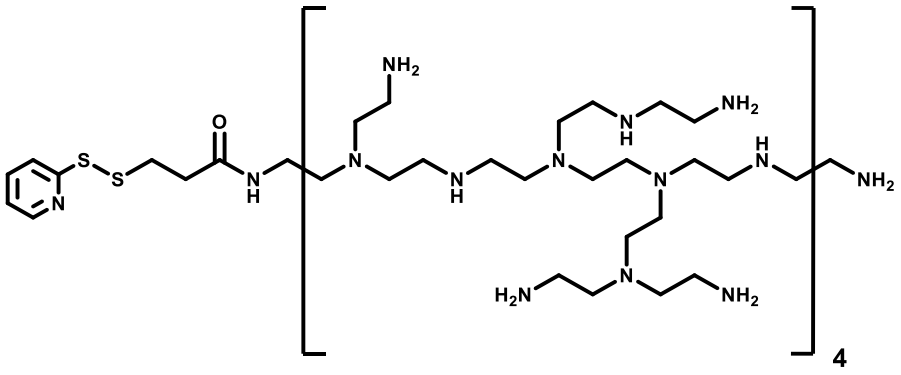

To a solution of polyethylenimine (2000 M.W.) (37.5 mg, 0.018 mmol) in DCM (1.5 mL) at 0 °C, a solution of SPDP (8.42 mg, 0.027 mmol) in DCM (0.5 mL) was added. The reaction was allowed to warm up to room temperature under vigorous stirring for 16 h. Then, the solvent was removed under vacuum and re-dissolved in methanol (2 mL). The product was purified by dialysis using a 3.5 KDa. dialysis membrane during 16 h at 6 °C against distilled water. After this time, the solution

turned cloudy and the solvent was removed under vacuum affording a greyish oil (21% of yield, 18.5 mg). **^{1}H NMR** (DMSO-D6, 400 MHz): δ 8.49 (m, 2H), 8 (m, 37H), 7.77 (m, 4H), 7.30 (2H), 4.1-2.8 (m, 1436H), 2.02-0.84 (m, 414H). **^{13}C NMR** (DMSO-D6, 101 MHz): δ 172.88, 164.18, 148.89, 137.25, 124.35, 120.73, 60.78, 53.50, 47.99, 33.64, 32.62, 29.47, 24.44, 21.73. **MS (MALDI):** 169.1 and 212.2, corresponding to polymer fragments due to their difference of 43 units, which corresponds with the monomer [C2H4NH].

7.3.3.4. Synthesis of PDP-bPEI (25 KDa) (8)

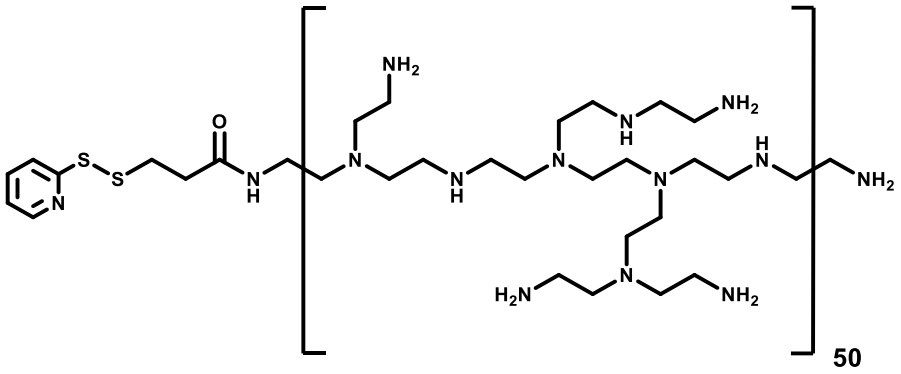

To a solution of polyethylenimine (25000 M.W.) (250 mg, 0.01 mmol) in THF (1.5 mL) at 0 °C, a solution of SPDP (4.7 mg, 0.015 mmol) in THF (0.5 mL) was added. The reaction was allowed to warm up to room temperature under vigorous stirring for 16 h. Then, the solvent was removed under vacuum and re-dissolved in methanol (2 mL). The product was purified by dialysis using a 1 KDa. dialysis membrane during 16 h at 6 °C against distilled water. After this time, the solution turned cloudy and the solvent was removed under vacuum affording a greyish oil (16% of yield, 62.4.2 mg). **^{1}H NMR** (DMSO-D6, 400 MHz): δ 8.49 (m, 2H), 7.77 (m, 5H), 7.30 (1H), 4.1-2.8 (m, 2000H), 2.02-0.84 (m, 545H) **^{13}C NMR** (DMSO-D6, 126 MHz): δ 172.85, 165.19, 163.22, 161.72, 150.67, 149.98, 138.26, 137.11, 134.92, 124.33, 120.79, 60.75, 54.20, 53.13, 48.81, 47.72, 37.85, 36.14, 32.47, 30.77, 30.10, 29.47, 29.10, 26.30, 22.01. **MS (MALDI):** 169.1 and 341.3, corresponding to polymer fragments due to their difference of 172 units, which corresponds with the fragment $[C2H4NH]_4$.

7.3.4. Chapter 5

7.3.4.1. Synthesis of N-(1,3-dihydroxybutan-2-yl)-3-mercaptopropanamide (9)[224]

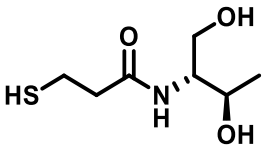

To a stirring solution of 3-mercaptopropionic acid (727 mg, 6.84 mmol), NHS (918 mg, 8 mmol) and DCC (1.646 g, 8 mmol) in THF (60 mL) at 0 ºC, L-threoninol (600 mg, 5.7 mmol) was added and left for 16 h. Then, the solvent is removed under vacuum and the product was purified by column chromatography in silica gel with CH_2Cl_2/MeOH 15:1 (Rf 0.4) obtaining compound **9** as a pale yellow oil. (97% of yield, 1.08 g). **^{1}H NMR** (CDCl3, 400 MHz): δ 4.09 (dq, 1H), 3.81 (m, 1H), 3.70 (d, 2H), 2.76 (t, 2H), 2.56 (t,2 H), 1.62 (t, 1H), 1.16 (d, 3H). **^{13}C NMR** (CDCl3, 101 MHz): δ 172.32, 68.28, 64.40, 55.16, 20.71, 20.54. **MS (ESI)**: m/z (%) 194 (56), 216 $[M+Na]^+$ (100). (ESI) calculated for $C_7H_{15}NO_3S$ $[M+H]^+$ 194.08, found 194.08.

7.3.4.2. Synthesis of N-(1,3-dihydroxybutan-2-yl)-3-(pyridin-2-yldisulfanyl)-propanamide (10)

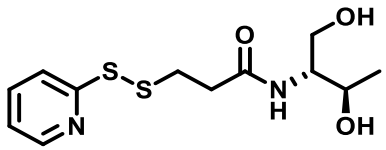

To a stirring solution of 2-aldithriol (1.83 g, 8.31 mmol) in MeOH under N_2, a solution of compound **9** (1.08 g, 5.54mmol) in MeOH was added slowly. The reaction is allowed to react for 16 h at room temperature. After this time, the solvent is removed under vacuum and purified by column chromatography in silica gel with CH_2Cl_2/MeOH 15:1 (Rf 0.3). Compound **10** was obtained as a colorless oil (60% of yield, 1.00 g). **^{1}H NMR** (CDCl3, 400 MHz): δ 8.45 (d, 1H), 7.70 (m, 2H), 7.14 (t, 1H), 4.13 (m, 1H), 3.89-3.73 (m, 3H), 3.04 (td, 2H), 2.70 (m,1H), 2.64 (m,1H), 1.17 (d, 3H). **^{13}C NMR** (CDCl3, 101 MHz): δ 172.75, 159.58, 149.59, 137.95, 121.52, 120.62, 68.50, 64.42, 55.35, 35.87, 34.66, 20.47. **MS-**

ESI: m/z (%) 142 (9), 221 (15), 303 $[M+1]^+$ (100). (ESI) calculated for $C_{12}H_{18}N_2O_3S_2$ $[M+H]^+$ 302.08, found 302.08.

7.3.4.3. Synthesis of N-(1-(bis(4-methoxyphenyl)(phenyl)methoxy)-3-hydroxybutan-2-yl)-3-(pyridin-2-yldisulfanyl)propenamide (11)

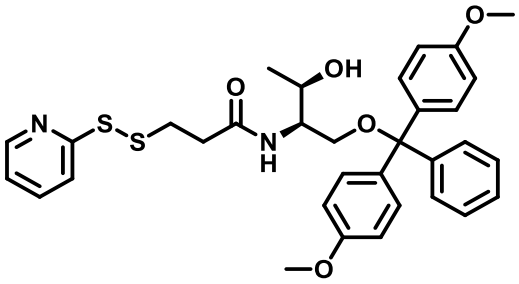

To a stirred solution of **10** (120 mg, 0.39 mmol) and DMAP (1 mg) in anhydrous pyridine (500 µL) under N_2 and at 0 °C, a solution of DMTr-Cl (264 mg, 0.78 mmol) in anhydrous pyridine (1.5 mL) was added. The reaction is allowed to get room temperature and after 16 h a yellow solution is obtained. Then, it is added toluene, and the solvents are removed under vacuum. After completely remove the pyridine, the compound is purified by column chromatography in deactivated silica gel using Hexane: Ethyl Acetate 1:1. Then compound **11** is obtained as a brownish oil (26 % of yield, 60.8 mg). **^{1}H NMR** (CDCl3, 400 MHz): δ 8.49 (d, 1H), 7.79-762 (m, 2H), 7.40(d, 2H), 7.32-7.27 (m, 6H), 7.21 (t, 1H), 7.07 (m,1H), 6.83 (d, 4H), 4.11 (m, 1H), 3.99 (m, 1H), 3.78 (s, 6H), 3.44 (dd, 1H), 3.31 (dd, 1H), 3.08 (t, 2H), 2.67 (t, 2H), 1.15 (d, 3H). **^{13}C NMR** (CDCl3, 101 MHz): δ 171.27, 159.52, 158.73, 149.99, 144.43, 137.12, 135.60, 135.42, 130.09, 130.06, 128.09, 127.11, 121.06, 120.27, 113.39, 86.91, 68.55, 65.22, 55.32, 53.80, 36.13, 35.29, 20.10. **MS-ESI**: m/z (%) 129 (14), 303 (10), 627 $[M+Na]^+$ (100). (ESI) calculated for $C_{33}H_{36}N_2O_5S_2$ $[M+Na]^+$ 627.19, found 627.19

7.3.4.4. Synthesis of CPG-Building block (4-(((2R,3R)-4-(bis(4-methoxyphenyl)(phenyl)methoxy)-3-(3-(pyridin-2-yldisulfanyl)propanamido)butan-2-yl)oxy)-4-oxobutanamido)CPG (12)

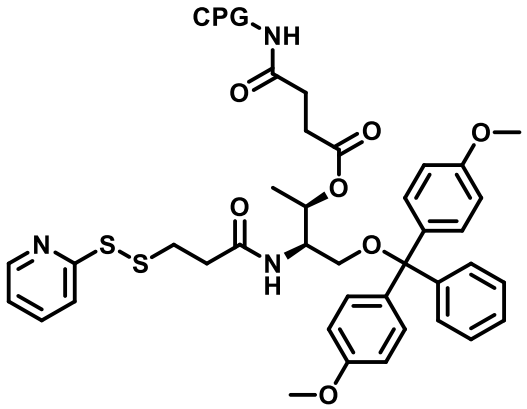

To a stirring solution of compound **11** (28 mg, 0.047 mmol) and DMAP (catalytic amount) in anhydrous pyridine (500 µL) under Ar, a solution of succinic anhydride (6.5 mg, 0.065 mmol) in anhydrous pyridine (500 µL) under Ar was added. The reaction was stirred for 16h at room temperature. Then, the pyridine was removed completely under vacuum with the addition of toluene. The solid obtained was dissolved in dry ACN (2 mL) under Ar, cooled at 0 ºC, and stirred vigorously. After that, a solution of HOBt (8.8 mg, 0.065 mmol) and DCC (13.4 mg, 0.065 mmol) in dry ACN (1 mL) under Ar was added, and the mixture was stirred for 24 hours. Then, the white solid generated during the reaction was removed by filtration, and the filtrated solvent was concentrated under vacuum, generating a solid which was dissolved in dry ACN (1.5 mL). The solution is added to CPG 1000 Å (130 mg) and the mixture was shaken 24 h. The white solid was then washed with 30 mL of ACN, DCM and hexane. The excess of solvent was removed by suction and a mixture solution 1:1 of capping reagents used in oligonucleotides synthesis [CAP MIX A: Acetic anhydride (400 µL)/Pyridine (600 µL)/THF (500 µL); CAP MIX B: 1-Methylimidazol (400 µL)/ THF (1 mL)] was added and incubated for 1 h. Finally, the modified CPG was washed with 60 mL of methanol and acetonitrile and dried. **Functionalization (F)** = 22 (µmol/g)

Bibliography

1. Stratton, M. R., Campbell, P. J. & Futreal, P. A. The cancer genome. *Nature* **458**, 719–724 (2009).
2. Bertram, J. S. The molecular biology of cancer. *Mol Asp. Med.* **21**, 167–223 (2000).
3. Hassanpour, S. H. & Dehghani, M. Review of cancer from perspective of molecular. *J. Cancer Res. Pract.* **4**, 127–129 (2017).
4. Vineis, P. & Berwick, M. The population dynamics of cancer: A Darwinian perspective. *Int. J. Epidemiol.* **35**, 1151–1159 (2006).
5. Hanselmann, R. G. & Welter, C. Origin of cancer: An information, energy, and matter disease. *Front. Cell Dev. Biol.* **4**, (2016).
6. Wang, L. H., Wu, C. F., Rajasekaran, N. & Shin, Y. K. Loss of tumor suppressor gene function in human cancer: An overview. *Cell. Physiol. Biochem.* **51**, 2647–2693 (2019).
7. Guo, H. & Tsung, K. Tumor reductive therapies and antitumor immunity. *Oncotarget* **8**, 55736–55749 (2017).
8. Schirrmacher, V. From chemotherapy to biological therapy: A review of novel concepts to reduce the side effects of systemic cancer treatment (Review). *Int. J. Oncol.* **54**, 407–419 (2019).
9. Baldo, B. A. & Pham, N. H. Adverse reactions to targeted and non-targeted chemotherapeutic drugs with emphasis on hypersensitivity responses and the invasive metastatic switch. *Cancer Metastasis Rev.* **32**, 723–761 (2013).
10. Wu, H.-C. & , De-Kuan Chang, and C.-T. H. Targeted Therapy for Cancer. *J. Cancer Mol.* **2**, 57–66 (2006).
11. Yan, L., Rosen, N. & Arteaga, C. Targeted cancer therapies. *Chin. J. Cancer* **30**, 1–4 (2011).
12. Padeletti, G., Fermo, P. & Gilardoni, S. Technological investigation of luster decorated ancient majolicas. *Mater. Res. Soc. Symp. - Proc.* **712**, 383–389 (2002).
13. Bayda, S., Adeel, M., Tuccinardi, T., Cordani, M. & Rizzolio, F. The history of nanoscience and nanotechnology: From chemical-physical applications to nanomedicine. *Molecules* **25**, 1–15 (2020).
14. Custance, O., Perez, R. & Morita, S. Atomic force microscopy as a tool for atom manipulation. *Nat. Nanotechnol.* **4**, 803–810 (2009).
15. Cheng, L. C., Jiang, X., Wang, J., Chen, C. & Liu, R. S. Nano-bio effects: Interaction of nanomaterials with cells. *Nanoscale* **5**, 3547–3569 (2013).
16. Tinkle, S. *et al.* Nanomedicines: Addressing the scientific and regulatory gap. *Ann. N. Y. Acad. Sci.* **1313**, 35–56 (2014).

17. Kotov, N. A. Inorganic nanoparticles as protein mimics. *Science (80-.).* **330**, 188–189 (2010).

18. Wang, H. *et al.* Noble metal nanoparticles growth-based colorimetric strategies: From monocolorimetric to multicolorimetric sensors. *Coord. Chem. Rev.* **398**, 113003 (2019).

19. Gao, Z., Deng, K., Wang, X. D., Miró, M. & Tang, D. High-resolution colorimetric assay for rapid visual readout of phosphatase activity based on gold/silver core/shell nanorod. *ACS Appl. Mater. Interfaces* **6**, 18243–18250 (2014).

20. Cheng, Z., Al Zaki, A., Hui, J. Z., Muzykantov, V. R. & Tsourkas, A. Multifunctional nanoparticles: Cost versus benefit of adding targeting and imaging capabilities. *Science (80-.).* **338**, 903–910 (2012).

21. Sun, Q. *et al.* Integration of nanoassembly functions for an effective delivery cascade for cancer drugs. *Adv. Mater.* **26**, 7615–7621 (2014).

22. Torchilin, V. Tumor delivery of macromolecular drugs based on the EPR effect. *Adv. Drug Deliv. Rev.* **63**, 131–135 (2011).

23. Zaloga, J. *et al.* Development of a lauric acid/albumin hybrid iron oxide nanoparticle system with improved biocompatibility. *Int. J. Nanomedicine* **9**, 4847–4866 (2014).

24. Liberti, M. V & Locasale, J. W. The Warburg Effect: How Does it Benefit Cancer Cells? (vol 41, pg 211, 2016). *Trends Biochem. Sci.* **41**, 287 (2016).

25. Zhang, X., Malhotra, S., Molina, M. & Haag, R. Micro- and nanogels with labile crosslinks-from synthesis to biomedical applications. *Chem. Soc. Rev.* **44**, 1948–1973 (2015).

26. He, Y. *et al.* Viral mimicking ternary polyplexes: A reduction-controlled hierarchical unpacking vector for gene delivery. *Adv. Mater.* **26**, 1534–1540 (2014).

27. Jing Li, Yan Wang, Yu Zhu, D. O. Recent Advances in Delivery of Drug-Nucleic Acid Combinations for Cancer Treatment. *J. Control Release* **172**, 589–600 (2013).

28. Lucky, S. S., Soo, K. C. & Zhang, Y. Nanoparticles in photodynamic therapy. *Chem. Rev.* **115**, 1990–2042 (2015).

29. Deatsch, A. E. & Evans, B. A. Heating efficiency in magnetic nanoparticle hyperthermia. *J. Magn. Magn. Mater.* **354**, 163–172 (2014).

30. Jaque, D. *et al.* Nanoparticles for photothermal therapies. *Nanoscale* **6**, 9494–9530 (2014).

31. Xie, J., Lee, S. & Chen, X. Nanoparticle-based theranostic agents. *Adv. Drug Deliv. Rev.* **62**, 1064–1079 (2010).

32. Gad, S. C., Sharp, K. L., Montgomery, C., Payne, J. D. & Goodrich, G. P. Evaluation of the toxicity of intravenous delivery of auroshell particles (Gold-Silica

Nanoshells). *Int. J. Toxicol.* **31**, 584–594 (2012).

33. Feliu, N. *et al.* In vivo degeneration and the fate of inorganic nanoparticles. *Chem. Soc. Rev.* **45**, 2440–2457 (2016).

34. Dykman, L. A. & N. G. Khlebtsov. Gold Nanoparticles in Biology and Medicine: Recent Advances and Prospects. *Acta Naturae* **3**, 34–56 (2011).

35. Edwards, P. P. & Thomas, J. M. Gold in a metallic divided state - From Faraday to present-day nanoscience. *Angew. Chemie - Int. Ed.* **46**, 5480–5486 (2007).

36. Turkevich, J., Stevenson, P. C. & Hillier, J. A study of the nucleation and growth processes in the synthesis of colloidal gold. *Discuss. Faraday Soc.* **11**, 55–75 (1951).

37. Frens, G. Controlled nucleation for the regulation of the particle size in monodisperse gold suspensions. *Nat. Phys. Sci.* **241**, 20–22 (1973).

38. Brust, M., Walker, M., Bethell, D., Schiffrin, D. J. & Whyman, R. Synthesis of Thiol-derivatised Gold Nanoparticles in. 801–802 (2000).

39. Khan, A. K., Rashid, R., Murtaza, G. & Zahra, A. Gold nanoparticles: Synthesis and applications in drug delivery. *Trop. J. Pharm. Res.* **13**, 1169–1177 (2014).

40. Hu, M. *et al.* Gold nanostructures: Engineering their plasmonic properties for biomedical applications. *Chem. Soc. Rev.* **35**, 1084–1094 (2006).

41. Murphy, C. J. *et al.* Gold Nanoparticles in Biology: Beyond Toxicity to Cellular Imaging. *Acc. Chem. Res.* **41**, (2008).

42. Gomes, A. *et al.* Lysozyme–aunps interactions: Determination of binding free energy. *Nanomaterials* **11**, (2021).

43. Pensa, E. *et al.* The chemistry of the sulfur-gold interface: In search of a unified model. *Acc. Chem. Res.* (2012) doi:10.1021/ar200260p.

44. Templeton, A. C., Wuelfing, W. P. & Murray, R. W. Monolayer-Protected Cluster Molecules. **33**, 27–36 (2000).

45. Ciaurriz, P., Fernández, F., Tellechea, E., Moran, J. F. & Asensio, A. C. Comparison of four functionalization methods of gold nanoparticles for enhancing the enzyme-linked immunosorbent assay (ELISA). *Beilstein J. Nanotechnol.* **8**, 244–253 (2017).

46. Bao, C. *et al.* A promising road with challenges: Where are gold nanoparticles in translational research? *Nanomedicine* **9**, 2353–2370 (2014).

47. Zhang, C. *et al.* Gold nanoclusters-based nanoprobes for simultaneous fluorescence imaging and targeted photodynamic therapy with superior penetration and retention behavior in tumors. *Adv. Funct. Mater.* **25**, 1314–1325 (2015).

48. Leuvering, J. H. W., Thal, P. J. H. M., Van der Waart, M. & Schuurs, A. H. W. M. A sol particle agglutination assay for human chorionic gonadotrophin. *J. Immunol. Methods* **45**, 183–194 (1981).

49. Stehr, J. *et al.* Gold NanoStoves for microsecond DNA melting analysis. *Nano Lett.* **8**, 619–623 (2008).

50. Reynolds, R. A., Mirkin, C. A. & Letsinger, R. L. Homogeneous, nanoparticle-based quantitative colorimetric detection of oligonucleotides. *J. Am. Chem. Soc.* **122**, 3795–3796 (2000).

51. Daniel Aili, Morgan Mager, David Roche, and M. M. S. Hybrid Nanoparticle−Liposome Detection of Phospholipase Activity. *Nano Lett.* **11**, 1401–1405 (2011).

52. Valentini, P. *et al.* Gold-nanoparticle-based colorimetric discrimination of cancer-related point mutations with picomolar sensitivity. *ACS Nano* **7**, 5530–5538 (2013).

53. Yang, L. *et al.* Comparisons of the biodistribution and toxicological examinations after repeated intravenous administration of silver and gold nanoparticles in mice. *Sci. Rep.* **7**, 1–12 (2017).

54. Alric, C. *et al.* The biodistribution of gold nanoparticles designed for renal clearance. *Nanoscale* **5**, 5930–5939 (2013).

55. Rosi, N. L. *et al.* Oligonucleotide-modified gold nanoparticles for infracellular gene regulation. *Science (80-.).* **312**, 1027–1030 (2006).

56. Ghosh, P. S., Kim, C. K., Han, G., Forbes, N. S. & Rotello, V. M. Efficient gene delivery vectors by tuning the surface charge density of amino acid-functionalized gold nanoparticles. *ACS Nano* **2**, 2213–2218 (2008).

57. Kim, C. K. *et al.* Entrapment of hydrophobic drugs in nanoparticle monolayers with efficient release into cancer cells. *J. Am. Chem. Soc.* **131**, 1360–1361 (2009).

58. Cheng, Y. *et al.* Deep penetration of a PDT drug into tumors by noncovalent drug-gold nanoparticle conjugates. *J. Am. Chem. Soc.* **133**, 2583–2591 (2011).

59. Kim, B. *et al.* Tuning payload delivery in tumour cylindroids using gold nanoparticles. *Nat. Nanotechnol.* **5**, 465–472 (2010).

60. Bhattacharya, R. *et al.* Gold nanoparticles inhibit the proliferation of multiple myeloma cells. *Adv. Mater.* **19**, 711–716 (2007).

61. Bresee, J., Maier, K. E., Boncella, A. E., Melander, C. & Feldheim, D. L. Growth inhibition of staphylococcus aureus by mixed monolayer gold nanoparticles. *Small* **7**, 2027–2031 (2011).

62. Deng, J., Yao, M. & Gao, C. Cytotoxicity of gold nanoparticles with different structures and surface-anchored chiral polymers. *Acta Biomater.* **53**, 610–618 (2017).

63. Bobo, D., Robinson, K. J., Islam, J., Thurecht, K. J. & Corrie, S. R. Nanoparticle-Based Medicines: A Review of FDA-Approved Materials and Clinical Trials to Date. *Pharm. Res.* **33**, 2373–2387 (2016).

64. Libutti, S. K. *et al.* Phase I and pharmacokinetic studies of CYT-6091, a novel PEGylated colloidal gold-rhTNF nanomedicine. *Clin. Cancer Res.* **16**, 6139–6149 (2010).

65. Anselmo, A. C. & Mitragotri, S. Nanoparticles in the clinic. *Bioeng. Transl. Med.* **1**, 10–29 (2016).

66. Caffery, B., Lee, J. S. & Alexander-Bryant, A. A. Vectors for glioblastoma gene therapy: Viral & non-viral delivery strategies. *Nanomaterials* **9**, (2019).

67. Robinson, A. P. *et al.* Nanocatalytic activity of clean-surfaced, faceted nanocrystalline gold enhances remyelination in animal models of multiple sclerosis. *Sci. Rep.* **10**, 1–16 (2020).

68. Ferreira, D. *et al.* Gold nanoparticles for vectorization of nucleic acids for cancer therapeutics. *Molecules* **25**, (2020).

69. Sheridan, C. Gene therapy finds its niche. **29**, 121–129 (2011).

70. Miller, A. D. Retroviral Vectors. **158**, 1–24 (1992).

71. Weichselbaum, R. R. & Kufe, D. Gene therapy of cancer. **34**, 10–12 (1997).

72. Armstrong, A. C., Eaton, D. & Ewing, J. C. Clinical review Cellular immunotherapy for cancer. **323**, 1289–1293 (2001).

73. Cross, D. & Burmester, J. K. Gene Therapy for Cancer Treatment : Past , Present and Future. **4**, 218–227 (2006).

74. Amer, M. H. Gene therapy for cancer : present status and future perspective. 1–19 (2014).

75. Morille, M., Passirani, C., Vonarbourg, A., Clavreul, A. & Benoit, J. Biomaterials Progress in developing cationic vectors for non-viral systemic gene therapy against cancer. **29**, 3477–3496 (2008).

76. YANG, N.-S., BURKHOLDER, J., ROBERTS, B., MARTINELL, B. & MCCABE, D. In vivo and in vitro gene transfer to mammalian somatic cells by particle bombardment. **87**, 9568–9572 (1990).

77. Sandhu, K. K., Mcintosh, C. M., Simard, J. M., Smith, S. W. & Rotello, V. M. Gold Nanoparticle-Mediated Transfection of Mammalian Cells. 7–10 (2002) doi:10.1021/bc015545c.

78. Moghimi, S. M. *et al.* A Two-Stage Poly(ethylenimine) Mediated Cytotoxicity :Implications for Gene Transfer/Therapy. *Mol. Ther.* **11**, 990–995 (2005).

79. Kawano, T., Yamagata, M., Takahashi, H., Niidome, Y. & Yamada, S. Stabilizing of plasmid DNA in vivo by PEG-modified cationic gold nanoparticles and the gene expression assisted with electrical pulses. **111**, 382–389 (2006).

80. Li, P., Li, D., Zhang, L., Li, G. & Wang, E. Cationic lipid bilayer coated gold nanoparticles-mediated transfection of mammalian cells. *Biomaterials* **29**, 3617–

3624 (2008).

81. Lee, M. *et al.* Target-Specific Gene Silencing of Layer-by-Layer Assembled Gold Cysteamine/siRNA/PEI /HA Nanocomplex. 6138–6147 (2011).

82. Mendes, R., Fernandes, A. R. & Baptista, P. V. Gold nanoparticle approach to the selective delivery of gene silencing in cancer-The case for combined delivery? *Genes (Basel).* **8**, (2017).

83. Ding, Y. *et al.* Gold nanoparticles for nucleic acid delivery. *Mol. Ther.* **22**, 1075–1083 (2014).

84. Jazayeri, M. H., Amani, H., Pourfatollah, A. A., Pazoki-Toroudi, H. & Sedighimoghaddam, B. Various methods of gold nanoparticles (GNPs) conjugation to antibodies. *Sens. Bio-Sensing Res.* **9**, 17–22 (2016).

85. Zhang, Y., Xu, D., Li, W., Yu, J. & Chen, Y. Effect of size, shape, and surface modification on cytotoxicity of gold nanoparticles to human HEp-2 and Canine MDCK Cells. *J. Nanomater.* **2012**, (2012).

86. De Jong, W. H. *et al.* Particle size-dependent organ distribution of gold nanoparticles after intravenous administration. *Biomaterials* **29**, 1912–1919 (2008).

87. Huo, S. *et al.* Ultrasmall gold nanoparticles as carriers for nucleus-based gene therapy due to size-dependent nuclear entry. *ACS Nano* **8**, 5852–5862 (2014).

88. Huo, S. *et al.* Superior penetration and retention behavior of 50 nm gold nanoparticles in tumors. *Cancer Res.* **73**, 319–330 (2013).

89. Truong, L. *et al.* Systematic determination of the relationship between nanoparticle core diameter and toxicity for a series of structurally analogous gold nanoparticles in zebrafish. *Nanotoxicology* **13**, 879–893 (2019).

90. Hurst, S. J., Lytton-Jean, A. K. R. & Mirkin, C. A. Maximizing DNA loading on a range of gold nanoparticle sizes. *Anal. Chem.* **78**, 8313–8318 (2006).

91. Xie, X., Liao, J., Shao, X., Li, Q. & Lin, Y. The Effect of shape on Cellular Uptake of Gold Nanoparticles in the forms of Stars, Rods, and Triangles. *Sci. Rep.* **7**, 1–9 (2017).

92. Turkevich, J., Stevenson, P. C. & Hillier, J. A study of the nucleation and growth processes in the synthesis of colloidal gold. *Discuss. Faraday Soc.* **11**, 55 (1951).

93. Rodríguez-González, B., Mulvaney, P. & Liz-Marzán, L. M. An electrochemical model for gold colloid formation via citrate reduction. *Zeitschrift fur Phys. Chemie* **221**, 415–426 (2007).

94. Ding, W. *et al.* Effect of latent heat in boiling water on the synthesis of gold nanoparticles of different sizes by using the Turkevich method. *ChemPhysChem* **16**, 447–454 (2015).

95. Ji, X. *et al.* Size control of gold nanocrystals in citrate reduction: The third role of

citrate. *J. Am. Chem. Soc.* **129**, 13939–13948 (2007).

96. Xia, H., Xiahou, Y., Zhang, P., Ding, W. & Wang, D. Revitalizing the Frens Method to Synthesize Uniform, Quasi-Spherical Gold Nanoparticles with Deliberately Regulated Sizes from 2 to 330 nm. *Langmuir* **32**, 5870–5880 (2016).

97. Haiss, W., Thanh, N. T. K., Aveyard, J. & Fernig, D. G. Determination of size and concentration of gold nanoparticles from UV-Vis spectra. *Anal. Chem.* **79**, 4215–4221 (2007).

98. Giljohann, D. *et al.* Gold Nanoparticles for Biology and Medicine. *Angew. Chem. Int. Ed. Engl.* **49**, 3280–3294 (2014).

99. Dumur, F., Dumas, E. & Mayer, C. R. Functionalization of gold nanoparticles by inorganic entities. *Nanomaterials* **10**, (2020).

100. Ochoa, S. & Milam, V. T. Modified nucleic acids: Expanding the capabilities of functional oligonucleotides. *Molecules* **25**, 1–23 (2020).

101. Boussif, O. T. *et al.* A versatile vector for gene and oligonucleotide transfer into cells in culture and in vivo: Polyethylenimine. *Proc Natl Acad Sci U S A .* **92**, 7297–7301 (1995).

102. Godbey, W. T., Wu, K. K. & Mikos, A. G. Poly(ethylenimine) and its role in gene delivery. *J. Control. Release* **60**, 149–160 (1999).

103. Akinc, A., Thomas, M., Klibanov, A. M. & Langer, R. Exploring polyethylenimine-mediated DNA transfection and the proton sponge hypothesis. *J. Gene Med.* **7**, 657–663 (2005).

104. Vicennati, P., Giuliano, A., Ortaggi, G. & Masotti, A. Polyethylenimine In Medicinal Chemistry. *Curr. Med. Chem.* **15**, 2826–2839 (2008).

105. Pang, S. T., Lin, F. W., Chuang, C. K. & Yang, H. W. Co-Delivery of Docetaxel and p44/42 MAPK siRNA Using PSMA Antibody-Conjugated BSA-PEI Layer-by-Layer Nanoparticles for Prostate Cancer Target Therapy. *Macromol. Biosci.* **17**, 1–9 (2017).

106. Ow Sullivan, M. M., Green, J. J. & Przybycien, T. M. Development of a novel gene delivery scaffold utilizing colloidal gold-polyethylenimine conjugates for DNA condensation. *Gene Ther.* **10**, 1882–1890 (2003).

107. Dong, S., Zhou, X. & Yang, J. TAT modified and lipid – PEI hybrid nanoparticles for co-delivery of docetaxel and pDNA. *Biomed. Pharmacother.* **84**, 954–961 (2016).

108. Li, Y. *et al.* Polyethylenimine-functionalized silver nanoparticle-based co-delivery of paclitaxel to induce HepG2 cell apoptosis. *Int. J. Nanomedicine* **11**, 6693–6702 (2016).

109. Jäger, M., Schubert, S., Ochrimenko, S., Fischer, D. & Schubert, U. S. Branched and linear poly(ethylene imine)-based conjugates: Synthetic modification, characterization, and application. *Chem. Soc. Rev.* **41**, 4755–4767 (2012).

110. Moghimi, S. M. *et al.* A two-stage poly(ethylenimine)-mediated cytotoxicity: Implications for gene transfer/therapy. *Mol. Ther.* **11**, 990–995 (2005).

111. Morimoto, K. *et al.* Molecular weight-dependent gene transfection activity of unmodified and galactosylated polyethyleneimine on hepatoma cells and mouse liver. *Mol. Ther.* **7**, 254–261 (2003).

112. Zintchenko, A., Philipp, A., Dehshahri, A. & Wagner, E. Simple modifications of branched PEI lead to highly efficient siRNA carriers with low toxicity. *Bioconjug. Chem.* **19**, 1448–1455 (2008).

113. Anna Graczyk, Roza Pawlowska, Dominika Jedrzejczyk, A. C. Gold Nanoparticles in Conjunction with Nucleic Cellular Delivery. *Molecules* **25**, 204 (2020).

114. Zezin, A. A. Synthesis of hybrid materials in polyelectrolyte matrixes: Control over sizes and spatial organization of metallic nanostructures. *Polym. Sci. - Ser. C* **58**, 118–130 (2016).

115. Note, C., Kosmella, S. & Koetz, J. Poly(ethyleneimine) as reducing and stabilizing agent for the formation of gold nanoparticles in w/o microemulsions. *Colloids Surfaces A Physicochem. Eng. Asp.* **290**, 150–156 (2006).

116. Gullapalli, R. P. & Mazzitelli, C. L. *Polyethylene glycols in oral and parenteral formulations - A critical review*. *International Journal of Pharmaceutics* vol. 496 (Elsevier B.V., 2015).

117. Wali, R. K., Kunte, D. P., Koetsier, J. L., Bissonnette, M. & Roy, H. K. Polyethylene Glycol Mediated Colorectal Cancer Chemoprevention: Roles of Epidermal Growth Factor Receptor and Snail. **7**, 3103–3111 (2009).

118. Parnaud, G., Taché, S., Peiffer, G. & Corpet, D. E. Polyethylene-glycol suppresses colon cancer and causes dose-dependent regression of azoxymethane-induced aberrant crypt foci in rats. *Cancer Res.* **59**, 5143–5147 (1999).

119. Bharadwaj, S. *et al.* Higher molecular weight polyethylene glycol increases cell proliferation while improving barrier function in an in vitro colon cancer model. *J. Biomed. Biotechnol.* **2011**, (2011).

120. Cole, A. J., Yang, V. C. & David, A. E. Cancer theranostics: The rise of targeted magnetic nanoparticles. *Trends Biotechnol.* **29**, 323–332 (2011).

121. Abuchowski, A., McCoy, J. R., Palczuk, N. C., van Es, T. & Davis, F. F. Effect of covalent attachment of polyethylene glycol on immunogenicity and circulating life of bovine liver catalase. *J. Biol. Chem.* **252**, 3582–3586 (1977).

122. Suk, J. S. *et al.* PEGylation as a strategy for improving nanoparticle-based drug and gene delivery. **99**, 28–51 (2017).

123. Mishra, P., Nayak, B. & Dey, R. K. PEGylation in anti-cancer therapy: An overview. *Asian J. Pharm. Sci.* **11**, 337–348 (2016).

124. Manson, J., Kumar, D. & Meenan, B. J. Polyethylene glycol functionalized gold nanoparticles : the influence of capping density on stability in various media. 99–

105 (2011) doi:10.1007/s13404-011-0015-8.

125. Singh, P. *et al.* Gold nanoparticles in diagnostics and therapeutics for human cancer. *Int. J. Mol. Sci.* **19**, (2018).

126. Shen, Z., Fisher, A., Liu, W. K. & Li, Y. *PEGylated 'stealth' nanoparticles and liposomes*. *Engineering of Biomaterials for Drug Delivery Systems: Beyond Polyethylene Glycol* (Elsevier Ltd, 2018). doi:10.1016/B978-0-08-101750-0.00001-5.

127. Friedman, A., Claypool, S. & Liu, R. The Smart Targeting of Nanoparticles. *Curr. Pharm. Des.* **19**, 6315–6329 (2013).

128. Jacob, S. *et al.* The antioxidant α-lipoic acid enhances insulin-stimulated glucose metabolism in insulin-resistant rat skeletal muscle. *Diabetes* **45**, 1024–1029 (1996).

129. Raschke, G. *et al.* Biomolecular recognition based on single gold nanoparticle light scattering. *Nano Lett.* **3**, 935–938 (2003).

130. Rastogi, L., Kora, A. J. & Arunachalam, J. Highly stable, protein capped gold nanoparticles as effective drug delivery vehicles for amino-glycosidic antibiotics. *Mater. Sci. Eng. C* **32**, 1571–1577 (2012).

131. Volkert, A. A., Subramaniam, V., Ivanov, M. R., Goodman, A. M. & Haes, A. J. Salt-mediated self-assembly of thioctic acid on gold nanoparticles. *ACS Nano* **5**, 4570–4580 (2011).

132. Tan, Y. H. *et al.* Characterization of protein immobilization on nanoporous gold using atomic force microscopy and scanning electron microscopy. *Nanoscale* **3**, 3395–3407 (2011).

133. Zeni, L. *et al.* A portable optical-fibre-based surface plasmon resonance biosensor for the detection of therapeutic antibodies in human serum. *Sci. Rep.* **10**, 1–9 (2020).

134. Jad, Y. E. *et al.* Peptide synthesis beyond DMF: THF and ACN as excellent and friendlier alternatives. *Org. Biomol. Chem.* **13**, 2393–2398 (2015).

135. Kunath, K. *et al.* Low-molecular-weight polyethylenimine as a non-viral vector for DNA delivery: Comparison of physicochemical properties, transfection efficiency and in vivo distribution with high-molecular-weight polyethylenimine. *J. Control. Release* **89**, 113–125 (2003).

136. Altunta, E. *et al.* Tandem mass spectrometry of poly (ethylene imine) s by electrospray ionization (ESI) and matrix-assisted laser desorption / ionization. 105–114 (2012) doi:10.1002/jms.2032.

137. Rivera-tirado, E. & Wesdemiotis, C. Characterization of polyethylenimine by electrospray ionization and matrix-assisted laser desorption / ionization. 876–883 (2011) doi:10.1002/jms.1964.

138. Rahme, K. *et al.* PEGylated gold nanoparticles: Polymer quantification as a

function of PEG lengths and nanoparticle dimensions. *RSC Adv.* **3**, 6085–6094 (2013).

139. Liu, Y. *et al.* Synthesis, stability, and cellular internalization of gold nanoparticles containing mixed peptide-poly(ethylene glycol) monolayers. *Anal. Chem.* **79**, 2221–2229 (2007).

140. Stiufiuc, R. *et al.* One-step synthesis of PEGylated gold nanoparticles with tunable surface charge. *J. Nanomater.* **2013**, (2013).

141. Hernández, S. Tunable Nanocomposite Membranes for Water Remediation and Separations. (2017) doi:10.13023/ETD.2017.042.

142. Amirova, A., Kirila, T., Kurlykin, M., Tenkovtsev, A. & Filippov, A. Influence of cross-linking degree on hydrodynamic behavior and stimulus-sensitivity of derivatives of branched polyethyleneimine. *Polymers (Basel).* **12**, (2020).

143. Curtis, K. A. *et al.* Unusual salt and pH induced changes in polyethylenimine solutions. *PLoS One* **11**, 1–20 (2016).

144. Carnerero, J. M., Sánchez-Coronilla, A., Martín, E. I., Jimenez-Ruiz, A. & Prado-Gotor, R. Quantification of nucleobases/gold nanoparticles interactions: Energetics of the interactions through apparent binding constants determination. *Phys. Chem. Chem. Phys.* **19**, 22121–22128 (2017).

145. Shin, J. Y. *et al.* Low molecular weight polyethylenimine for efficient transfection of human hematopoietic and umbilical cord blood-derived CD34+ cells. *Biochim. Biophys. Acta - Gen. Subj.* **1725**, 377–384 (2005).

146. Malloggi, C. *et al.* Comparative evaluation and optimization of off-the-shelf cationic polymers for gene delivery purposes. *Polym. Chem.* **6**, 6325–6339 (2015).

147. Liu, B. & Liu, J. Methods for preparing DNA-functionalized gold nanoparticles, a key reagent of bioanalytical chemistry. *Anal. Methods* **9**, 2633–2643 (2017).

148. Zhang, X., Servos, M. R. & Liu, J. Instantaneous and quantitative functionalization of gold nanoparticles with thiolated DNA using a pH-assisted and surfactant-free route. *J. Am. Chem. Soc.* **134**, 7266–7269 (2012).

149. Karumuthil-Melethil, S. *et al.* Dendritic Cell-Directed CTLA-4 Engagement during Pancreatic β Cell Antigen Presentation Delays Type 1 Diabetes. *J. Immunol.* **184**, 6695–6708 (2010).

150. You, H., Iino, R., Watanabe, R. & Noji, H. Winding single-molecule double-stranded DNA on a nanometer-sized reel. *Nucleic Acids Res.* **40**, (2012).

151. Symmons, M. F., Bokma, E., Koronakis, E., Hughes, C. & Koronakis, V. The assembled structure of a complete tripartite bacterial multidrug efflux pump. *Proc. Natl. Acad. Sci. U. S. A.* **106**, 7173–7178 (2009).

152. Janganan, T. K. *et al.* Evidence for the assembly of a bacterial tripartite multidrug pump with a stoichiometry of 3:6:3. *J. Biol. Chem.* **286**, 26900–26912 (2011).

153. Backer, M. V. *et al.* Vascular endothelial growth factor selectively targets boronated dendrimers to tumor vasculature. *Mol. Cancer Ther.* **4**, 1423–1429 (2005).

154. Zhou, H. *et al.* Development and characterization of a potent immunoconjugate targeting the Fn14 receptor on solid tumor cells. *Mol. Cancer Ther.* **10**, 1276–1288 (2011).

155. Vijayakameswara Rao, N., Ko, H., Lee, J. & Park, J. H. Recent progress and advances in stimuli-responsive polymers for cancer therapy. *Front. Bioeng. Biotechnol.* **6**, (2018).

156. Chang, M. *et al.* Smart linkers in polymer-drug conjugates for tumor-targeted delivery. *J. Drug Target.* **24**, 475–491 (2016).

157. Gamcsik, M. P., Kasibhatla, M. S., Teeter, S. D. & Colvin, O. M. Glutathione levels in human tumors. *Biomarkers* **17**, 671–691 (2012).

158. Gosselin, M. A., Guo, W. & Lee, R. J. Efficient gene transfer using reversibly cross-linked low molecular weight polyethylenimine. *Bioconjug. Chem.* **12**, 989–994 (2001).

159. Latorre, A., Couleaud, P., Aires, A., Cortajarena, A. L. & Somoza, Á. Multifunctionalization of magnetic nanoparticles for controlled drug release: A general approach. *Eur. J. Med. Chem.* **82**, 355–362 (2014).

160. Liu, Q. & Zhu, M. Determination of molar ratio of primary secondary and tertiary amines in polymers by applying derivatization and NMR spectroscopy. *Polym. Test.* **56**, 174–179 (2016).

161. Arbab, A. S. *et al.* Comparison of transfection agents in forming complexes with ferumoxides, cell labeling efficiency, and cellular viability. *Mol. Imaging* **3**, 24–32 (2004).

162. Peters, J. P. & Maher, L. J. *DNA curvature and flexibility in vitro and in vivo*. *Quarterly Reviews of Biophysics* vol. 43 (2010).

163. Carvalho, J. *et al.* Aptamer-based Targeted Delivery of a G-quadruplex Ligand in Cervical Cancer Cells. *Sci. Rep.* **9**, 1–12 (2019).

164. Dias, N. & Stein, C. A. Antisense oligonucleotides: Basic concepts and mechanisms. *Mol. Cancer Ther.* **1**, 347–355 (2002).

165. Roberts, T. C., Langer, R. & Wood, M. J. A. Advances in oligonucleotide drug delivery. *Nat. Rev. Drug Discov.* **19**, 673–694 (2020).

166. Mehta, M. *et al.* Chemico-Biological Interactions Oligonucleotide therapy : An emerging focus area for drug delivery in chronic in fl ammatory respiratory diseases. *Chem. Biol. Interact.* **308**, 206–215 (2019).

167. Jackson, A. L. *et al.* Expression profiling reveals off-target gene regulation by RNAi. *Nat. Biotechnol.* **21**, 635–638 (2003).

168. Grimm, D. *et al.* Fatality in mice due to oversaturation of cellular microRNA/short hairpin RNA pathways. *Nat. Biotechnol.* **441**, 537–541 (2006).

169. Dominski, Z. & Kole, R. Restoration of correct splicing in thalassemic pre-mRNA by antisense oligonucleotides. *Proc Natl Acad Sci USA* **90**, 8673–8677 (1993).

170. Wan, L. & Dreyfuss, G. Splicing-Correcting Therapy for SMA. *Cell* **170**, 5 (2017).

171. Ward, A. J., Norrbom, M., Chun, S., Bennett, C. F. & Rigo, F. Nonsense-mediated decay as a terminating mechanism for antisense oligonucleotides. *Nucleic Acids Res.* **42**, 5871–5879 (2014).

172. Wu, H. *et al.* Determination of the Role of the Human RNase H1 in the Pharmacology of DNA-like Antisense Drugs. *J. Biol. Chem.* **279**, 17181–17189 (2004).

173. Crooke, S. T. Molecular Mechanisms of Antisense Oligonucleotides. *Nucleic Acids Ther.* 1–8 (2017) doi:10.1089/nat.2016.0656.

174. Devos, S. L. & Miller, T. M. Antisense Oligonucleotides : Treating Neurodegeneration at the Level of RNA. *J. Am. Soc. Exp. Neurother.* (2013) doi:10.1007/s13311-013-0194-5.

175. Danielsen, M. B. *et al.* Gapmer Antisense Oligonucleotides Containing 2',3'-Dideoxy-2'-fluoro-3'-C-hydroxymethyl-β-d-lyxofuranosyl Nucleotides Display Site-Specific RNase H Cleavage and Induce Gene Silencing. *Chem. - A Eur. J.* **26**, 1368–1379 (2020).

176. Stanton, R. *et al.* Chemical modification study of antisense gapmers. *Nucleic Acid Ther.* **22**, 344–359 (2012).

177. Lima, W. F., De Hoyos, C. L., Liang, X. H. & Crooke, S. T. RNA cleavage products generated by antisense oligonucleotides and siRNAs are processed by the RNA surveillance machinery. *Nucleic Acids Res.* **44**, 3351–3363 (2016).

178. Parikh, N. *et al.* Effects of TP53 mutational status on gene expression patterns across 10 human cancer types. *J. Pathol.* **232**, 522–533 (2014).

179. Royds, J. A. & Iacopetta, B. p53 and diseas : when the guardian angel fails. *Cell Death Differ.* 1017–1026 (2006) doi:10.1038/sj.cdd.4401913.

180. Laptenko, O. & Prives, C. Transcriptional regulation by p53: one protein , many possibilities. *Cell Death Differ.* 951–961 (2006) doi:10.1038/sj.cdd.4401916.

181. Xie, M. *et al.* Mutational landscape and significance across 12 major cancer types. *Nature* **502**, 333–339 (2014).

182. Kim, M. P. & Lozano, G. Mutant p53 partners in crime. *Cell Death Differ.* (2018) doi:10.1038/cdd.2017.185.

183. Blandino, G., Levine, A. J. & Oren, M. Mutant p53 gain of function: Differential effects of different p53 mutants on resistance of cultured cells to chemotherapy. *Oncogene* (1999) doi:10.1038/sj.onc.1202314.

184. Valenti, F. *et al.* Gain of function mutant p53 proteins cooperate with E2F4 to transcriptionally downregulate RAD17 and BRCA1 gene expression. *Oncotarget* **6**, 5547–5566 (2015).

185. Di Agostino, S. *et al.* Gain of function of mutant p53: The mutant p53/NF-Y protein complex reveals an aberrant transcriptional mechanism of cell cycle regulation. *Cancer Cell* **10**, 191–202 (2006).

186. Fiorini, C. *et al.* Mutant p53 stimulates chemoresistance of pancreatic adenocarcinoma cells to gemcitabine. *Biochim. Biophys. Acta - Mol. Cell Res.* **1853**, 89–100 (2015).

187. Zhou, G. *et al.* Gain-of-Function Mutant p53 Promotes Cell Growth and Cancer Cell Metabolism via Inhibition of AMPK Activation. *Mol. Cell* **54**, 960–974 (2014).

188. Cordani, M. *et al.* Mutant p53 proteins counteract autophagic mechanism sensitizing cancer cells to mTOR inhibition. *Mol. Oncol.* **10**, 1008–1029 (2016).

189. Cordani, M. *et al.* Mutant p53 proteins alter cancer cell secretome and tumour microenvironment: Involvement in cancer invasion and metastasis. *Cancer Letters* vol. 376 303–309 (2016).

190. Chuang, H. C. *et al.* The p53-reactivating small molecule RITA induces senescence in head and neck cancer cells. *PLoS One* (2014) doi:10.1371/journal.pone.0104821.

191. Lambert, J. M. R. *et al.* PRIMA-1 Reactivates Mutant p53 by Covalent Binding to the Core Domain. *Cancer Cell* (2009) doi:10.1016/j.ccr.2009.03.003.

192. Zhang, S. *et al.* Small-molecule NSC59984 restores p53 pathway signaling and antitumor effects against colorectal cancer via p73 activation and degradation of mutant p53. *Cancer Res.* (2015) doi:10.1158/0008-5472.CAN-13-1079.

193. Foggetti, G. *et al.* Autophagy induced by SAHA affects mutant P53 degradation and cancer cell survival. *Biosci. Rep.* (2019) doi:10.1042/BSR20181345.

194. Selivanova, G. & Wiman, K. G. Reactivation of mutant p53: Molecular mechanisms and therapeutic potential. *Oncogene* (2007) doi:10.1038/sj.onc.1210295.

195. Ubby, I. *et al.* Cancer therapeutic targeting using mutant–p53-specific siRNAs. *Oncogene* (2019) doi:10.1038/s41388-018-0652-y.

196. Kundu, A. K. *et al.* Novel siRNA formulation to effectively knockdown mutant p53 in osteosarcoma. *PLoS One* (2017) doi:10.1371/journal.pone.0179168.

197. Toschi, L., Finocchiaro, G., Bartolini, S., Gioia, V. & Cappuzzo, F. Role of gemcitabine in cancer therapy. *Futur. Oncol.* **1**, 7–17 (2005).

198. Emmrich, S., Wang, W., John, K., Li, W. & Pützer, B. M. Antisense gapmers selectively suppress individual oncogenic p73 splice isoforms and inhibit tumor growth in vivo. *Mol. Cancer* **8**, 1–13 (2009).

199. Shimojo, M. *et al.* A gapmer antisense oligonucleotide targeting SRRM4 is a novel

therapeutic medicine for lung cancer. *Sci. Rep.* **9**, 2–5 (2019).

200. Blattner, C., Tobiasch, E., Litfen, M., Rahmsdorf, H. J. & Herrlich, P. DNA damage induced p53 stabilization: No indication for an involvement of p53 phosphorylation. *Oncogene* (1999) doi:10.1038/sj.onc.1202480.

201. Liang, S. Q. *et al.* mTOR mediates a mechanism of resistance to chemotherapy and defines a rational combination strategy to treat KRAS-mutant lung cancer. *Oncogene* **38**, 622–636 (2019).

202. Brown, D. M. A brief history of oligonucleotide synthesis. *Methods Mol. Biol.* **20**, 1–17 (1993).

203. Guzaev, A. P. *Solid-phase supports for oligonucleotide synthesis*. *Current Protocols in Nucleic Acid Chemistry* (2013). doi:10.1002/0471142700.nc0301s53.

204. Beaucage, S. L. & Caruthers, M. H. Deoxynucleoside phosphoramidites-A new class of key intermediates for deoxypolynucleotide synthesis. *Tetrahedron Lett.* **22**, 1859–1862 (1981).

205. Schaller, H., Weimann, G., Lerch, B. & Khorana, H. G. Studies on Polynucleotides. XXIV. The Stepwise Synthesis of Specific Deoxyribopolynucleotides. Protected Derivatives of Deoxyribonucleosides and New Syntheses of Deoxyribonucleoside-3' Phosphates. *J. Am. Chem. Soc.* **85**, 3821–3827 (1963).

206. McBride, L. J. & Caruthers, M. H. An investigation of several deoxynucleoside phosphoramidire useful for synthesizing deoxyoligonucleotides. *Tetrahedron Lett.* **14**, 245–248 (1983).

207. Brown, T., Brown (Jr), T., Broown, D. & Brown, A. Solid-phase oligonucleotides synthesis. https://www.atdbio.com/nucleic-acids-book.

208. Nimse, S. B., Song, K., Sonawane, M. D., Sayyed, D. R. & Kim, T. Immobilization techniques for microarray: Challenges and applications. *Sensors (Switzerland)* **14**, 22208–22229 (2014).

209. Mirkin, C. A., Letsinger, R. L., Mucic, R. C. & Storhoff, J. J. A DNA-based method for rationally assembling nanoparticles into macroscopic materials. *Nature* vol. 382 607–609 (1996).

210. Pérez-rentero, S., Grijalvo, S., Peñuelas, G., Fàbrega, C. & Eritja, R. Thioctic Acid Derivatives as Building Blocks to Incorporate DNA Oligonucleotides onto Gold Nanoparticles. 10495–10523 (2014) doi:10.3390/molecules190710495.

211. Winkler, J. Oligonucleotide conjugates for therapeutic applications. *Ther. Deliv.* **4**, 791–809 (2013).

212. Mollaev, M. *et al.* Type of pH sensitive linker reveals different time-dependent intracellular localization, in vitro and in vivo efficiency in alpha-fetoprotein receptor targeted doxorubicin conjugate. *Int. J. Pharm.* **559**, 138–146 (2019).

213. Latorre, A., Couleaud, P., Aires, A., Cortajarena, A. L. & Somoza, Á. Multifunctionalization of magnetic nanoparticles for controlled drug release: A

general approach. *Eur. J. Med. Chem.* **82**, 355–362 (2014).

214. Giljohann, D. A. *et al.* Oligonucleotide loading determines cellular uptake of DNA-modified gold nanoparticles. *Nano Lett.* **7**, 3818–3821 (2007).

215. Kashida, H., Liang, X. & Asanuma, H. Rational Design of Functional DNA with a Non-Ribose Acyclic Scaffold. *Curr. Org. Chem.* **13**, 1065–1084 (2012).

216. Shahsavari, S. *et al.* Tritylation of Alcohols under Mild Conditions without Using Silver Salts. *Tetrahedron Lett.* **57**, 3877–3880 (2016).

217. Reese, C. B. Oligo- and poly-nucleotides: 50 years of chemical synthesis. *Org. Biomol. Chem.* **2**, 3851–3868 (2005).

218. Serafinowski, P. J. & Garland, P. B. Substituted 2-nitrobenzyltrichloroacetate esters for photodirected oligonucleotide detritylation in solid films. 3284–3291 (2008) doi:10.1039/b806902f.

219. Chaudhary, S. K., Cox, R. H. & Porter, J. Synthesis and characterization of 4-dimethylamino-k-triphenylmethylpyridinium chloride, a postulated intermediate in the tritylation of alcohols. *Tetrahedron Lett.* **22**, 1491–1494 (1981).

220. Porcaro, F. *et al.* Fluctuation Spectroscopy Analysis of Glucose Capped Gold Nanoparticles. *Langmuir* **32**, 13409–13417 (2016).

221. Zheng, M., Zhong, Y., Meng, F., Peng, R. & Zhong, Z. Lipoic acid modified low molecular weight polyethylenimine mediates nontoxic and highly potent in vitro gene transfection. *Mol. Pharm.* **8**, 2434–2443 (2011).

222. Kim, J.-H. *et al.* Synthesis and anti-melanogenic effects of lipoic acid-polyethylene glycol ester. *J. Pharm. Pharmacol.* **60**, 863–870 (2008).

223. Liu, Y. *et al.* Enhanced Reactive Oxygen Species Generation by Mitochondria Targeting of Anticancer Drug to Overcome Tumor Multidrug Resistance. *Biomacromolecules* **20**, 3755–3766 (2019).

224. Posch, C. *et al.* Detection of GNAQ mutations and reduction of cell viability in uveal melanoma cells with functionalized gold nanoparticles. *Biomed. Microdevices* **17**, (2015).

Annex

^{1}H-NMR Spectres

2,5-dioxopyrrolidin-1-yl-5-(1,2-dithiolan-3-yl)pentanoate (1)

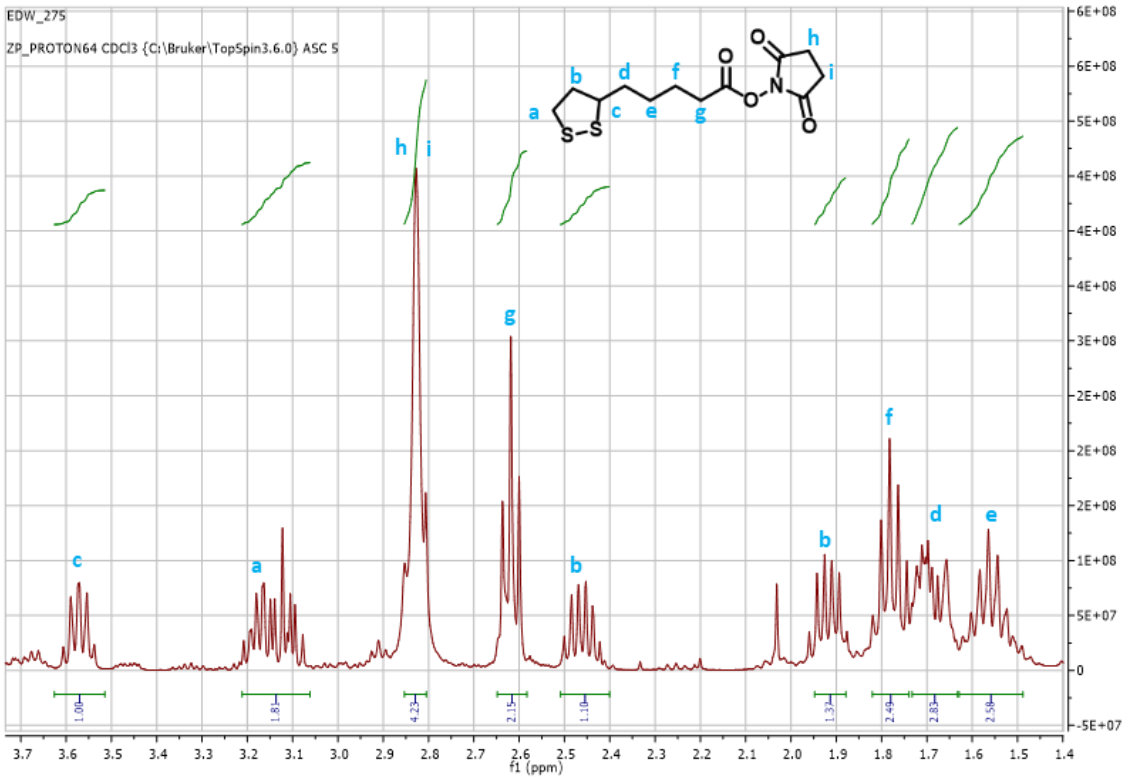

Annex Figure 1. ^{1}H-NMR spectrum of 2,5-dioxopyrrolidin-1-yl 5-(1,2-dithiolan-3-yl)pentanoate. (CDCl3, 400 MHz): δ 3.54 (dq, 1H), 3.11 (m, 2H), 2.8 (s, 4H), 2.57 (t, 2H), 2.41 (m, 1H), 1.88 (m, 1H), 1.72 (m, 2H), 1.67 (m, 2H), 1.52 (m, 2H).

LP-PEG (3000 MW) (4)

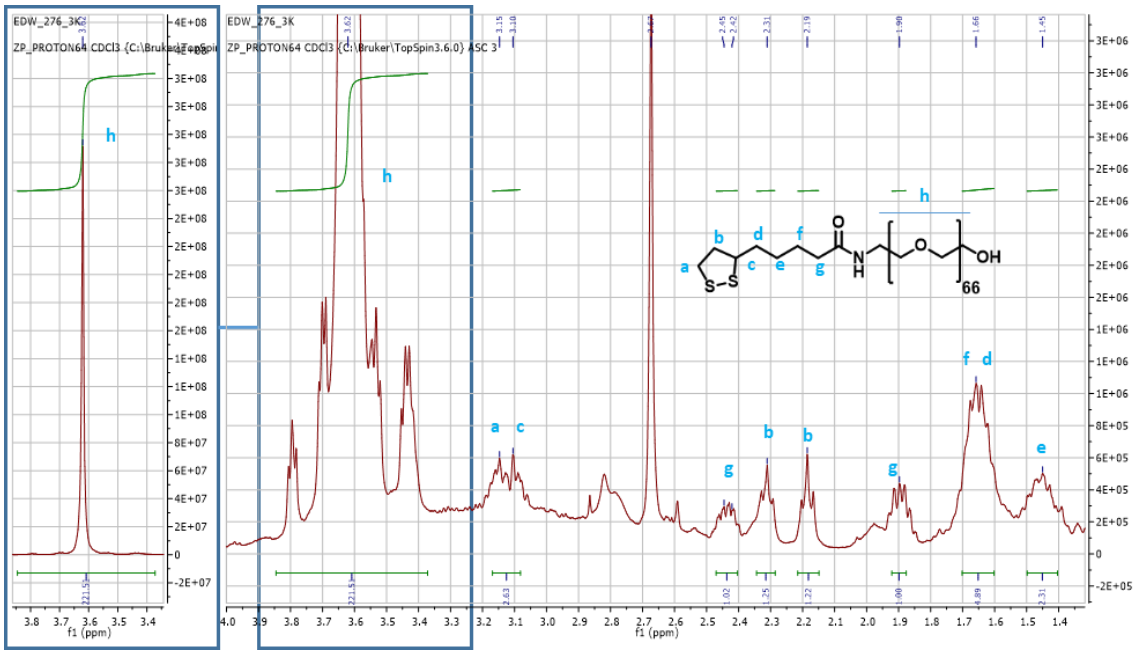

Annex Figure 2. ^{1}H-NMR spectrum of LP-PEG. ($CDCl_3$, 400 MHz): δ 3.74 (s, 258H), 3.42 (t, 2H), 3.24 (dd.47 (m, 1H), 2.53 (t, 2H), 2,3(t,2H), 2.03 (m, 1H), 1.79 (m, 1H), 1.66 (m, 4H), 1.46 (m, 2H).

LP-bPEI (2000 MW) (2)

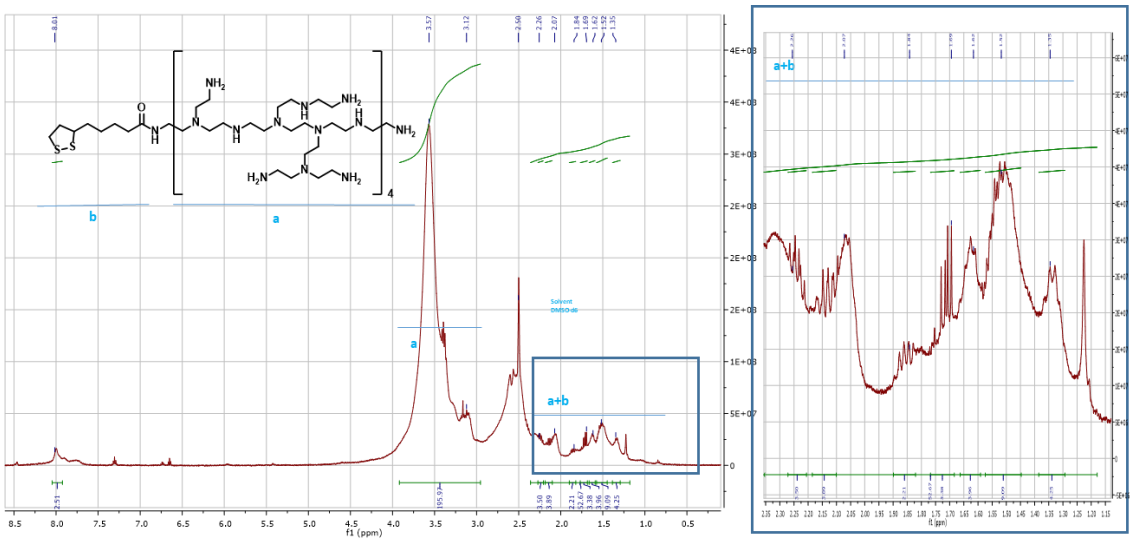

Annex Figure 3. ^{1}H-NMR spectrum of LP-bPEI 2 KDa. (DMSO-D6, 400 MHz): δ 8 (m, 3H), 4-2.82 (m, 199H), 1.88-0.98 (m, 57H).

LP- bPEI (25000 MW) (3)

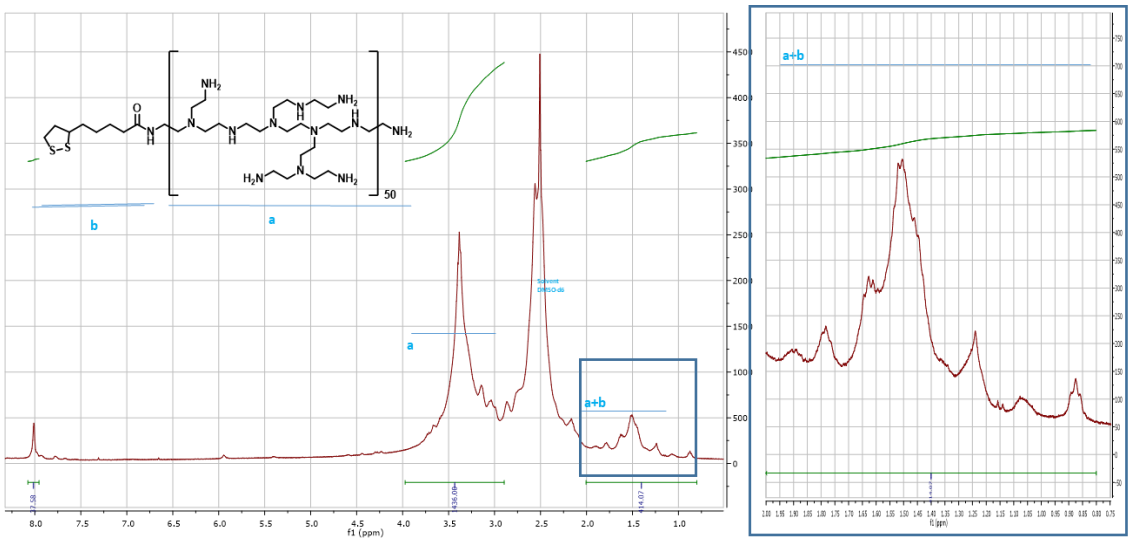

Annex Figure 4. ^{1}H-NMR spectrum of LP-bPEI 25 KDa. (DMSO-D6, 400 MHz): δ 8 (m, 37H), 4-2.82 (m, 1436H), 1.88-0.98 (m, 414H).

(2-pyridyldithio)propanoic acid (5)

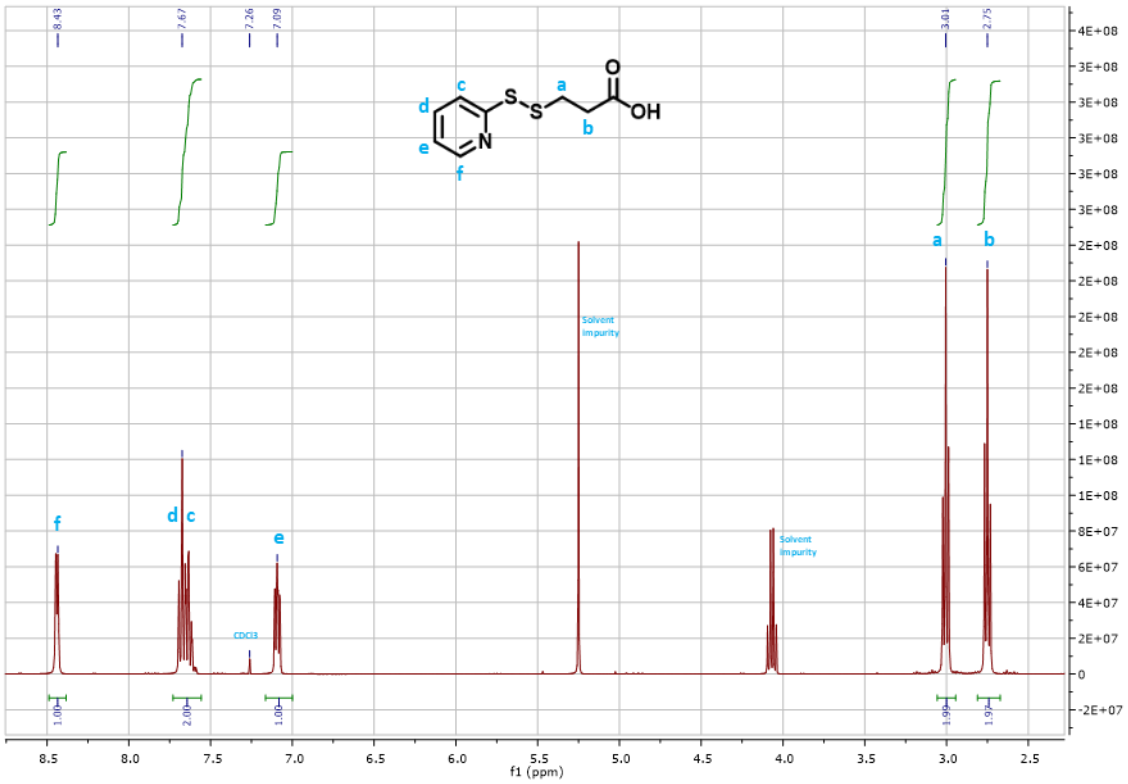

Annex Figure 5. ^{1}H-NMR spectrum of (2-pyridyldithio)propanoic acid. (CDCl3, 400 MHz): δ 8.43 (d, 1H), 7.67 (m, 2H), 7.09 (td, 1H), 3.01 (t, 2H), 2.75 (t, 2H).

Succinimidyl 3-(2-pyridyldithio)propionate (SPDP) (6)

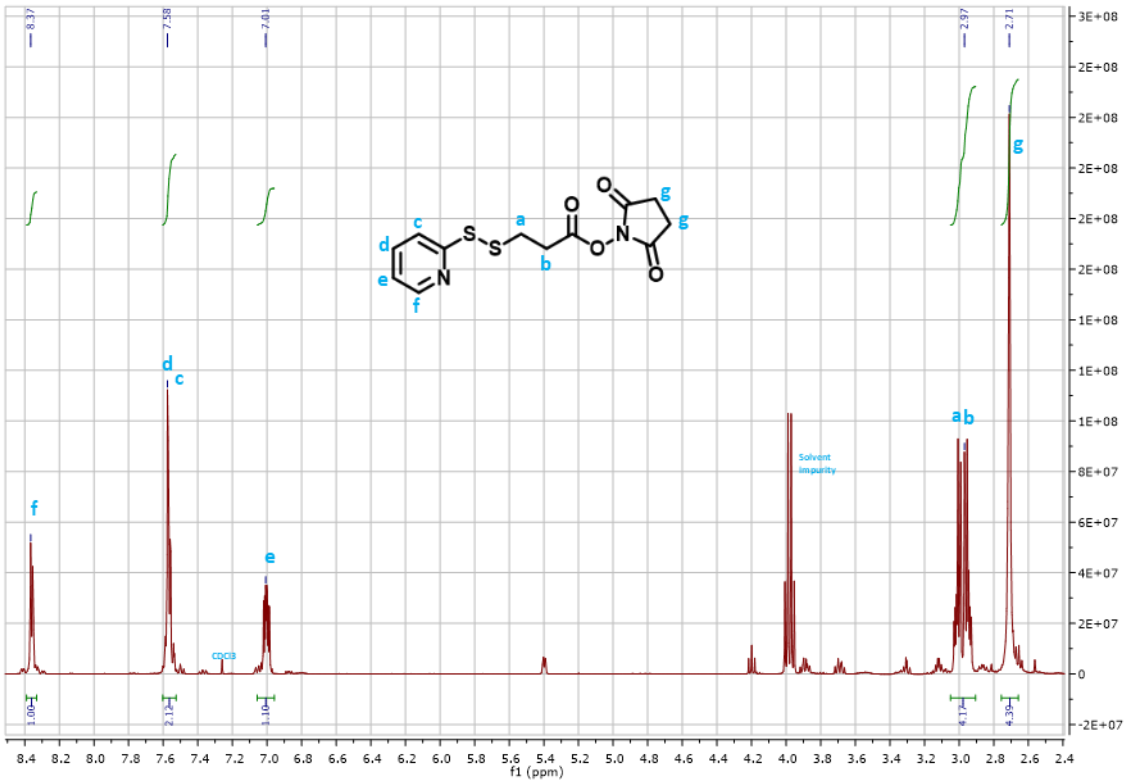

Annex Figure 6. ^{1}H-NMR spectrum of Succinimidyl 3-(2-pyridyldithio)propionate (PDP). ($CDCl_3$, 400 MHz): δ 8.37 (d, 1H), 7.58 (m, 2H), 7.01 (dt, 1H), 2.87 (m, 4H), 2.71 (s, 4H).

PDP-bPEI (2000 MW) (7)

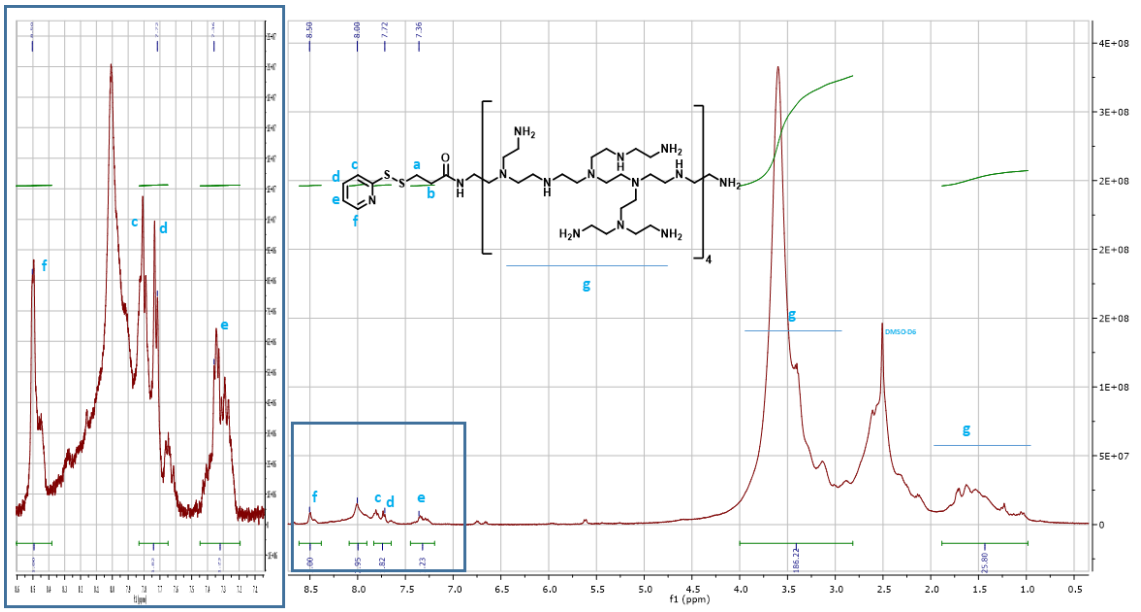

Annex Figure 7. ^{1}H-NMR spectrum of PDP-bPEI 2 KDa. (DMSO-D6, 400 MHz): δ 8.5 (m, 1H), 8 (m, 3H), 7.72 (m, 2H), 7.36 (1H), 4-2.82 (m, 185H), 1.88-0.98 (m, 25H).

PDP- bPEI (25000 MW) (8)

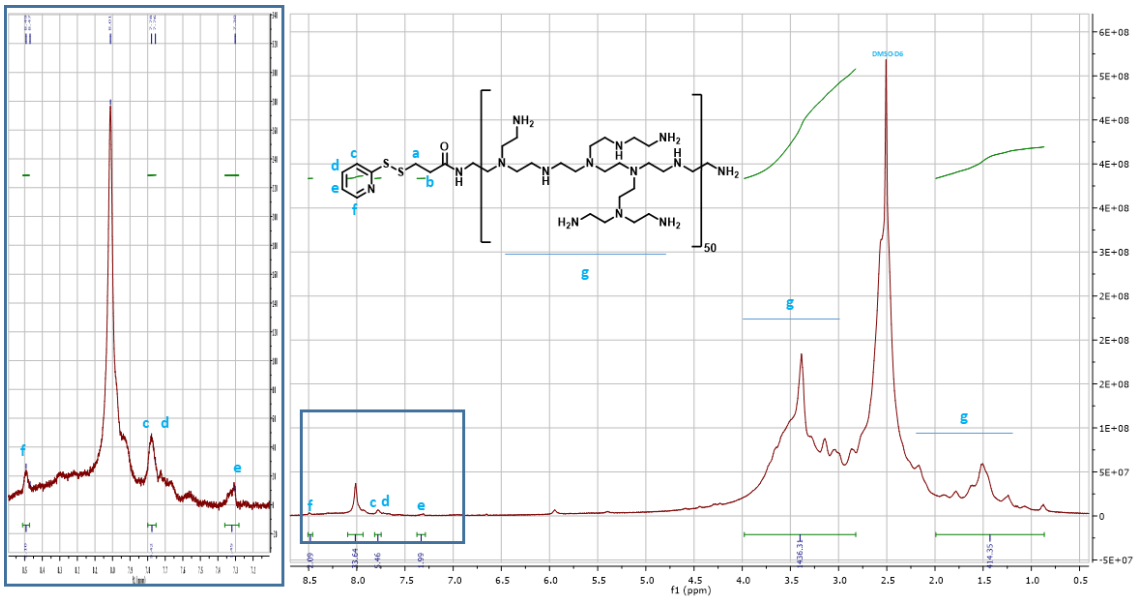

Annex Figure 8. ^{1}H-NMR spectrum of PDP-bPEI 25 KDa. (DMSO-D6, 400 MHz): δ 8.49 (m, 2H), 8 (m, 37H), 7.77 (m, 4H), 7.30 (2H), 4.1-2.8 (m, 1436H), 2.02-0.84 (m, 414H).

N-((2R,3R)-1,3-dihydroxybutan-2-yl)-3-mercaptopropanamide (9)

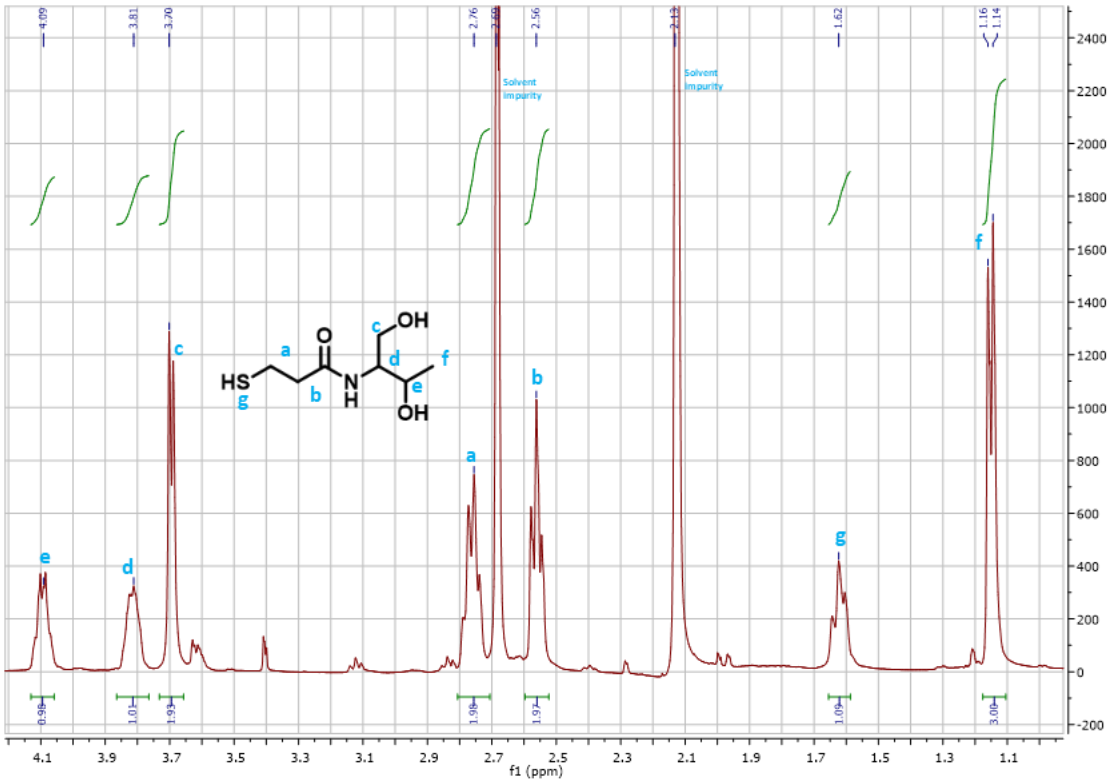

Annex Figure 9. ^{1}H-NMR spectrum of N-((2R,3R)-1,3-dihydroxybutan-2-yl)-3-mercaptopropanamide(9). (CDCl3, 400 MHz): δ 4.09 (dq, 1H), 3.81 (m, 1H), 3.70 (d, 2H), 2.76 (t, 2H), 2.56 (t,2 H), 1.62 (t, 1H), 1.16 (d, 3H).

N-((2R,3R)-1,3-dihydroxybutan-2-yl)-3-(pyridin-2-yldisulfanyl)-propanamide (10)

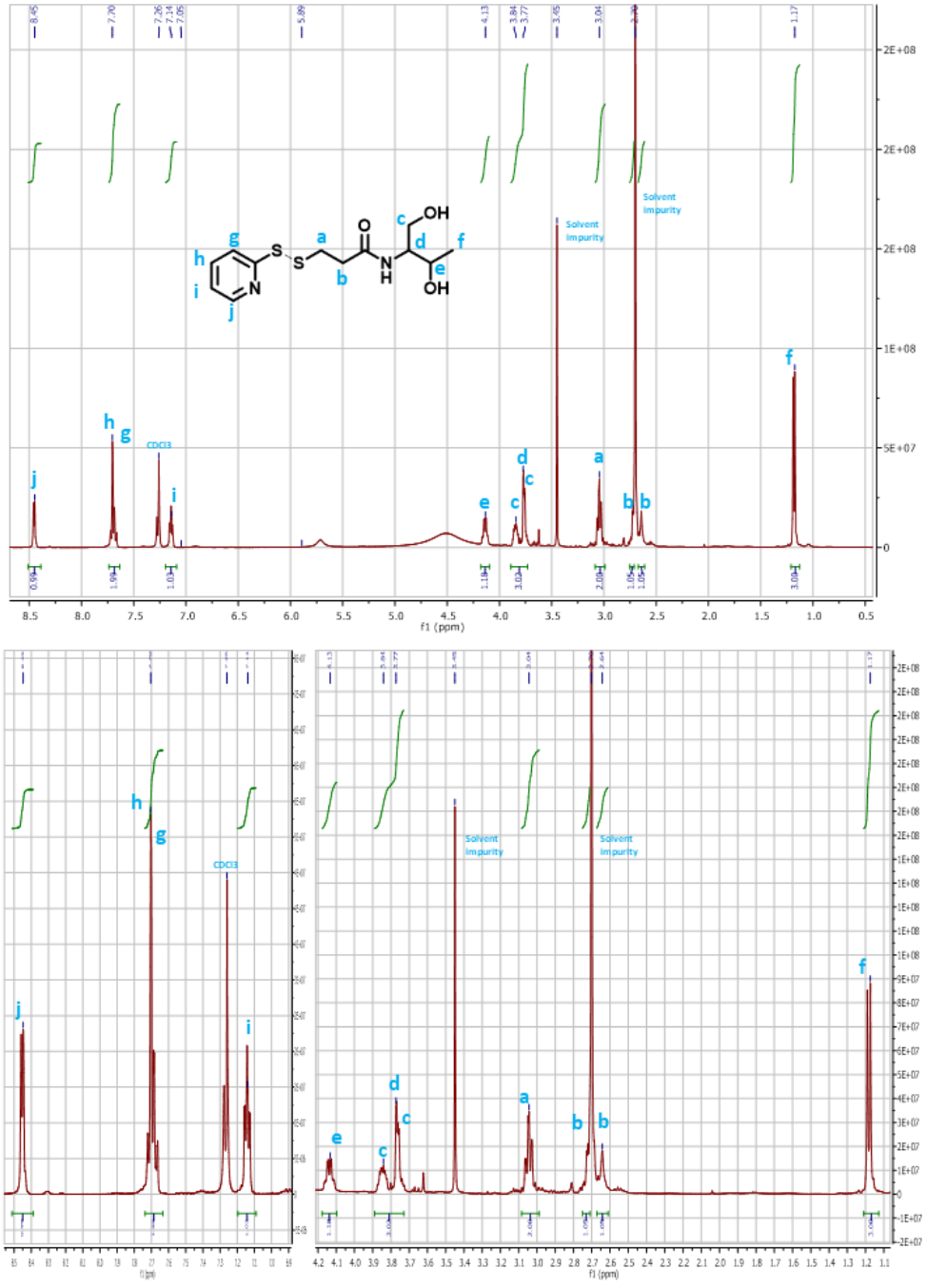

Annex Figure 10. ^{1}H-NMR spectrum of N-((2R,3R)-1,3-dihydroxybutan-2-yl)-3-(pyridin-2-yldisulfanyl)-propanamide (10)**.** (CDCl3, 400 MHz): δ 8.45 (d, 1H), 7.70 (m, 2H), 7.14 (t, 1H), 4.13 (m, 1H), 3.89-3.73 (m, 3H), 3.04 (td, 2H), 2.70 (m,1H), 2.64 (m,1H), 1.17 (d, 3H).

N-((2R,3R)-1-(bis(4-methoxyphenyl)(phenyl)methoxy)-3-hydroxybutan-2-yl)-3-(pyridin-2-yldisulfanyl)propenamide (11)

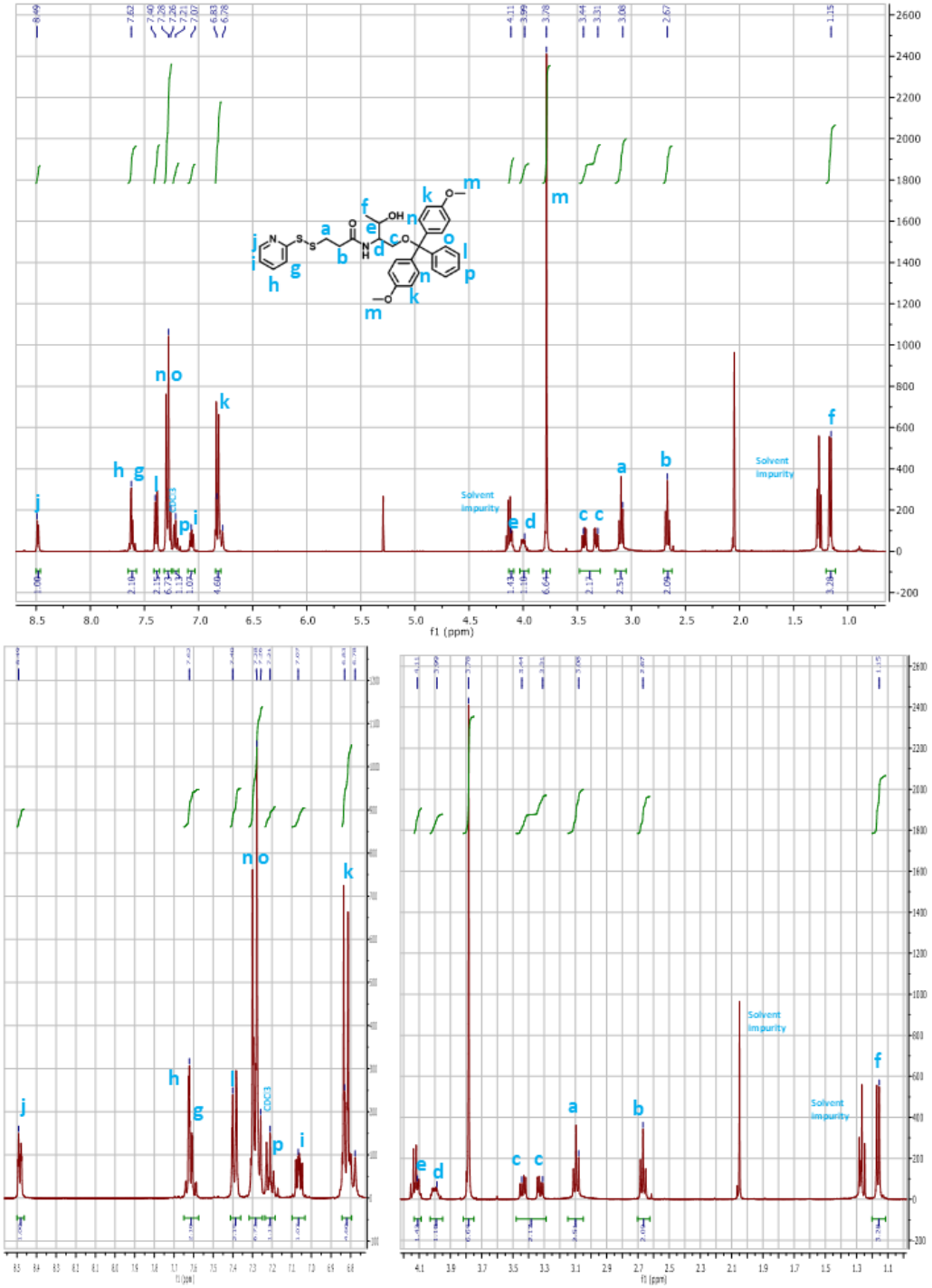

Annex Figure 11. ^{1}H-NMR spectrum of N-((2R,3R)-1-(bis(4-methoxyphenyl)(phenyl)methoxy)-3-hydroxybutan-2-yl)-3-(pyridin-2-yldisulfanyl)propenamide (11). (CDCl3, 400 MHz): δ 8.49 (d, 1H), 7.79-762 (m, 2H), 7.40(d, 2H), 7.32-7.27 (m, 6H), 7.21 (t, 1H), 7.07 (m,1H), 6.83 (d, 4H), 4.11 (m, 1H), 3.99 (m, 1H), 3.78 (s, 6H), 3.44 (dd, 1H), 3.31 (dd, 1H), 3.08 (t, 2H), 2.67 (t, 2H), 1.15 (d, 3H).

^{13}C-NMR Spectres

2,5-dioxopyrrolidin-1-yl-5-(1,2-dithiolan-3-yl)pentanoate(1)

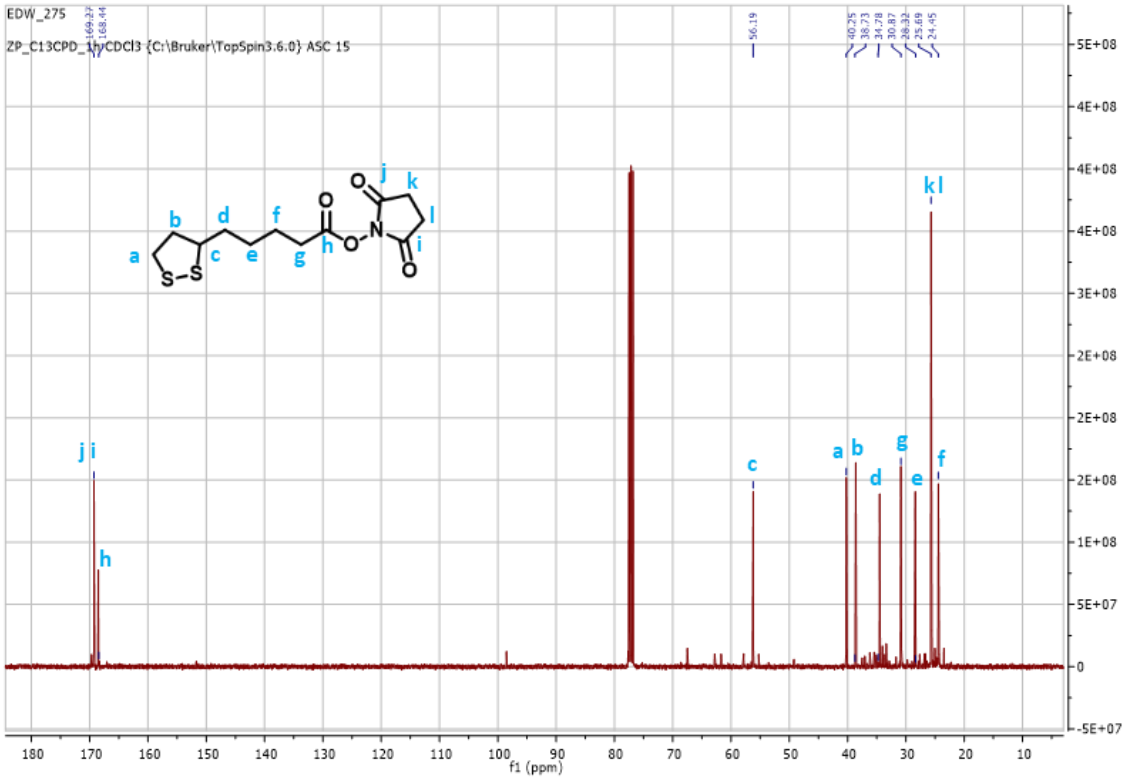

Annex Figure 12. ^{13}C-NMR spectrum of 2,5-dioxopyrrolidin-1-yl 5-(1,2-dithiolan-3-yl)pentanoate. ($CDCl_3$, 101 MHz): δ 169.27, 168.44, 56.19, 40.25, 38.73, 34.78, 30.87, 28.32, 25.69, 24.45.

LP-PEG (3000 MW)(4)

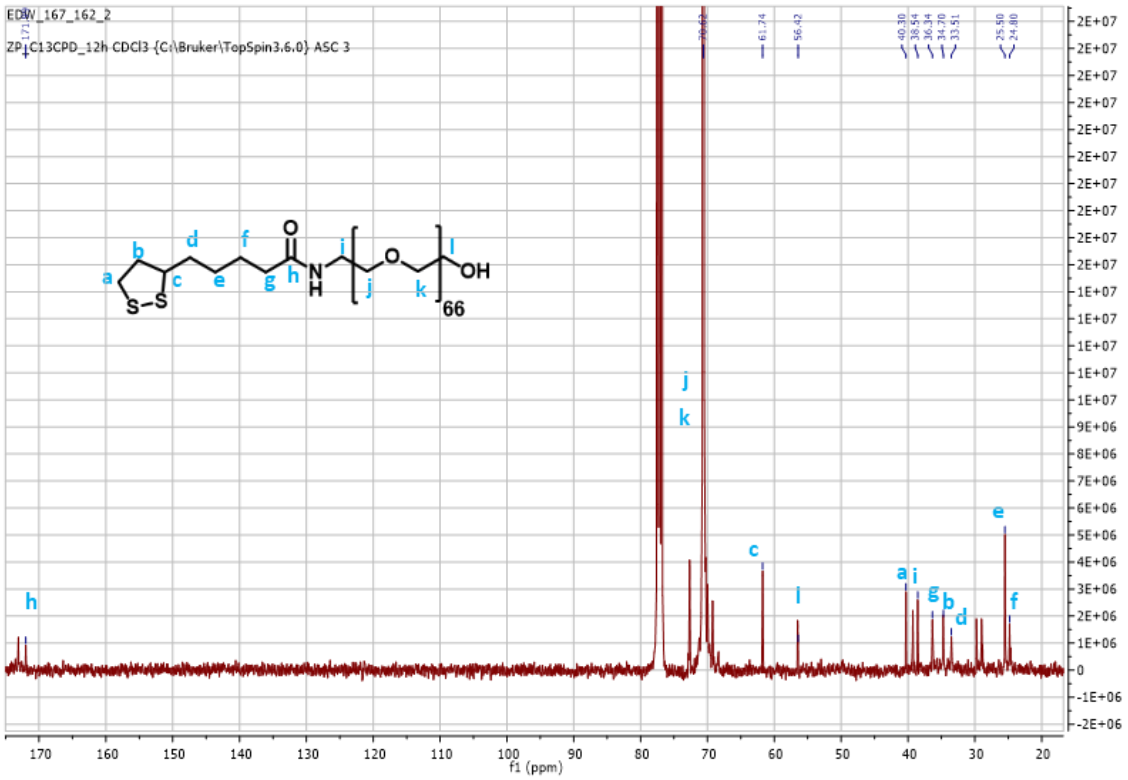

Annex Figure 13. ^{13}C-NMR spectrum of LP-PEG. ($CDCl_3$, 400 MHz): δ 173.1, 171.9, 70.6, 56.4, 40.3, 39.28, 38.5, 36.3, 34.7, 33.51, 29.8, 25.5, 24.8.

LP-bPEI (2000 MW) (2)

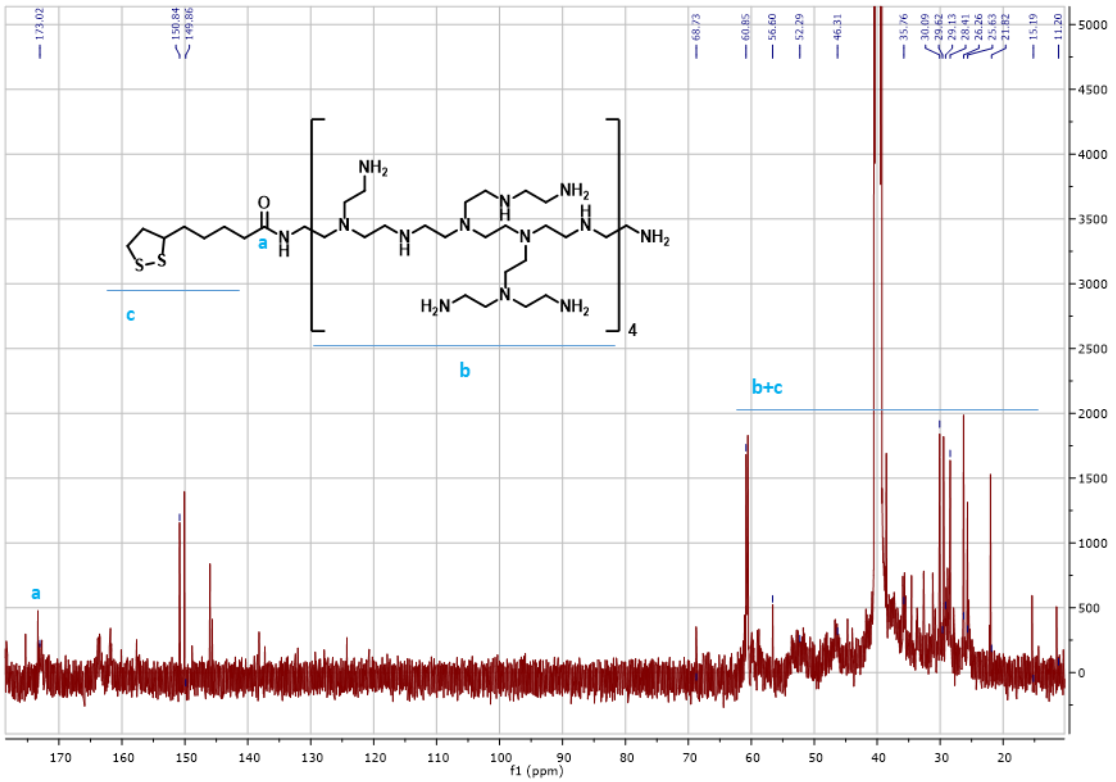

Annex Figure 14. ^{13}C-NMR spectrum of LP-bPEI 2 KDa. (DMSO-D6, 121 MHz,) δ 173.02, 150.84, 149.86, 68.73, 60.85, 56.60, 52.29, 46.31, 35.76, 30.09, 29.62, 29.13, 28.41, 26.26, 25.63, 21.82, 15.19, 11.20

LP- bPEI (25000 MW) (3)

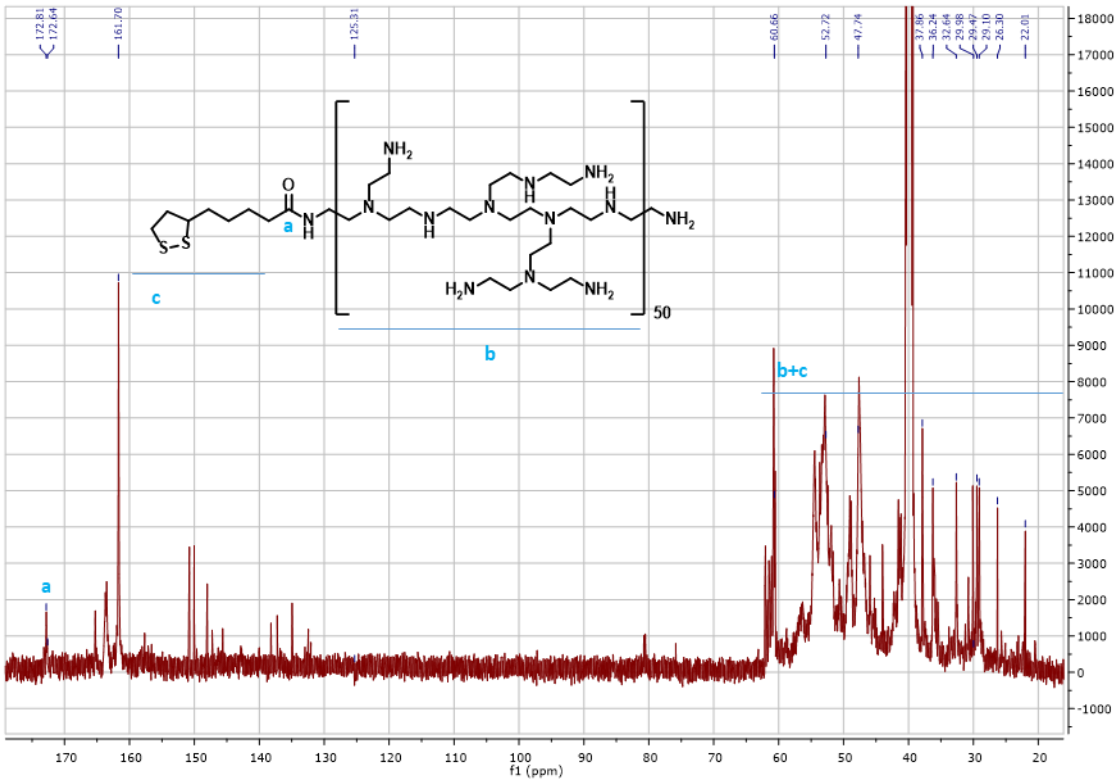

Annex Figure 15. ^{13}C-NMR spectrum of LP-bPEI 25 KDa. (DMSO-D6, 121 MHz,) δ 172.81, 161.70, 125.31, 60.66, 52.72, 47.74, 37.86, 36.24, 32.64, 29.98, 29.47, 29.10, 26.30, 22.01.

(2-pyridyldithio)propanoic acid(5)

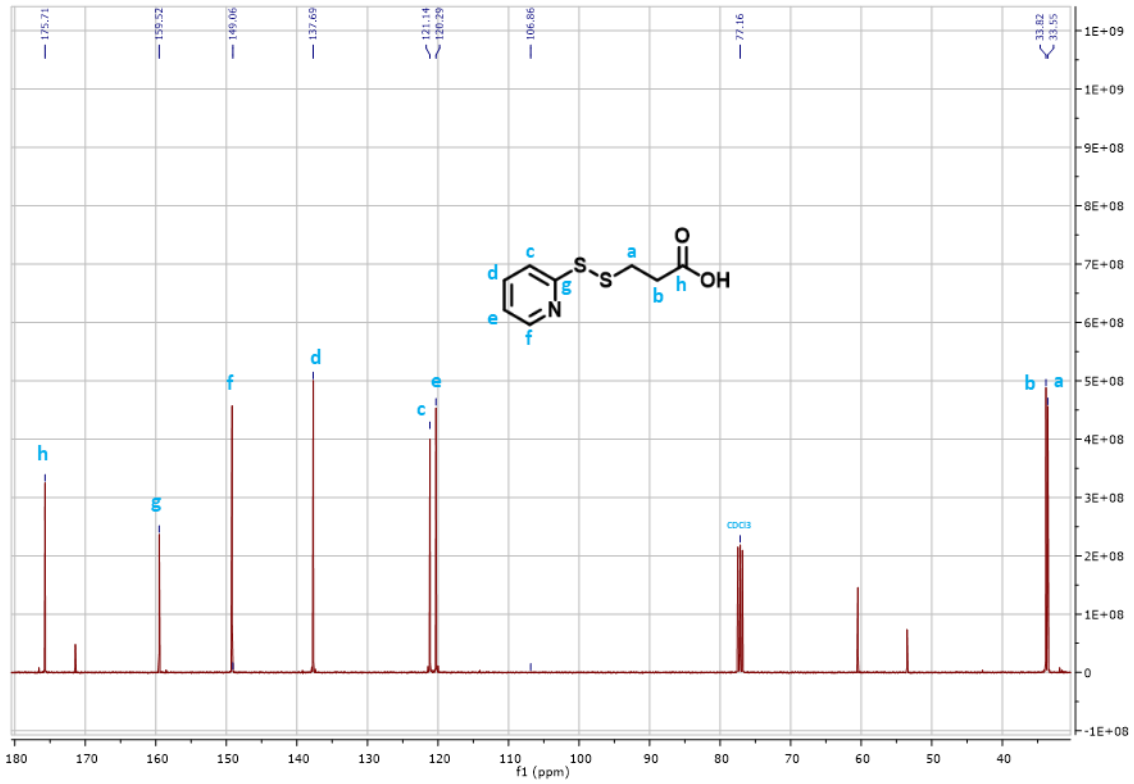

Annex Figure 16. ^{13}C-NMR spectrum of (2-pyridyldithio)-propanoic acid. ($CDCl_3$, 101 MHz): δ 175.72, 159.52, 149.06, 137.69, 121.14, 120.29, 33.82, 33.55.

Succinimidyl 3-(2-pyridyldithio)propionate (SPDP) (6)

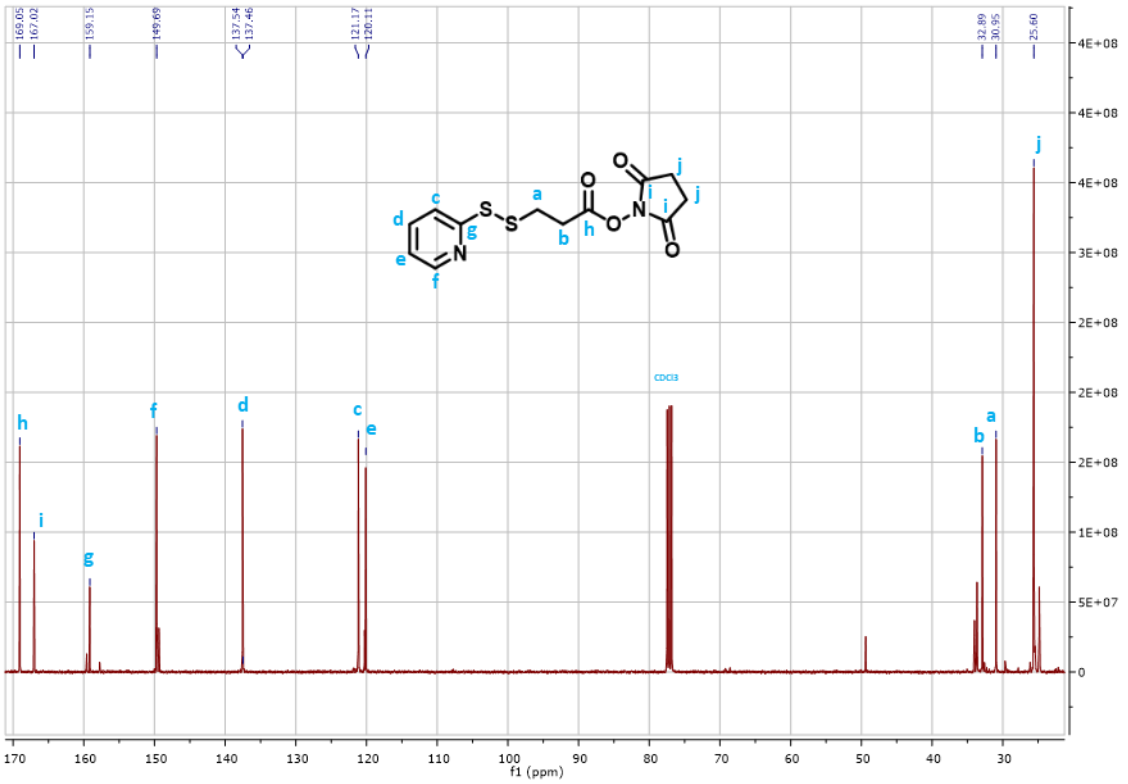

Annex Figure 17. ^{13}C-NMR spectrum of Succinimidyl 3-(2-pyridyldithio)propionate (SPDP). (CDCl3, 101 MHz): δ 169.05, 167.02, 159.15, 149.69, 137.54, 121.17, 120.11, 32.89, 30.95, 25.6.

PDP-bPEI (2000 MW) (7)

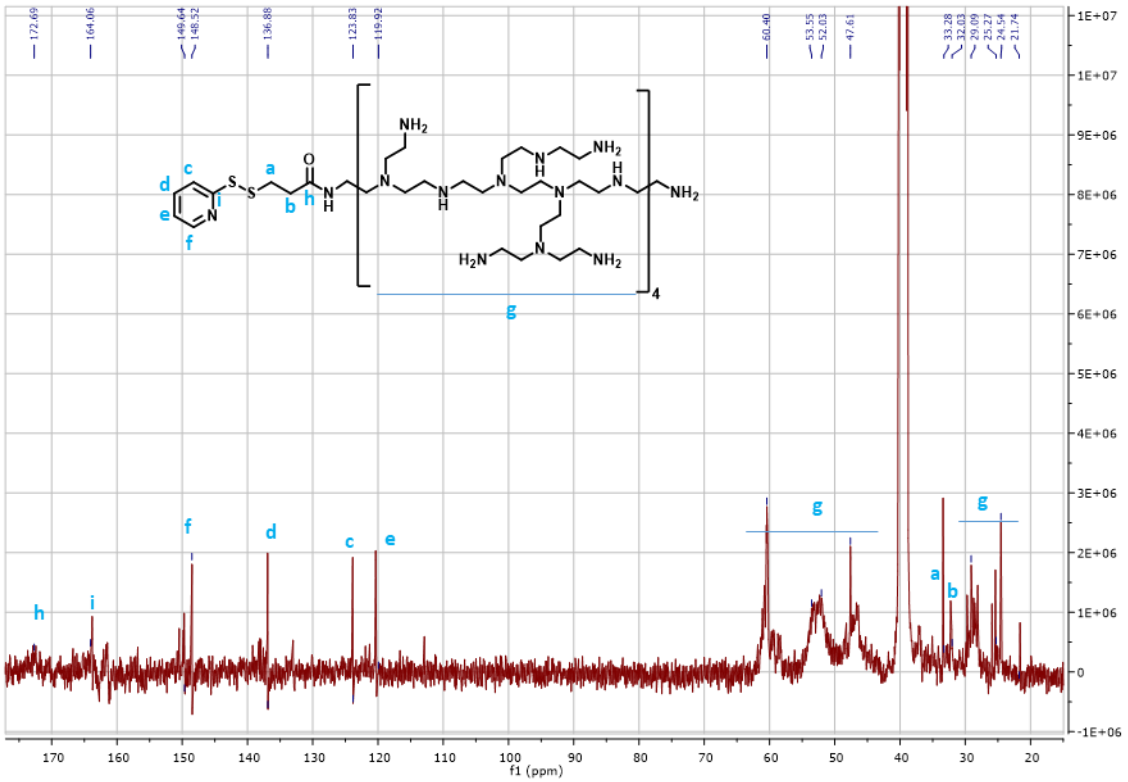

Annex Figure 18. ^{13}C-NMR spectrum of PDP-bPEI 2 KDa. (DMSO-D6, 101 MHz): δ 172.88, 164.18, 148.89, 137.25, 124.35, 120.73, 60.78, 53.50, 47.99, 33.64, 32.62, 29.47, 24.44, 21.73.

PDP-bPEI (25000 MW) (8)

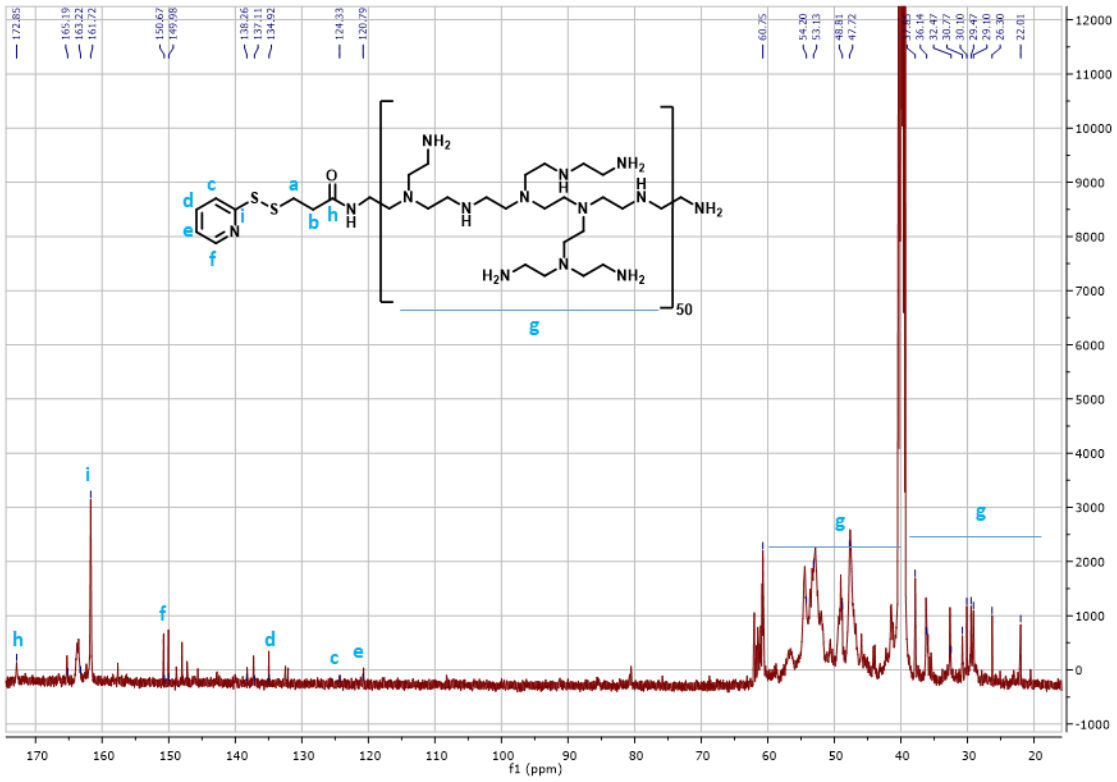

Annex Figure 19. ^{13}C-NMR spectrum of PDP-bPEI 25 KDa. (DMSO-D6, 126 MHz): δ 172.85, 165.19, 163.22, 161.72, 150.67, 149.98, 138.26, 137.11, 134.92, 124.33, 120.79, 60.75, 54.20, 53.13, 48.81, 47.72, 37.85, 36.14, 32.47, 30.77, 30.10, 29.47, 29.10, 26.30, 22.01.

N-((2R,3R)-1,3-dihydroxybutan-2-yl)-3-mercaptopropanamide(9)

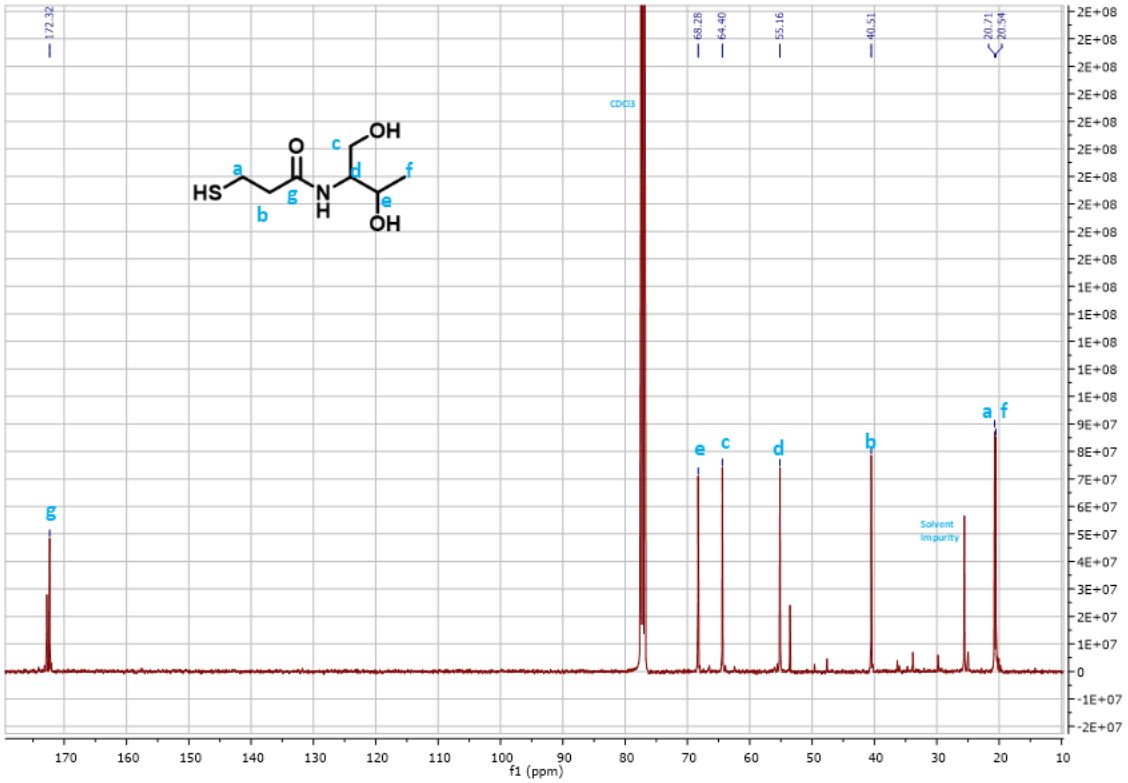

Annex Figure 20. ^{13}C-NMR spectrum of N-((2R,3R)-1,3-dihydroxybutan-2-yl)-3-mercaptopropanamide(9). (CDCl3, 101 MHz): δ 172.32, 68.28, 64.40, 55.16, 20.71, 20.54.

N-((2R,3R)-1,3-dihydroxybutan-2-yl)-3-(pyridin-2-yldisulfanyl)-propanamide (10)

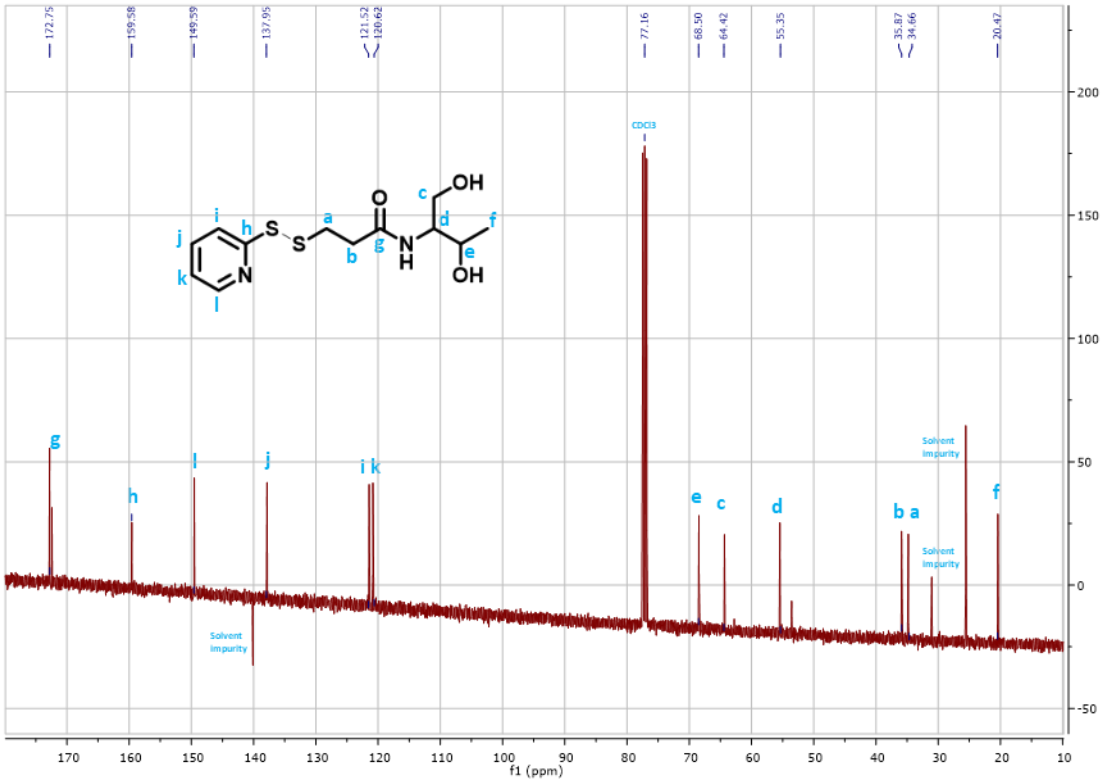

Annex Figure 21. ^{13}C-NMR spectrum of N-((2R,3R)-1,3-dihydroxybutan-2-yl)-3-(pyridin-2-yldisulfanyl)-propanamide (10)**.** (CDCl3, 101 MHz): δ 172.75, 159.58, 149.59, 137.95, 121.52, 120.62, 68.50, 64.42, 55.35, 35.87, 34.66, 20.47

N-((2R,3R)-1-(bis(4-methoxyphenyl)(phenyl)methoxy)-3-hydroxybutan-2-yl)-3-(pyridin-2-yldisulfanyl)propenamide (11)

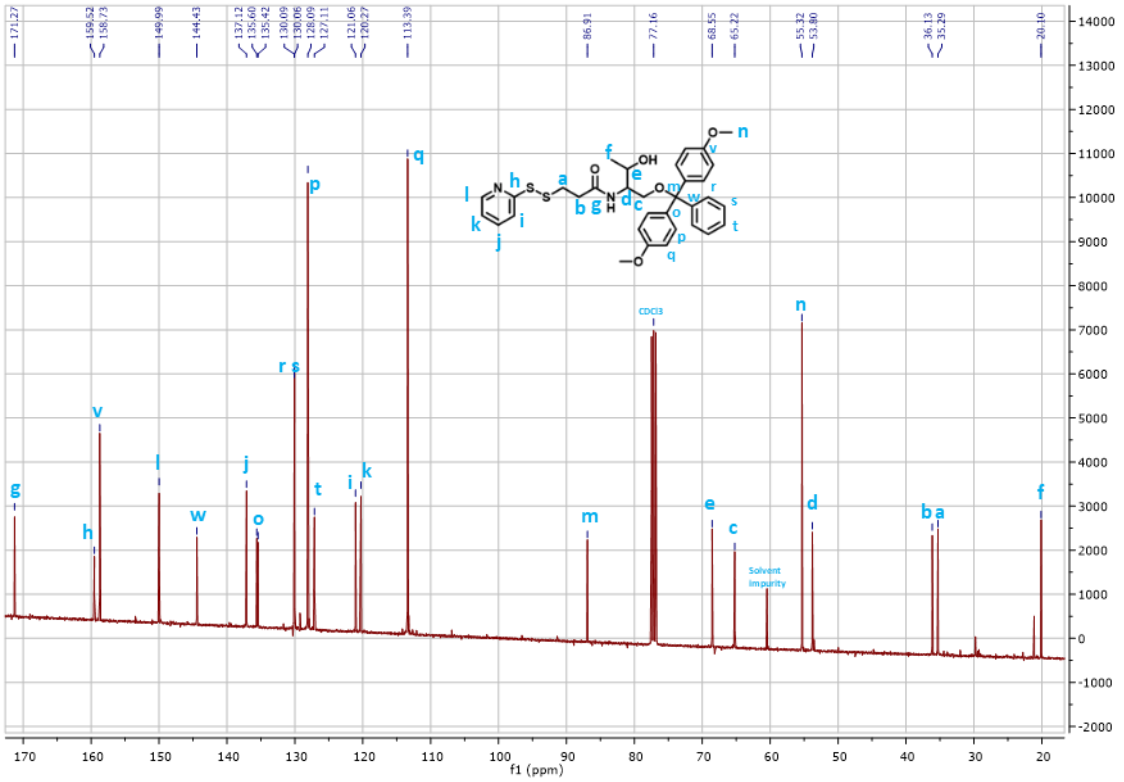

Annex Figure 22. ^{13}C-NMR spectrum of N-((2R,3R)-1-(bis(4-methoxyphenyl)(phenyl)methoxy)-3-hydroxybutan-2-yl)-3-(pyridin-2-yldisulfanyl)propenamide (11). (CDCl3, 101 MHz): δ 171.27, 159.52, 158.73, 149.99, 144.43, 137.12, 135.60, 135.42, 130.09, 130.06, 128.09, 127.11, 121.06, 120.27, 113.39, 86.91, 68.55, 65.22, 55.32, 53.80, 36.13, 35.29, 20.10

Mass spectrometry (MS)

2,5-dioxopyrrolidin-1-yl-5-(1,2-dithiolan-3-yl)pentanoate(1)

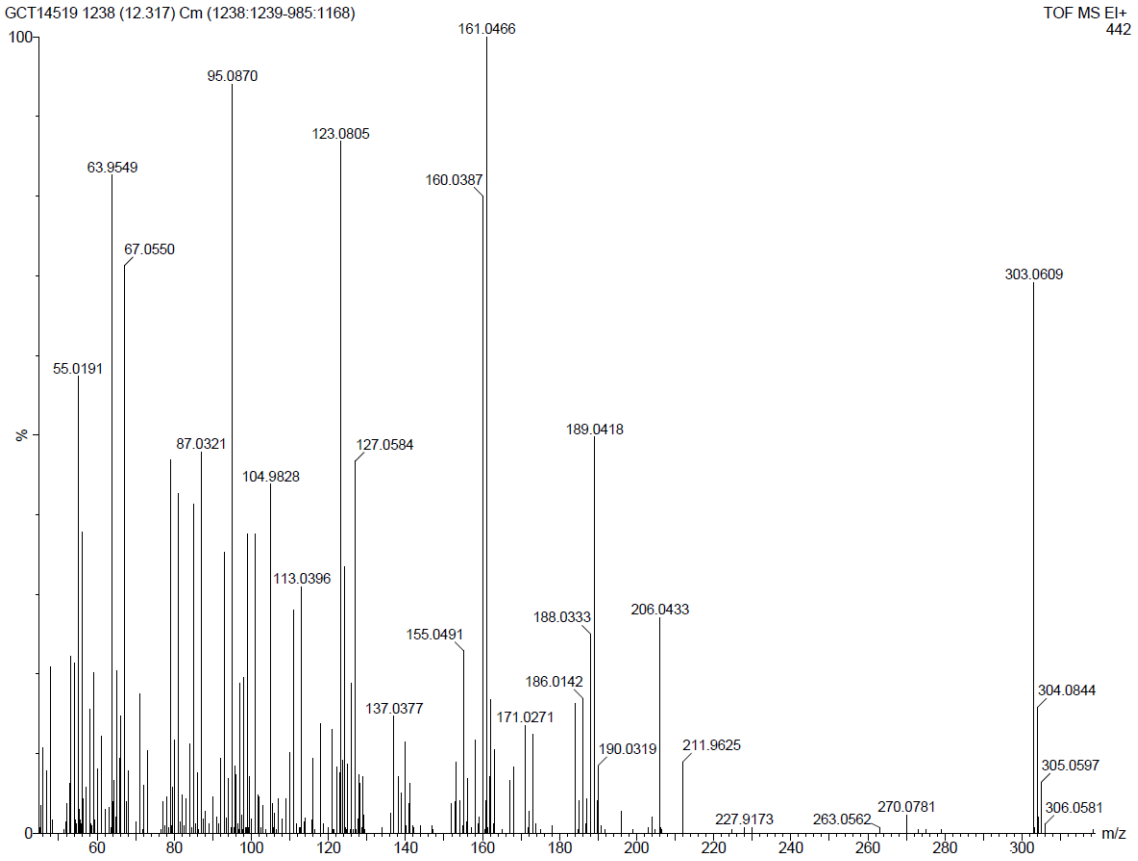

Annex Figure 23. MS (EI) spectrum of 2,5-dioxopyrrolidin-1-yl-5-(1,2-dithiolan-3-yl)pentanoate. *m/z* calculated for $C_{12}H_{17}NO_4S_2$ (M^+) 303.05, found 303.05.

LP-PEG (3000 MW).(4)

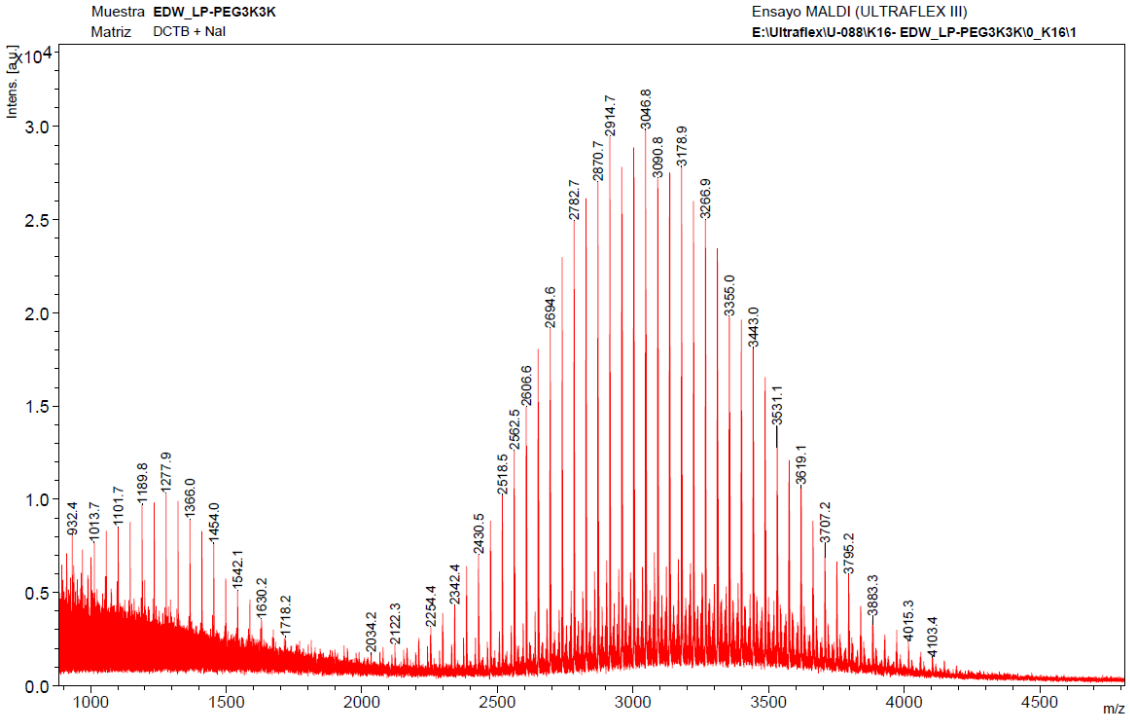

Annex Figure 24. MS (MALDI) spectrum of LP-PEG 3 KDa. m/z calculated for $C_8H_{13}OS_2(PEG)_{66}$ 3047.7, found 3046.8

LP-bPEI (2000 MW)(2)

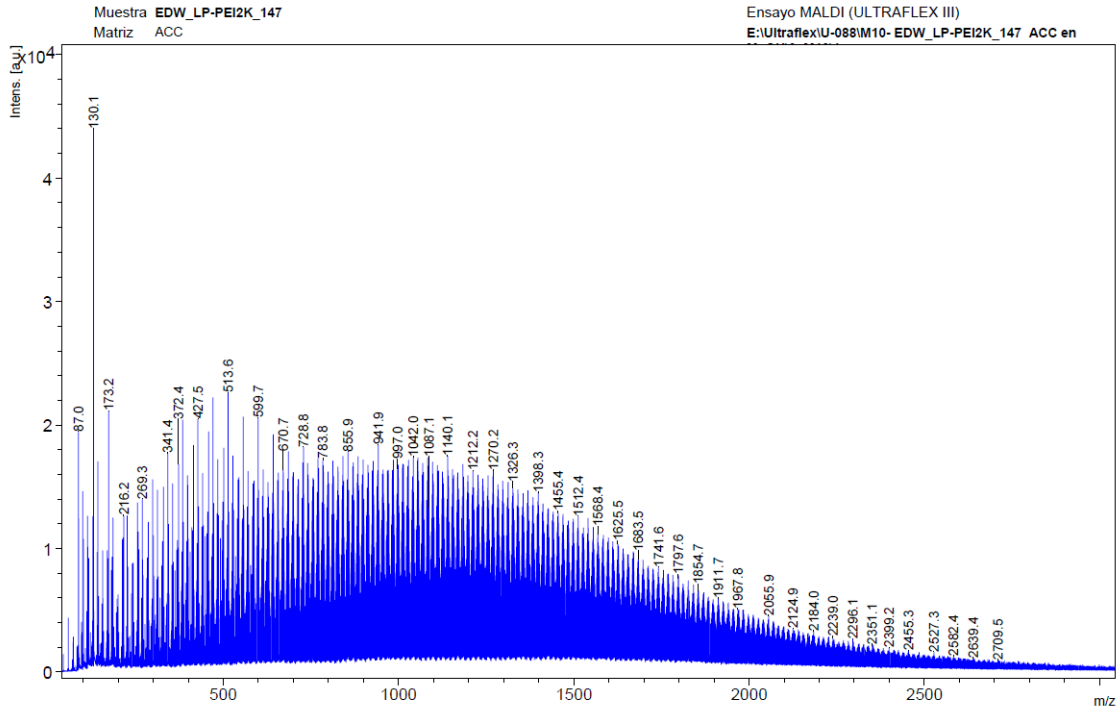

Annex Figure 25. MS (MALDI) spectrum of LP-bPEI 2 KDa. 130.1 corresponding to the polymer fragment $[C_2H_4NH]_3$.

LP- bPEI (25000 MW) (3)

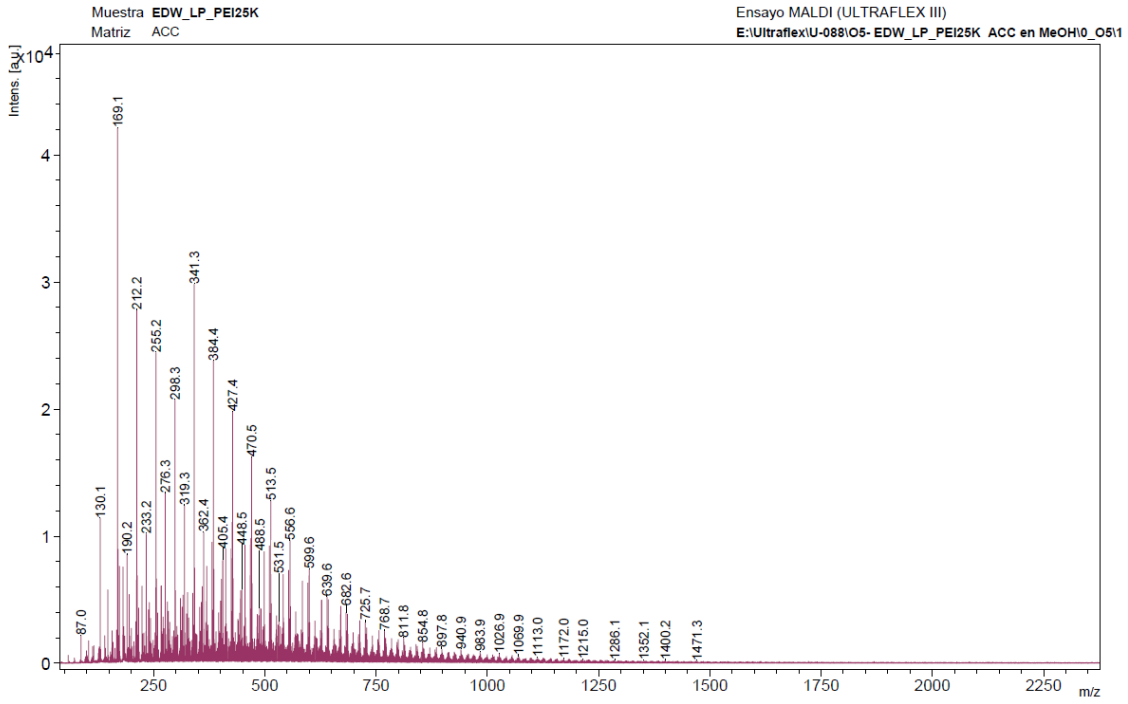

Annex Figure 26. MS (MALDI) spectrum of LP-bPEI 25 KDa. 159.1 corresponding to the polymer fragment $[C_2H_4NH]_3$

(2-pyridyldithio)propanoic acid (5)

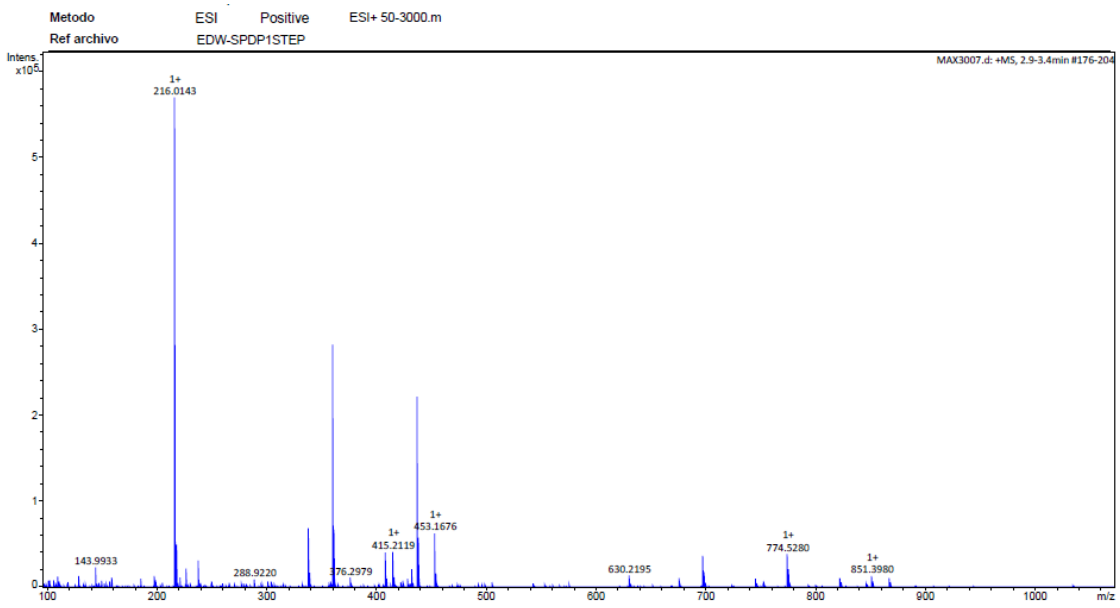

Annex Figure 27. MS (ESI) spectrum of (2-pyridyldithio)propanoic acid. 216 (100) [M+H], 218 (5) [M+Na]. (ESI) calculated for C8H9NO2S2 (M+H) 216.01, found 216.014

Succinimidyl 3-(2-pyridyldithio)propionate (SPDP) (6)

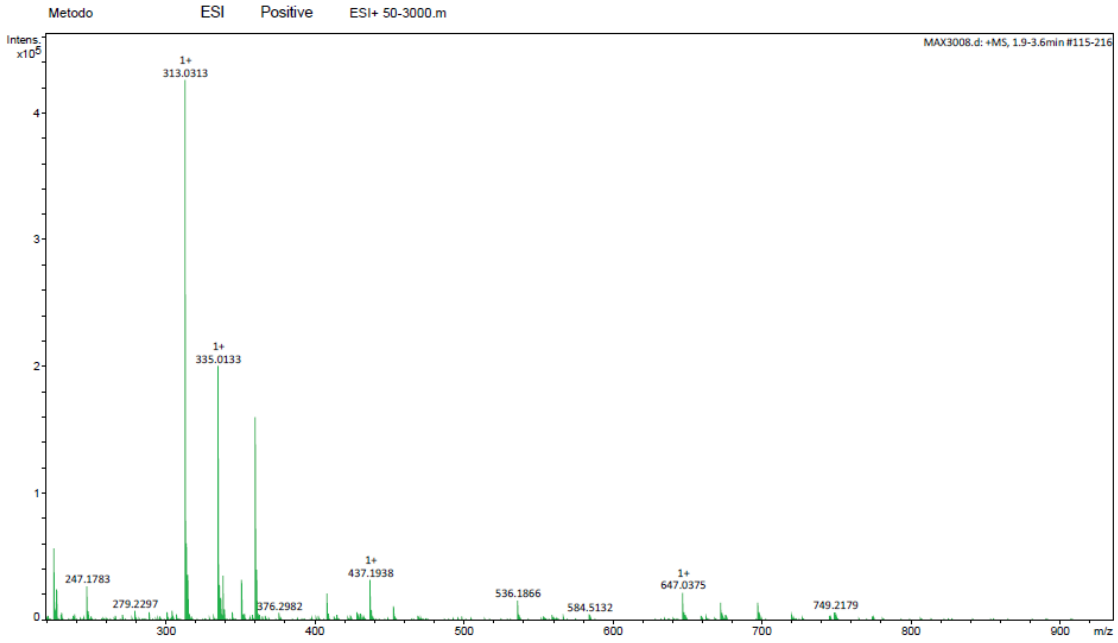

Annex Figure 28. MS (ESI) spectrum of Succinimidyl 3-(2-pyridyldithio)propionate (SPDP). 313 (100) [M+H], 335(47) [M+Na]. (ESI) calculated for C13H13NO4S2 (M+H) 312.03, found 313.01

PDP- bPEI (2000 MW) (7)

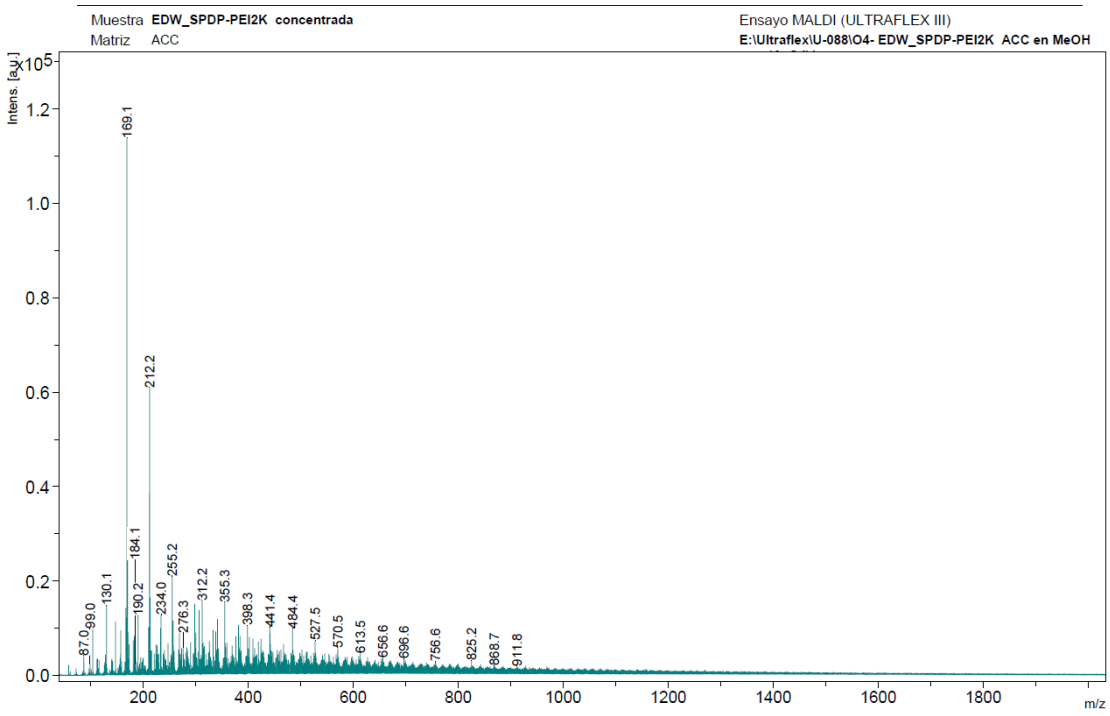

Annex Figure 29. MS (MALDI) spectrum of PDP-bPEI 2 KDa . 169.1 and 212.2, corresponding to polymer fragments due to their difference of 43 units, which corresponds with the monomer [C2H4NH].

PDP- bPEI (25000 MW) (8)

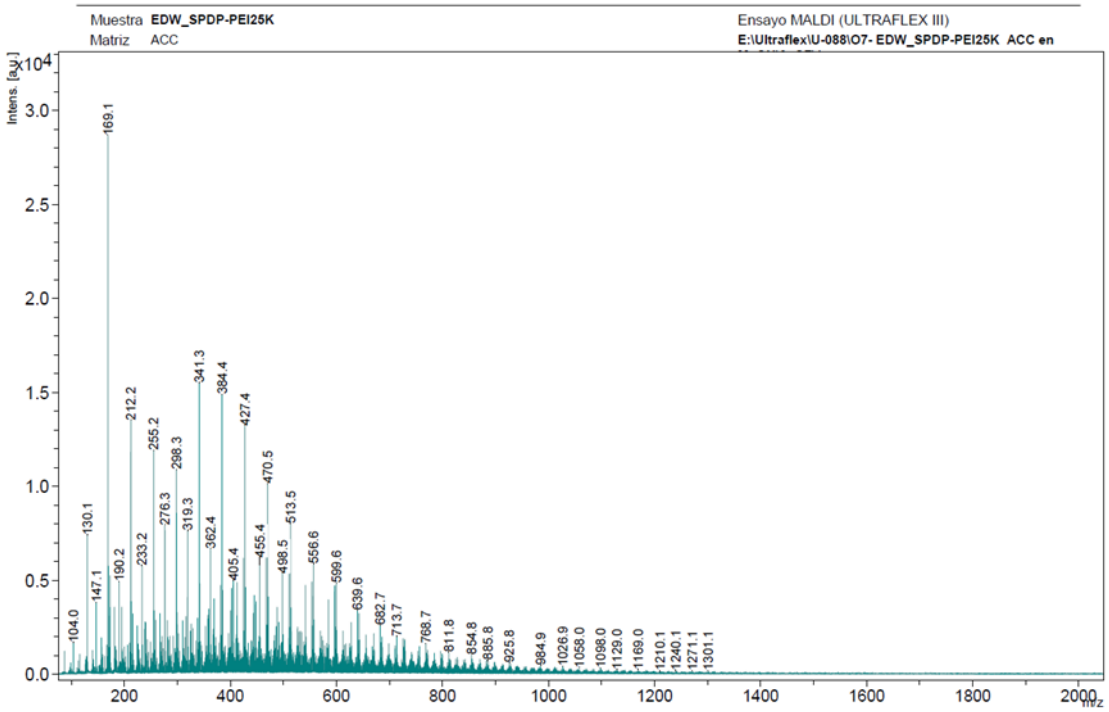

Annex Figure 30. MS (MALDI) spectrum of PDP-bPEI 25 KDa. 169.1 and 341.3, corresponding to polymer fragments due to their difference of 172 units, which corresponds with the fragment $[C_2H_4NH]_4$.

N-((2R,3R)-1,3-dihydroxybutan-2-yl)-3-mercaptopropanamide(9)

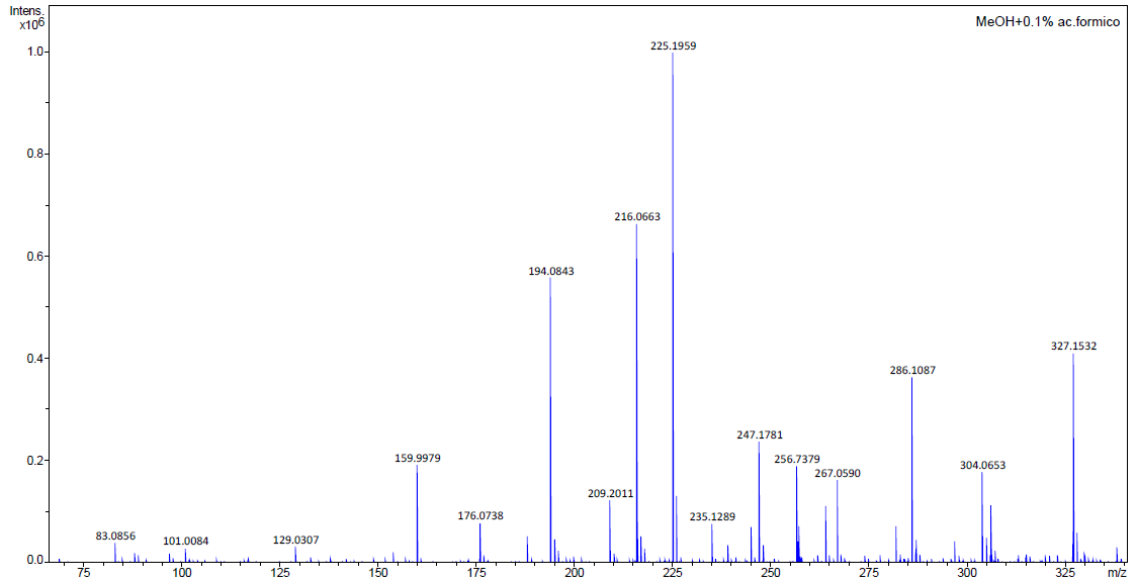

Annex Figure 31. MS(ESI) spectrum of N-((2R,3R)-1,3-dihydroxybutan-2-yl)-3-mercaptopropanamide(9). m/z (%) 194 (56), 216 $[M+Na]^+$ (100). (ESI) calculated for $C_7H_{15}NO_3S$ $[M+H]^+$ 194.08, found 194.08.

N-((2R,3R)-1,3-dihydroxybutan-2-yl)-3-(pyridin-2-yldisulfanyl)-propanamide (10)

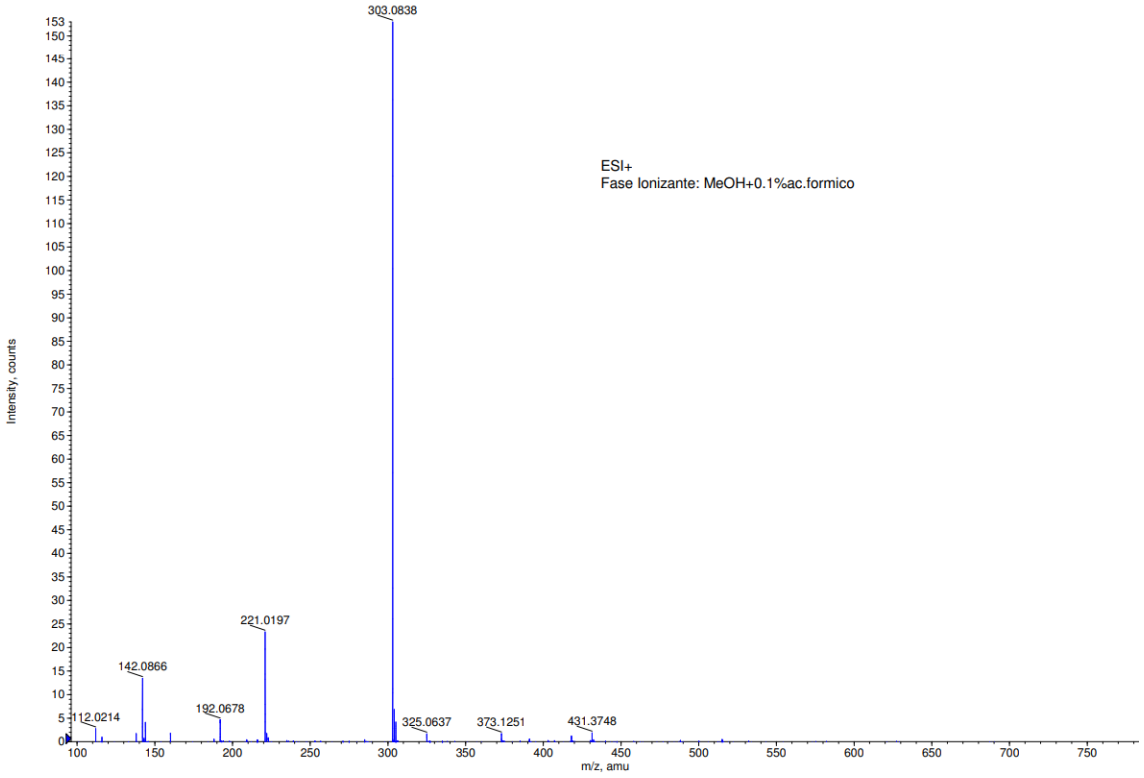

Annex Figure 32. MS(ESI) spectrum of N-((2R,3R)-1,3-dihydroxybutan-2-yl)-3-(pyridin-2-yldisulfanyl)-propanamide (10)**.** m/z (%) 142 (9), 221 (15), 303 $[M+1]^+$ (100). (ESI) calculated for $C_{12}H_{18}N_2O_3S_2$ $[M+H]^+$ 302.08, found 302.08.

N-((2R,3R)-1-(bis(4-methoxyphenyl)(phenyl)methoxy)-3-hydroxybutan-2-yl)-3-(pyridin-2-yldisulfanyl)propenamide (11)

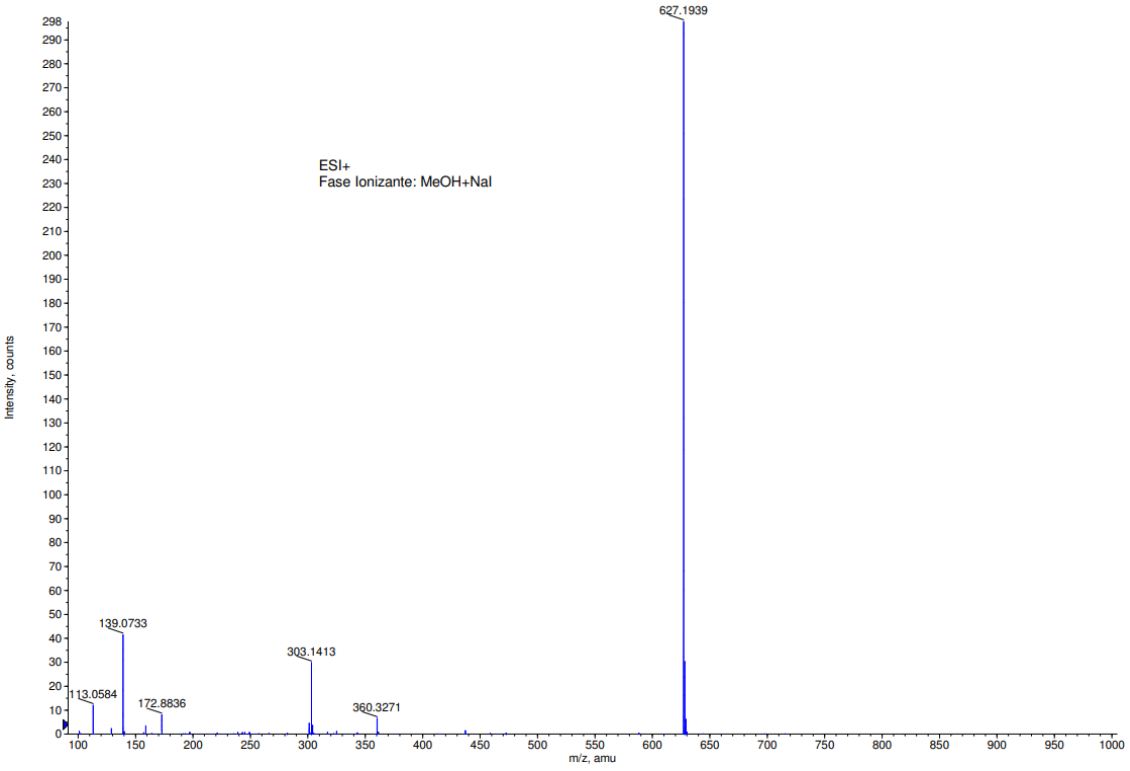

Annex Figure 33. MS(ESI) spectrum of N-((2R,3R)-1-(bis(4-methoxyphenyl)(phenyl)methoxy)-3-hydroxybutan-2-yl)-3-(pyridin-2-yldisulfanyl)propenamide (11). m/z (%) 129 (14), 303 (10), 627 $[M+Na]^+$ (100). (ESI) calculated for $C_{33}H_{36}N_2O_5S_2$ $[M+Na]^+$ 627.19, found 627.19.